Optimisation du contrôle fluidique de décollement en écoulement transsonique de canal

Quentin Chanzy

INSTITUT POLYTECHNIQUE DE PARIS

NNT : 2020IPPAX004

Thèse de doctorat

Optimization of fluidic control of separation in a transonic channel flow

Thèse de doctorat de l'Institut Polytechnique de Paris
préparée à l'Ecole polytechnique

École doctorale n°626 Institut Polytechnique de Paris (IP Paris)
Spécialité de doctorat : Mécanique des fluides

Thèse présentée et soutenue à Meudon, le 20 janvier 2020, par

QUENTIN CHANZY

Composition du Jury :

Holger Babinsky Professeur, University of Cambridge	Rapporteur
Éric Goncalves Professeur, ENSMA - Institut P'	Rapporteur
Azeddine Kourta Professeur,Université d'Orléans - PRISME	Examinateur
Lionel Larchevêque Maître de Conférence, Aix-Marseille Université IUSTI (UMR 7343)	Examinateur
Christian Tenaud Directeur de Recherche CNRS, LIMSI (UPR 3251)	Président
Éric Garnier Directeur de recherche, ONERA (DAAA)	Directeur de thèse
Reynald Bur Maître de recherche, ONERA (DAAA)	Co-directeur de thèse
Franck Hervy Responsable Innovation, DGA/AID	Invité

ONERA
THE FRENCH AEROSPACE LAB

Remerciements

Avant toute chose, je souhaite remercier le Professeur Azzedine Kourta, Lionel Larchévêque, Christian Tenaud et Franck Hervy d'avoir accepté de participer au jury de ma thèse.

Je tiens, également, à remercier le Professeur Éric Goncalves pour sa relecture de ce long manuscrit.

A special thank you to Professor Holger Babinsky for all his remarks and discussions on the manuscript. Your challenging questions allowed me to improve the quality of this thesis and to deepen my understanding of the subject.

Je remercie également Éric et Reynald de m'avoir encadré et guidé sur ce vaste sujet qu'est le contrôle fluidique de l'interaction onde de choc / couche limite. Merci de m'avoir permis de creuser pendant trois ans, à fond, un seul et même sujet; cela ne m'arrivera pas souvent. Merci pour la partie num' Éric et, grâce à toi Reynald, j'ai appris que la gestion des plannings expérimentaux, c'est complexe et que quoi que l'on fasse, ça finit toujours à la "Bur".

Cette thèse n'a pas été réalisée entièrement seul et j'ai pu compter sur le soutien de nombreuses personnes, notamment pour la complexe implémentation de la Tomo-PIV. Un merci tout particulier à Carlos Lopez-Hernandez, Cédric Illoul, Gilles Losfeld, Caroline Goudeau, Philippe Cornic et Benjamin Leclaire pour leur aide tout au long de cette entreprise ardue.

Merci à Pascal M, le spécialiste de S8 qui m'a suivi pendant mes essais. Merci à Pascal A, Jean-Pierre, Pierre et Jérôme spécialistes ès capteurs et actionneurs pour leur aide dans la conception du montage de contrôle. Merci aussi à Gilles, Jean Marc, Joel, Nicolas, Thierry, François pour toute la partie technique des essais.

Merci à Paulo, Philippe, Fabien, Fulvio, Nicolas, Guillaume et David, pour leur aide et leurs conseils sur la partie numérique : RANS, ZDES, elsA, Cassiopée, etc.

Et pour la partie administrative et organisationnelle, merci à Claire, Tanya et Claudine.

Je tiens aussi à remercier mes co-bureaux : Georg, Léopold, Guillaume et Camille pour nos discussions plus ou moins constructives en fonction de nos avancées respectives.

Merci aux habitués du rituel de la pause-café pour nos bons fous rires : Mathieu, Luis, Romain, Simon, Euryale, Lucas, Léopold, Tristan, Johann, Jean Lou et Carlos.

Merci à tous les doctorants pour nos joyeux déjeuners et pour les bons moments passés à la conférence de Vienne : Benjamin, Anthony, Arnold, Catherine, Diogo, Tobias, Damien, Nicolas, Ye Bonne et Jhanavi.

Merci à la dream team maintenant renommée 2-2: Johann, Jean-Lou et Carlos. Pour avoir souffert ensemble sur cette étrange période de notre vie, à galérer comme des forcenés sur des sujets plus obscures les uns que les autres, le tout ponctué de jeux de mots plus ou moins réussis qui nous ont permis de tenir jusqu'au bout ! ou presque...

Un grand merci à ma famille et belle famille qui m'ont toutes les deux soutenu, notamment pendant les longs mois d'été de la rédaction. Sans votre aide je n'y serais pas arrivé, et presque dans les temps ! Oui j'étais en avance par rapport à beaucoup d'autres ! Et merci pour les superbes macarons de soutenance !

Un immense merci enfin à Astrid qui est devenu ma femme juste avant le début de cette thèse et grâce à qui je suis devenu papa pendant cette thèse. Et comme une thèse et un bébé, c'est trop facile, tu as rajouté à cela des semaines de papa en solitaire pendant tes longs déplacements professionnels. Merci d'avoir été à mes côtés pendant tout ce temps, et d'avoir supporté un mari collé à son manuscrit. Tout ça pour ça !

Merci enfin à ma fille Isaure de m'avoir émerveillé pendant ses premières années, on apprend tellement plus vite à cet âge-là ...

Abstract

Flow control of a transonic Shock-Wave / Boundary-Layer Interaction (SWBLI) is investigated in the context of transonic air inlets. A shock-wave / turbulent boundary-layer configuration with separation zones is considered in the transonic wind tunnel S8Ch at ONERA Meudon.

After an introduction on the general context of the study, a state of the art is developed on the different control methods used for SWBLI with separation. This part focuses especially on the mechanical (vane-type) and fluidic Vortex Generators (VGs). Of particular interest are the studies on the interaction between a jet and a transverse flow.

Then, presentation of various experimental means of investigation and numerical tools is considered. On the experimental side, a careful attention is paid to the description of the tomographic Particle Image Velocimetry technique (Tomo-PIV). On the numerical side, both Reynolds Averaged Navier Stokes (RANS) and Zonal Detached Eddy Simulation (ZDES, a hybrid method between RANS and Large Eddy Simulation, LES) are described as well as their implementation for the modeling of the SWBLI. The overset meshing method used for an automatic and rapid modification of the small jets configuration is also specified.

The third part presents the RANS simulations of the uncontrolled SWBLI, the results are compared to previous experimental results. The structure of the central and corner flow separations are highlighted.

A Kriging-based optimization process applied to a fluidic control of the SWBLI is detailed. In a first step, the pitch and skew angles of ten fluidic VGs are optimized. An optimal configuration found during this process is then used as a central control while a jet is added to control specifically the corner flow separation. A second optimization is applied to four parameters defining the lateral jet: the pitch and skew angles, as well as the spanwise and streamwise locations of this added jet. All these processes aim at improving the homogeneity of the flow and reducing the total pressure losses downstream of the interaction. The optimal control configuration found uses jets blowing slightly in the upstream direction (opposite to the main flow direction). The vorticity patterns developed by these jets are investigated.

Using the results of the optimizations, two control configurations are adapted to the wind tunnel test section constraints. Actuators are specified and tested in order to modulate the flow inside the VGs. The first configuration is close to classical configurations found in the literature (i.e. jets oriented in the main flow direction) and the second one is derived from the optimal jets configuration thanks to the optimization process.

Finally, comparisons of results are carried out between the clean case and the two controlled cases using notably steady and unsteady pressure measurements and tomographic Particle Image Velocimetry (Tomo-PIV). This confirms the capacity of fluidic VGs to control a tridimensional SWBLI with massive central separation and the interest of using slightly reversed jets to control corner flow separation.

For French readers, a digest of this manuscript is presented in the Appendix A.1.

Contents

Introduction:
Shock-Wave / Boundary-layer Interaction

If we knew what it was we were doing, it would not be called research, would it?
Albert Einstein

Context

Traveling faster than sound remains a dream, which since 2003 and the Concorde's last flight, is reserved to fighter pilots. The recent revival of interest for the civilians supersonic airplanes brings to the fore once more the high complexity of the conception of effective supersonic aircraft. Notably, the conception of the air intakes remains a preeminent challenge during the design process.

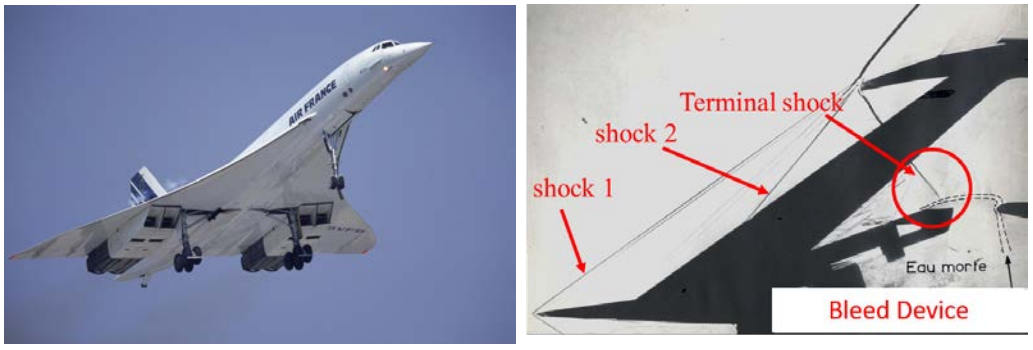

(a) View of the air intakes positioned under the ogival delta wings of a Concorde.

(b) Schlieren visualization of the flow pattern in the air intake.

Figure 1: Air intakes of a Concorde.

The shock-wave system allows to decelerate the supersonic flow to subsonic velocity inside the inlet before its injection into the engine. Due to total pressure losses through the shocks, the efficiency of the aircraft propulsion is going to decrease with an increase in Mach number. The role of the air intake is to provide the maximum thrust for the minimum induced drag (see Laruelle [111]). The maximum thrust is ensured by converting

the maximum of kinetic energy of the incoming flow to pressure before the engine. The minimum drag will be ensured by the capacity of capturing just the flow needed by the engine without needing to dismiss some part of it. This energy conversion (from kinetic to potential) must be done with the minimum induced inhomogeneities in order not to generate non uniform constraints in the engine.

The development of the air intakes has been historically a long process of experimental tests and step by step improvements (see Surber and Tinapple [163]). These improvements led to complex system such as the one used for the Concorde air inlet presented on Fig. 1. The air inlet is a combination of several external oblique shocks, a normal shock in the vicinity of the inlet entrance and a boundary-layer trap shown on Fig.1. This device is used to control the interaction between the normal shock and the boundary-layer to prevent separation, and also to damp the unsteadiness linked to such interaction.

Indeed, one difficulty of the air inlet conception lies in the fact that the shock-wave necessary to this mechanism is going to interact with the turbulent boundary-layer developing at the wall. The well known phenomenon of Shock-Wave / Boundary-Layer Interaction(SWBLI) often provokes the separation of the flow. Therefore, this separation leads to losses, inhomogeneities and unsteadiness of the flow.

Shock-wave

Shock-waves are discontinuities that happen in supersonic flows. The flow endures a rapid rise of pressure, density and temperature with a deceleration among a really small length (close to 10 to 20 times the incident flow molecular mean free path). If the shock-wave takes place on a surface, the surface experiences a local high load and high temperature which can be problematic on high speed vehicles. Furthermore, shock-waves generate a rise in the entropy of the flow and thus a decrease of total pressure.

Physical quantities' variation through the shock-waves are governed by the Rankine-Hugoniot equations (see for example Babinsky and Harvey [6]). These equations for two types of shock-waves, normal and oblique. Normal shock-waves are encountered when the shock-wave is perpendicular to the main flow whereas oblique shock-waves are linked to a variation in flow direction. An oblique shock-wave decelerates the flow but the latter may remain supersonic downstream of the shock-wave. For the oblique shock-waves, two solutions coexist: a strong one where the resulting flow is subsonic and a weak one where it normally remains supersonic. Strong shock-waves and especially normal shock-waves, induce more entropy creation and thus more loss of total pressure. This is why several oblique shock-waves are frequently preferred to a normal shock-wave.

A common source of drag Hence shock-waves are a source of drag which can be significant at high velocities. shock-waves are quite common in aerodynamic configurations, they happen in air inlets as seen before but also on civil aircraft wing, turbojet's or helicopter's blades. Even for aircraft flight at Mach 0.8 cruise condition, shock-waves appear on parts where the flow is accelerated, as the wings and the fuselage. A visualization of the shock-waves producing drag on the Common Research Model airliner is presented on Fig. 2. The recent calculations of Hue et al. [91] evaluate to 5% the portion of drag produced by shock-waves on a commercial airline. So shock-waves are a common and complex problematic both in internal and external aerodynamic.

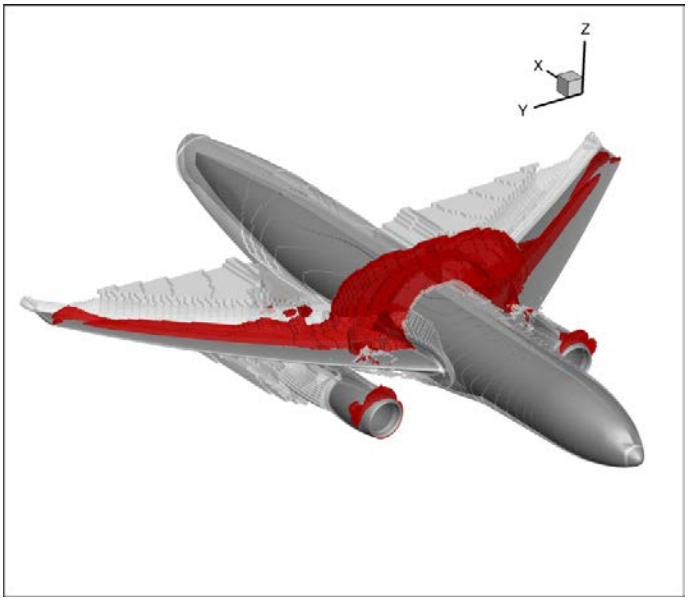

Figure 2: Visualization of the volumes (in red) where shock-waves produce drag on the Common Research Model Airliner (from Hue et al. [91]).

Air inlet In the context of air inlet design, the shock-waves can be chosen to be placed internally or externally. The use of Pitot type air inlet[1] generates a single normal shock which is penalizing at high Mach numbers. Since the work of Oswatitsch [128], several oblique shock-waves are used to decelerate the flow on supersonic aircraft. Indeed, the number of shock-waves used to decelerate the flow also influences the theoretical pressure recovery and thus the efficiency of the air inlet (see Fig. 3). Nevertheless, Pitot air inlets may still be chosen depending on a compromise between efficiency, maximum velocity and stealth (see for example the Rafale from Dassault Aviation). Indeed, on recent aircraft, the stealth is a researched characteristic and external shock-waves which are induced using external diverters increase the radar signature of the airplanes (see Laruelle [111]).

In a nutshell, all air inlets present different complex combinations of shock-waves depending on a compromise between several parameters: their efficiency and so the consumption of the aircraft, their radar discretion, their weight and their objective of maximum velocity (see Laruelle [111]). Nevertheless, all inlets present shock-waves which are going to interact with boundary-layers.

Boundary-layer

When a flow passes along a surface, viscous phenomena set up a velocity distribution which goes from the main flow velocity far from the wall down to a null velocity at the wall. For flows where the Reynolds number[2] is high enough, the flow transitions from laminar to turbulent and small structures appear near the wall. In this study, only the fully turbulent flows will be considered. Turbulent boundary-layers are a wide subject of study Lighthill [114], George [80]. Their numerical modeling remains a challenge for

[1] Pitot air inlets are the simplest air intakes, only composed of a single tube without compression system.
[2] The Reynolds number characterizes the ratio between the inertial effects and viscous effects.

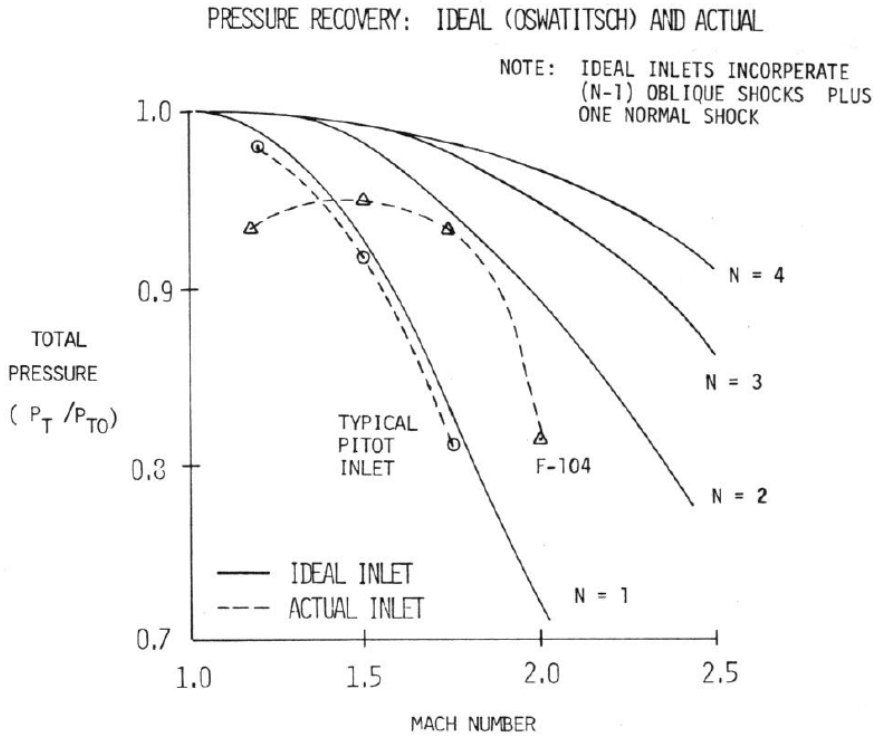

Figure 3: Theoretical pressure recovery with respect to the Mach number and the number of shock-waves used in the air inlet (from Surber and Tinapple [163]).

complex configurations at high Reynolds numbers. This subject will be rapidly addressed in the choice of numerical method; the reader is referred to the work done at ONERA for a more detailed presentation of their characterization and numerical modeling (see Pamiès [131], Renard [139], Bannier [10] for example).

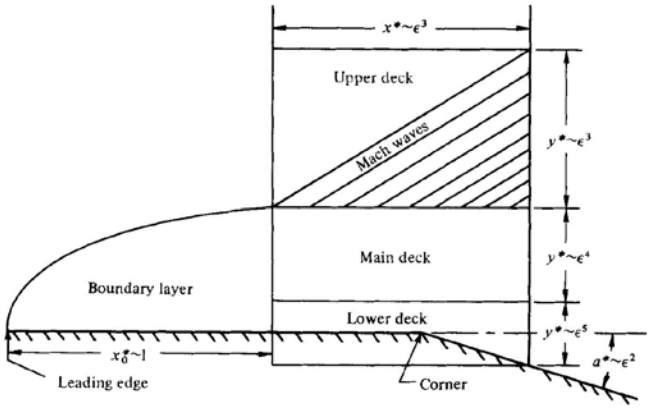

Figure 4: Boundary-layer triple deck decomposition from Rizzetta et al. [141] with $\epsilon \sim Re^{-1/8}$.

The main characteristics to keep in mind for the following study are described hereafter. A turbulent boundary-layer can be decomposed into three main parts (called triple deck

decomposition by Lighthill [114]) which are presented on Fig. 4. The outer boundary-layer is where the turbulent structures dominate the flow, the lower deck is the region really close to the wall where the viscous effects dominate the flow. In between an overlap region or middle deck takes place. The part of the flow close to the wall is really sensitive to adverse pressure gradient. Even if more resistant than laminar boundary-layer due to a smaller viscous sublayer, the turbulent boundary-layers may detach when suffering a strong adverse pressure gradient.

The turbulent boundary-layer is also the location of an energy transfer, the kinetic energy of the flow is transferred along a cascade of turbulent structures down to really small scales where the energy is dissipated into heat. This dissipation is thus a source of drag which is damaging for the vehicle.

Corner flow boundary-layers The development of turbulent boundary-layers in corner is also of interest for internal flows as it adds complexity to the flow. Indeed, the boundary-layer at a corner for turbulent flows differs from laminar ones. The velocity does not only depend on the distance to the closest wall. On a slice perpendicular to the corner, secondary flows have been identified. They have been measured and explained in Gessner [81]. The turbulent shear stress in the corner induces a flow directing to the corner, going along the corner bisector. This secondary flow is going to provoke local thickening of the boundary-layers on the two walls forming the corner as it can be seen on Fig. 5. These parts of the boundary-layer are more sensitive to interaction with shock-waves.

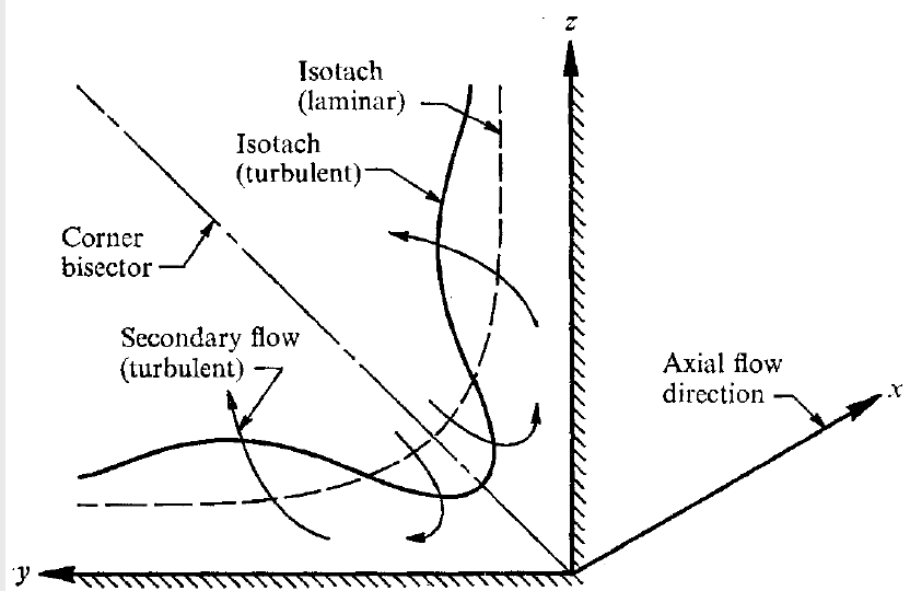

Figure 5: Modification of the isotach in a turbulent corner flow with respect to laminar corner flow (from Gessner [81]).

Interaction

The Shock-Wave / Boundary-Layer Interaction (SWBLI) is a common problem in aerodynamic as it takes place in a wide variety of configurations and leads to unwanted situations

such as buffet on wings (see for example Sartor et al. [152], Délery [48]), separations on subsonic air inlets (see for example Coschignano and Babinsky [37, 38], Coschignano et al. [39]), and buzz phenomenon in supersonic air inlets which is the starting point of the current study.

From a more theoretical point of view, several configurations have been studied: incident reflected shock, ramp induced shock or normal shock-wave. The latter one will be the one studied here. The reader is referred to the reference books Délery [50], Babinsky and Harvey [6] for a more precise description of the other configurations and for a more applied point of view to Seddon and GoldSmith [156].

When a normal shock-wave is impinging a boundary-layer, it provokes locally a severe adverse pressure gradient which competes with the longitudinal momentum. For strong enough pressure gradient, separation happens and the normal shock-wave takes the form presented on Fig. 6, called λ shock-wave near the wall. The normal shock-wave is decomposed into two oblique weak shock-waves. The leading oblique shock-wave provokes the separation and the thickening of the boundary-layer. The rear oblique shock-wave appears at the triple point where the leading shock and the normal shock meet. It ensures the compatibility between the flow passing through the leading shock-wave with the one passing through the normal shock. It should be noticed that the flow may remain supersonic after the rear shock , forming a supersonic tongue. With the mixing effects of turbulence, the flow then reattaches.

The main sources of drag are the separation zone, which is responsible for the main losses (viscous drag) but also the normal shock-wave (wave drag). Indeed the compression system composed of the two 'legs' of the shock (leading shock and rear shock on Fig. 6) is almost isentropic and this part of the shock system is more effective in terms of pressure recovery than the normal shock part.

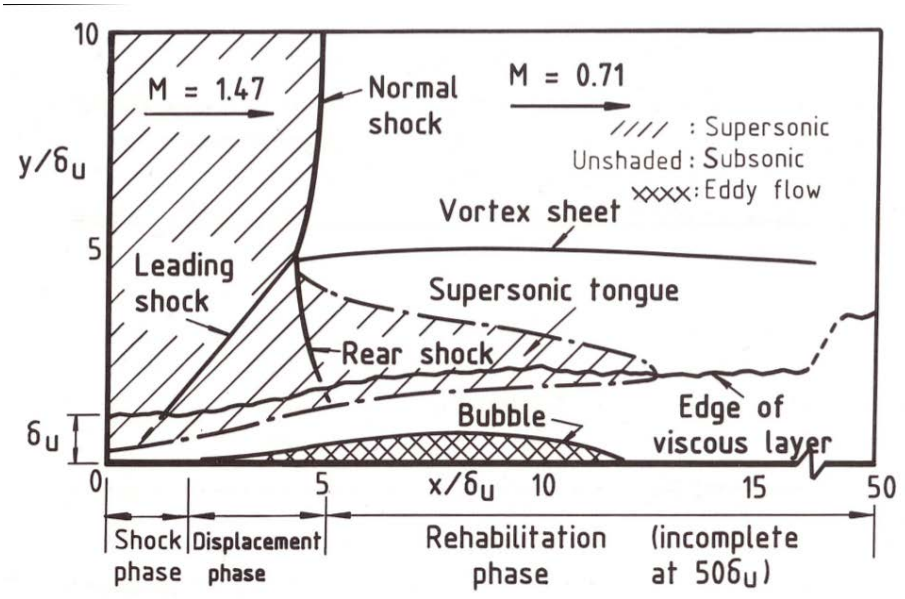

Figure 6: Scheme of a transonic separated interaction between a normal shock and a turbulent boundary-layer (from Seddon and GoldSmith [156]).

Another important aspect of this kind of interaction is that, due to the fact that the flow is subsonic after the interaction, the shock-wave is not "shielded" from any acoustic

perturbation coming back from downstream. This makes this interaction really dependent of downstream conditions.

Unsteadiness It has been noticed during experiments that, in separated transonic SWBLI, natural unsteadiness frequencies appear and drive the shock movement. This phenomenon has been widely studied (see Délery [50], Dupont et al. [58], Dussauge et al. [59], Dolling [56], Babinsky and Harvey [6], Doerffer et al. [55], Sartor et al. [154], Gaitonde [69] among others), and the unsteadiness have been linked to an acoustic interaction with the downstream flow. This differs from the unsteadiness found in different SWBLI configurations where the unsteadiness may be linked to the incoming turbulent structures in the boundary-layer and to a "respiration of the recirculation bubble" (see Babinsky and Harvey [6], Piponniau et al. [136], Humble et al. [92], Clemens and Narayanaswamy [32], Robinet and Casalis [142]).

This unsteadiness may provoke strong movement of the shock-wave which can be damageable to the structure where the interaction takes place.

Buzz In particular, this unsteadiness may be linked to the buzz phenomenon which takes place in air inlets and may lead to their unstart. This is obviously damageable for the engine. Two different scenarios from Dailey [42] and Ferri and Nucci [64] are considered for the buzz phenomena which itself can be decomposed in two distinct phases: little and big buzz. Recent numerical works of Trapier et al. [170, 171] manage to reproduce, using Delayed Detached Eddy Simulation (DDES), the big buzz phenomenon. The different steps of this phenomenon linked to the Dailey criterion (a massive separation on the compression ramp), are presented on Fig. 7. The apparition of a huge separated zone (b) provokes a strong oscillation of the last shock-wave which adopts a super-critical configuration (d) and (e) before going back to the beginning of the cycle. This may lead to a reversed flow and an unstart of the engine in the sub-critical regime (a).

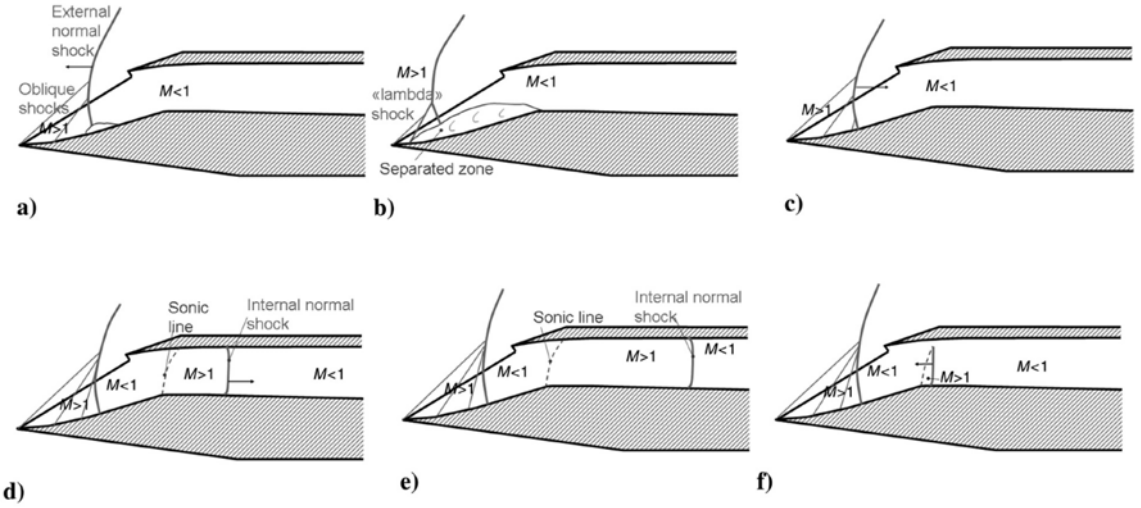

Figure 7: Big buzz steps decomposition obtained from a DDES modeling (from Trapier et al. [171])

It can also be noticed that the study of Trapier et al. [171] emphasizes the importance of the corner flow separation in the buzz phenomenon, this specific separation zone should

be precisely controlled in order to improve the operation of air inlets close to buzz limit.

Objective

In order to prevent the drawbacks linked to the buzz phenomenon which limit the flight envelop, many different control devices have been studied: bleeding, blowing, adaptive geometries like 2D and 3D bumps, diverters, and Vortex Generators(VGs)(see Lin et al. [115], Babinsky and Ogawa [7], Rosenblum [143], Ternoy et al. [165] for examples of review of the control methods). These methods require a full understanding of the complete problem. They should improve the efficiency of the air intake, taking into account their added mass and relative energy consumption. The physic field of flow control is detailed including its fallacies and limits in Crowther et al. [40]. Indeed, the technology of flow control using VGs, even if widely explored over the past 50 years, only resulted in few usages on real aircraft air intakes. For Vortex Generators, they can be seen on the air inlet of the F111 only. The preferred options for control are bump, diverter and bleed device as on the Concorde. Nevertheless, as it can be seen on Fig. 8, at high velocities, the bleed becomes the main source of drag for supersonic aircraft and so this control method should be improved with other control methods in order to gain efficiency.

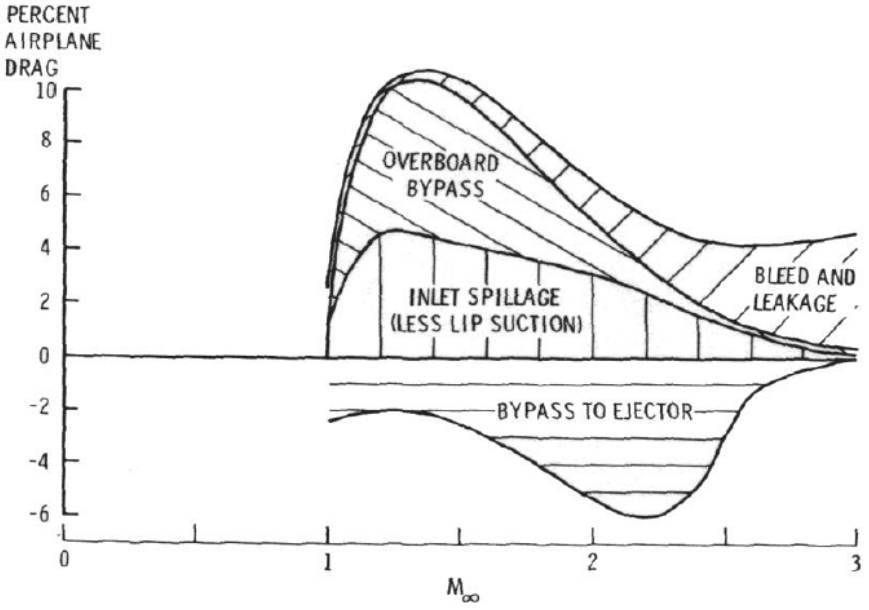

Figure 8: Decomposition of drag for a supersonic aircraft intake with respect to the Mach number (from Surber and Tinapple [163]).

Following the conclusion of Laruelle [111], "Air intakes must be designed by a 'system' approach. Optimising them is a long and difficult process", the author of the current study choose to investigate the control technique of air jet Vortex Generators from a fully 3D point of view. This control device seems promising as it displays the same advantage as the mechanical VGs which have been proven to be efficient to reduce the separation zone (see Lin [116], Lee et al. [112], Titchener and Babinsky [167], Bur et al. [20]). Furthermore it has the advantage of being energy efficient, generating less compression waves than the mechanical VGs thus improving the drag of the air intake and it can easily be turned off when not necessary and so not be a drawback in other flight conditions.

The goal of the study is to decrease the total pressure losses and to recover as much

as possible the homogeneity of the flow of a transonic separated normal Shock-Wave / turbulent Boundary-Layer Interaction by using air Vortex Generators.

Outline

The study is organized as follow: firstly, a presentation of the different control methods of the shock-wave boundary-layer interaction is developed in Chap. I, with a particular interest taken to the mechanical and fluidic Vortex Generators and to the physical phenomenon resulting from the interaction between a jet and a transverse flow.

Secondly, Chap. II is dedicated to the presentation of the main experimental and numerical tools used. The transonic wind tunnel studied is introduced as well as the measurement techniques implemented, with a special attention paid to the tomographic Particle Image Velocimetry (PIV). The numerical methods of Reynolds Averaged Navier Stokes (RANS) and Zonal Detached Eddy Simulation (ZDES) and parameters used to simulate the flow without and with the presence of fluidic vortex generators are then developed.

Thirdly, the RANS numerical modeling of the 3D uncontrolled Shock-Wave / Boundary-Layer Interaction are displayed in Chap. III. The central and corner flow separations are examined and compared to experimental results from previous studies.

Fourthly, a global optimization process devoted mainly to the pitch and skew angles of the air Vortex Generators is presented as well as its results in Chap. IV. This Kriging optimization is decomposed in two steps, the first one is focused on the central separation control while the second one adds a corner flow separation control. The control configurations are detailed as well as an explanation of their effectiveness based on a study of the vortices developed by the interaction of a single pitched and skewed jet with a transverse flow.

Fifthly, the process of conception and implementation of two control configurations for the wind tunnel tests, derived from the optimization, is described in Chap. V. The dynamic capacities of the actuators chosen for the control are presented as well as the limitations deriving from their characterization.

Sixthly, Chap. VI and Chap. VII presents comparison of experimental and numerical results of the characterization of the uncontrolled and fluidic Vortex Generators controlled configurations. Schlieren flow visualizations and measurements (wall pressure by Kulite sensors and velocity field by tomographic PIV) give information on the effective capacity of control of the air vortex generators.

Lastly, a summary of the principle results and conclusions and perspectives of this study are detailed in Chap. VIII.

I

Flow control context

Je sens que je progresse à ceci que je recommence à ne rien comprendre à rien.
Charles-Ferdinand Ramuz

Objectives

This chapter is dedicated to the presentation and the comparison of the different methods of control of SWBLI existing in the literature. Their presentations follow the classical arrangement presented in Ashill et al. [4] which decomposes the mean of control of the SWBLI between the ones controlling the shock and the ones controlling the boundary-layer. After a presentation of the general concepts, shock control methods are briefly presented before a more precise display of the boundary-layer controls. In this category, a reinforced attention will be paid at the fluidic Vortex Generators (VGs). Noticeably, the works on the structure of vorticity developed by the interaction between an angled jet and a cross flow, and more applied studies of fluidic control, will be presented following the historical approach. The method of control of the corner flow separation will be presented as well, before a sum up of all the results and a presentation of the specificities of the current study.

Contents

I.1 General concept

The idea of controlling the Shock-Wave / Boundary-Layer Interaction has been a long and vast domain of research over the past eighty years due to the fact that the unsteadiness and the losses associated with SWBLI can be really damageable to wings in the case of buffet phenomenon, and to air inlet in the case of buzz phenomenon. The interested reader is referred to Délery [50], Joslin et al. [98], Ashill et al. [4], Babinsky and Harvey [6], Ternoy et al. [165] for regular reviews of the whole diversity of control methods. The wide diversity of control methods are composed of basic principles: the control either of the shock-wave, by the use of specific geometries such as bump or cavities, or the control of the incoming boundary-layer by the use of mechanisms to re-inject energy into it. This classification does not imply that some tools can control the boundary-layer without controlling the shock-wave and vice versa. Nevertheless, it considers the part the method is meant to control directly, the other one (the boundary-layer or the shock-waverespectively) being modified by the retro-action of the modification of the pressure gradient. This pressure gradient along the wall, is linked to both the shock-wave intensity and the size of the boundary-layer.

The precise definition of a perfect control for a SWBLI is arduous since, as explained in Délery and Bur [52], the control of the shock-wave influences the boundary-layer and vice versa in opposite direction. Indeed, when trying to reduce the drag generated by the shock-wave, the control smears the shock-waves and thus provokes a thickening of the boundary-layer. This increases the friction drag due to the boundary-layer. On the contrary, in the case of separation, the control of the incoming boundary-layer diminishes the separation and thus, the width of the oblique shock-wave (the "legs" of the λ shock-wave) and so expands the normal shock-wave. This increases the wave drag. The impact of each method on the total pressure losses, is detailed on Fig. I.1. The total pressure loss can be linked to friction or wave drag.

In the case of an air inlet, the most important part of the interaction to control, is the boundary-layer since the separation may lead to the buzz phenomena. In the case of the wing of a civil aircraft, the control of the shock-wave may be more interesting since the balance between wave drag and friction drag may be in favor of friction drag (see Délery and Bur [52], Babinsky and Ogawa [7]).

The definition of a control device also have to take into account the feasibility and the efficiency of the system. Indeed, the advantage brought by the control system needs to overcome its weight.

In the following, a short presentation of the shock control methods is undertaken before a more complete presentation of the boundary-layer control methods. Especially, the mechanical VGs studies are detailed as well as the lessons learned which can be used for fluidic VGs. Then, the vortices produced by normal and angled jets in cross flow are presented as well as some studies of control using fluidic VGs.

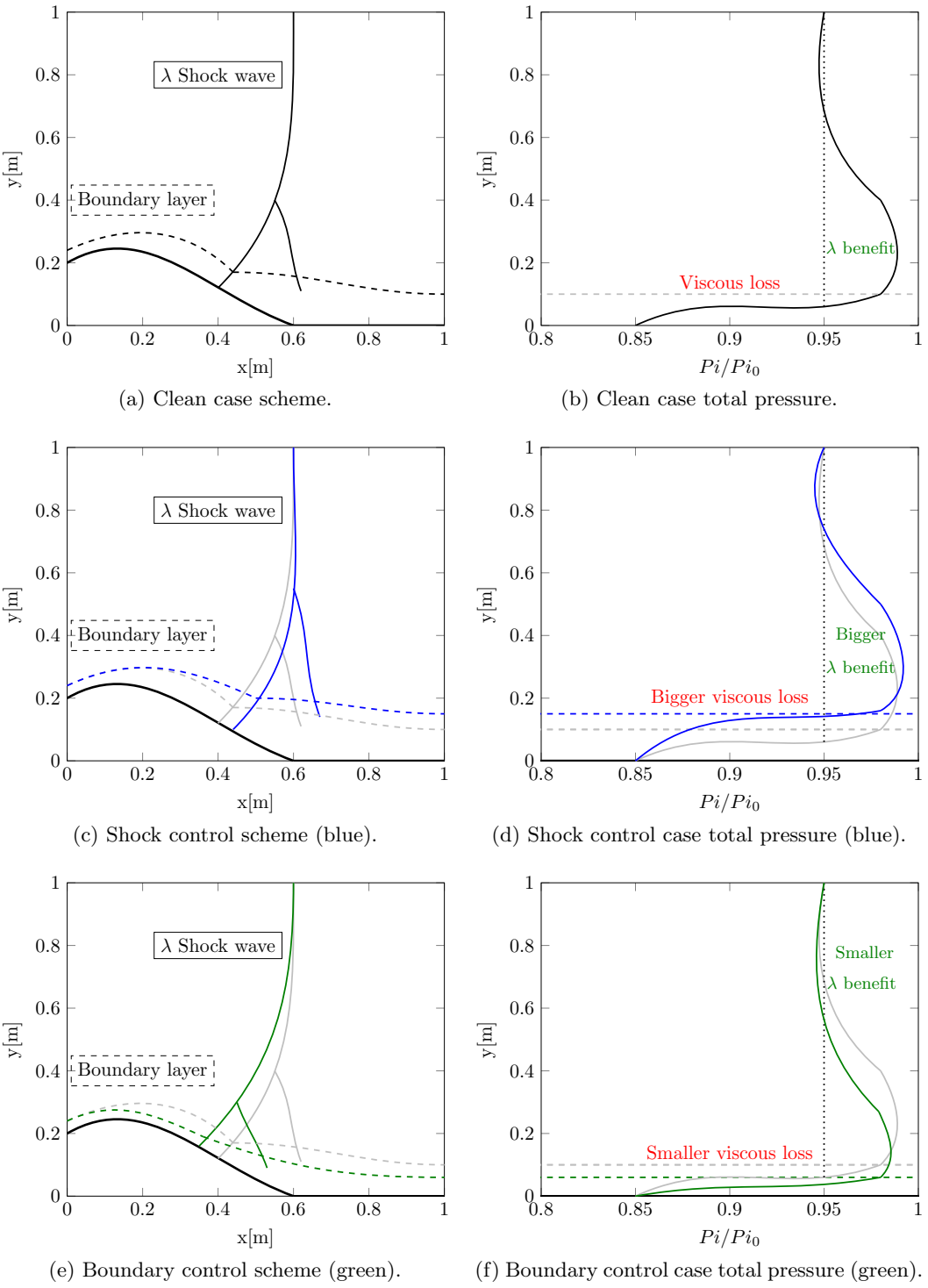

(a) Clean case scheme.

(b) Clean case total pressure.

(c) Shock control scheme (blue).

(d) Shock control case total pressure (blue).

(e) Boundary control scheme (green).

(f) Boundary control case total pressure (green).

Figure I.1: Influence of the shock and boundary control on the total pressure losses through the Shock-Wave / Boundary-Layer interaction.

I.2 Shock control

2.a Bump

One way to control the flow is to use a special geometry which is going to modify the pressure gradient near the wall and thus modify the intensity of the shock system. This control is optimized generally for wings (see Ogawa et al. [127], Babinsky and Ogawa [7]) or for subsonic inlets with locally supersonic regions due to high angles of aero-engine intake lips (see Coschignano and Babinsky [37, 38], Coschignano et al. [39]). The general idea is to use 2D or 3D bumps to wider the λ and this causes the triple point to rise, this decreases the wave drag as the two oblique shock-waves generate a lower rise of entropy than the normal shock-wave. The drawback of this mechanism is that it is really depending on the position of the bump relative to the shock-wave. Indeed, as it can be seen on Fig. I.2, if the normal shock-wave is positioned to far upstream, the flow re-expands on the bump and forms a secondary shock-wave which generates new losses. On the contrary, if the shock-wave is positioned to far downstream, the re-expansion takes place before the rear shock of the λ. Furthermore, the interaction between the rear shock-wave and the end of the bump may generate non expected vortices if the bump is 3D.

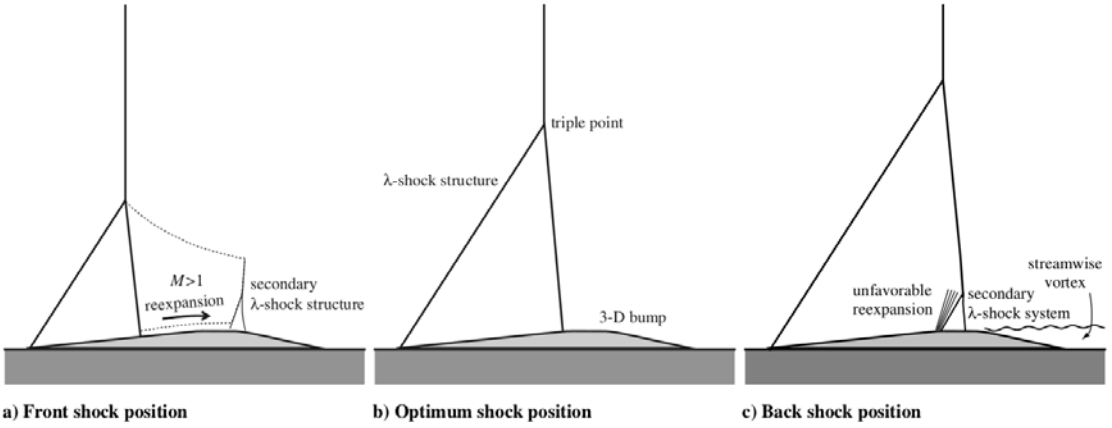

Figure I.2: Limitation of the control using 3D bump from Ogawa et al. [127].

2.b Cavity

Another way to modify the shock system shape is to place a cavity covered by a porous wall in the region of the SWBLI interaction, the pressure difference between the two part of the cavity will induce a natural re-circulation in the cavity and decompose the normal shock into a λ shape. This system has been studied for example in Bur et al. [18], Galli et al. [71], Galli [70], Délery and Bur [52]. The disadvantage of this system is that it provokes a huge thickening of the boundary-layer and thus provokes viscous losses. In order to reduce this drawback, more sophisticated system have been tested such as the combination of a cavity with a suction system which remove part of the thickened boundary-layer as it can be seen on Fig. I.3. This system necessitates an active control and thus the weight induced by this control may overcome its benefits.

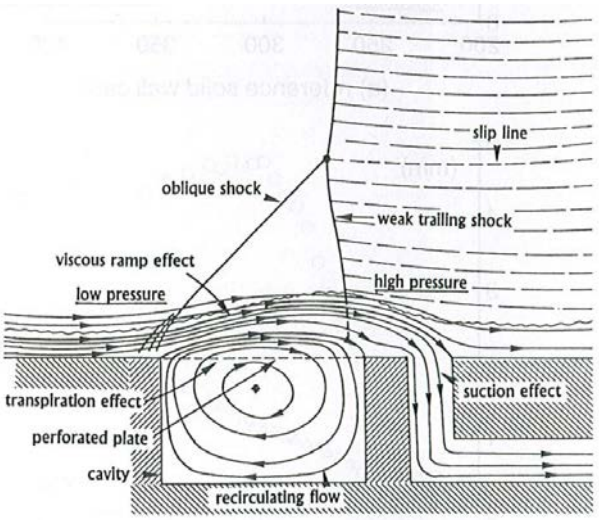

Figure I.3: Mixed control device using cavity and suction (from Délery and Bur [52]).

I.3 Boundary-layer control

3.a Bleed

A classical system used for the control of SWBLI is the removal of the boundary-layer after the interaction. This limits the losses and inhomogeneities in the downstream flow and prevents the boundary-layer developing into the inlet to separate. Furthermore, it allows to stabilize the interaction. This system can be seen for example on the Concorde (see Délery and Marvin [53], Seddon and GoldSmith [156] for more details). Nevertheless, the energy absorbed by the air inlet and dismissed by the bleed is lost. This can be limiting at high speed as seen in the Introduction on Fig. 8. Thus, others systems have been developed which work on the boundary-layer before the interaction in order to inject some energy from the inviscid flow into the boundary-layer.

3.b Mechanical vortex generators

The idea of mechanical vortex generators is to place small devices in front of the interaction in order to induce vortices which are going to mix the boundary-layer. This passive device have been largely studied and precise literature reviews can be found in Lin [116], Lu et al. [120], Panaras and Lu [132], Titchener and Babinsky [167].

Most of the VGs studied present the form of vanes shape or wedge presented on Fig. I.4. Different shapes have also been studied such as in Rybalko et al. [145], Cohen and Motallebi [33], Humrutha et al. [93] without clear improvement. The general idea is the same for all VGs: to produce one or two vortices. The vanes are designed to create one strong vortex and the classical wedge with the upper part downstream, a pair of counter-rotating vortices. The vanes are paired either in a co-rotating arrangement as presented on Fig. I.5(a) or in counter-rotating pair as presented on Fig. I.5(b). The pressure contours presented on these figures allow to distinguish the presence of the vortices produced by these configurations.

The main conclusions of the reviews by Lin [116], Lu et al. [120], Titchener and Babin-

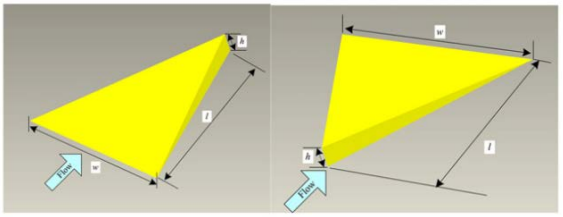

(a) Wedge shapes.

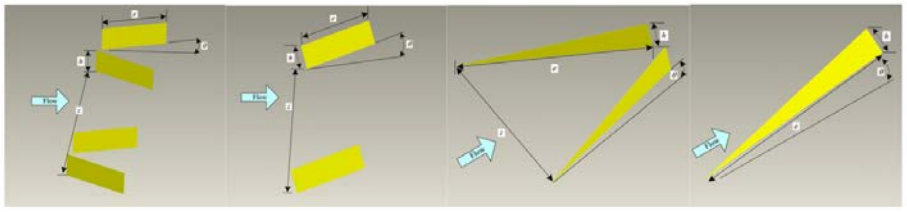

(b) Vanes shapes.

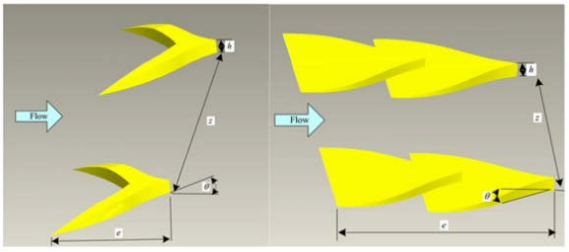

(c) More complex shapes.

Figure I.4: Different geometries of mechanical Vortex Generators (from Lu et al. [120]).

sky [167] for the control of transonic separated SWBLI are the following:

1. micro VGs of size close to $0.2 - 0.5\delta$ are sufficient to control these separations,
2. the VGs should be placed around 10δ upstream of the interaction in order to leave the time to the vortices to mitigate the boundary-layer,
3. the control induced by the VGs generally does not erase completely the separation but instead generates a strongly 3D pattern with numerous smaller zones of separation,
4. the counter-rotating configurations seem to be more efficient,
5. for wind tunnel of small width, the control of the central separation is strongly influenced by the corner flow separation.

A control using mechanical VGs worth mentioning is the one which took place in the wind tunnel of the current study. In Bur et al. [20] and Sartor et al. [153], the authors used different configurations of mechanical VGs in the form of vanes in co and counter-rotating pairs. These configurations managed to reduce the size of the central separation as it can be seen on the oil flow visualization presented on Fig. I.6. It can also be noticed that the control of the central separation zone increased the corner flow separation. Furthermore,

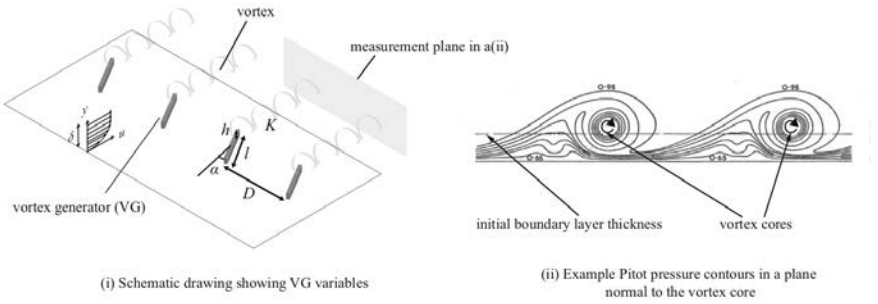

(a) Co-rotating vanes.

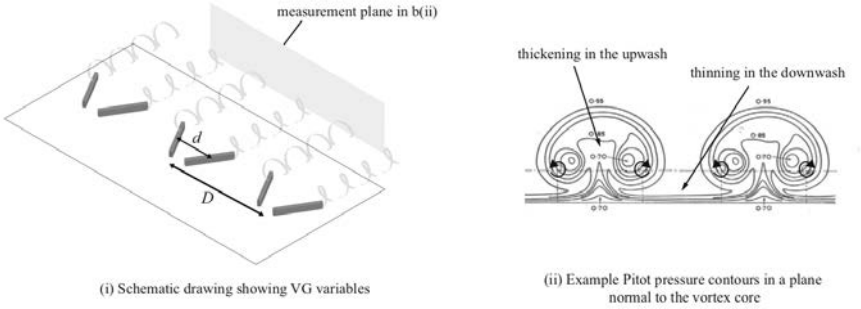

(b) Counter-rotating vanes.

Figure I.5: Representation of the two different common configurations of mechanical VGs and of the vortices they produce (from Titchener and Babinsky [167], Pearcey [134]).

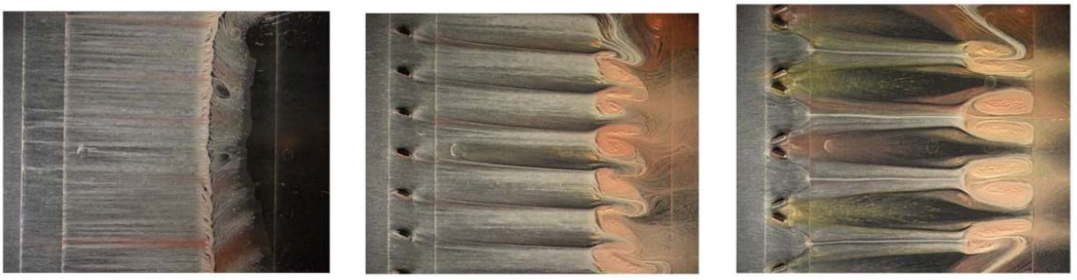

(a) Clean case. (b) Co-rotating vanes case. (c) Counter-rotating vanes case.

Figure I.6: Oil flow visualizations of the friction lines on the lower wall of the Délery bump with mechanical VGs (from Bur et al. [20]).

the co-rotating configuration is generating an asymmetrical flow with one corner separation stronger than the other one. This is may be damageable in the case of a real air inlet.

The mechanical VGs have proven to be efficient to control transonic separated SWBLI, however, they have a drawback. In configurations where they are not necessary, they induce drag and thus losses. This is the major advantage of the following method of control: the air VGs. Indeed, even if more complicated to design and test experimentally due to their wide number of parameters and to the fact that they are more complicated to implement in wind tunnel, the air VGs have the advantage of being easily turned off when they are not needed. Furthermore, they remove the risk of a mechanical VG being sucked into the engine in case of failure. Before presenting the air VGs, a short digression

on the co and counter-rotating vortices pair is developed.

Streamwise vortices close to a wall In order to understand the advantages and the drawbacks of the co and counter-rotating configurations, the induced velocities resulting from a pair of co and counter-rotating vortices close to a wall have been plotted on Fig. I.8 and Fig. I.7. Following the law of Biot-Savart, the velocities induced by each vortex on the other one is reproduced as well as the velocity induced by the presence of the close viscous wall. The latter one is equal to the velocity induced by an image vortex placed virtually symmetrically with respect to the wall. It should be noticed that the velocity induced by the image of the vortex 1 is neglected on the vortex 2 with respect to the two other induced velocities and vice versa.

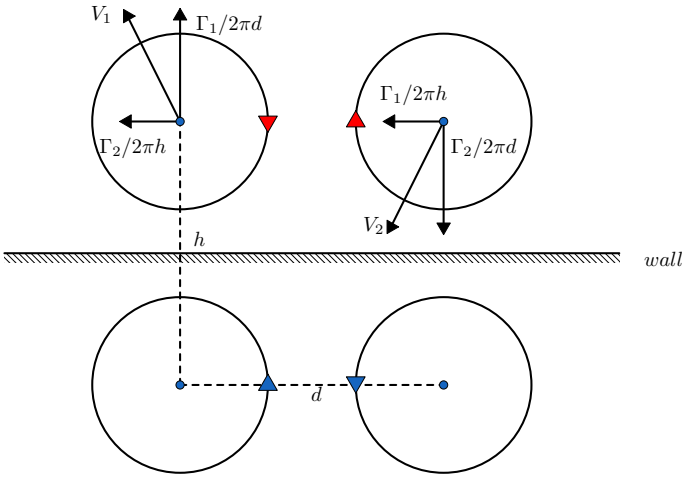

Figure I.7: Induced velocities for a pair of co-rotating vortices close to a wall (diagonal effects are neglected).

In the case of co-rotating vortices, the general induced velocity is going generate a lateral movement of the two vortices. During this movement, the induced velocity is going to repel the vortex number 1 from the wall and to bring closer the vortex 2. It should be noticed that the ratio between the distance from the wall of the vortices, and the distance between the vortices is going to influence strongly the movement of the vortices. Similarly, if the two vortices do not have the same vorticity, the induced velocity will be modified. The weaker vortex will be moved up or down more efficiently. Another important point is that for a theoretical infinite range of co-rotating vortices, the up or down movement will be annihilated.

In the case of the counter-rotating vortices, the resulting movement will be an elevation of the two vortices far from the wall and the two vortices will be attracted toward each other. Again, small variations in intensity and distances will modify the resulting velocities.

All these interactions should be taken into account while designing a control system. This made the system complex. Furthermore, when considering the corner flow, the lateral wall will also interact with the vortices and thus induced other velocities.

To conclude, the counter-rotating vortices seems to be more rapidly ejected from the boundary-layer. Nevertheless, they have been reported to be more efficient for the control in the literature. This seems to be due to a positive interaction between the two vortices, delaying their collapse, see Leweke et al. [113] and Gardarin et al. [73]. Another effect worth

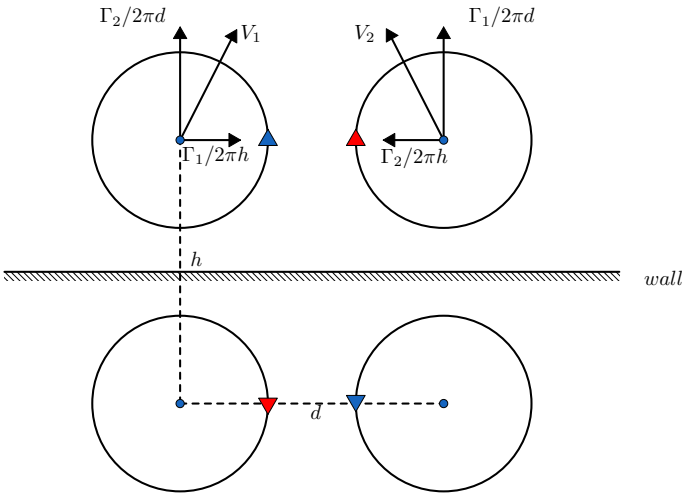

Figure I.8: Induced velocities for a pair of counter-rotating vortices close to a wall (diagonal effects are neglected).

mentioning described in Leweke et al. [113] is the "rebound" effect, when a unique vortex is placed close to a viscous flow, it manages to create and extract from the boundary-layer another vortex of opposite direction. This produces a vertical velocity for the main vortex and thus makes it look like the vortex rebound on the surface of the wall. Nevertheless, in case of sub micro vortex VGs, the VGs need to be placed close to the SWBLI and thus, the rebound phenomena has no time to happen and is not observed most of the time. The same happens with the Crow instability which can develop between two vortices.

3.c Fluidic vortex generators

The mechanical VGs have a considerable advantage with respect to fluidic VGs, they are easy to implement in wind tunnels for tests. On the contrary, the latter VGs necessitate more adaptations as well as a circuit of injection. Nevertheless, these last ones may be preferred to the mechanical VGs because they have one major advantage, they can be easily turned off during flight phases when they are not necessary. Indeed mechanical VGs generate drag in off-design situations. Furthermore, the fluidic VGs may be adjustable and even activated at different frequencies as pulsed jets. Thus, if they do not require a too high fluidic mass flow rate, they could be really attractive for SWBLI control.

The idea of using fluidic jets to generate vortices goes back to the work of Wallis [174]. He noticed that small jets managed to reduce the separation zones on a wing close to stall. The interaction between a jet and a cross flow has also been widely studied in fluid dynamic research since this fundamental phenomenon can be found in lot of different situations in which a mixing is necessary like combustion for example.

This study of fluidic generators will be presented in three parts, first a quick reminder of the characteristics of a perpendicular jet in cross-flow, then a more detailed presentation of the studies on pitched and skewed jets in cross-flow and then finally a presentation of some of the studies where pitched and skewed jets are used as fluidic vortex generators to control separation in diverse configurations.

i Perpendicular jet

The interaction between a perpendicular jet and a transverse flow is well characterized (see Margason [121], Jacquin [95], Karagozian [99, 100]), it produces a counter-rotating pair of vortices which can be used to mix the boundary-layer with the upper flow. The topology of vortices produced by a normal jet is presented on Fig. I.9. The principal vortices are the ones denoted CVP for Counter-rotating Vortex Pair. Three other types of vortices are also visible: shear layer vortices, horseshoe vortices and wake vortices. Nevertheless, they are really less energetic than the counter-rotating vortex pair and they will not be considered in the following study.

The trajectories of the vortices are self similar and depend on the momentum flux ratio r defined in Eq.I.1 and the diameter of the jet d (or on the velocity ratio VR for incompressible flow). For more details, the interested reader is reported to Margason [121].

$$r = \frac{\rho_j U_j^2}{\rho_\infty U_\infty^2} \tag{I.1}$$

Where ρ designates the density and U the velocity, the subscript j is for jet and ∞ stands for the cross flow.

However, the normal jet may not be optimal for flow control as the CVP is projected vertically and may leave easily the boundary-layer, due to the impulse of the jet penetration and due to the vertical velocity induced by the vorticity of the two vortices. Thus pitched and skewed jets seem to be a better alternative.

ii Pitched and skewed jets

The literature on pitched and skewed jets is less extensive to the author's knowledge. Most of the literature being composed of non exhaustive experimental tests. This is due to the

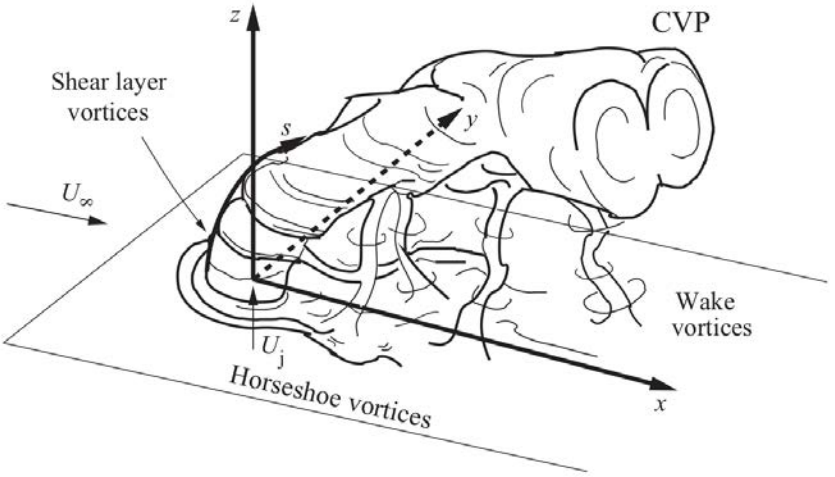

Figure I.9: Principal vortex structures produced by a jet normal to a main transverse flow (from Karagozian [100]).

complexity of testing a lot of different parameters such as the pitch and skew angles, the velocity ratio, the Reynolds number, the jet diameter or even the frequency of excitation. Furthermore, the two angles variations need to be considered at the same time as they both influence the vorticity pattern formed by the jet.

First of all, for the following study, the pitch and skew angles noted respectively α and β are defined following the convention defined on Fig. I.10. The configuration $(\alpha, \beta) = (0, 0)$ corresponding to a jet parallel to the main flow.

Some important studies, essentially incompressible, are detailed in the following, their general characteristics are reported in Table I.1 and their main physical parameters are presented in Table I.2.

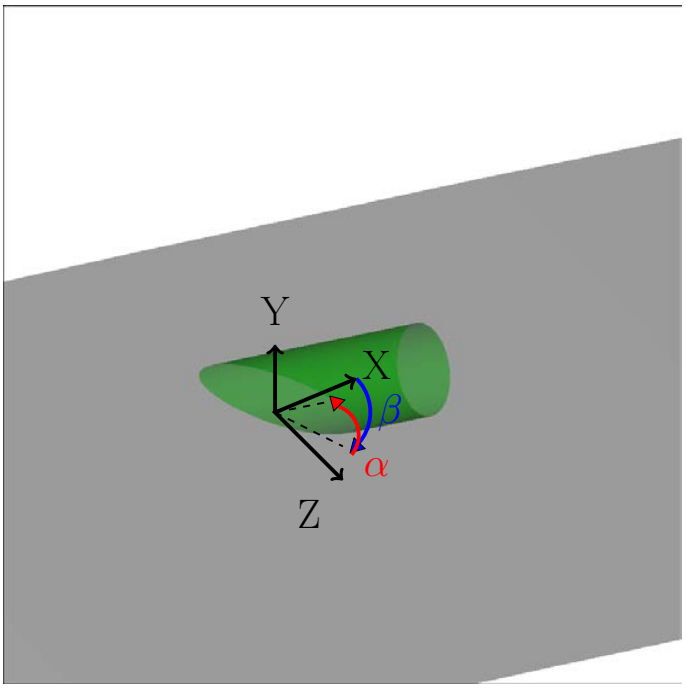

Figure I.10: Definition of the pitch and skew angles, respectively named (α, β) used in this study.

Table I.1: Main pitched and skewed jets studies: general characteristics

Author	Year	Type	Subject	Means of investigation	Conclusion
Compton and Johnston [34]	1992	Expe	Single jet	5hole P probe/ vorticity	Best (45,45-90)
Zhang [181]	1993	RANS	Single jet	Velocity /vorticity	Small VR Best(45,60-90)
		RANS	CoR jets	Velocity /vorticity	independent distance, $\Gamma \searrow$ quicker CtR
		RANS	CtR jets	Velocity /vorticity	$\omega \nearrow$ for closer VGs
Bray and Garry [15]	1999	Theorical	Single jet	Vortex circulation	circulation=f(mass flow,P) best(30,60)
Han et al. [88]	2000	Expe	Single Jet	Mie-scattering visu	$\nearrow$ spreading reverse jet, trajectory prevision
Khan and Johnston [102]	2000	Expe	Single jet	LDV	Best (30,60)
Rixon and Johari [140]	2003	Expe	Single jet	LDV/PIV	linear variation of circulation with VR
Godard and Stanislas [84]	2006	Expe	CoR jets	Friction/ PIV	small influence skew, distance
		Expe	CtR jets	Friction/ PIV	3D Cf, best(45,90)
Shapiro et al. [157]	2006	Expe	Pulsed single jet	Hot wire/photograph	Influence f on jet penetration
Kostas et al. [105]	2007	Expe	CoR jets pulsed	Hot wire/ friction/ SPIV	impulse $\nearrow$ penetration, influence f, best(45,90)
		Expe	CtR jets pulsed	Hot wire/ friction/ SPIV	best (45,135)
Beresh et al. [13]	2007	Expe	Single jet	SPIV	Structures vortices, close to sonic velocity
Dai et al. [41]	2016	Expe/LES	Single jet	PIV/ LIFD/ LES	frequency, influence VR

Table I.2: Main pitched and skewed jets studies: detailed characteristics

Author	f [Hz]	VR	Reynolds	d [mm]	Pitch angle[°]	Skew angle[°]	Number	δ [mm]	U_∞ [m/s]
Compton	0	0.7-1.3	δ_1 1500	6.35	45	0–90–180	1	14	15
Zhang	0	0.25-3	δ_1 1500	6.35	45	0–45–90–120	1	14	15
	0	1.5	δ_1 1500	6.35	45	60	2	14	15
	0	1.5	δ_1 1500	6.35	45	60	2	14	15
Bray	0	MaR=0.7-2	-	2.25-13.5	30-60	30-60	1	41.5	Ma 0.06
Han	0	r = 5-10-20	-	4.6	45-135	0	1	0	1.65
Khan	0	1	δ_1 1100	2.54	30-30-30-45	60-45-90-60	1	5	0.2
Rixon	0	1-2-003	δ_1 715	4.76	45	90	1	3.4	0.2
Godard	0	1.6-4.7	-	4-6.	45	45-90	3-006	7	10
	0	1.6-4.7	-	4-6.	45	45-90	2	7	10
Shapiro	0-130	2.5-4	Dj 1420–36600	7.62	90	0	1	7.6	1.1-1.8-2.2
Kostas	2-10-40	2.3-3	δ 125000	6	45	90	7	150	10
	2-10-40	2.3	δ 125000	6	45	135	4	150	10
Beresh	0	4.62	$20 * 10^6$	9	45-60-75-90	90	1	14.8	Ma 0.8
Dai	0	0.5-2	1712	23	35	0	1	-	-

The first study of a pitched and skewed jet is an experiment by Compton and Johnston [34], the authors measured using a five hole pressure probe, the vorticity produced by a jet with a pitch angle of 45° and of varying skew angle. As most of the studied presented here, the skew angles are limited to downstream oriented jets (for which the longitudinal velocity component is aligned with the flow). This study claims that the jet parameters producing the maximum vorticity are $(\alpha, \beta) = (45, 90)$.

This study was corroborated by the numerical RANS calculations of Zhang [181]. It confirmed also that pitched and skewed jet manage to produce strong vortices even for small velocity ratio. Zhang [181] tested more skew angles and found that the maximum vorticity for a jet of pitch angle equal to 45° is for a skew angle between 60 and 90° (see Fig. I.11).

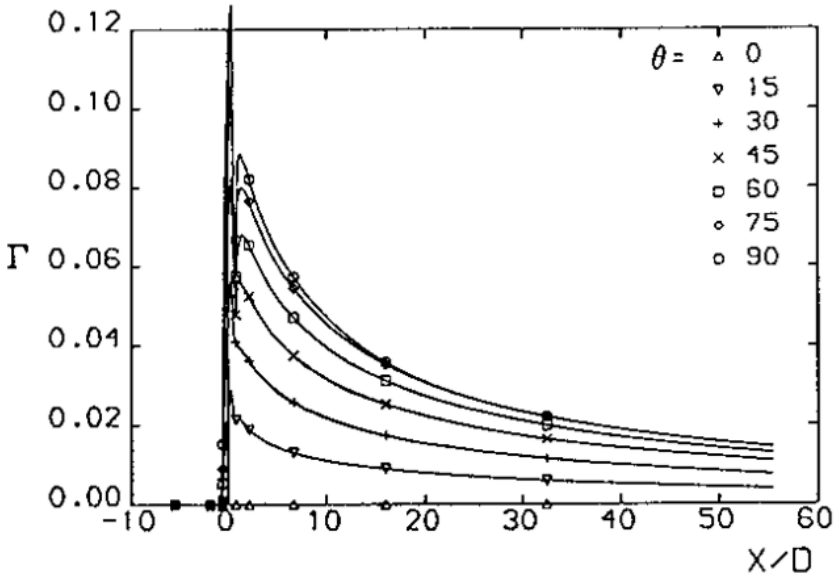

Figure I.11: Influence of the skew angle on the cross plane circulation for a jet of pitch angle equal to 45° from Zhang [181]

Zhang [181] also tested for the first time co-rotating and counter-rotating couples of jets. He noticed that the level of vorticity is independent of the distance between the jets for co-rotating jets and higher for closer jets in the counter-rotating configuration. He also noticed that the co-rotating jets vorticities decreased quicker than for the counter-rotating jets.

In 1999, Bray and Garry [15] developed a model using the result of the experimental tests of his PhD Thesis (Bray [14]) for angles, both between 0 to 60°. This really complex model used 25 constants. His conclusion was that the optimal angles are $(\alpha, \beta) = (30, 60)$.

After this, Han et al. [88] studied experimentally the effect of the pitch angle for a jet aligned with the flow. He noticed that for a jet oriented upstream, the vorticity produced by the jet is better dispersed in the flow as it can be seen on Fig. I.12. Once again only one angle was modified, the skew angle being fixed to 0°. The authors also proposed a change of variable based on the angle of the jet with the normal which allows to retrieve the prediction of trajectory using the model of the normal jet.

Khan and Johnston [102] have performed LDV measurements for four different couples

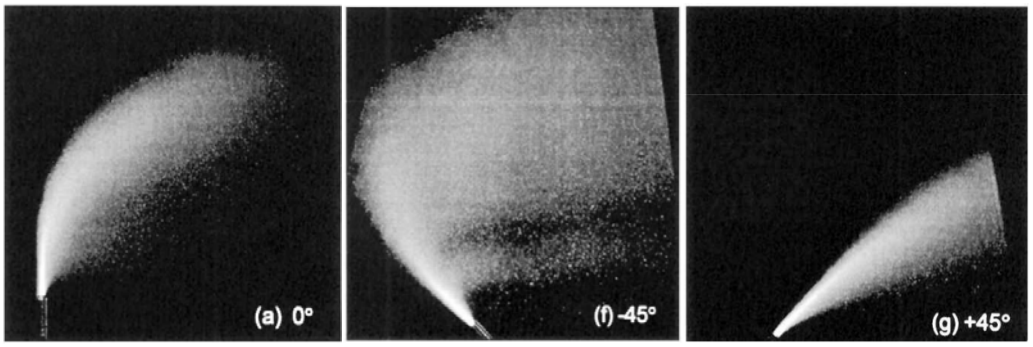

(a) Pitch angle equal to 90° (b) Pitch angle equal to 135° (c) Pitch angle equal to 45°

Figure I.12: Influence of the pitch angle on the dispersion of the flow (from Han et al. [88]).

of pitch and skew angles, they noticed that the jet producing the maximum vorticity was oriented following $(\alpha, \beta) = (30, 60)$. They also managed to measure the first turbulent field for pitched and skewed jets.

Rixon and Johari [140] studied one jet of parameters $(\alpha, \beta) = (45, 90)$ using PIV and LDV. They found that the vorticity was linearly depending on the velocity ratio.

The work of Godard and Stanislas [84] on rounded jets is part of a more global work comparing the mechanical VGs (Godard and Stanislas [83]) and slotted jets (Godard et al. [85]). This study concludes that counter-rotating fluidic VGs may be as effective as mechanical VGs for relatively low velocity ratio (around 1.5). They studied only a pitch angle of 45° and found an optimal skew angle of 90°. Nevertheless, the small number of angles studied do not allow to be fully affirmative. The measure of friction allows to confirm a control varying along the width of the wind tunnel. This complicates the comparison of velocity profiles they measured, as the latter were only measured at one transverse position.

Beresh et al. [13] studied experimentally the effect of the variation of pitch angle on the vorticity structures produced by a jet with skew angle equal to 90°. These structures are visible on Fig. I.13. The map of vorticity discloses vorticity structures that are more complex than just two vortices for some angles. Beyond these precise measurements, this study is also of interest as the main flow is close to sonic velocity and it found similar structure as the previous subsonic studies.

Pulsed Jets The work by Kostas et al. [105] and Shapiro et al. [157] is interesting as they tested the effect of frequency excitation on normal and pitched jets. Indeed, at some particular frequencies, called fundamental frequency and subharmonics, the main behavior of the jet is modified and the penetration of the jets is amplified (see also Johari [96], Karagozian [100]). This phenomenon can be observed on the photograph of Shapiro et al. [157] on Fig.I.14. Kostas et al. [105] presented a small literature review of pulsed pitched and skewed jets. They measured the impact of the frequency on the mean friction for low frequency actuation. They found that the friction is lowered by the actuation, this may also be linked to the fact that they worked at constant velocity ratio. Nevertheless, they found that the vortices were directly impacted by the actuation, meaning that they present the same frequency as the actuator farther downstream. These considerations

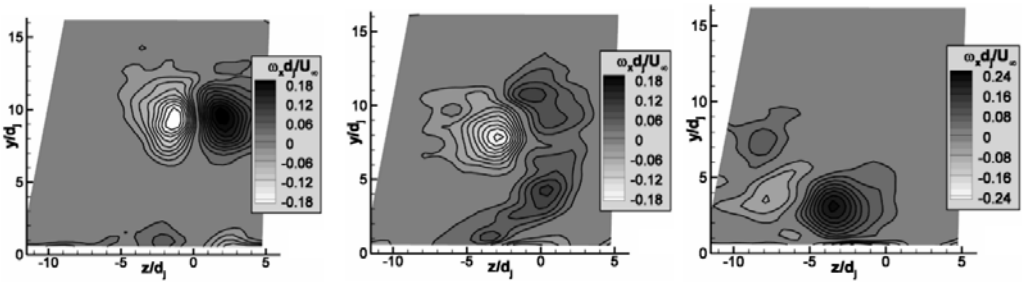

(a) Pitch angle equal to 90° (b) Pitch angle equal to 75° (c) Pitch angle equal to 45°

Figure I.13: Influence of the pitch angle on the vorticity produced by a jet with a skew angle of 90° (from Beresh et al. [13]).

should be taken into account when trying to activate the air VGs in an hypothetical closed-loop control.

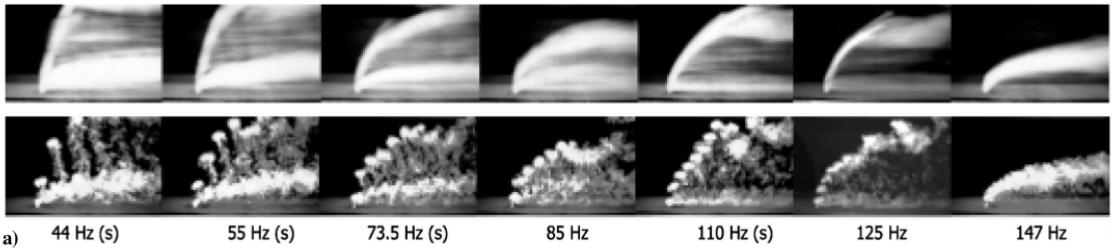

Figure I.14: Influence of the frequency on the trajectory and penetration of a normal jet, short exposure above an long exposure below. The frequencies denoted (s) are subharmonic frequencies (from Shapiro et al. [157].)

More recently, Dai et al. [41] have carried out LES calculation of the interaction between a jet pitched by 35° and a cross flow. They were able to noticed the presence of streamwise vortices developing above the plume. More work should be done in order to understand their interaction with the principle counter-rotating vortex pair. This structure may be linked to the fundamental frequency of the jet found in the preceding studies.

The elegant work of Feng et al. [63] is also noticeable, they develop a model for the trajectory of a pitched and skewed jet from the model of trajectory of a normal jet. Nevertheless, this model is incomplete as it only takes into account the velocity of the jet projected on the normal axis. This model should be furthermore false for jet pointing in an upward direction, as it does not take into account the re-direction of the velocity of the jet going backward.

Even if this review is not exhaustive, it shows that physics of a pitched and skewed jet in a cross flow are highly complex, depending on both angles. It also shows that no general model was found to predict the vorticity developed by the jet. A jet can form either a pair of counter-rotating vortices, or a unique strong vortex for small pitch angles and skew angle close to 90°. Furthermore, the notion of vorticity level developed by a jet is not enough to quantify the control efficiency, indeed, the structure of vortices can modify strongly the efficiency of the resulting mixing.

Another important aspect is that most of the studies focused on the jet "aligned with the flow", not considering the jet oriented upstream which however may present better mixing properties.

iii Pitched and skewed jets used for flow control

Several studies on fluidic VGs are now presented. These studies differ from the previous ones as they attempted to directly control a separation and not to study the vorticity developed by the VGs. They take a more general and applied point of view on the fluidic control. Once again this presentation is not intended to be exhaustive but rather gives a good overview of the different aspects of fluidic control. The main characteristics and conclusions of theses studies are presented in Table I.3 and the physical details are presented in Table I.4. In the physical details, the momentum coefficient c_μ is notably given. This coefficient characterizes the energy of the jets compared to the one of the main flow, it is defined in Eq. I.2. This coefficient is used to give an idea of the energy cost of the control, it is nevertheless, highly sensitive to the choice of reference surface for the main flow S.

$$c_\mu = \frac{\Sigma \rho_{jet} U_{jet}^2 S_{jet}}{0.5 \rho U_\infty^2 S} \tag{I.2}$$

The oldest paper found in which the author used small jets to inject energy in the boundary-layer in order to prevent separation is the one by Wallis [174]. The small perpendicular jets are used to delay the separation occurring on thin swept wings. The control managed to suppress laminar separation and to delay the turbulent separation and thus to increase the lift performances of the wing.

A more detailed study has been done in the PhD Thesis of Rao [138] with some of its results presented in Pearcey et al. [135]. Rao [138] has performed visualization in water tunnel to understand the formation of vortices. This formation is coherent with the works presented above. He parameterized the shape of the jet exit. He found that for a constant blowing pressure, the jets exiting from a rectangular shape are producing stronger vortices. Nevertheless, to maintain a constant blowing pressure, the mass flow rate needs to be augmented so there is no real gain in terms of efficiency on the control with respect to its cost. This study proved the interest of fluidic VGs to reduce or delay the separation occurring on transonic wings. Different tests were done in terms of pitch and skew angles, the best configuration found was for pitch angles varying between 30 and 45° and with a skew angle of 45°. Nevertheless, once again only a small number of combinations of angles were tested. This study also confirmed the importance of the blowing pressure for the formation of vortices. The minimum pressure ratio found for the formation of a vortex was 1.0. It also underlines without explaining it, the strong impact of the distance between VGs on the efficiency of the control system. Indeed, strong vortices tend to dissipate quicker if they are formed to close to each other.

In Lin et al. [115], the authors studied a lot of different control methods on a backward facing ramp. The subsonic flow separation was, inter alia, controlled using fluidic VGs. Several configurations of pitched and skewed VGs were tested. First, the impact of the skew angle was tested with the pitch angle fixed at 45°, the best results were found for a skew angle chosen between 60 and 90°. Then the skew angle was fixed at 90° and the pitch angle was varied from 15 to 90°. This time the best control was for a pitch angle between 15 and 25°. They found that the normal jet did not control the separation. This may be due to the fact that the pressure is too high and the counter-rotating pair of vortices is

pushed away of the boundary-layer. This study once again exhibited the interest of the fluidic VGs. However, the pressure measurements were only done on a longitudinal line in the symmetric plane of the wind tunnel. This may induced errors in the interpretation of the results as 3D phenomena may happen between two VGs.

Table I.3: Main fluidic VGs control studies: principal characteristics

Author	Year	Configuration	Means of investigation	Conclusion
Wallis [174]	1952	Thin wing	Pressure measurement	Improved lift
Rao [138]	1988	SWBLI bump	Pressure measurement	Separation reduced best (30-45,45)
Lin et al. [115]	1990	Subsonic bump	Pressure measure/Oil flow visu	Separation reduced best (15,90)
Pearcey et al. [135]	1993	SWBLI bump	Pressure measurement	Separation reduced
Hansen and Bons [89]	2006	Turbine blade	SPIV	Comp mormal pitch skew, phase pulsed, 3D
Kumar and Alvi [108]	2006	Subsonic bump	PIV/Pressure/Oil flow visu	Subsonic, only center plane, relatively hight blowing
Kumar and Alvi [109]	2009	Subsonic bump	PIV / Unsteady pressure	Study angle position, best low $c\mu$, slightly reversed
Souverein and Debiève [159]	2010	Impinging Shock	Hotwire 2D PIV	Small separation's reduction
Dandois et al. [44]	2010	Buffet	RANS/ Oil flow visu / Pressure	Pitch skew comp meca, best (30,60)
Molton et al. [125]	2013	Buffet	Pressure unsteady/LDV/PIV	Separation controlled, pulsed effect low freq $\nearrow$ mvt choc
Garnier [75]	2015	Sduct	Pressure Rake/ Pressure unsteady	Frequency, avoid natural frequency
Verma et al. [172]	2015	SWBLI cylinder obstacle	Oil flow visu / Schlieren/ pressure	Separation reduced, pitched better than normal

Table I.4: Main fluidic VGs control studies: detailed characteristics

Author	f [Hz]	c_μ [%]	Reynolds 10^6	d [mm]	Orientation	Number	P[bar]	δ [mm]	U_∞ [m/s]
Wallis	0	$\sim$ 0.04	0.75-3.75	$\sim$7	?(45,90)	?	-	-	18
Rao	0	-	$\sim$3	3.81	(45,60-90)	9 CoR	5.5	θ 0.6	Ma 1-1.5
Lin	0	-	θ 9000	1.6	(45,60-120),(15-90,90)	CoR	-	2.54	40
Pearcey	0	-	3	7.6*1.6	(30-45,45-90)	6 CoR	1.-1.8P0	? θ 0.6	Ma 1-1.5
Hansen	5	-	0.04	4	(90,0)(30,90)	9 CoR	-	8?	$\sim$20
Kumar	0	δ 29	1.3	0.4	(112.5,0)	60	0.69-1.7	18	40
Kumar	0	δ 17	1.3	0.4	(75-90-112,0)	12	0-1.7	18	40-65
Souverein	0	3	5.5	0.8	(45,90)	10 CoR	0.4	9.9	Ma 2.3
Dandois	0	0.033	3	1	(30, 60)	40 CoR	1.76	1.3	Ma 0.843
Molton	10-510	0.005	2.5	1	(30,60)*	40 CoR	-	1.8	Ma 0.82
Garnier	50-1000	3 and more	1.5	1	(30,75)	14 CoR	-	-	Ma 0.4
Verma	0	r 0.77-3.43	7.6	0.6	(90-45-45-0,0-90-135-0)	16 CoR	1.40-6.40	3.35	Ma 2.18

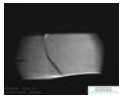

In 2006, Hansen and Bons [89] studied the impact of fluidic VGs on the separation occurring on subsonic turbine blade. They used Stereo Particle Image Velocimetry (SPIV) to study more precisely the structure of the vortices for a normal jet and a jet oriented following $(\alpha, \beta) = (30, 90)$. The advantage of this study is that they were able to disclose the 3D deformation induced to the boundary-layer and thus to the separation. They concluded that a normal jet was less efficient in mixing than the pitched and skewed jet.

Another interesting point is presented on Fig. I.15. They studied the impact of pulsed jets on the boundary-layer. Using several SPIV measurement planes, they were able to reconstruct a 3D visualization of the impact of the pulsed jet on the boundary-layer at several instant of the pulse cycle. The jets seem to have an impact on the separation even during the phase of the pulse when the jet is OFF as it can be seen on Fig. I.15. This may be due to the induced velocity field developed by the jet but it needs other measurements for a better physical understanding. This can be a huge advantage for pulsed jets which necessitate less mass flow rate and thus less energy than continuous jets.

Another study by Kumar and Alvi [108, 109] looked at the control of a subsonic bump using small diameter supersonic jets. They used PIV to validate the impact of the VGs on the flow. They validate the control and then carried out an optimization on the control parameters, meaning the pitch angle of the jet and the blowing pressure in order to reduce the energy needed. It should be noticed that their momentum coefficient c_μ is based on the area represented by the boundary-layer times the width of the wind tunnel. This criterion of efficiency is more severe than the usual one considering the whole height of the wind tunnel, even if maybe it has more physical sense for this configuration. With a classical definition of c_μ, they are closer to 0.4% which makes this control quite efficient. The optimization found that a jet with a pitch angle slightly above 90° is more efficient, even if this is also dependent on the blowing pressure.

The control of separation in supersonic SWBLI has also been tested by Souverein and Debiève [159]. Using co-rotating fluidic VGs, pitched and skewed, they tried to suppress the separation zone. This was not achieved completely. The separation was however reduced, displaying a separation line corrugated at the spanwise positions of the VGs. This confirmed the preceding conclusions of Titchener and Babinsky [167] for mechanical VGs, that the use of VGs is more efficient for transonic flows than for supersonic ones.

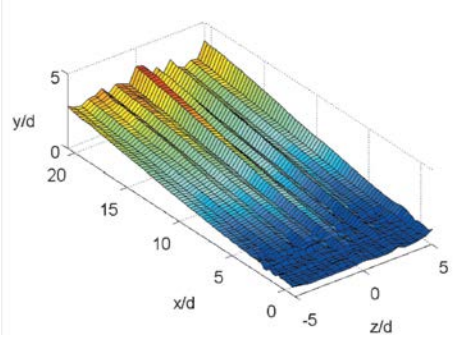

(a) Clean boundary-layer.

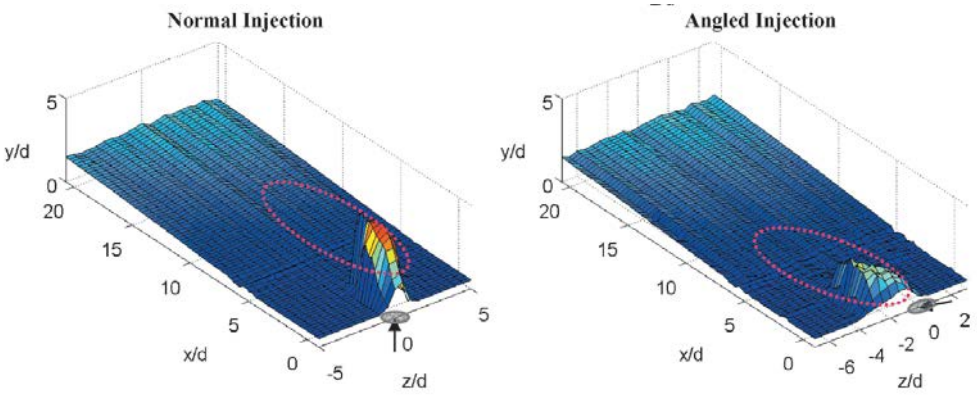

(b) Controlled boundary-layer, t/T =0, jet ON.

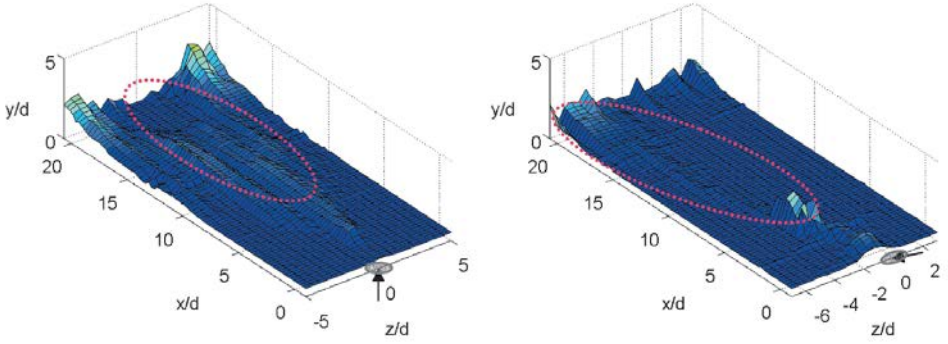

(c) Controlled boundary-layer, t/T =0.275, jet OFF.

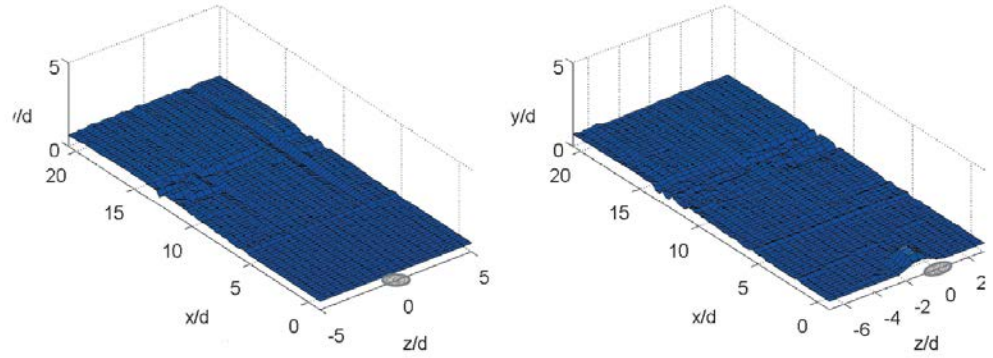

(d) Controlled boundary-layer, t/T =0.775, jet OFF

Figure I.15: 3D visualization of the iso surface of velocity($u/U_\infty = 0.5$) colored by y/d, pink oval represents the position of the jet pulse (from Hansen and Bons [89]).

Another study of transonic SWBLI is the work of Dandois et al. [44] and Molton et al. [125]. They used first RANS modeling techniques to test the influence of pitch and skew angles of fluidic VGs for the control of buffet phenomenon on a wing. This confirmed again that optimum pitch angle is dependent of the choice of the skew angle and vice versa. By doing one study at fixed skew angle and one at fixed pitch angle, the most effective configuration is found for $(\alpha, \beta) = (30, 60)$. This configuration was implemented in wind tunnel and tested as well as mechanical VGs. Both fluidic and mechanical VGs managed to reduce the separation zone linked to the buffet onset which is visible on Fig. I.16. They also studied the effect of pulsed fluidic VGs on the buffet phenomenon. They found that at low frequency, the shock-wave was really sensitive, with an amplitude of movement increased. At higher frequencies, the shock-wave amplitude and position are close to the one of continuous jets.

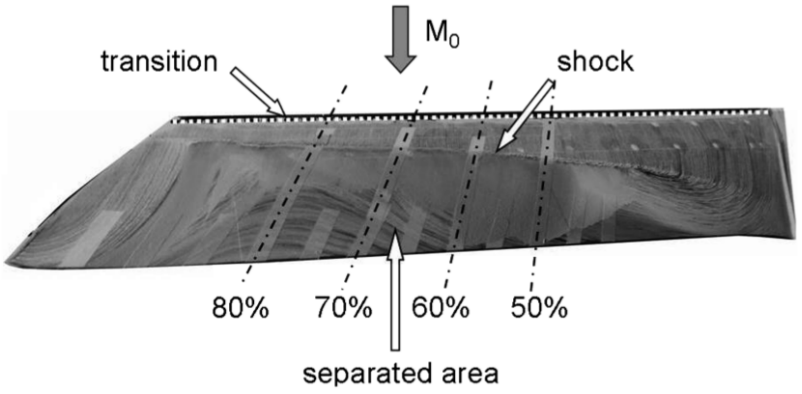

(a) Uncontrolled wing.

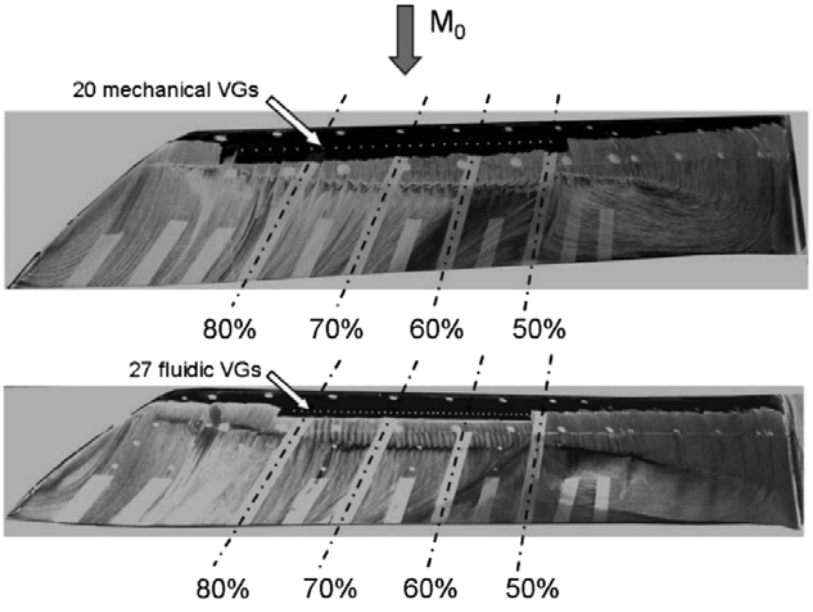

(b) Controlled wing, using mechanical VGs (above) and fluidic VGs (below).

Figure I.16: Oil flow visualizations of the impact of mechanical and fluidic VGs on a wing in buffet regime (from Molton et al. [125]).

In Garnier [75], the author presented the experimental results of a control of a S-Duct with pulsed fluidic VGs. The position and angles of the VGs have been chosen following numerical modeling (see Garnier et al. [78]). This study proved once more the interest of using fluidic pulsed VGs in the case of subsonic separation, by actuating the VGs at the natural frequencies of the separation zone and above. Surprisingly at the natural frequencies of the flow, the control can be detrimental for the flow distortion compared to the clean case. This study is also interesting for another point, as this configuration is intended to represent an air inlet, the authors considered the distortion of the flow in the channel using a criterion called $DC60$. This criterion will be considered in the optimization process presented in Chap. IV.

Finally, Verma et al. [172] used fluidic VGs to control a SWBLI separation which is fully 3D. They controlled the separation caused by a cylinder protuberance in a supersonic flow. Once more the separation is reduced using the VGs and the authors found a better result for pitched and skewed jets than for normal jets at higher pressure. A disadvantage of this study was that that only the pressure measurements on the central plane are presented even if the flow may be asymmetric for the angled jets positioned in co-rotating configuration.

Another study on subsonic flow control is presented in Chabert [24]. The configuration tested is a flap at varying angles of attack. The control method differs slightly from the ones presented in the current review as the control is undertaken using longitudinal slots which generate longitudinal vortices. However, this study is notable as they managed to use friction sensors in order to have an information about the separation and thus design a closed-loop control. This is another advantage of the fluidic control, it can be used for closed loop control.

3.d Corner flow separation control

In order to understand more precisely the 3D aspect of a SWBLI in a rectangular air inlet, a review of the studies on corner flow separation is then presented.

Flow structure in corner As it was presented earlier, the turbulent flow in corner has been precisely described in Gessner [81]. Nevertheless, recent experimental works of Sabnis and Babinsky [146] have emphasized the importance of the history on this corner flow in transonic flows. Indeed, the pressure distribution in the channel due to expansion waves, is going to break the symmetry between the two walls of the corner and thus increase more importantly the boundary-layer on one of the walls. The vorticity distributions induced by the two configurations presented on Fig. I.17, the full and half set up one, are shown on Fig. I.18. The asymmetric configuration may result into asymmetric corner flow separation. This statement also supports the idea that in numerical computations, the whole channel should be computed in order to take into account the real corner flow distribution which can influence strongly the separation zones.

Complex structure of flow separation in corner The corner flow separation happening in the corners of rectangular wind tunnel has not been deeply studied to the author knowledge in the literature, excepted the early work of Chriss et al. [31]. Most of the researches focused on different kind of corner separation (see for example Gand [72], Babinsky and Harvey [6], Verma et al. [172]) happening over obstacles in a transonic flows. However,

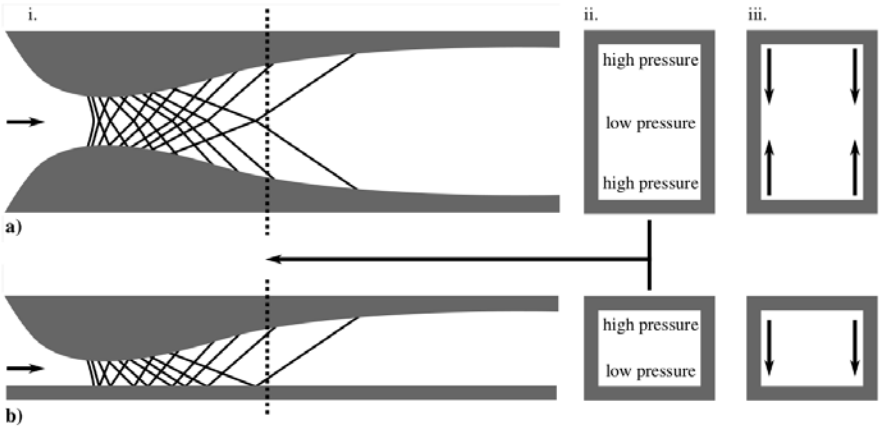

Figure I.17: Two configurations studied by Sabnis and Babinsky [146].

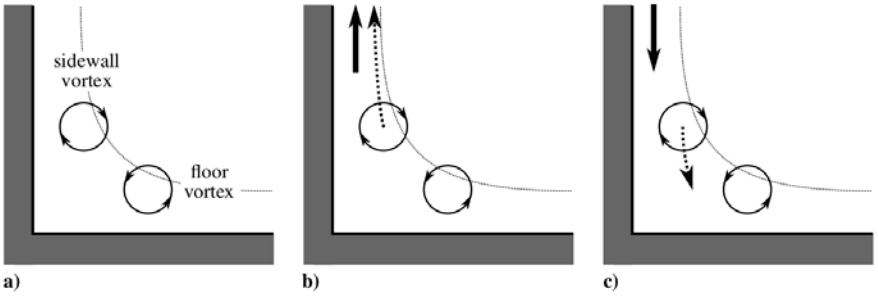

Figure I.18: Influence of history on corner flow, vorticity distribution for the ideal case a), the full configuration b) and the half configuration c) (from Sabnis and Babinsky [146]).

a flow visualization of the corner flow separation topology in a rectangular channel can be found in Babinsky and Harvey [6], presented on Fig. I.19. This representation, obtained following the critical point theory developed by Legendre (see Délery [51] for an overview of Legendre work) on oil flow visualization allows to observe the influence of the corner flow separations on the central separation. The central separation is composed of a line of separation (S) and a line of attachment (A) perpendicular to the main flow. On the border, the central separation ceases to be two dimensional and is corrugated by a focus point positioned on the lower wall slightly in advance of the central separation. On the lateral wall, another focus point is visible, the separation linked to this latter one being more important than the lower one.

Bruce et al. [16] and Burton and Babinsky [21] proposed the configuration presented on Fig. I.20 as an interpretation of the surface flow topologies found in their study. The corner separation is linked to compression waves, modifying the central λ shock-wave and the one appearing on the wall. Bruce et al. [16] introduced a criterion based on the ratio between the boundary-layer displacement thickness δ_1 and the width of the wind tunnel which allow to predict if a central separation will occur, this last one being linked to the existence and the width of corner flow separation. The recent experimental works of Xiang and Babinsky [178], Xiang [177], Xiang and Babinsky [179] on the separations formed by a reflecting shock-wave at Mach 2.5, shown that the corner flow separations influence strongly the central one. Indeed, when the compression waves linked to the corner flow

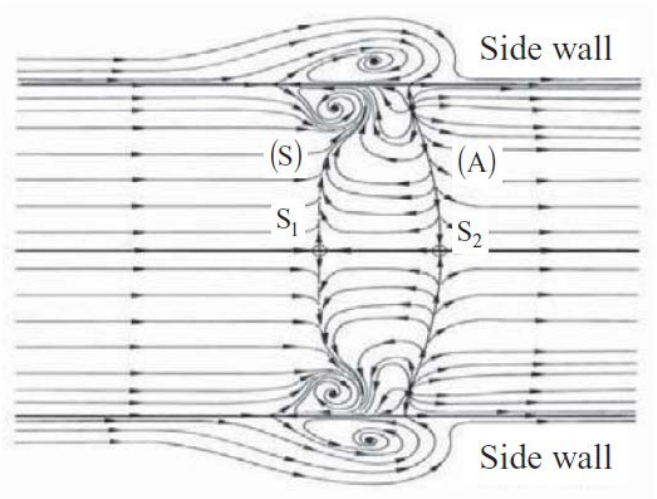

Figure I.19: 3D topology of friction lines of a SWBLI with separation in a channel flow from Babinsky and Harvey [6].

separations intersect in the center of the wind tunnel before the central separation, the latter one is reduced. When these lines intersect in the central separation, the central separation is increased. Finally, when the lines crossed behind the central separation, this latter one is close to a quasi 2D separation with small influence from the corner flow separation.

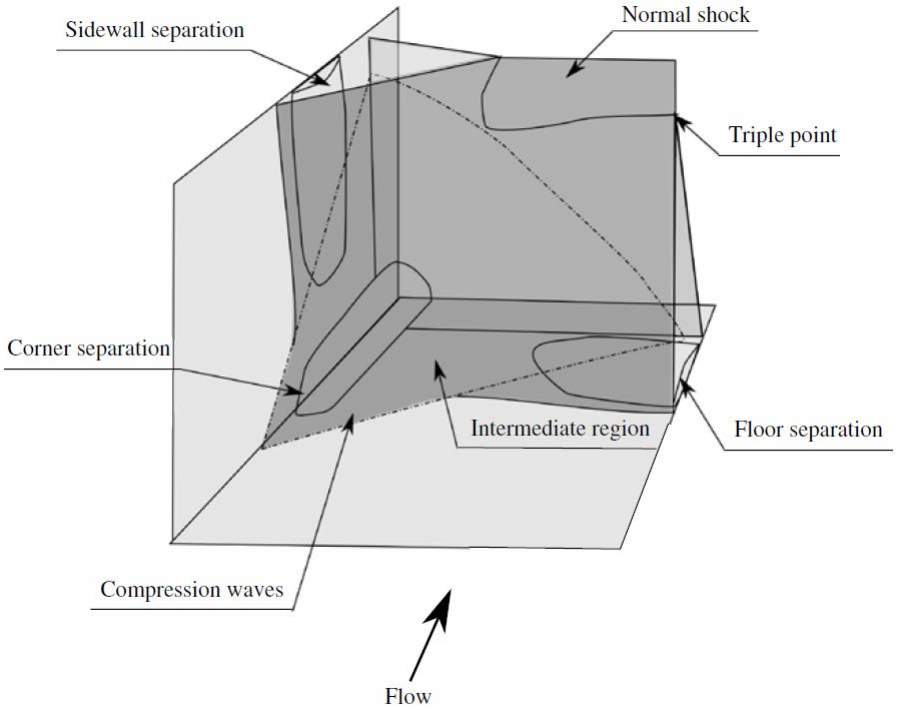

Figure I.20: Proposed topology for the corner flow separation produced by a normal shock-wave in a rectangular channel (from Burton and Babinsky [21]).

The strong influence of the corner flow separation on the central separation was observed experimentally in Rybalko et al. [145], Bur et al. [20] and was also observed numerically in the LES or DES of Garnier [74], Roussel [144], Wang et al. [175]. Nevertheless, on the dynamical point of view, these studies did not manage to find a clear correlation between the dynamic of the central shock-wave and the ones of the corners.

Control of corner separation Different methods of control have been tested by Babinsky's group to control the corner flow separation (see Babinsky et al. [8], Titchener and Babinsky [166], Burton and Babinsky [21], Koike and Babinsky [103], Xiang and Babinsky [178], Xiang [177]). Notably for our study, Koike and Babinsky [103] used mechanical VGs in the shape of vanes to control the corner flow separation. The result of the study shows that in some precise configurations, the vortex developed by the VG, oriented in the direction that lift up the flow in the corner, managed to reduce the corner flow separation. Nonetheless, this reduction is linked to the formation of a side-wall separation. Furthermore, a lot of different VG configurations are disadvantageous for the flow as they increase the corner flow separation or they induce new separation regions. The control of the corner flow is really sensitive and its benefit should be assessed with respect to the whole configuration in the case of a 3D air inlet.

I.4 Conclusion and specificity of the current study

Different methods of control of the SWBLI have been developed along the years, the most promising one being the control of the upcoming boundary-layer as these methods allow to control the interaction for a wider range of shock position, and they are more efficient than bleed.

A lot of studies have focused on the development and the optimization of mechanical Vortex Generators due to the fact that they can be easily mounted in wind tunnels. They have proven their capability to control SWBLI (see Bur et al. [20], Babinsky et al. [9], Baydar et al. [11] for example). The different studies allow to draw conclusions which can be used for every control using vortices: the use of micro VGs is validated and encouraged as it diminishes the drag generated by the VGs, the VGs should be placed in front of the interaction, closer if the VGs are smaller. In addition, the counter-rotating pairing of VGs seems to generate a more efficient control than the co-rotating configuration.

Nevertheless, these actuators generate drag when they are not useful, that is why fluidic VGs, which can be easily turned off, appear to be a better option. Furthermore, recent work of Giepman et al. [82] on Mach effect on the mechanical VGs displayed that an increase in Mach number has a negative effect on the efficiency of the VGs. On the contrary the fluidic VGs pressure can be augmented in order to tackle the Mach variation. Besides, the fluidic VGs can be actuated in frequency and potentially integrated in an active closed-loop control which can improve again their efficiency (Chabert [24]).

In that respect, the fluidic VGs have been compared to mechanical VGs (see for example Lin et al. [115], Godard and Stanislas [83], Godard et al. [85], Godard and Stanislas [84], Dandois et al. [44], Molton et al. [125]). The fluidic VGs performed as well as mechanical VGs. They managed to control subsonic separation (Lin et al. [115], Hansen and Bons [89], Kumar and Alvi [108, 109], Garnier [75], Chabert [24]) and 2D SWBLI without

corner flow separation consideration (see Rao [138], Pearcey et al. [135], Souverein and Debiève [159], Dandois et al. [44], Molton et al. [125]).

However, the fluidic VGs appeared to be more complex to optimize as they present more parameters than the mechanical VGs, e.g. the jet diameter, the velocity ratio and the pitch and skew angles. Indeed, the vortices developed by a jet in a cross flow have been the subject of several studies (Compton and Johnston [34], Zhang [181], Bray and Garry [15], Han et al. [88], Khan and Johnston [102], Rixon and Johari [140] Godard and Stanislas [84], Shapiro et al. [157], Kostas et al. [105], Beresh et al. [13], Dai et al. [41]). The latter were able to test only a small number of combination of parameters and thus no clear preferential couple of angles is found neither for the level of vorticity developed nor for the control efficiency (see Compton and Johnston [34], Zhang [181], Bray and Garry [15], Khan and Johnston [102], Godard and Stanislas [84], Kostas et al. [105]Rao [138], Lin et al. [115], Dandois et al. [44]).

Noticeably, few VGs with jets pointing upward have been tested (only Kumar and Alvi [109], Verma et al. [172]) even if they present a better mixing (Han et al. [88]).

On another note, the fluidic VGs allow to pulse the control and so to lower the mass flow needed with a still efficient control. Few studies have been undertaken on this subject but they disclosed promising results (see Shapiro et al. [157], Molton et al. [125], Chabert [24], Garnier [75]).

As the fluidic VGs are complex to optimize, an optimization based on numerical calculation is chosen. Since the studies of Dandois et al. [44], Albugues [1] validate the use of RANS modeling in elsA (Cambier et al. [22]) for control using blowing methods. This modeling technique will be used in an optimization process in order to find a efficient control of SWBLI. Other studies using the numerical optimization were carried out to find optimum control parameters for subsonic configurations using mechanical VGs in Anderson et al. [2, 3] and fluidic VGs in Flaszynski and Szwaba [65].

The current study develops an optimization process focusing mainly on the skew and pitch angles of the fluidic VGs and the control of the global flow separation. Indeed the pitch and skew angles can be of crucial importance, they influence other parameters as the separation distance between two VGs, the height and intensity of the vortices and thus the efficiency of the control system. Furthermore, the study will consider the effect of corner flow separation which appear to be critical for the global efficiency of the control. The control of the corner separation itself is conceivable since it was achieved using mechanical VGs.

II

Tools for the study

Every machine is a smoke machine if you operate it wrong enough.
Anonymous

Objectives

This chapter is dedicated to the presentation of the transonic wind tunnel and the reference uncontrolled flow in a first step. Then the different experimental means of investigation are described; especially, a more detailed presentation of the implementation of the tomographic PIV measurement is highlighted. In a third step, the RANS modeling used for the optimization is presented. Finally, the method of Zonal Detached Eddy Simulation (ZDES) and its implementation in the elsA code is stressed out.

Contents

II.1 S8ch wind tunnel and measurement tools presentation

1.a S8ch wind tunnel

The present study takes place in the Laboratoire de Mécanique des Fluides (LMF) at ONERA Meudon center in the S8Ch wind tunnel. This transonic wind tunnel presented on Fig. II.1, is supplied with desiccated atmospheric air using two downstream compressors. This open-loop wind tunnel has the advantage of being easily used for several hours continuously. The air dryer upstream of the test section allows to control the humidity level of the flow allowing to constraint the rise of temperature under 5° along long duration experiments.

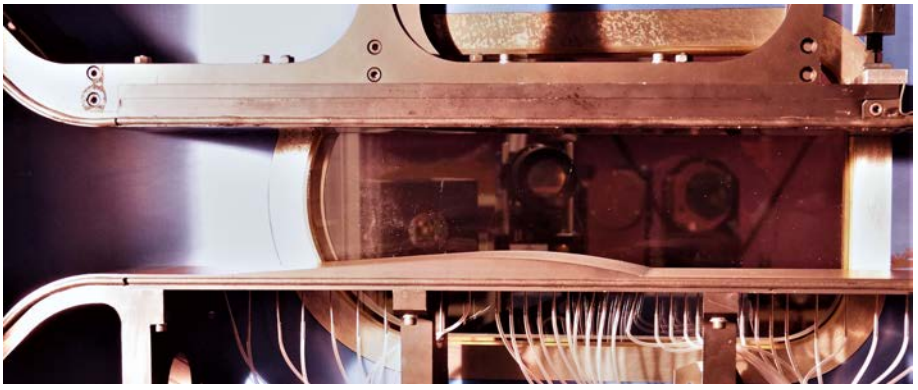

(a) Photography

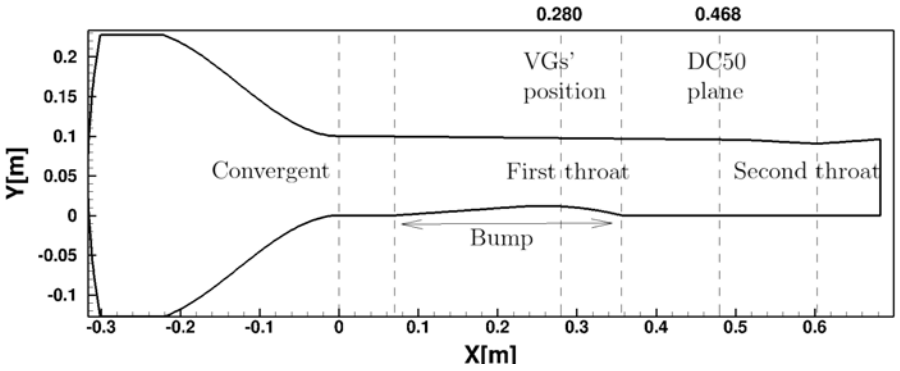

(b) Sketch

Figure II.1: S8Ch wind tunnel presentation

The wind tunnel is composed of a settling chamber where the stagnation conditions are measured, a convergent part, the test section in which a bump forms the first throat and a second throat of adjustable cross section at the outlet. This second throat represents the critical section of the wind tunnel and provokes by chocking effect a shock-wave on the Délery bump. The position of the shock-wave on the bump is accurately fixed by modifying the height of the second throat. The test section's dimensions are 120mm wide and 100mm high at the entrance of the channel. The origin of the co-ordinate system is at the beginning of the lower wall (see Fig. II.1). The X-axis is along the lower wall in the streamwise direction, Y is normal to the lower wall and Z corresponds to the transverse direction.

The stagnation conditions of the flow are near atmospheric pressure and ambient temperature: $P_{st} = 0.96 \cdot 10^5 \pm 300$Pa and $T_{st} = 300 \pm 10$K.

The incoming boundary-layer is fully turbulent and its properties at $x = 135\,\text{mm}$, just upstream of the interaction obtained by LDV measurements in Bur et al. [18] are: physical thickness $\delta = 3.9\,\text{mm}$, displacement thickness $\delta_1 = 0.46\,\text{mm}$, momentum thickness $\theta = 0.25\,\text{mm}$, and incompressible shape parameter $Hi = 1.6$. The associated unit Reynolds number is around $14 \times 10^6\,\text{m}^{-1}$, which leads to a value of $Re_\theta = 3500$ for the incoming flow. Due to the design of the bump (moderate pressure gradient along the growing part of the bump), the properties of the boundary-layer on the rear part of the bump are close to the one of the incoming flow. This has already been measured on the same configuration by Délery [48].

1.b Shock-wave / boundary-layer interaction

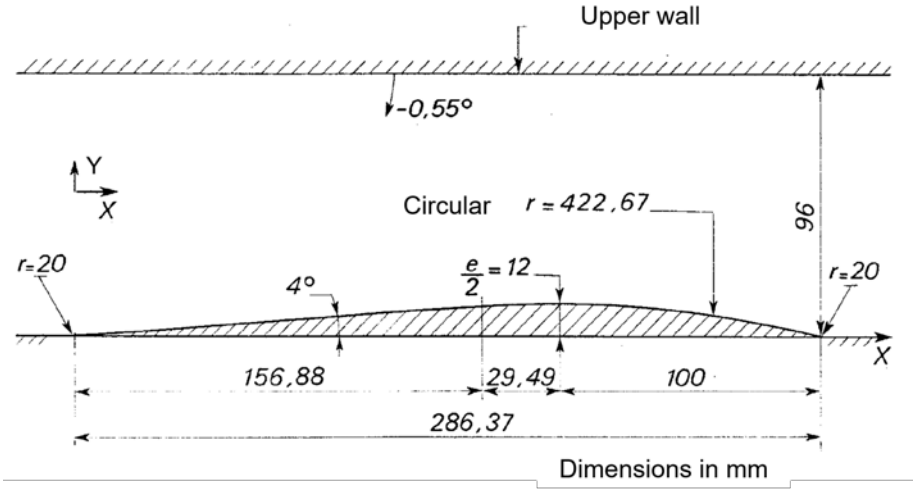

Figure II.2: Délery bump

This study is realized on the well-documented geometry called the Délery bump (case C) configuration which is detailed in Délery [48], studied in Bur et al. [20], Galli et al. [71], Galli [70], Sartor et al. [152, 154], Merienne et al. [124] and presented on Fig. II.2. The shape of the bump has been specially designed to induce a strong interaction between the boundary-layer and the shock at a nominal Mach number being equal to 1.4, which generates a massive separated zone. A sketch of the interaction and its corresponding polar

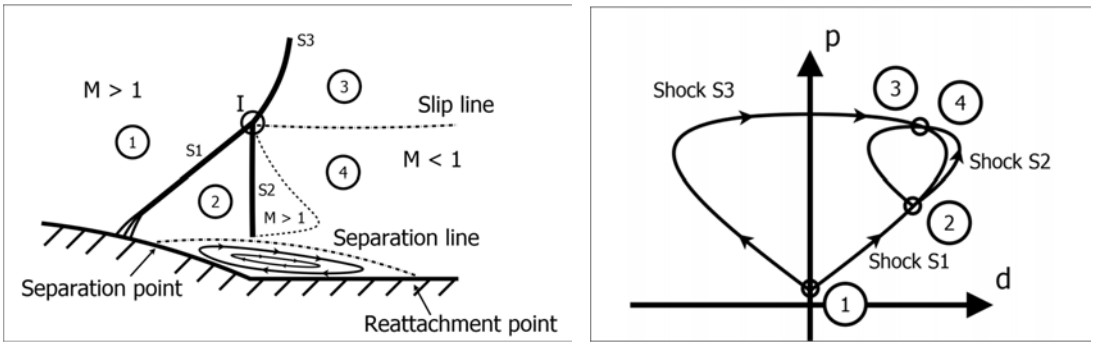

(a) Shock structure (b) Shock polar diagram

Figure II.3: Shock-Wave / Boundary-Layer Interaction (from Sartor et al. [154]).

shock are presented on Fig. II.3. The interaction presents a λ shock pattern. This shock pattern can be decomposed in two parts: the first one is composed of the weak oblique shock-wave S1 and the near normal 'trailing' shock S2, the second one is composed of the normal shock S3. These two parts merge at the triple point I from which a slip line is generated due to different upstream properties of the flow. This structure separates the flow in four states, the ③ and ④ being compatible separated by the slip line -i.e. different velocities but same static pressure level- on both sides of the slip line.

Following the recommendations of Galli et al. [71], the tangent to the mean position of the normal part of the λ shock-wave is positioned at 12.5 mm from the end of the bump. This position maximizes the size of the separation zone and ensures a nominal Mach number of 1.4 before the shock-wave.

In order to characterize the flow, the wind tunnel is equipped with different equipments which are detailed below.

1.c Pressure taps and sensors

i Static pressure measurement

Thirty nine continuous pressure taps are positioned on the lower wall along a line at 10 mm of the centerline with a higher concentration close to the end of the separated zone. Their positions are summed up in Table II.1 and represented on Fig. II.4. They are 0.4 mm diameter wide and are connected to ESP-32HD transducers via rubber tubes. They have pressure measurement uncertainties for $\pm$500 Pa. 300 measurements are done at 3Hz before averaging.

N°	X(mm)	N°	X(mm)	N°	X(mm)	N°	X(mm)
1	45	11	245	21	343.4	31	425
2	65	12	255	22	356.4	32	435
3	85	13	265	23	366.4	33	445
4	105	14	275	24	376.4	34	465
5	125	15	285	25	385	35	485
6	145	16	295	26	390	36	505
7	165	17	305	27	395	37	525
8	185	18	314	28	400	38	545
9	205	19	323.4	29	405	39	575
10	225	20	333.4	30	415		

Table II.1: Static pressure sensors' position

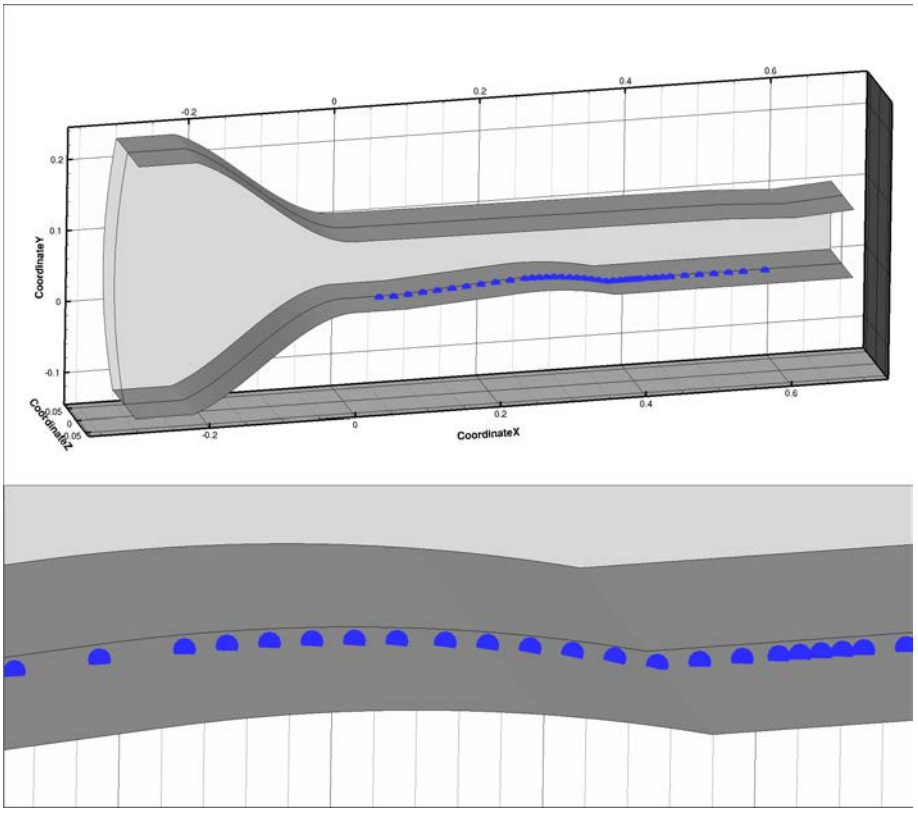

Figure II.4: Pressure taps location on the wind tunnel lower wall.

ii Kulite sensors

The bump is also equipped with five absolute unsteady pressure sensors, Kulite series XCQ-093-15A positioned along the center-line. The first one is close to the shock foot, two are in the separation zone, one close to the end of the central separation zone and the last one downstream of the reattachment. A further three sensors are positioned laterally in the central separation zone in order to measure the sidewall effects due to the corner flow separation. Their positions are summed up in Table II.2 and represented on Fig. II.5. The sensors are 0.8 mm diameter and have a pressure measurement uncertainties of ±105 Pa. They manage a 100 kHz acquisition which is sufficient to measure low and medium frequencies characteristic of the interaction (Sartor [151]). Some of the positions are close to the one of previous studies Sartor [151], Galli et al. [71] which allows to compare the measurements to previous data.

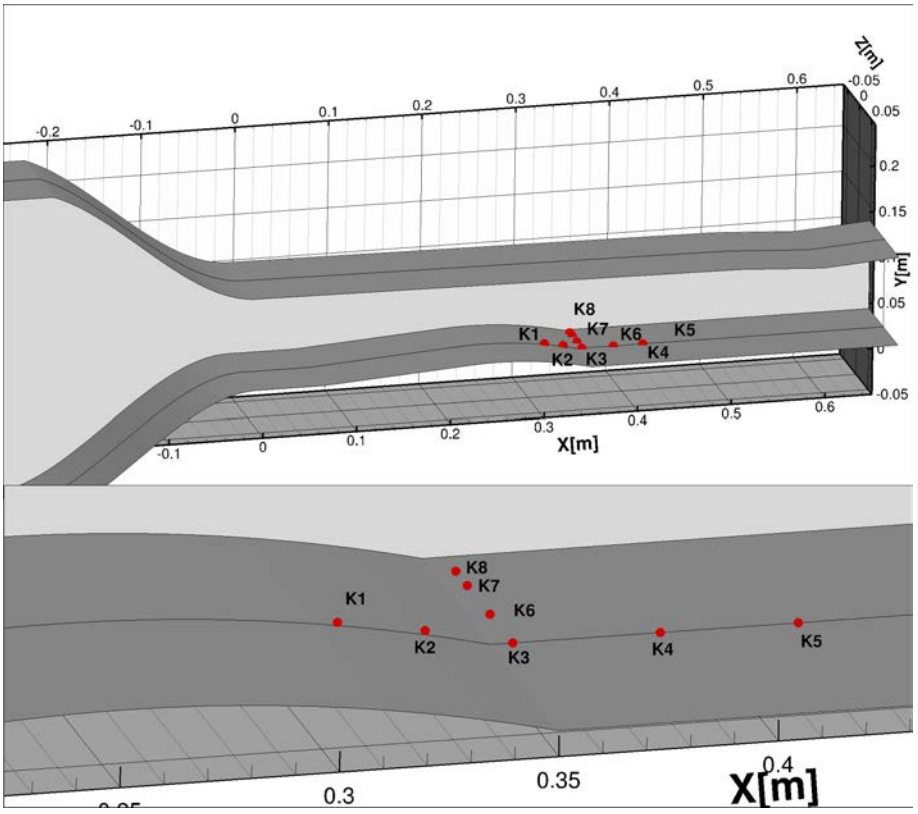

Figure II.5: Kulites sensors' position.

1.d Pitot rake

In order to be able to characterize the effects of the control on the shock-wave boundary-layer interaction and on the subsequent downstream flow, a movable Pitot rake has been conceived to measure the stagnation pressure losses far downstream of the interaction, both for reference and controlled cases. A CAD modeling and a photography of its implementation in the downstream part of the wind tunnel are presented on Fig. II.6. The rake is monitored using a stepper motor and Pitot tubes could be in contact with the wind tunnel lower and upper wall. The rake is composed of eight Pitot tubes whose shape allows

Name	X(mm)	Z(mm)
K1	316.4	0.0
K2	336.4	0.0
K3	356.4	0.0
K4	390.0	0.0
K5	421.4	0.0
K6	356.4	-20.0
K7	356.4	-40.0
K8	356.4	-50.0

Table II.2: Kulites sensors position on the lower wall.

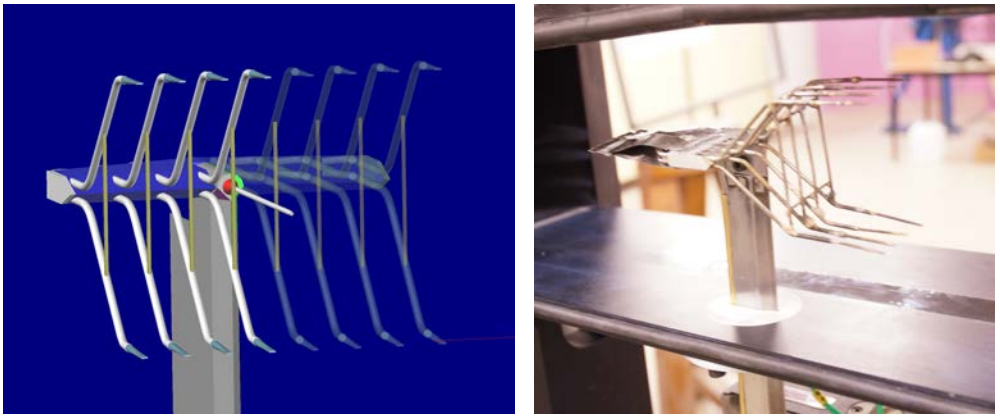

(a) CAD visualization

(b) Implementation near the second throat of the wind tunnel

Figure II.6: Pitot rake device.

to safely reach the walls and are placed in two ranges of four. Its head can be rotated in order to measure in two passes half of the wind tunnel, the two positions are visible on Fig. II.6a). Two Pitot tubes are placed less than 1 mm away from the lateral wall. The plane measured is positioned in the subsonic zone after the interaction, at $x = 468.4$ mm, 112 mm away from the end of the bump and 96 mm downstream of the normal shock-wave. Its position can be visualized on Fig. II.7. The resulting measurements will be presented in Chap. VII. The size of the rake at its maximum amplitude has been designed to be less than the critical area of the second throat. Nevertheless, as the wake generated by the rake is perturbing the flow, the second throat needs to be regulated during the measurement in order to maintain the shock-wave at its nominal position. Furthermore, at its maximum amplitude, some additional flow needs to be collected by using an external pump to ensure stable flow conditions.

1.e Schlieren visualization apparatus

In order to get an instantaneous general appreciation of the main flow features and to accurately place the shock-wave, Schlieren visualization apparatus has been set up using a Jai camera (acquisition up to 10kHz) and a blue Led activated for a pulse of 0.5 µs.

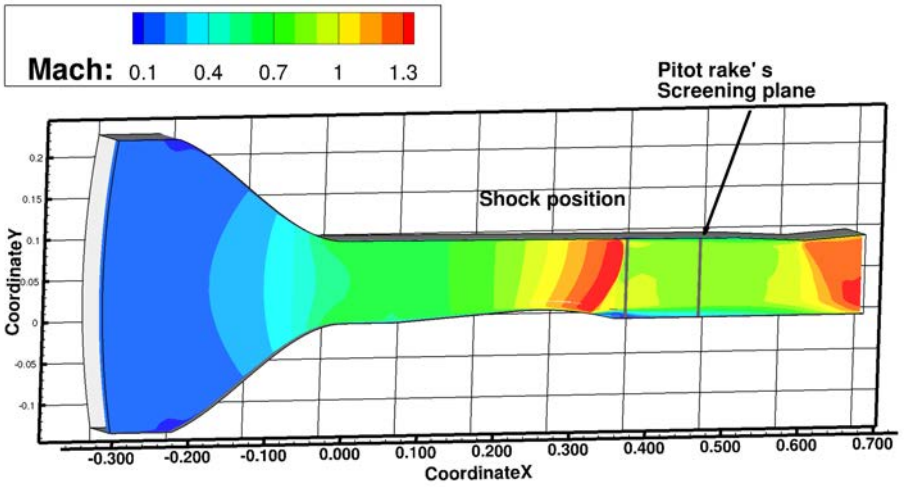

Figure II.7: Mach number map of the central plane of the wind tunnel showing the position of Pitot rake's screening plane (RANS result see Chap. III).

The Schlieren visualization is a common technique in fluid visualization, based on the Gladstone Dale law: the light rays are deflected due to variations of the flow density, such as boundary-layer and shock-wave.The light is cut using a knife edge at the focal point of a spherical mirror in the emitting part of the bench, before being send through the wind tunnel. The light is again cut at the focal point of a spherical mirror on the receiving part of the bench. The resulting light is then send to a receipting camera. During the crossing of the flow, the light is deflected toward or away from the knife edge and thus produces a shadow pattern that is a light-intensity representation of the expansion zones (low density) and compression zones (high density) which characterize the flow.

II.2 Tomographic PIV implementation and treatment

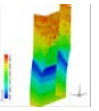

Tomographic Particle Image Velocimetry (PIV) is a 3D extension of the 2D PIV method, this method was introduced by Elsinga et al. [61]. It consists, using a set up of cameras and a laser volume illumination, of reconstructing the full 3D velocity field of a seeded flow. Even if this technique is more complex and longer to implement, it permits to study coherent 3D structures in the flow. The implementation of tomographic PIV in the S8Ch wind tunnel is quite a challenge as it has few optic accesses and the Délery bump lower wall increases the difficulty by being a wide surface of laser reflection. First, a detailed presentation of the technical implementation of the image capture system in the wind tunnel is developed before an explanation of the main process of tomographic PIV.

Tomographic PIV is a complex method which has not been applied to strong SWBLI on large volume except in the work of Humble et al. [92]. Nevertheless, the latter differs from the current study as the shock studied was an impinging shock-wave which is thus not transonic and occurs on a plane surface. Furthermore, the boundary-layer thickness of their case was more than six time higher than the one of the current study ($\delta_{Humble} = 20\,\text{mm}$). They measured a volume which was 2 mm above the plane surface. Their work was also more oriented on instantaneous flow field characteristics including the correlation with the shock movement, whereas the present study is oriented to 3D mean flow topology measurements with the goal of characterizing the impact of the control method on the mean flow.

2.a Implementation

i Characteristics of the material

The laser used for the illumination is a Nd-YAG Q-Smart Twins Quantel developing 380 mJ per flash at a wavelength of 532 nm. The two pulses are distant of 2 µs. The laser beam is then expanded in two directions using a set of lenses in a volume generator and cut using a diaphragm, providing a volume of $100 \times 100 \times 20$ mm rectangular parallelepiped in the (X,Y,Z) frame defined on Fig. II.1 b). This laser beam is sent using three mirrors visible on the CAD representation of the set-up presented on Fig. II.8, until a last mirror itself mounted on a rotating plate allowing to change the angle of entrance of the laser volume in the wind tunnel from above. This property is used for the corner flow study detailed below.

The image recording is done using four cameras LaVision Imager Pro provided with 4 Mpixel 2048×2048 CCD sensors. The cameras are placed on both sides of the wind tunnel, their physical positions are chosen due to optical limitations detailed below. All the cameras are equipped with 105 mm lens set at an aperture number $f\# = 8$ and a two tilts Scheimpflug to compensate the distortion due to the perspective viewing and placed with the focus plane parallel to the illuminated volume. This prevents some particles to be out of focus in the outer part of the field of view. In order to strongly limit the reflection on the lower wall of the wind tunnel, this has been painted with rhodamine. This fluorescent paint has the capacity of absorbing the wavelength around 532 nm and to re-emit it in a different wavelength which is filtered before the camera sensor. Filters lens which only transmit 532 nm are placed in front of the cameras to remove the re emission of the paint, the noise due to ambient light and the blue led of the Schlieren visualization. Even if this

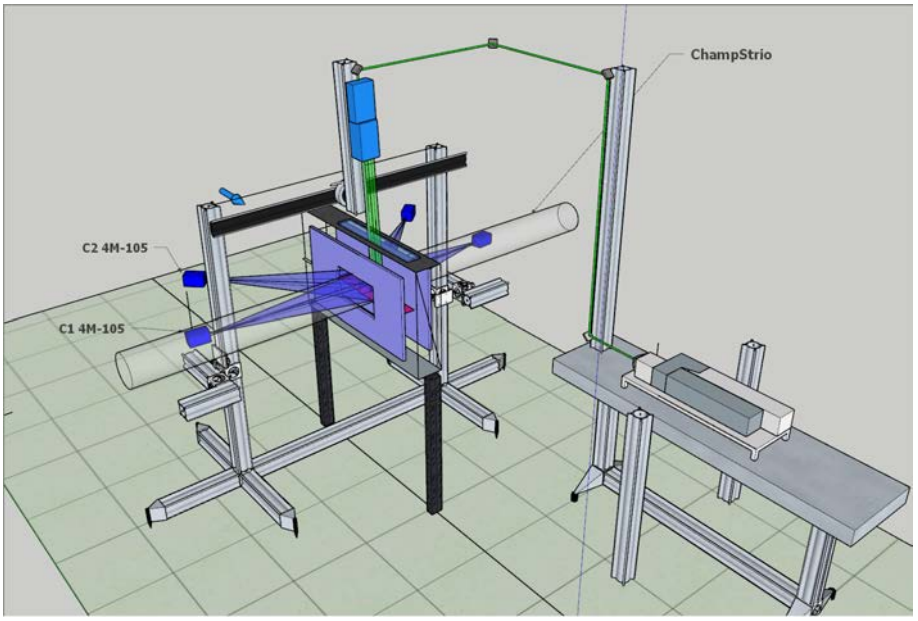

Figure II.8: CAD representation of the PIV and Schlieren apparatus (the Schlieren optical range is represented by the transparent tube).

Interrogation volume (×3)	$1.55 \times 1.55 \times 1.55$ mm
Objective focal length	105 mm
f-number	8
Laser pulse separation	2 µs
Seeding density	0.05ppp
Spatial resolution	16 pixels/mm
Estimated uncertainty	0.1 pixel
Number of runs per volume	10
Number of images per run	100

Table II.3: Summary of the tomographic PIV recording parameters.

does not remove completely the reflection, it allows to diminish them drastically. Without this painting, the strong reflection corrupts near-wall flow zones on a quite large extent. This prevents the images to be processed as the contrast is too high and an important part of the images are corrupted. The paint appears with a pink color on the different pictures of the bump as on Fig. II.13. The details of the tomographic PIV recording are summed up in Table II.3.

The flow is seeded using sub-micronic droplets of Di-Ethyl-Hexyl-Sebacate (DEHS), provided by a TOPAS, an atomiser aerosol generator placed far away upstream of the test section in order to ensure a uniform distribution of the particles in the flow. These particles have a density of $900\,\mathrm{kg\,m^{-3}}$ and a typical particle size of about 0.5 µm. The Stokes number (ratio between the particle response time and the flow characteristic time) has been calculated by Sartor et al. [154]. It is equal to 0.07 which indicates that the particle response lag is below the limit of a PIV study in compressible flow with presence of shock-wave.

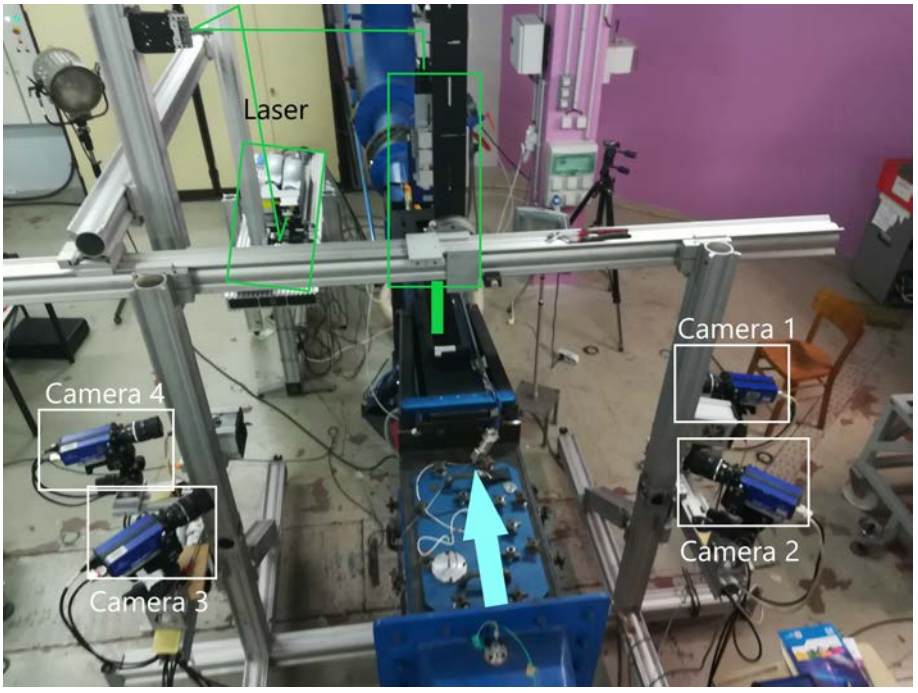

Figure II.9: Upper view of the tomographic PIV installation.

ii Optical and geometrical limitations of the implementation

The optical set-up has the advantage of providing all cameras with a complete view of the whole illuminated volume. Nevertheless, several optical aspects limit the positions of the cameras.

First of all, the high intensity laser flash provokes significant reflections of the lower wall, these reflections even limited by the rhodamine paint generate zones non measured in the field of view of the cameras (as visible on Fig. II.10 b)). Due to the shape of the bump, it prevents the cameras from being placed downstream of the flow because the end of the bump provokes a strong reflection even if the camera are placed parallel to the lower wall.

Furthermore, the limited size of the test section optical accesses also imposes restrictions on the possible camera placements.

Besides, the density gradient provoked by the shock-wave is going to deviate the light rays. In order to take this into account, previous studies (Lopez Hernandez [118]), advise to place the optical axis of the cameras either in the plane formed by the shock-wave either more than 20° away from this plane.

The best compromise has been found by placing two cameras (number 1 and 4) at the lower wall height with a shallow angle, this allows them not to see any lower wall reflection and two cameras (number 2 and 3) upstream with a slightly upper view, with a shallow angle to the tangent of the end of the bump. This allows them to have a small reflection zone with a view on the whole illuminated zone. The field of view of the cameras 1 and 2 is presented on Fig. II.10 with the illuminated volume delimited by the green lines. A photograph of the lateral view of the set-up is provided on Fig. II.11. The cameras still see some reflections on the lateral and upper windows of the wind tunnel but these are limited to zones of less interest except the boundary-layer for the cameras 2 and 3.

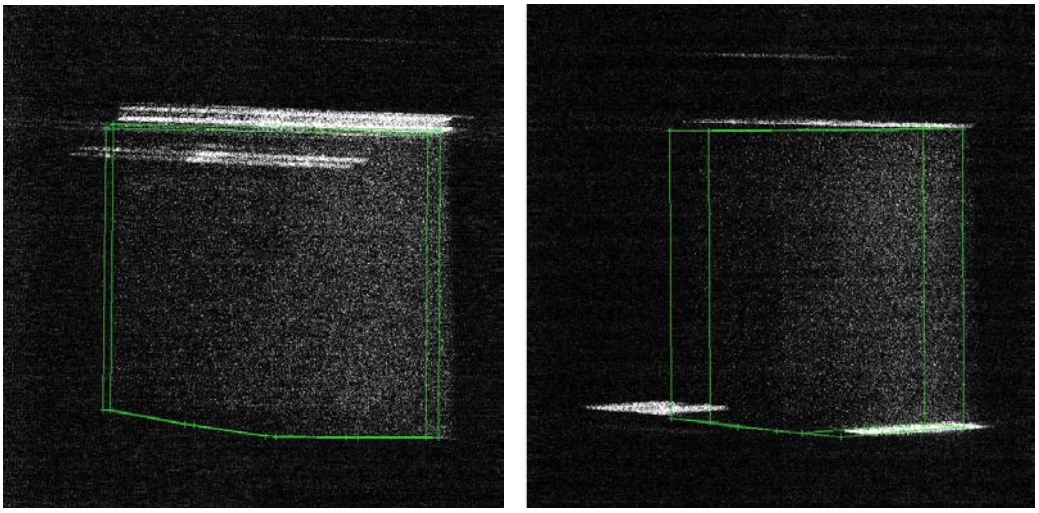

(a) Camera 1 (b) Camera 2

Figure II.10: Field of view of the cameras 1 and 2 (symmetric of cameras 3 and 4).

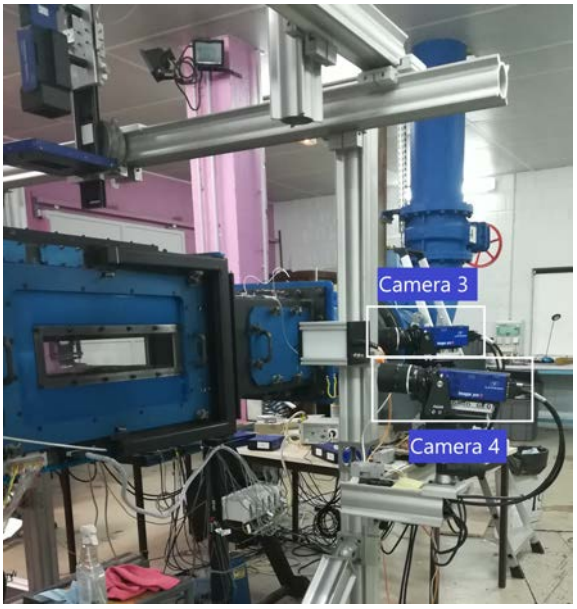

Figure II.11: Side view of the position of the cameras.

2.b Treatment

Tomographic PIV is mainly composed of two main steps: first a 3D reconstruction of a distribution of particles and their intensities in a volume using a tomographic algorithm method and then the classical correlation method used in 2D PIV, extended to 3D, to deduce the velocity field using two instantaneous distribution of particles. These two steps are presented on Fig. II.12.

In order to be able to achieve the two main steps of tomographic PIV, several pre-processing need to be performed. First a calibration, then a pre treatment of the images before the reconstruction. These steps are detailed below.

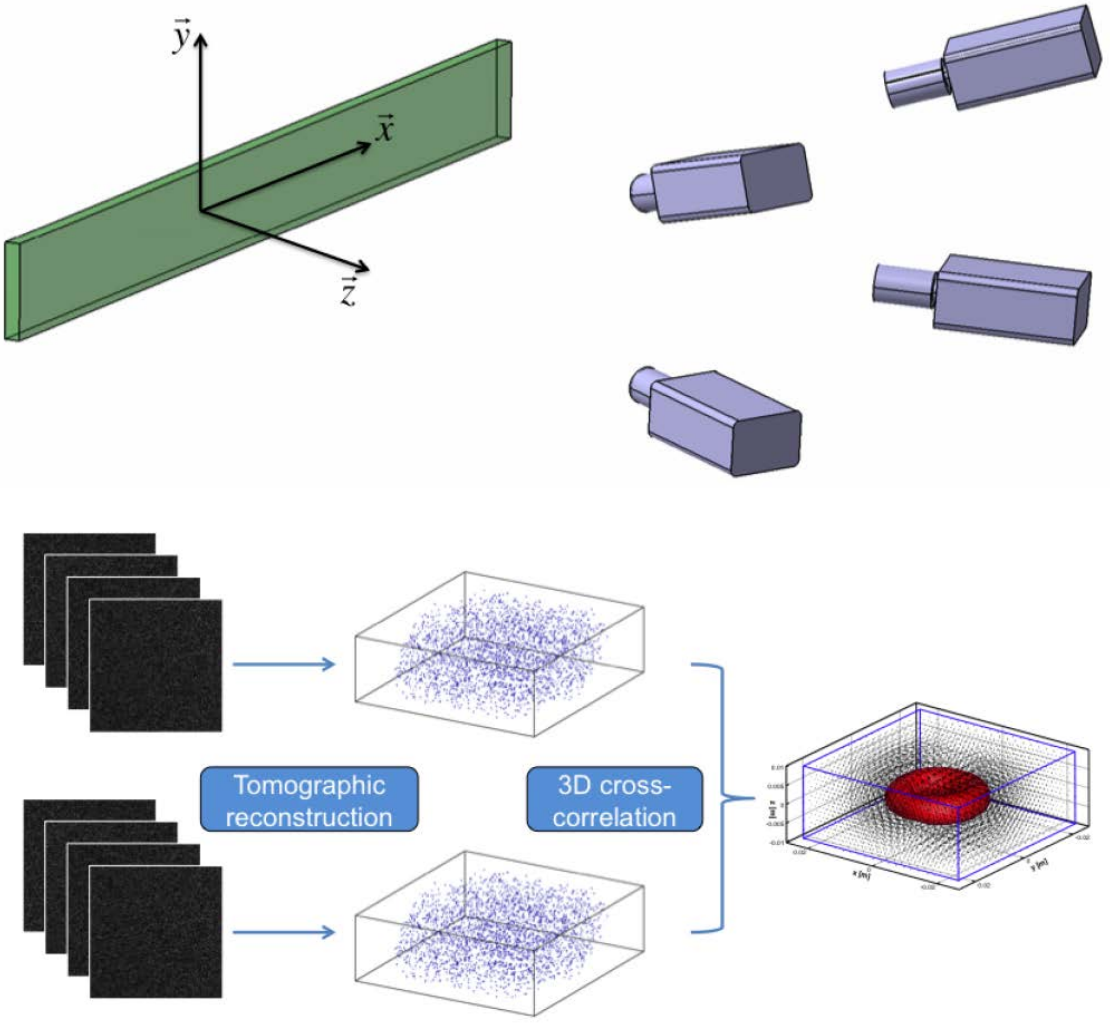

Figure II.12: Main steps of tomographic PIV from Cheminet [29]

i Calibration

The calibration is a crucial step in the tomographic PIV process as it allows to accurately know the physical position of each of the cameras of the set up, and thus the exact position of each light ray coming to each pixel of the camera sensor. It maps the physical 3D points of the studied volume on the 2D images of the four cameras. In order to do this, an object of well-defined geometry is used to calibrate the cameras. This object called a calibration target is presented on Fig. II.13a). Due to the fact that the cameras are positioned on both sides of the wind tunnel, all windows need to be closed during the calibration process and thus the calibration target cannot be varied in position easily. Therefore, a rotating calibration target has been designed in order to be easily moved using only two wires actuated through a hole drilled in the wind tunnel. The mechanism is presented on Fig. II.13. The calibration target is only visible by two cameras at a time so the first image taken by two cameras defined the work frame and then this work frame is transmitted to the two others cameras when they start to share pictures with the two first cameras. The calibration process and the pinhole models of the cameras provided with two Scheimpflug

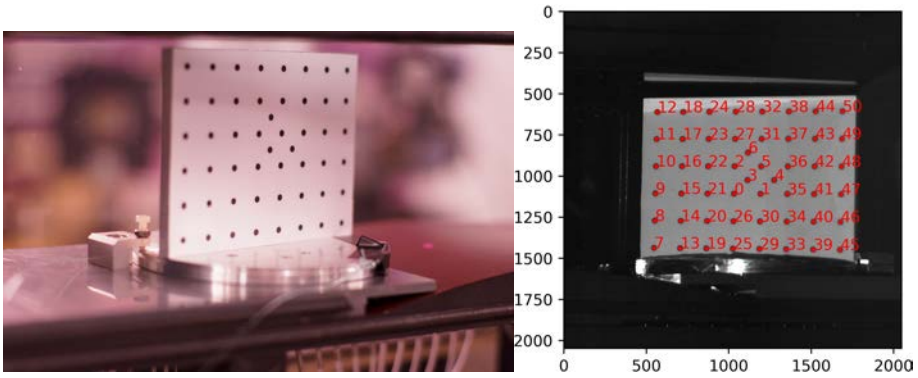

(a) On the rotating system (b) Motif automatically detected

Figure II.13: Calibration target.

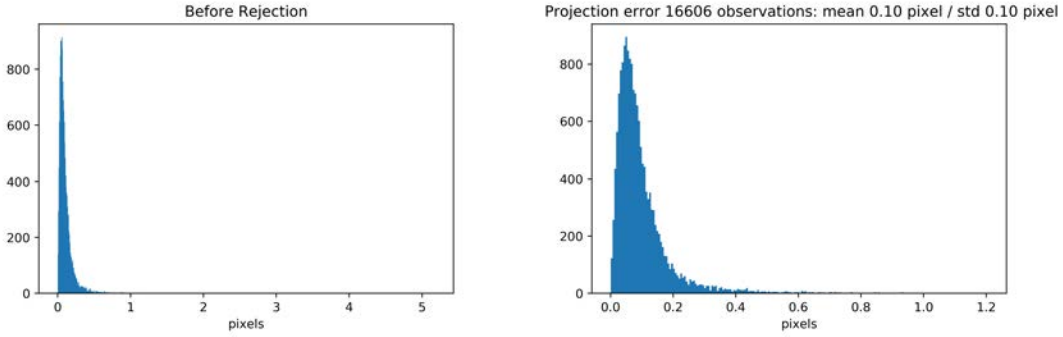

(a) Before rejection. (b) After rejection.

Figure II.14: Calibration error.

tilts are presented in Cornic et al. [35, 36]. The two Scheimpflug tilts are optical adapters which allow to place the whole illuminated volume in the wind tunnel parallel and in the focus volume even if the cameras are not parallel. The position of the calibration target is estimated through an automatic algorithm detecting the centers of the markers and recognizing the special central pattern. Furthermore, after a first optimization of the matrix linking the 2D images to the 3D reality, a rejection of the outliers positions and a bundle adjustment (see Cornic et al. [35]) of the movements of the calibration target, the mean error of the calibration goes down to 0.1 pixel which is the recommended limit (see Wieneke [176]). The resulting error distribution is visible on Fig. II.14.

The usual self-calibration process (re-calibration of the cameras using the position of particles during the tests see Cornic et al. [36], Wieneke [176]) has been considered for these tests. Nevertheless, after several preliminary tests, this process is not necessary in this case as in Humble et al. [92], Elsinga [60]. This could be explained by the fact that the cameras are sufficiently far from the wind tunnel and solidly mounted on a separated structure. Furthermore, the test runs are really short, less than two minutes due to the deposit of seeding particles on the windows, and so the calibrations are always done less than 30 minutes before or after the runs.

ii Pre-processing of the images

The images taken by the four cameras are first pre-processed before the tomographic reconstruction. The first step is to subtract the historical minimum over 100 images in order to remove the permanent reflections on the windows, the lower wall and more importantly on the scratches on the windows. Then intensities of the four images are adjusted in order to have corresponding intensity distributions levels. And finally, a low pass Gaussian filter of size 3 by 3 pixels kernel is applied to increase the particle image size and diminish the impact of remaining calibration errors. This is doable without affecting the reconstruction quality as the seeding is very low (close to 0.005 µs).

Besides, a mask is applied on the images to retain only the studied volume for the following process. As it can be seen on Fig. II.10, all the cameras see the whole illuminated volume which allows to consider that the reconstructed volume is equal to the illuminated volume which improves the quality of the reconstruction (see Cheminet [29]).

iii Processing

Tomographic reconstruction Reconstruction of the position and intensities of the particles is performed using an MLOS (Multiplicative Line-Of-Sight) initialization, followed by SMART (Simultaneous Multiplicative Algebraic Reconstruction Technique) iterations (see Atkinson and Soria [5]). It allows to quickly and memory saving construct a volume of possible particles distribution in the studied volume by multiplying the voxels crossed by lines of sight of non null intensity. The voxels distribution are then corrected to take into account the growth of general light intensity in the volume resulting from the multiplication.

The reconstruction problem, which amounts to an inverse problem, consists in recreating the volume distribution of intensity $E(X, Y, Z)$ from a set of 2D intensity maps $I(x, y)$ with the corresponding weight of intensity, $w_{i,j}$ which are supposed to be simply summed along the line-of-sight. A figurative description of the problem is presented on Fig. II.15, N_i being the number of j voxels contributing to the image intensity of the i^{th} pixel. The relation expressing the inversion problem is presented in equation II.1.

$$\sum_{j \in N_i} w_{i,j} E(X_j, Y_j, Z_j) = I(x_i, y_i) \tag{II.1}$$

The inversion problem consists in finding the field E using the images I, the weighting matrix W, gathering the $w_{i,j}$ being geometrically defined by the calibration process. This problem presents naturally multiple solutions due to the fact that the limited number of cameras does not enable to distinguish between physical particles and so called "ghost particles" which are the results of crossing line-of-sight from different physical particles. Iterative processes are the best and most common process to address this problem.

The SMART algorithm iteratively updates the volume distribution E corrected by the ratio of the measured pixel intensity I with the current pixel intensity resulting from the precedent volume distribution. The exponent $w_{i,j}$ allows to only update the voxels affected by the i^{th} pixel and the μ exponent is a relaxation parameter chosen below or equal to one to ensure the convergence of the algorithm. The resulting formula used at $k+1$ iteration is presented in Eq. II.2.

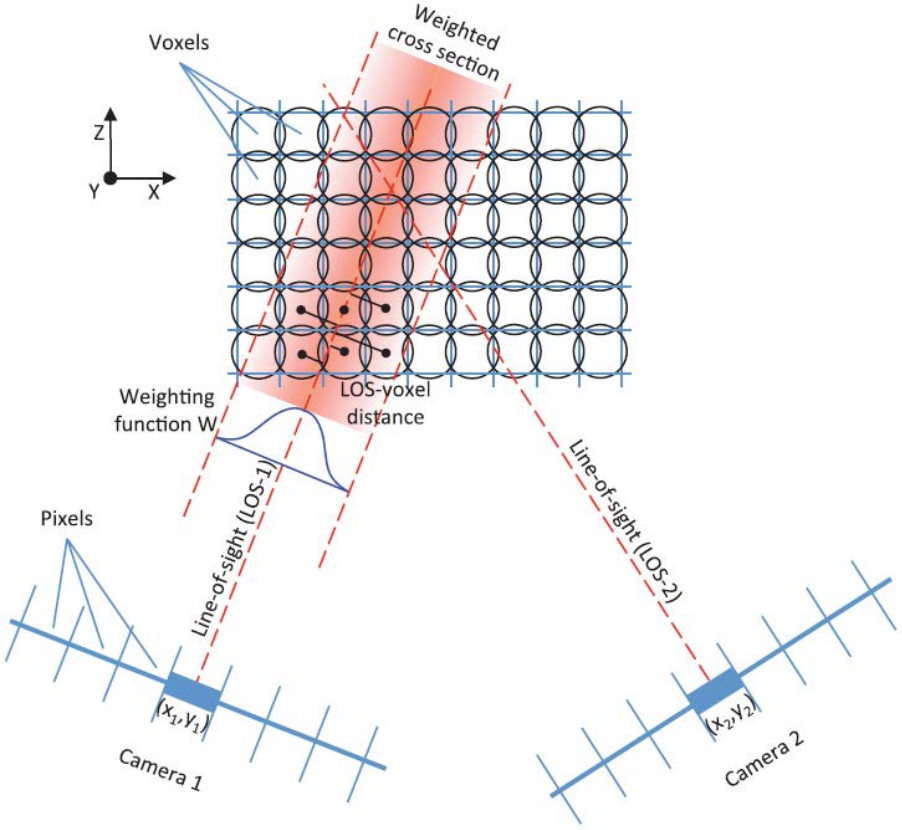

Figure II.15: Representation of the imaging model used in tomographic reconstruction. The voxels are represented as sphere which simplifies the calculation of the weight of the voxel intensity projected on the pixel intensity through the line-of-sight (from Scarano [155]).

$$E(X_j, Y_j, Z_j)^{k+1} = E(X_j, Y_j, Z_j)^k \left(\frac{I(x_i, y_i)}{\sum_{j \in N_i} w_{i,j} E(X_j, Y_j, Z_j)^k} \right)^{\mu w_{i,j}} \tag{II.2}$$

Following the recommendations of Cheminet [29], Champagnat et al. [26], 25 steps of SMART algorithm are applied to the reconstructed volume after the MLOS first guess, this allows to reconstruct sufficiently clean volume of particles which are next used in the cross correlation step for the reconstruction of the volume velocity field.

Cross correlation The cross correlation is done by the FOLKI-3D algorithm presented in Cheminet et al. [30] and is an adaptation to 3D of the planar PIV software exposed in Champagnat et al. [25] The idea of the algorithm is to find the best correlated volume to each interrogation volume by minimizing a functional built as the sum of squared intensity differences between the two instants, in the given interrogation volume. The problem is then solve iteratively by introducing a multi-resolution pyramid, whereby the particle volumes are averaged with a low-pass filter, and then decimated, the operation being repeated several times, building several pyramid levels. Progressing one level up in

the pyramid leads to a volume with each dimension, and displacements in each direction, divided by two. This technique, also referred to as multigrid coarse to fine resolution, allows to have really small displacements in terms of voxel per instant for the coarsest level. Thus these small displacements are close to the solution $u = 0$, allowing this solution to be the first guess of the Gauss-Newton iterations which minimizes the cost function. Between each Gauss-Newton iteration, the volumes are deformed using the current velocity field, using cubic B-Spline interpolation. The solution of the biggest level is then projected on the level below and used as first guess in the following Gauss-Newton minimization. The exact derivation of the algorithm can be found in Cheminet et al. [30], Champagnat et al. [25].

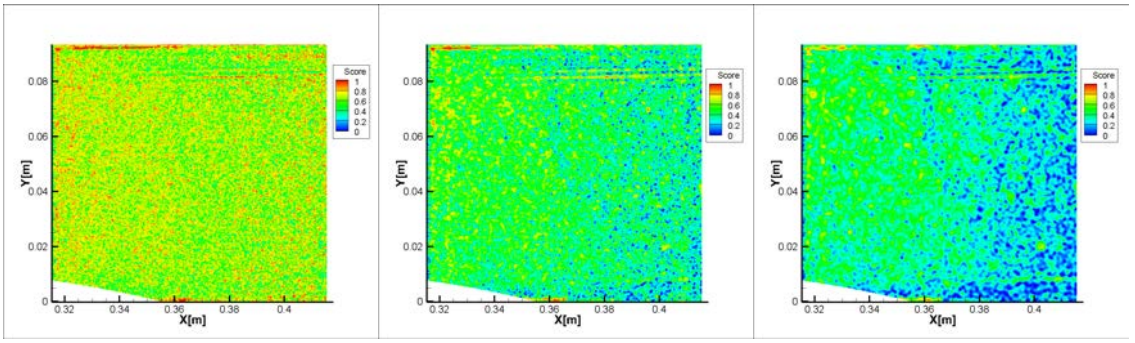

(a) Correlation coefficient: IV size 11 voxels (b) Correlation coefficient: IV size 21 voxels (c) Correlation coefficient: IV size 31 voxels

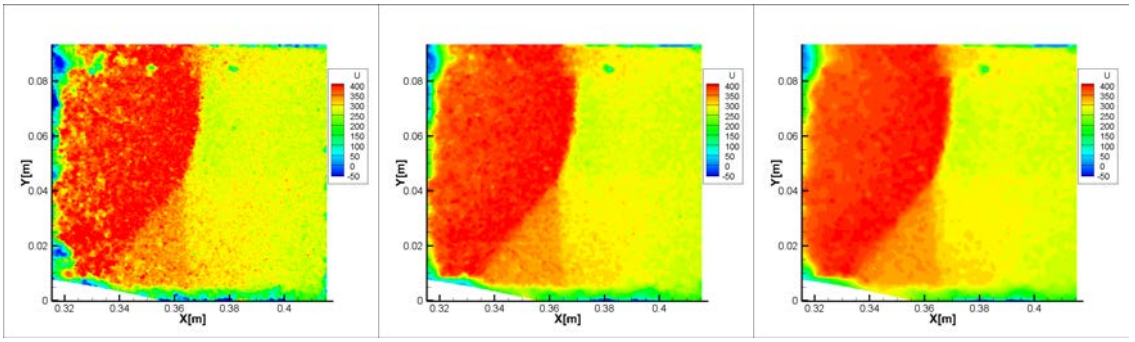

(d) U: IV size 11 voxels (e) U: IV size 21 voxels (f) U: IV size 31 voxels

Figure II.16: Study of the effect of the IV size, visualized in the median plane of a snapshot.

The size of the interrogation volume has been chosen following a parametric study, three results of which are presented on Fig. II.16. The size of the interrogation volume should be a good compromise between the number of particles in the volume and the smallest scales resolved by the tomographic PIV. Looking at the correlation coefficient for the three different sizes of interrogation volume (IV) on the median plane of the studied volume presented on Fig. II.16 a),b) and c), it is visible that the IV size of 11 voxels is too small as the resulting velocity field is highly noisy (the small size of the IV allow to have volumes of small gradient highly correlated, but also zones with less particles causing noise) and the IV size of 31 voxels is too high as it smooths too much the turbulent structures in the mixing layer and complicates the correlation in downstream zones. The correlation coefficient below 0.1 regions represent zones where the algorithm has difficulty

to correlate due to high gradient in the volume, this is why the phenomenon is more prominent in the zone after the SWBLI where more turbulent structures develop (this can be seen on Schlieren visualization on Fig. VI.3a presented in Chap. VI). Therefore the IV size of 21 voxels, which is a fair compromise between noise and precision, is always used in the following results. This size of interrogation volume, of 1.55 mm is bigger to the one used in 2D PIV due to the inherent limitations of the tomographic PIV.

These two steps are realized on four GTX 1080 Ti GPU cards with 3584 CUDA cores and a total memory of 2Go, the complete process of tomographic reconstruction and cross correlation takes 4 minutes.

Volume masks During this whole process, a volume mask is taken into account by the algorithm, it prevents the algorithm from creating particles below the level of the lower wall of the wind tunnel and imposes a zero velocity at the wall. This process improves the physical validity of the reconstruction in a region with less particles. The volume mask corresponds to the volume delimited by the green lines on Fig. II.10.

iv Post Processing

The reconstructed velocity field is then re-projected on the "real world" frame, converted from voxel per instant to $\mathrm{m\,s^{-1}}$, masked and analysed using Cassiopee, ONERA's in house software Cambier et al. [22]. The instantaneous data allows to calculate on 1000 images the mean and fluctuating flow velocities which are presented in Chap. VI and Chap VII.

Convergence This number of images has been verified to allow the convergence of the mean and turbulent quantities. This is presented for four points disclosed on Fig. II.17. the first point studied is placed close to the triple point, but in the clean zone just after the normal shock-wave, the two following points are located close to the two others shocks and the last one is placed in the mixing layer.

The accumulative mean of the velocities for the four selected points at the 1000 instants are presented on Fig. II.18 a), c),e). These curves certified the satisfactory convergence of the velocities for the four points. On Fig. II.18 b), d) and f), the accumulative mean of the three turbulent velocities of the four points are presented. The values are fully converged for the four points with higher levels and more complicate convergence for the point number 3 which is placed in the turbulent mixing layer. The transverse fluctuations, w'^2 quantity seems less converged due to the smallest scale of the w'^2 curve.

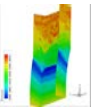

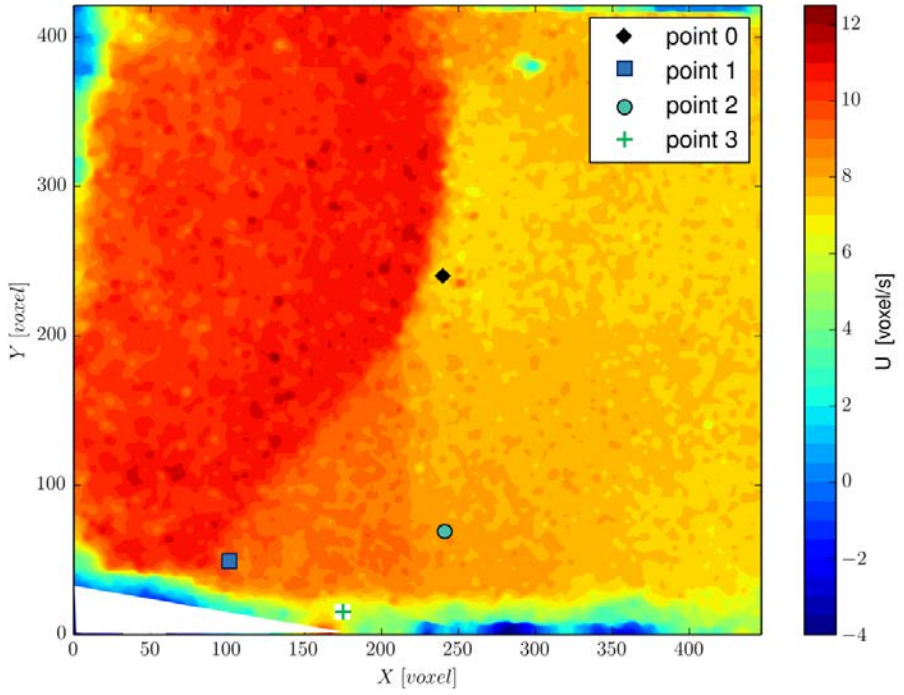

Figure II.17: Four points studied for the physical quantities' convergence study presented on an instantaneous field of U velocity of the median plane of the central volume. The central volume is visible on Fig. II.19.

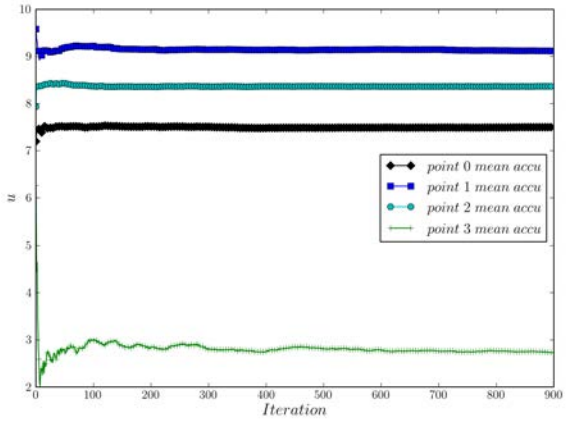

(a) U velocity along X axis

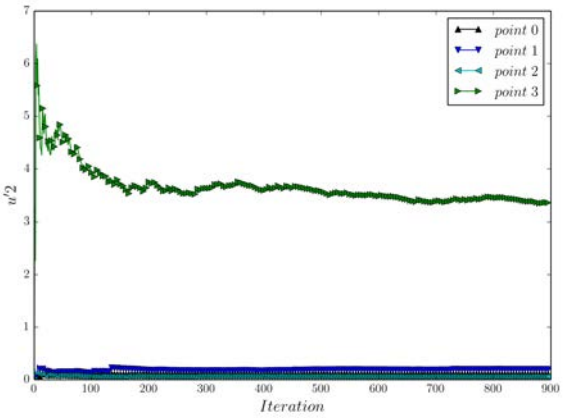

(b) u'^2 shear stress along X axis

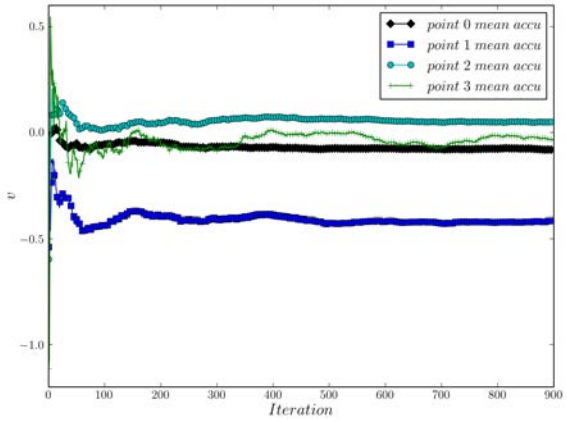

(c) V velocity along Y axis

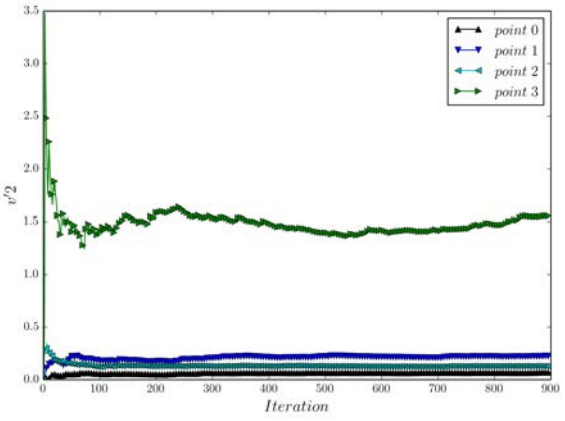

(d) v'^2 shear stress along Y axis

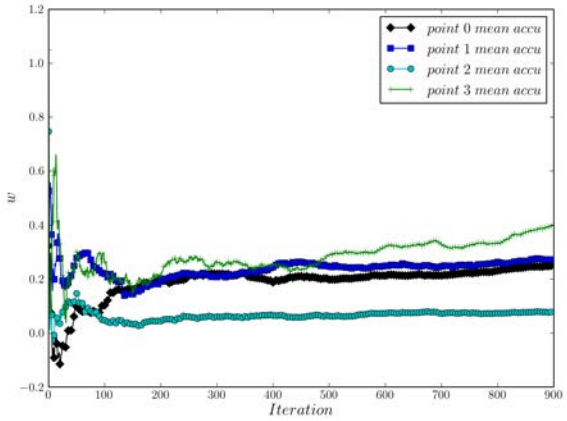

(e) W velocity along Z axis

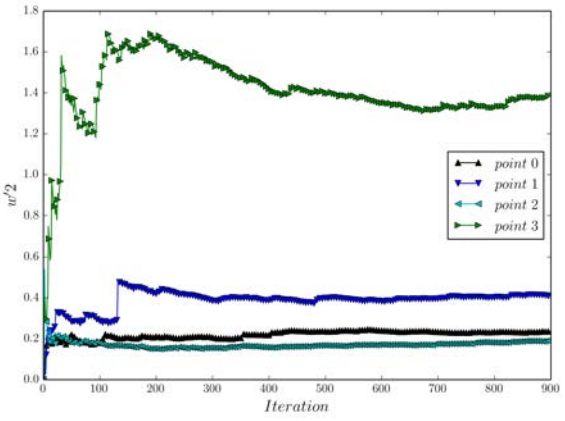

(f) w'^2 shear stress along Z axis

Figure II.18: Convergence curves of the accumulative mean of the mean velocities and diagonal terms of the Reynolds stress tensor for the 1000 instants, for the four points presented on Fig. II.17.

v Reconstructed volumes

Four different volumes have been measured for this study, the three one which finally could provide exploitable results are represented on Fig. II.19. These volumes of same size $100 \times 100 \times 20$ mm are the central one and three shifted in the spanwise direction (with median plane at $z = -0\,\text{mm}$, $z = -14\,\text{mm}$, $z = -26\,\text{mm}$ and $z = -38\,\text{mm}$) of the wind tunnel close enough to measure as close as 2 cm from the lateral wall. The fourth volume studied closer to the side wall needs a rotation of the incoming laser volume due to an opaque part of the upper wall. This oblique angle provokes an oblique reflection on the lower wall and thus a stronger intensity on the lateral windows. Some scratches on the windows generate strong brightness at several positions and thus strong noise on the final velocity field.

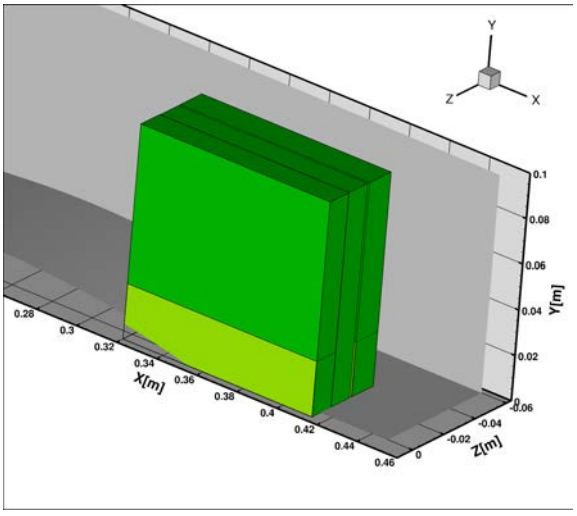

Figure II.19: Three volumes studied in the wind tunnel by tomographic PIV. The lighter zones correspond to volumes reconstructed with only two cameras.

vi 2 cameras reconstruction

The reflection on the lower wall of the wind tunnel present in the images of cameras 2 and 3 induce masked zones in the turbulent boundary-layer. In order to remove these zones, tomographic reconstruction have also been done with only the cameras 1 and 4. These reconstructions are done on zones of only 2.5 cm height, with the same parameters as the previous ones. Due to the fact that the reconstruction only uses two cameras, the position is less accurate in the lateral direction but improved close to the wall. A correlation coefficient map of the reconstruction with two cameras is presented on Fig. II.20. Unfortunately, the zone delimited by black lines is badly correlated due to the fact that the thickness of the bump still hides part of the field of view of the cameras. Nevertheless, these reconstruction allows to study more precisely the separation zone and the mixing layer downstream of the bump.

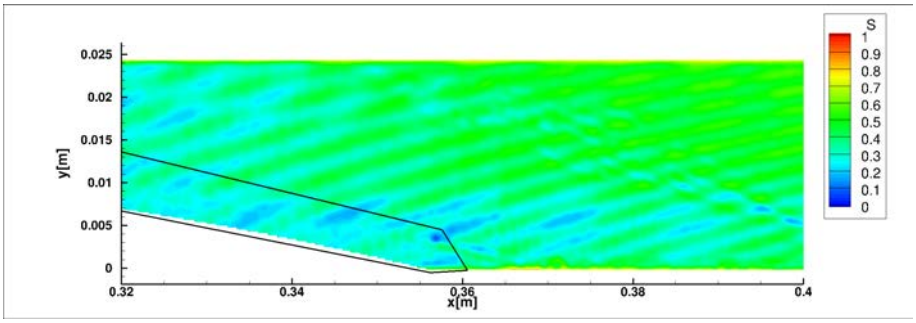

Figure II.20: Correlation coefficient map on the central plane of the wind tunnel for a reconstruction for two cameras.

II.3 Numerical modeling: RANS principle method and implementation

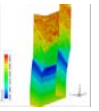

In this section, a first quick reminder of the fluid mechanics equations is presented with an overview of the different numerical methods of resolution. Then the Reynolds Averaged Navier Stokes equations[1] are detailed along with the implementation parameters used within this study in Chap. IV and Chap. III.

3.a Fluid mechanics equations and numerical methods of resolution

In the context of compressible transonic flow, the system can be modeled using the classical Navier Stokes equations for a compressible, non weighting fluid.

The first equation is the conservation of mass:

$$\frac{\partial \rho}{\partial t} + \nabla \cdot \rho \mathbf{u} = 0 \tag{II.3}$$

with ρ the density of the flow, $\mathbf{u}$ the velocity vector and t the time.

The second equation is the conservation of momentum:

$$\frac{\partial \rho \mathbf{u}}{\partial t} + \nabla \cdot (\rho \mathbf{u} \times \mathbf{u}) = \nabla \cdot \bar{\bar{\sigma}} \tag{II.4}$$

With $\bar{\bar{\sigma}}$ the Cauchy's strain tensor.

And the last one is the conservation of total energy:

$$\frac{\partial \rho e}{\partial t} + \nabla \cdot (\rho e \mathbf{u}) = \nabla \cdot (\bar{\bar{\sigma}} \cdot \mathbf{u} + \mathbf{q}) \tag{II.5}$$

With e the total energy. The Cauchy's strain tensor can be decomposed as $\bar{\bar{\sigma}} = -p\bar{\bar{\mathbb{I}}} + \bar{\bar{\tau}}$ with p the pressure, $\bar{\bar{\mathbb{I}}}$ the identity tensor and $\bar{\bar{\tau}}$ the viscous stress tensor.

This leaves a system of 5 equations for 18 scalar unknowns ($\rho, \mathbf{u}, e, p, \mathbf{q}$ and $\bar{\bar{\tau}}$), which calls for some closure models.

i Constitutive equations

Considering that air is a Newtonian fluid for the pressure and temperature ranges considered here, the viscous stress tensor can be further decomposed as:

$$\bar{\bar{\tau}} = \lambda(\nabla \cdot \mathbf{u})\bar{\bar{\mathbb{I}}} + 2\mu\bar{\bar{\mathbb{d}}} \tag{II.6}$$

Where λ and μ respectively represent the volumic and shear viscosity and $\bar{\bar{\mathbb{d}}}$ is the strain rate tensor equal to the symmetrical part of the Jacobian of velocity: $\frac{1}{2}(\nabla \mathbf{u} + {}^t\nabla \mathbf{u})$.

Supposing the Stokes hypothesis is valid: $\lambda = -\frac{2}{3}\mu$.

Using the Fourier law to model the heat flux vector:

$$\mathbf{q} = -\kappa \nabla T \tag{II.7}$$

with κ the thermal coefficient of conductivity and T the absolute temperature.

[1] Along these calculations, the following conventions are chosen: bold characters as $\mathbf{u}$ represent vectors of dimension 3 and capital letters with double bar as $\bar{\bar{\tau}}$ represent matrix of size 3×3.

ii Laws of state

Considering that air is a perfect gas, with constant specific heats, of ratio $\gamma = c_p/c_v$, pressure and internal energy (and so total energy sum of internal energy and kinetic energy) can be linked to absolute temperature by:

$$p = \rho r T \tag{II.8}$$

$$e = c_v T + \frac{1}{2} \sum_{i \in [1,2,3]} u_i^2 \tag{II.9}$$

μ and κ still have to be modeled, this will be done using the Sutherland law for the dynamic viscosity:

$$\mu = \mu_0 \sqrt{\frac{T}{T_0}} \frac{1 + C_s/T_0}{1 + C_s/T} \tag{II.10}$$

With C_s the Sutherland constant and μ_0 and T_0 a reference state.

κ, the thermal conductivity is modeled as linearly dependent of the viscosity following the law:

$$\kappa = \frac{\gamma r}{\gamma - 1} \frac{\mu}{Pr} \tag{II.11}$$

With Pr the Prandtl number supposed to be constant and equal to 0.72.

The whole system is now closed but not easy to solve, due notably to the non linearity of the advection term $\nabla \cdot (\rho \mathbf{u} \times \mathbf{u})$.

3.b Overview of methods of resolution

Several techniques have been developed along the years to solve this complex system of non linear equations. The main methods found in the literature are presented on Fig. II.21. The method involving less empirical notions is called Direct Numerical Simulations (DNS) and consists in directly solving the discretized Navier Stokes equations. Nevertheless, this technique necessitate to solve the smallest dynamically active scales of the flow. These scales, at which the dissipation occurs are typically of few micro meters. This leads to extremely small grid size and time steps which make this method very computationally demanding and not usable for high Reynolds flows.

In order to simplify the resolution of these strongly non-linear system, Reynolds introduced a decomposition which consists into a separation of each physical quantity between a temporally averaged field and a fluctuating field. Using a model, called turbulence model, for the fluctuating terms included in the mean flow equations, the mean quantities can therefore be calculated. This technique is denominated Reynolds Averaged Navier Stokes (RANS) method. RANS relies on empirical dimensioning of turbulent constants. The precise equation system used is described in section 3.c. This modeling gives satisfying results for simple configurations with small detached flow. Furthermore, a temporal component of the flow can be introduced in this system if the main phenomenal frequencies are clearly separated from the higher frequencies linked to turbulence (approached called URANS for Unsteady RANS). Nevertheless it fails at capturing the dynamics of some phenomena such as SWBLI on the Délery bump (see Sartor [151]) while being able to capture it in other configurations such as a wing in buffet condition (see Goncalves and Houdeville

[87], Kourta et al. [106], Sartor [151]). In order to set up an optimization process involving a high number of calculations (see Chap. IV), the RANS method of modeling has been chosen, taking advantage of its relatively small calculation's cost.

Closer to DNS, another method called Large Eddy Simulation allows to get a more precise modeling of the flow by calculating more turbulent structures. The main idea is to filter the smallest structures and so the high frequencies of turbulence, and to introduce a model to take into account the dissipation of energy the filtered structures produce. This method rapidly presented in section 4.a, loosens slightly the constraint on the size of the mesh relative to DNS, and allows to capture the dynamic of SWBLI (see for instance Garnier et al. [76], Sandham et al. [150]). However, the study of a full channel with the four walls remains a major challenge due to the massive mesh size and will not be treated in this study.

In order to take advantage of both RANS and LES techniques, hybrid methods have been developed which allow to alleviate the resolution constraint in the near-wall regions. The first one to become largely used is called Detached Eddy Simulation (DES) presented in Spalart et al. [161]. The method which is used in this study, referred to as Zonal Detached Eddy Simulation (ZDES), introduced in Deck [46], is an improvement on this DES method and is detailed in 4.b.

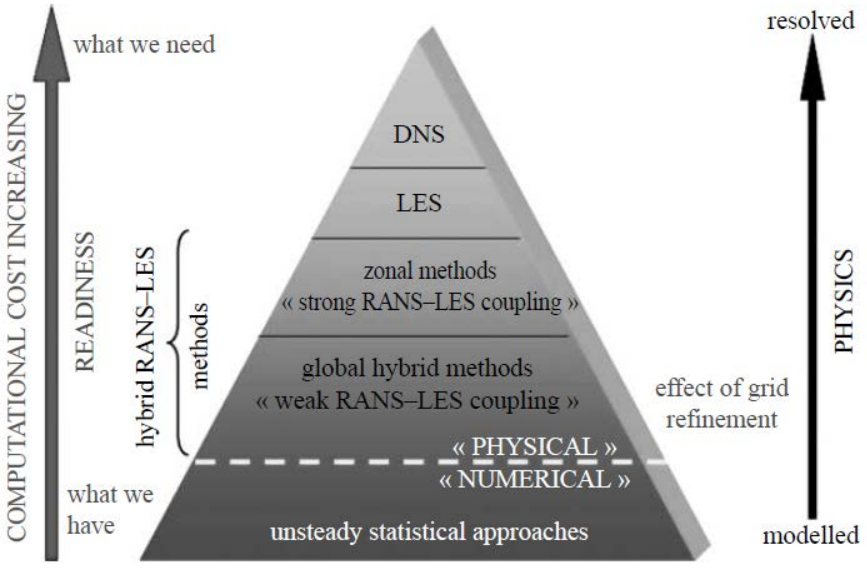

Figure II.21: Classification of the methods of numeric calculation with respect to their level of modeling (from Sagaut and Deck [148]).

3.c Reynolds Averaged Navier-Stokes equations

As explain above, the Reynolds Averaged Navier Stokes equations are found by introducing for every physical quantity ϕ, a mean over time part noted $\bar{\phi}$ and a fluctuating part noted ϕ':

$$\phi = \bar{\phi} + \phi' \tag{II.12}$$

For flows with variable density, it is common to introduce the Favre decomposition:

$$\phi = \tilde{\phi} + \phi'' \tag{II.13}$$

with $\tilde{\phi} = \frac{\overline{\rho\phi}}{\bar{\rho}}$ the mass weighted average and ϕ'', the fluctuations of ϕ such as $\widetilde{\rho\phi''} = 0$ and $\overline{\phi''} \neq 0$.

By applying the Favre operator to the total energy and to the velocity, and the Reynolds operator to the density and the pressure in the equations II.3, II.4 and II.5, it gives the system[2]:

$$\frac{\partial \bar{\rho}}{\partial t} = -\nabla \cdot \bar{\rho}\tilde{\mathbf{u}} \tag{II.14}$$

$$\frac{\partial \bar{\rho}\tilde{\mathbf{u}}}{\partial t} = -\nabla \cdot (\bar{\rho}\tilde{\mathbf{u}} \times \tilde{\mathbf{u}} + \bar{p}\mathbb{I}) + \nabla \cdot (\bar{\boldsymbol{\tau}} - \bar{\rho}(\widetilde{\mathbf{u}'' \times \mathbf{u}''})) \tag{II.15}$$

$$\frac{\partial \bar{\rho}\tilde{e}}{\partial t} = -\nabla \cdot (\bar{\rho}\tilde{e}\tilde{\mathbf{u}} + \overline{p\mathbf{u}}) + \nabla \cdot (\overline{\boldsymbol{\tau} \cdot \mathbf{u}} - \bar{\mathbf{q}}) - \nabla \cdot (\bar{\rho}\widetilde{e''\mathbf{u}''}) \tag{II.16}$$

The only fluctuating term remaining in the movement equation, $-\bar{\rho}(\widetilde{\mathbf{u}'' \times \mathbf{u}''})$ can be defined as the Reynolds stress tensor $\boldsymbol{\tau}_t$. Defining k the turbulent kinetic energy :

$$k = \frac{1}{2} \sum_{i \in [1,2,3]} \widetilde{u_i''}^2, \tag{II.17}$$

the Reynolds stress tensor can be identified using the Boussinesq hypothesis[3] and defining μ_t the eddy viscosity such as:

$$\boldsymbol{\tau}_t = -\frac{2}{3}\mu_t(\nabla \cdot \tilde{\mathbf{u}})\mathbb{I} + 2\mu_t\tilde{\mathbb{d}} - \frac{2}{3}k\mathbb{I} \tag{II.18}$$

In the energy conservation equation, some terms will be developed and approximated as following:

$$\bar{\mathbf{q}} = -c_p\overline{\frac{\mu}{Pr}\nabla T} \tag{II.19}$$

$$\bar{\mathbf{q}} \approx -c_p\frac{\mu}{Pr}\nabla\tilde{T} \tag{II.20}$$

The approximation II.20 is obtained by neglecting the fluctuations of the molecular viscosity μ and considering $\tilde{T} \gg \bar{T''}$.

$$\overline{\boldsymbol{\tau} \cdot \mathbf{u}} = \tilde{\boldsymbol{\tau}} \cdot \tilde{\mathbf{u}} + \overline{\boldsymbol{\tau} \cdot \mathbf{u}''} + \bar{\boldsymbol{\tau}''} \cdot \tilde{\mathbf{u}} \tag{II.21}$$

$$\overline{\boldsymbol{\tau} \cdot \mathbf{u}} \approx \tilde{\boldsymbol{\tau}} \cdot \tilde{\mathbf{u}} \tag{II.22}$$

[2]Noticing $\overline{\rho\phi} = \bar{\rho}\tilde{\phi}$ and $\overline{\rho\phi\psi} = \overline{\rho\tilde{\phi}\tilde{\psi}} + \overline{\rho\tilde{\phi}\psi''} + \overline{\rho\phi''\tilde{\psi}} + \overline{\rho\phi''\psi''} = \overline{\rho\tilde{\phi}\tilde{\psi}} + \overline{\rho\phi''\psi''}$

[3]Other RANS models can be derived without using the Boussinesq hypothesis see for instance Loyau et al. [119], Gand [72]

The approximation II.22 is obtained considering again $\tilde{T} \gg \bar{T}''$ and by neglecting the molecular diffusion of turbulent energy, $\overline{\boldsymbol{\tau} \cdot \mathbf{u}''}$, as the turbulent energy is small compared to the enthalpy.

The last two terms to simplify are considered at once:

$$\begin{aligned}
\overline{\bar{p}\bar{\mathbf{u}}} + \bar{\rho}\widetilde{e''\mathbf{u}''} &= \bar{p}\tilde{\mathbf{u}} + \overline{\bar{p}\mathbf{u}''} + \overline{\rho e''\mathbf{u}''} && \text{(II.23)}\\
&= \bar{p}\tilde{\mathbf{u}} + c_p\overline{\rho T\mathbf{u}''} + \overline{\rho\tilde{\mathbf{u}}\cdot\mathbf{u}''\mathbf{u}''} + \frac{1}{2}\overline{\rho\mathbf{u}''\cdot\mathbf{u}''\mathbf{u}''} && \text{(II.24)}\\
\overline{\bar{p}\bar{\mathbf{u}}} + \bar{\rho}\widetilde{e''\mathbf{u}''} &\approx \bar{p}\tilde{\mathbf{u}} + c_p\overline{\rho T\mathbf{u}''} + \boldsymbol{\tau}_t\cdot\tilde{\mathbf{u}} && \text{(II.25)}
\end{aligned}$$

Where the second equation II.24 is obtained using the law of state and the development of e'' and the approximation II.25 is obtained by neglecting the transport of the turbulent kinetic energy compared to the enthalpy and identifying as before the Reynolds stress tensor.

Finally, defining the turbulent transport of heat $\mathbf{q}_t$ as:

$$\begin{aligned}
\mathbf{q}_t &= -c_p\overline{\rho T\mathbf{u}''} && \text{(II.26)}\\
\mathbf{q}_t &\approx -c_p\frac{\mu_t}{Pr_t}\nabla\tilde{T} && \text{(II.27)}
\end{aligned}$$

with Pr_t the turbulent Prandtl number equal to 0.9.

The system of equation can be written as:

$$\begin{aligned}
\frac{\partial\bar{\rho}}{\partial t} &= -\nabla\cdot\bar{\rho}\tilde{\mathbf{u}} && \text{(II.28)}\\
\frac{\partial\bar{\rho}\tilde{\mathbf{u}}}{\partial t} &= -\nabla\cdot(\bar{\rho}\tilde{\mathbf{u}}\times\tilde{\mathbf{u}} + \bar{p}\mathbb{I}) + \nabla\cdot(\bar{\boldsymbol{\tau}} + \boldsymbol{\tau}_t) && \text{(II.29)}\\
\frac{\partial\bar{\rho}\tilde{e}}{\partial t} &= -\nabla\cdot(\bar{\rho}\tilde{e}\tilde{\mathbf{u}} + \bar{p}\tilde{\mathbf{u}}) + \nabla\cdot((\tilde{\boldsymbol{\tau}} + \boldsymbol{\tau}_t)\cdot\tilde{\mathbf{u}} + c_p(\frac{\mu}{Pr} + \frac{\mu_t}{Pr_t})\nabla\tilde{T}) && \text{(II.30)}
\end{aligned}$$

This system is closed as soon as a model is given for μ_t and k.

i Turbulent models

Two different turbulent models have been used in this study, they are detailed below.

1. Spalart Allmaras: The first turbulent model used in this study has been presented in Spalart and Allmaras [160]. It is based on only one variable (the turbulent kinetic energy is neglected in the Reynolds Stress Tensor), $\tilde{\nu}$ the kinematic viscosity transform[4]. This model is based on an equation for $\tilde{\nu}$ considering its convection, diffusion, production, cross diffusion and destruction with respect to one geometrical variable d_w the distance to the nearest wall. The equation is defined as:

$$\frac{\partial\tilde{\nu}}{\partial t} = -\nabla\cdot\tilde{\nu}\mathbf{u} + \underbrace{\frac{\mu+\tilde{\nu}}{\sigma}\nabla\tilde{\nu}}_{\text{diffusion}} + \underbrace{C_{b1}\tilde{S}\tilde{\nu}}_{\text{production}} + \underbrace{\frac{C_{b2}}{\sigma}\nabla\tilde{\nu}\cdot\nabla\tilde{\nu}}_{\text{cross diffusion}} - \underbrace{C_{w1}f_w\frac{\tilde{\nu}^2}{d_w^2}}_{\text{destruction}} \qquad \text{(II.31)}$$

[4]The classical notation has been used here even if this variable is not Favre averaged.

with, denoting Ω the vorticity:

$$\tilde{S} = |\Omega| + \frac{\tilde{\nu}}{K^2 d_w^2} f_{v2}, \quad f_{v2} = 1 - \frac{\chi}{1 + \chi f_{v1}}, \quad f_w = \left(\frac{1 + C_{w3}^6}{g^6 + C_{w3}^6}\right)^{1/6}$$
$$g = r + C_{w2}(r^6 - r) \quad r = \frac{\tilde{\nu}}{\tilde{S} K^2 d_w^2}, \quad C_{w1} = \frac{C_{b1}}{K^1} + \frac{(1 + C_{b2})}{\sigma}$$

The turbulent eddy viscosity is finally defined by $\mu_t = \rho \tilde{\nu} f_{v1}$ with:

$$f_{v1} = \frac{\chi^3}{\chi^3 + C_{v1}^3}, \quad \chi = \frac{\rho \tilde{\nu}}{\mu}$$

f_{v1}, f_{v2} functions are corrections dedicated to the near wall regions to guarantee the logarithmic law in the meso sub-layer (or log layer) for respectively $\tilde{\nu}$ and $\tilde{S}$. And the purpose of the f_w function is to accelerate the destruction of $\tilde{\nu}$ far from the wall.

All the constants of the model, summed up in Table II.4, have been dimensioned in Spalart and Allmaras [160] with respect to several experiments.

Table II.4: Parameters used for the Spalart-Allmaras model.

C_{b1}	C_{b2}	σ	K	C_{w2}	C_{w3}	C_{v1}
0.1355	0.622	2/3	0.41	0.3	2	7.1

2. $k - \omega$ Shear Stress Tensor:
The second turbulent model tested in this work is the $k - \omega$ Shear Stress Tensor ($k - \omega$ SST) model developed in Menter [123]. This model presents two equations for the two variables ρk the turbulent kinetic energy and $\omega = \epsilon/(\beta^* k)$, the specific rate of dissipation of the eddies.

The turbulent eddy viscosity μ_t is defined as:

$$\mu_t = \rho \nu_t = \frac{a_1 k}{\max(a_1 \omega, \Omega F_2)} \tag{II.32}$$

And the two equations of the model are:

$$\frac{\partial \rho k}{\partial t} = -\nabla \cdot (\rho k \mathbf{u}) + P - \beta^* \rho \omega k + \nabla \cdot \big((\mu + \sigma_k \mu_t) \nabla k\big) \tag{II.33}$$
$$\frac{\partial \rho \omega}{\partial t} = -\nabla \cdot (\rho \omega \mathbf{u}) + \rho \alpha \mathbb{d}^2 - \beta \rho \omega^2 + \nabla \cdot \big((\mu + \sigma_\omega \mu_t) \nabla \omega\big) + 2(1 - F1) \rho \sigma_{\omega 2} \frac{1}{\omega} \nabla k \cdot \nabla \omega \tag{II.34}$$

With the functions F_1 allowing the transition between a $k - \omega$ model in the near wall region and a $k - \epsilon$ model in the free stream region as the latter has a smaller free stream sensitivity. The function F_2 ensures that in boundary-layer region with

adverse pressure gradient (where the production of k is larger than its dissipation $\Omega > a_1\omega$), the shear stress tensor is proportional to the turbulent kinetic energy.

Their definitions are:

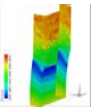

$$F_1 = \tanh(arg_1^4) \tag{II.35}$$

$$\text{with} \quad arg_1 = \min\Big(\max\Big(\frac{\sqrt{k}}{\beta^*\omega d_w}, \frac{500\nu}{d_w^2\omega}\Big)\frac{4\sigma_{\omega 2}k}{CD_{k\omega}d_w^2}\Big) \tag{II.36}$$

$$\text{and} \quad CD_{k\omega} = \max(2\rho\sigma_{\omega 2}\frac{1}{\omega}\nabla k \cdot \nabla\omega, 10^{-10}) \tag{II.37}$$

$$F_2 = \tanh(arg_2^2) \tag{II.38}$$

$$\text{with} \quad arg_2 = \max\Big(\frac{2\sqrt{k}}{\beta^*\omega d_w}, \frac{500\nu}{d_w^2\omega}\Big) \tag{II.39}$$

The production of turbulent kinetic energy is defined as:

$$P = \min\big(Tr(\boldsymbol{\tau} \cdot \nabla\mathbf{u}), 10\beta^* k\omega\big) \tag{II.40}$$

Finally, defining Φ_i the vector of constants: $(\alpha_i, \beta_i, \sigma_{\omega i}, \sigma_{ki})$ with $i \in [\emptyset, 1, 2]$, the constants terms in Φ are defined in order to switch from $k-\omega$ closure constants, Φ_1 in the near wall region to $k-\epsilon$ closure constants Φ_2 in the free stream, following the function:

$$\Phi = \Phi_1 F_1 + \Phi_2(1 - F_1) \tag{II.41}$$

The remaining constants are presented in II.5, more detail on their choice can be found in Menter [123].

Table II.5: Parameters used for the $k-\omega$ SST model.

α_1	α_2	β_1	β_2	β^*	σ_{k1}	σ_{k2}	$\sigma_{\omega 1}$	$\sigma_{\omega 2}$
5/9	0.44	3/40	0.0828	9/100	0.85	1	0.5	0.856

3.d Overset Meshes

The system of equations presented above are solved using numerical methods on meshes presented hereafter. Due to the objective of an automatic optimization, in order not to have to mesh several times the whole wind tunnel for each air VGs' configuration, overset meshes are employed. The whole preprocess is handled using the ONERA software Cassiopée [12].

The meshes are on display in Fig. II.22. The main idea is to have a really fine mesh (in blue in Fig. II.22) close to the VGs position in order to fully capture the flow coming from the jets and their interaction with the incoming boundary-layer. The dimensions of the cells of this mesh matches those used to mesh the jets. The numbers of grid points of the meshes are reported in Table II.6. Close to the walls, the cells are lower than 2 μm

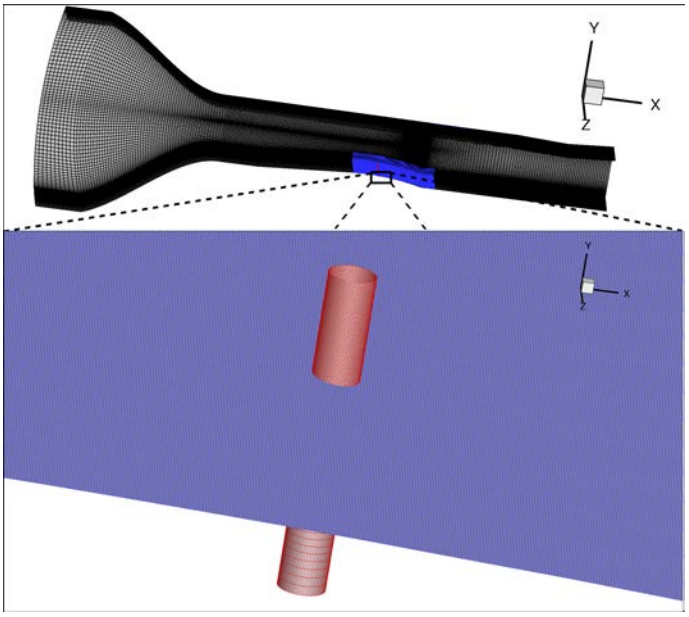

Figure II.22: Overset meshes of the wind tunnel with fluidic VGs: fine mesh (blue), jets' meshes (red) and coarser mesh (black).

Table II.6: Mesh characteristics

Number of Points:	Total	X direction	Y direction	Z direction
Unitary jet	252 681	57	57	143
Mesh in the jets vicinity	60 839 100	1 073	60	945
Whole wind tunnel mesh	4 922 640	344	159	90

which results in a dimensionless wall distance y^+ smaller than 1 almost everywhere. The boundary-layers thicknesses are described using about 50 points. This allows to capture at the same location as the experimentally measured one, a boundary-layer thickness $\delta = 3.3\,\text{mm}$, a displacement thickness $\delta_1 = 0.42\,\text{mm}$ and an incompressible shape parameter $H_i = 1.33$ which are close to the ones measured experimentally in the wind tunnel in [20].

3.e Boundary Conditions and Initial States

In order to accelerate the convergence of the calculations, three initial states have been used. They correspond to the same stagnation conditions $P_{st} = 0.96 \times 10^5\,\text{Pa}$ and $T_{st} = 300\,\text{K}$ with different Mach numbers. The first initial state of $Ma = 0.01$ is imposed on the almost static zone in the convergent of the channel, the second state with a $Ma = 0.6$ is imposed on the central part of the test section-including the first throat associated with the bump- and the last one with $Ma = 1.3$ is used to initialize the second throat which controls the flow rate.

At the entrance of the wind tunnel a subsonic injection condition is imposed using P_{st} and the stagnation enthalpy corresponding to the first state. At the end of the diffuser, a condition of supersonic outflow is imposed. As the mesh only represents half of the wind tunnel, a condition of symmetry is imposed on the median plane. Everywhere else is imposed a condition of viscous wall.

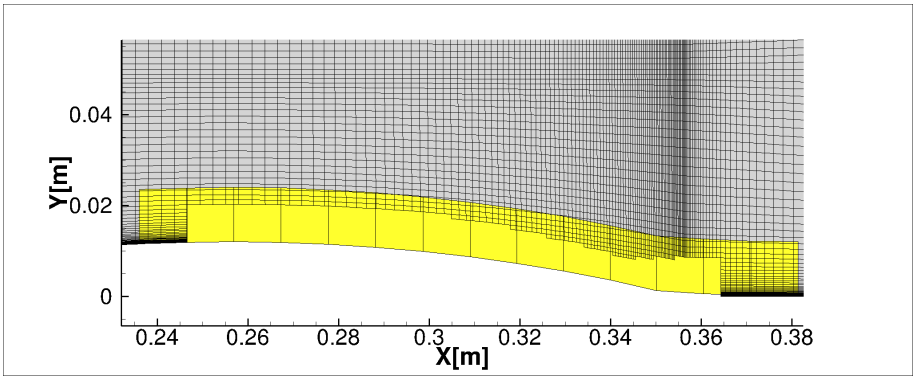

Figure II.23: Illustration of the blanking process.

When the jets are added, the coarser mesh is blanked by the fine one using a Cassiopee function. The process called chimera method is illustrated in Fig. II.23, the fine mesh is represented by the yellow shape, the non blanked cells of the coarser mesh are visible and the interpolation cells are localized at the intersection of both. At least two cells of each mesh are kept inside of the overset mesh in order to perform a proper interpolation. Some other examples of the use of this function can be found in [91]. Furthermore, the lower wall of the fine mesh is set to a doubly defined condition, meaning that the wall is considered as viscous wall, yet the cells crossed by a jet are considered as overlap boundary.

3.f Solver

The structured RANS computations are executed with an ONERA's in house software: elsA [22]. This software uses a cell-centered finite volume discretization on structured and overset grids. The spatial and time integration are respectively carried out using a upwind second-order Roe scheme with Harten entropy correction and a backward-Euler scheme with implicit lower/upper symmetric successive overrelaxation.

The turbulence is modeled using the one-equation Spalart–Allmaras and the $k-\omega$ SST model supplemented with the Quadratic Constitutive Relation (QCR) correction Dandois [43]. This correction enriched the Boussinesq relation with anisotropic terms, it allows to improve the precision of the model in the corner flow separation zone.

The calculations are processed on a NEC cluster, more precisely on 256 cores distributed on 10 processors. It takes an equivalent of 3800 CPU hours to achieve 30 000 iterations and a proper convergence of the residuals.

In order to demonstrate the sufficient convergence of the calculation, the criterion used in the optimization process (see Chap. IV) has been plotted for the case of the first optimization which is used in the second step of optimization along with the dimensionless mean stagnation pressure (Pi_{mean0}) and the dimensionless mean kinetic energy (q_{mean0}) in the transverse plane of interest on Fig. II.24.

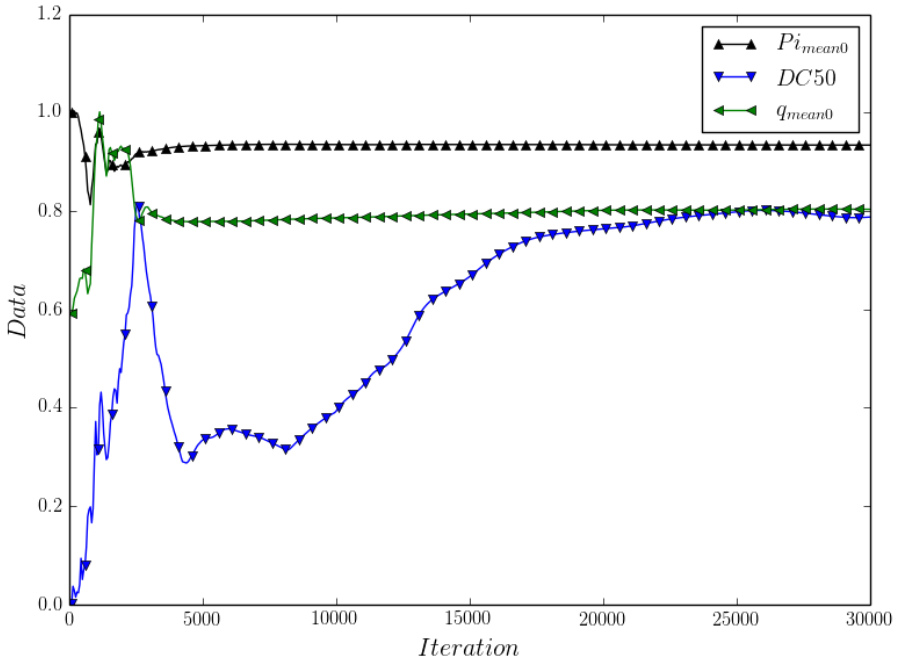

Figure II.24: Convergence of the DC50 criterion, the dimensionless Pi_{mean} and q_{mean}.

II.4 ZDES principle and method

In order to study the dynamics of the Shock-Wave / Boundary-Layer Interaction, different approaches have been considered. Unsteady RANS approach may has been used to initialize a ZDES calculation. Nevertheless, as in the 2D URANS made by Sartor [151] on the same configuration, it failed to retrieve clearly the unsteadiness of the interaction. Thus, more complex modeling approaches are now considered. Large Eddy Simulation (LES) has been proven to be able to capture such unsteadiness in closely similar interactions (see for instance Touber and Sandham [168], Garnier et al. [76]). However, the use of this modeling is unfeasible for this study due to the cumbersome meshes necessary to capture the full 3D flow in the channel, with four walls and thus, four boundary-layers to mesh (the estimated mesh size is about 30 billion points). In order to overcome this difficulty, a hybrid RANS-LES method, namely the Zonal Detached Eddy Simulation (ZDES) has been selected. Therefore, the philosophy and the equations of the LES are first briefly recalled before a presentation of the ZDES methodology and its implementation in the current study. For a more general and precise presentation of LES, the readers are reported to the books of Sagaut [147], Garnier et al. [77] for respectively incompressible and compressible flows.

4.a Large Eddy Simulation

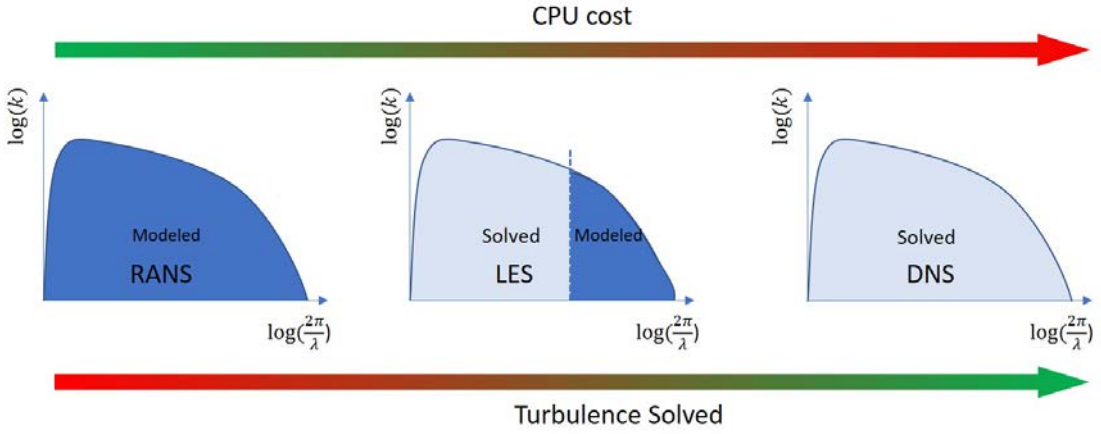

Figure II.25: Different modeling techniques of turbulent flows (adapted from Gand [72])

The main concept of the Large Eddy Simulation is to solve more turbulent scales than the RANS simulation (which only models their effects), and yet, less than the DNS. This allows to use coarser meshes as the scale constraint at the wall is relaxed. The biggest structures are calculated and the smallest ones are modeled. These structures of size smaller than the grid are called subgrid scale structures. These structures are exchanging energy with resolved scales. In the case of isotropic turbulence, the energy is injected by the advection into biggest scales and then transferred along the Kolmogorov logarithmic cascade down to the smallest scale, called Kolmogorov scale, where the energy is dissipated into heat (more details on this description of isotropic turbulence may be found in Kolmogorov [104]). The level of modelization of the turbulent structures are represented on the Kolmogorov energy cascade for RANS, LES and DNS on Fig. II.25.

In brief, the flows structures needs to be filtered with a low pass filter for the frequencies and wave length - meaning a high pass filter for the space and temporal variables - and the impact of the filtered structures has then to be modeled.

Using the same notation as the Reynolds average in the previous section for the LES filter in this section:

$$\Phi = \overline{\Phi} + \Phi' \tag{II.42}$$

This filter has to respect the following properties, conservation of the constants, linearity and commutativity with the derivatives.:

$$\overline{a} = a, \forall a \in \mathbb{R}, \quad \overline{\Phi + \Psi} = \overline{\Phi} + \overline{\Psi}, \quad \overline{\frac{\partial \Phi}{\partial x_i}} = \frac{\partial \overline{\Phi}}{\partial x_i}, \quad \overline{\frac{\partial \Phi}{\partial t}} = \frac{\partial \overline{\Phi}}{\partial t} \tag{II.43}$$

It is noticeable that the filter is not mandatory idempotent as the Reynolds average operator:

$$\overline{\overline{\Phi}} \neq \overline{\Phi} \tag{II.44}$$

Several examples of admissible filters can be found in Sagaut [147]. In practice, in a wide majority, the LES calculations are done with an inhomogeneous filter. This filter is carried out using the fact that the smallest structures are not captured by the mesh if they are smaller than two times the size of the cell and that the dissipation introduced by the numerical scheme damps the highest resolved frequencies of the flow. The filters are characterized by their cut-off length scale in the physical space: Δ_c. This inhomogeneous cutoff lengthscale is then defined for each cell by:

$$\Delta_c = \Delta_{max} = \max(\Delta_x, \Delta_y, \Delta_z) \tag{II.45}$$

Following the same practical objective as before, an operator, called improperly the Favre filter (even if it does not follow all the properties necessary to be a filter in the LES sense) can be defined. This filter, here considered homogeneous to alleviate the presentation, allows to simplify the expression of the filtered Navier Stokes equations for compressible flow.

Using again the same notations as before for a different operator:

$$\tilde{\phi} = \frac{\overline{\rho\phi}}{\bar{\rho}} \tag{II.46}$$

$$\phi = \tilde{\phi} + \phi'' \tag{II.47}$$

Filtered compressible Navier Stokes equations The equations obtained by applying the Favre filter to the equations II.3 and II.4 are the following:

$$\frac{\partial \bar{\rho}}{\partial t} = -\nabla \cdot \bar{\rho}\tilde{\mathbf{u}} \tag{II.48}$$

$$\frac{\partial \bar{\rho}\tilde{\mathbf{u}}}{\partial t} = -\nabla \cdot (\bar{\rho}\tilde{\mathbf{u}} \times \tilde{\mathbf{u}} + \bar{p}\mathbb{I}) + \nabla \cdot \tilde{\boldsymbol{\tau}} + \mathbb{A}_1 + \mathbb{A}_2 \tag{II.49}$$

$$\text{with } \mathbb{A}_1 = -\nabla \cdot (\bar{\rho}(\widetilde{\mathbf{u} \times} \mathbf{u} - \tilde{\mathbf{u}} \times \tilde{\mathbf{u}})) \tag{II.50}$$

$$\text{and } \mathbb{A}_2 = \nabla \cdot (\bar{\boldsymbol{\tau}} - \tilde{\boldsymbol{\tau}}) \tag{II.51}$$

The term $\bar{\rho}(\widetilde{\mathbf{u}\times\mathbf{u}} - \tilde{\mathbf{u}}\times\tilde{\mathbf{u}})$ is denoted $\boldsymbol{\tau}_{sgs}$ and called the subgrid stress tensor.

For the energy equation II.5, different form may be derived, following the chosen variable. The one presented here was proposed by Vreman [173]. The new variable of energy called calculable energy, denoted $\widehat{\rho e}$ is defined as:

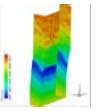

$$\widehat{\rho e} = \frac{\bar{\rho}}{\gamma - 1} + \frac{1}{2}\sum_{i\in[1,2,3]} \widetilde{u_i}^2 \tag{II.52}$$

Injecting this into the filtered equation of energy gives:

$$\begin{aligned}
\frac{\partial \widehat{\rho e}}{\partial t} &= -\nabla\cdot(\widehat{\rho e}\tilde{\mathbf{u}} + \bar{p}\tilde{\mathbf{u}}) + \nabla\cdot\tilde{\mathbf{q}} + B_1 + B_2 + B_3 + B_4 + B_5 + B_6 + B_7 && \text{(II.53)}\\
\text{with } B_1 &= -\frac{1}{\gamma-1}\nabla\cdot(\overline{p\mathbf{u}} - \bar{p}\tilde{\mathbf{u}}) && \text{(II.54)}\\
B_2 &= -\overline{p\nabla\cdot\mathbf{u}} + \bar{p}\nabla\cdot\tilde{\mathbf{u}} && \text{(II.55)}\\
B_3 &= -\nabla\cdot(\boldsymbol{\tau}_{sgs}\tilde{\mathbf{u}}) && \text{(II.56)}\\
B_4 &= \boldsymbol{\tau}_{sgs}\cdot\nabla\tilde{\mathbf{u}} && \text{(II.57)}\\
B_5 &= \overline{\boldsymbol{\tau}\cdot\nabla\cdot\mathbf{u}} - \overline{\boldsymbol{\tau}}\nabla\cdot\tilde{\mathbf{u}} && \text{(II.58)}\\
B_6 &= \nabla\cdot(\bar{\boldsymbol{\tau}}\tilde{\mathbf{u}} - \tilde{\boldsymbol{\tau}}\tilde{\mathbf{u}}) && \text{(II.59)}\\
B_7 &= -\nabla\cdot(\bar{\mathbf{q}} - \tilde{\mathbf{q}}) && \text{(II.60)}\\
& && \text{(II.61)}
\end{aligned}$$

Following the recommendations of Vreman [173] only the terms $\mathbb{A}_1, B_1, B_2$ and B_3 will be considered here. The other terms have been proven to be negligible with at least one order of magnitude of separation thanks to a DNS.

Closure and modeling The equations of LES claims for a model in order to be closed. The model proposed here is a functional model following the classification of Sagaut [147], meaning that it does not try to reproduce the mathematical structure of the subgrid stress tensor but only the dissipative mechanical action of the tensor. Several models can be found in Vreman [173], Sagaut [147], Garnier et al. [77]. Only the one used here will be described. It is the Smagorinsky model which is chosen as it is naturally used in the Zonal Detached Eddy Simulation method based on the Spalart Allmaras model.

The Smagorinsky model (Smagorinsky [158]) is an eddy viscosity model in which the subgrid stress tensor is defined as follow:

$$\begin{aligned}
\bar{\rho}\boldsymbol{\tau}_{sgs} &= \bar{\rho}C_S^2\Delta_c^2\tilde{S}\tilde{\mathbb{S}} && \text{(II.62)}\\
\text{with } \tilde{\mathbb{S}} &= \tilde{\mathbb{d}} - \frac{1}{3}tr(\tilde{\mathbb{d}}) && \text{(II.63)}\\
\text{and } \tilde{S} &= \sqrt{\frac{1}{2}\sum_{i,j\in[1,2,3]} \widetilde{\mathbb{S}_{ij}}\widetilde{\mathbb{S}_{ji}}} && \text{(II.64)}
\end{aligned}$$

The term C_S is called the Smagorinsky constant and Δ_c is the cut off length scale of the filter.

The equations are finally closed by the introduction of a subgrid scale thermic conductivity κ_{sgs} to model the last two terms B_1 and B_2 see Vreman [173].

$$B_1 + B_2 = \nabla \mathbf{q}_{sgs} \tag{II.65}$$
$$\text{with } \mathbf{q}_{sgs} = \kappa_{sgs} \nabla \tilde{T} \tag{II.66}$$
$$\text{and } \kappa_{sgs} = c_p \frac{\mu_{sgs}}{Pr} \nabla \tilde{T} \tag{II.67}$$
$$\tag{II.68}$$

μ_{sgs} being defined in the closure of the subgrid stress tensor.

The system is now closed and can be solved on a sufficiently precise mesh.

Due to computer limitations, the method used in this study is based on a mix between RANS ans LES method called Zonal Detached Eddy Simulation detailed below.

4.b Zonal Detached Eddy Simulation principle

The Zonal Detached Eddy Simulation (ZDES) is a general hybrid RANS / LES method proposed by Deck [46] based on the concepts of Detached Eddy Simulation (DES97) presented in Spalart et al. [161]. This method has now proven its ability to model for instance, the dynamic of launcher afterbody (Pain et al. [129]), civil aircraft buffet (Brunet and Deck [17]) and several complex configurations of the generic flight envelope of transport civil aircraft presented in the survey by Deck et al. [47].

This approach is a generalization and improvement of several preexisting hybrid RANS / LES method mainly DES97 and its improvement the Delayed Detached Eddy Simulation (DDES). For the sake of clarity, these methods will be explained before a presentation of the mode of ZDES used in this study. Indeed, the ZDES allows the user to impose 3 different modes in distinct zones of the flow, following the flow physics needs anticipated in these zones.

The three different modes are presented on II.26. The first mode, mode I, is dedicated to separation generated by a salient geometry, it consist in an improved version of the classical DES97. The second mode, mode II, is dedicated to separation generated by a pressure gradient, it consist in an improved version of the DDES which ensures to treat the boundary-layer in RANS and the detached flow in LES. And finally, the third mode, mode III, allows the user to capture separation strongly influenced by the dynamic of the turbulent boundary-layer. In this mode, the position of the interface between RANS and LES is imposed by the user and is positioned in the boundary-layer. Thus, some turbulent fluctuations should be prescribed on this limit in order for the LES part to match the low-order statistics given by the URANS calculation. The modes I and III will not be presented in this study but the interested reader can find a more precise presentation in Deck [46] and in french in Laraufie [110], Renard [139]. A fourth mode of the ZDES called mode 0 may be added, it simply consists in RANS mode which allows to "protect" , in some well defined zones, the boundary-layers known to be attached from switching into LES mode.

DES97 The DES proposed by Spalart et al. [161] is based on the Spalart Allmaras model presented in 3.c. Its equation II.31, is recalled below.

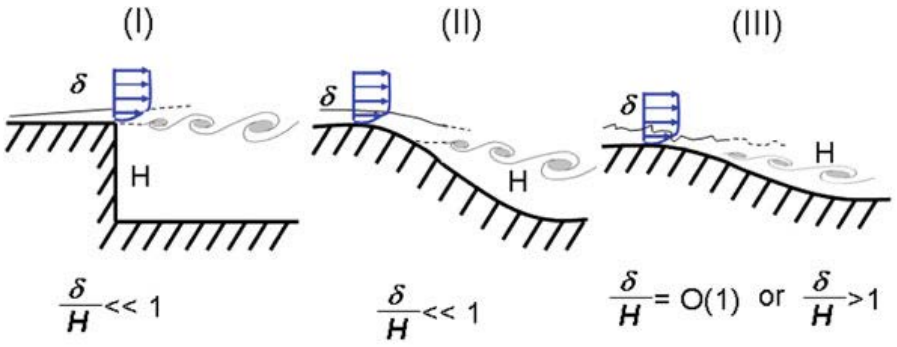

Figure II.26: Classification of separations in turbulent flows: I: separation fixed by the geometry, II: separation induced by a pressure gradient on a curved surface, III: separation strongly influenced by the dynamic of the incoming boundary-layer (from Deck [46]).

$$\frac{\partial \tilde{\nu}}{\partial t} + \nabla \cdot \tilde{\nu}\mathbf{u} = \underbrace{\frac{\mu + \tilde{\nu}}{\sigma}\nabla\tilde{\nu} + \frac{C_{b2}}{\sigma}\nabla\tilde{\nu}\cdot\nabla\tilde{\nu}}_{\text{diffusion}} + \underbrace{C_{b1}\tilde{S}\tilde{\nu}}_{\text{production}} - \underbrace{\frac{C_{w1}f_w\tilde{\nu}^2}{d_w^2}}_{\text{destruction}} \tag{II.69}$$

It can be noted that in the case of equilibrium between production and dissipation, the eddy viscosity scales with the distance to the closest wall d_w and the local vorticity modulus S as $\tilde{\nu} \propto \tilde{S}d_w^2$. This is the form of the subgrid scale Smagorinsky model presented in 4.a. Thus, Spalart proposed to replace the distance to the wall d_w with the cut off length scale Δ_c when this one is smaller than the distance to the wall. This allows to switch from a RANS model close to the wall with turbulence completely modeled to LES farther with the subgrid scale turbulent structures modeled. The distance used in the model becomes

$$\tilde{d}_{DES97} = \min(d_w, C_{DES}\Delta_c) \tag{II.70}$$
$$\text{with } \Delta_c = \Delta_{max} = \max(\Delta_x, \Delta_y, \Delta_z) \tag{II.71}$$
$$\text{and } C_{DES} = 0.65 \tag{II.72}$$

However, this model only depends on the mesh size to switch from LES to URANS. Furthermore, in the case of structured meshes, the size of the cells in the principal direction is the limiting factor and is transmitted down to the wall. Thus, LES is used in the boundary-layer, the DES97 becomes a Wall Modeled Large Eddy Simulation (WMLES) which suffers from Modeled Stress Depletion (MSD). The turbulent structures solved by the LES do not compensate the absence of the turbulent stress normally modeled by the RANS. This may provoke a diminution of the modeled turbulent kinetic energy and thus a re-laminarisation of the boundary-layer. The boundary-layer becomes more sensible to pressure gradient and generates non physical separations called Grid Induced Separations (see Deck [45], Sagaut et al. [149] for more details). This problem is treated by the development of the Delayed Detached Eddy Simulation (DDES).

DDES The DDES was proposed by Spalart et al. [162] to improve the behavior of DES for separation induced by a pressure gradient and not a physical salient geometry. The principal idea is to used a shield function f_d conceived to be equal to one in the logarithm

part of the boundary-layer and to tend toward zero outside of the boundary-layer. The detail of the shield function is:

$$f_d = 1 - \tanh((8r_d)^3) \tag{II.73}$$

$$\text{with } r_d = \frac{\nu_t + \nu}{\sqrt{\sum_{i,j\in[1,2,3]}(\frac{\partial u_i}{\partial x_j})^2 K^2 d_w^2}} \tag{II.74}$$

The DDES length scale is redefined as:

$$d_{DDES} = d_w - f_d \max(0, d_w - C_{DES}\Delta_c) \tag{II.75}$$

This solves the problem of GIS in many situations. Nevertheless the choice made in DDES of Δ_{max} as a cut-off length scale, even if physically justified, has been proven to slowly delay the development of instabilities in free shear layer. In addition to allowing a simple general framework for complex hybrid RANS / LES calculation, the ZDES addresses this problem by the use of a different length scale.

ZDES mode II The mode II of ZDES uses the classical Δ_{max} length scale in the boundary-layer-to shield the boundary-layer- and Δ_{vol} or Δ_ω in the LES region. The volumic length scale is defined as:

$$\Delta_{vol} = \sqrt[3]{\Delta_x \Delta_y \Delta_z} \tag{II.76}$$

This smaller length scale only depending on the mesh, allows to diminish the level of the eddy viscosity and thus promotes a more rapid and physical development of shear layer instabilities. The open discussion on the validity of this length scale can be found in Deck [46].

The second length scale considered here is linked to the mesh and the vorticity of the flow. It has been proposed by Chauvet et al. [28] and is defined as follows:

$$\Delta_\omega = \sqrt{N_x^2 \Delta_y \Delta_z + N_y^2 \Delta_x \Delta_z + N_z^2 \Delta_x \Delta_y} \tag{II.77}$$

$$\text{with } \mathbf{N} = \frac{\boldsymbol{\omega}}{|\boldsymbol{\omega}|} \tag{II.78}$$

$\boldsymbol{\omega}$ being the vorticity vector.

To sum up, the length scale of ZDES mode II, $\tilde{\Delta}_{DES}^{II}$ can be defined as follows using the shield function of the DDES:

$$\tilde{\Delta}_{DES}^{II} = (0.5 + \text{sign}(0.5, f_d - f_{d0}))\Delta_{max} + (0.5 - \text{sign}(0.5, f_d - f_{d0}))\Delta_{vol} \tag{II.79}$$

It should be noticed that $\tilde{\Delta}_{DES}^{II}$ is now a function of $\Delta_x, \Delta_y, \Delta_z, \mathbf{u}, \nu_t$ and f_{d0}, a parameter, here chosen equal to 0.8.

The length scale is then injected in the previous system of equations and the whole system is solved numerically using the implementation detailed below.

Table II.7: Principal characteristics of the ZDES meshes

	N_x	N_y	N_z	Δ^+_{xmin}	Δ^+_{ymin}	Δ^+_{zmin}	Δ^+_{xmax}	Δ^+_{ymax}	Δ^+_{zmax}
Part I	540	456	512	200	1	1	200	200	200
Part II	89	456	512	200	1	1	6100	200	200

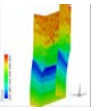

4.c Zonal Detached Eddy Simulation implementation

i Mesh

In order to alleviate the calculations, only the part of interest of the wind tunnel (from $x = 230\,\text{mm}$ to $x = 683\,\text{mm}$) is modeled using the ZDES mode II method. The RANS Spalart Allmaras calculation presented in Chap. III is used to impose the inflow and the wind tunnel is meshed all down to the supersonic outflow. This method has been chosen in order not to be influenced by the RANS calculation in the last part of the flow. The latter being less precisely modeled than the entrance of the wind tunnel. Furthermore, in order to alleviate a little more the mesh, only the part containing the SWBLI, named Part I, is meshed using a constant step in the x direction. In the second part, called Part II (from $x = 470\,\text{mm}$ to the end), Δ_x follows a geometric progression of common ratio 1.04. This can be done without degrading the result as the last part is the second throat where the supersonic acceleration blocks any compression wave. The different parts of the mesh are presented on Fig. II.27.

Following the recommendations found in Renard [139], the mesh has been designed with a maximum value of Δ^+_y and Δ^+_z of 200, a minimum one of 1 at the wall[5]. The size of the cells follows a geometric progression of common ratio 1.05, in the direction y and z. This allows to have around 90 cells in the boundary-layer. The distribution is presented on the slice $x = 468\,\text{mm}$ on Fig. II.28 with one over two points represented. The principal characteristics of the mesh of the two parts are reported in Table II.7. For both meshes, the number of grid points ($N_x, N_y,\ N_z$) in each direction are mentioned as well as the minimum and maximum size of the cells in wall units. The total mesh is of around 145 millions points with 125 millions in Part I and 20 millions in Part II.

ii Boundary Conditions

The boundary conditions prescribed are: viscous wall condition on the lateral, top and lower walls, a supersonic outflow at the end of the channel and an injection given by the precedent RANS simulation. This allows to impose the lower central boundary-layer which have been validated with respect to LDV measurement. The $\rho\tilde{\nu}$ field injected in the ZDES mode II at the inflow is presented on Fig. II.29. It can be noticed that the boundary-layers are already thicker in the corners and that, due to the pressure gradient on the lower wall, the boundary-layer is thinner on the bottom wall.

iii Solver

The computations are executed with an ONERA's in house software: elsA [22] as for the RANS calculations. The spatial integration is carried out using an Advection Upstream

[5]With $\cdot^+$ notation corresponding to the non dimensionalization using the classical internal boundary-layer units, $y^+ = \frac{u_\tau y}{\nu}$, with u_τ, the friction velocity at the nearest wall defined as $u_\tau = \sqrt{\frac{\mu(\frac{\partial u}{\partial y})_{y=0}}{\rho}}$.

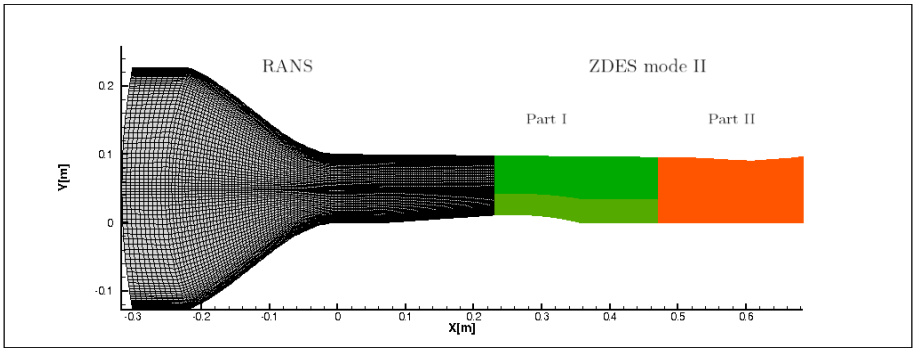

Figure II.27: Presentation of the partition of the modeling techniques, the black mesh correspond to the RANS steady model, while the green and orange meshes are modeled using ZDES mode II, the green part represents the zone of interest (the SWBLI).

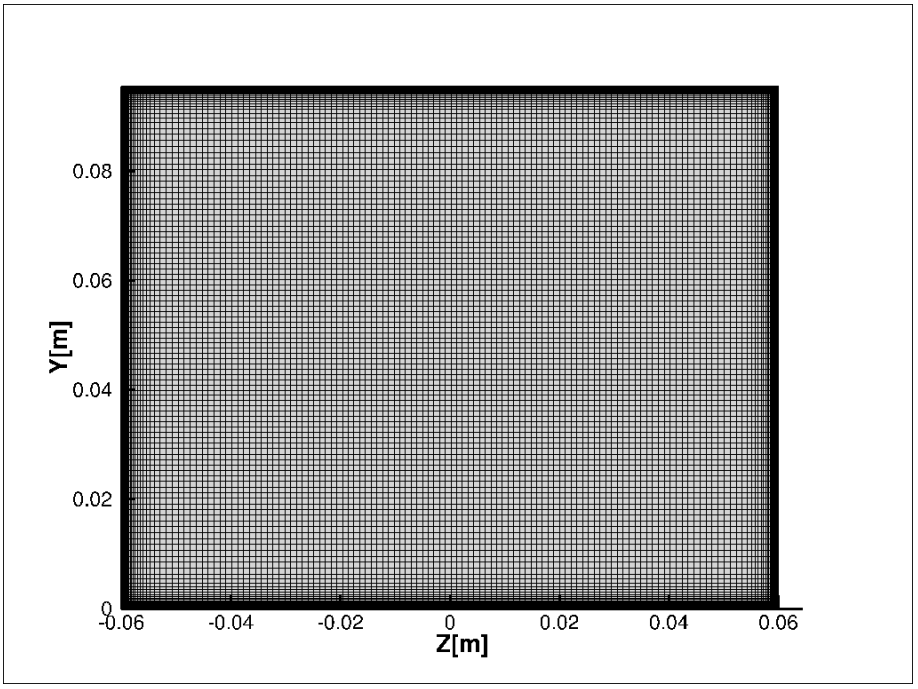

Figure II.28: Presentation of the y and z mesh distribution on the slice $x = 468\,\text{mm}$ for the ZDES calculation, one point over two is represented.

Splitting Method Plus (AUSMP) scheme. The use of an upwind scheme allows to stabilize the calculation.

A backward-Euler scheme proposed by Gear, with implicit lower/upper symmetric successive overrelaxation is used to proceed to time integration. The maximum of the Courant Friedrichs Lewy Number is fixed to 12 and the corresponding time step is equal to $5 \times 10^{-8} s$.

The details of these two methods can be found in french in Bannier [10] and the original version in Liou [117] and Gear [79] respectively.

In order to initialize the calculations, the calculation has been conducted for $0.004s$ in URANS and then $0.013s$ in ZDES with a time step of $1 \times 10^{-7} s$ before the beginning of the

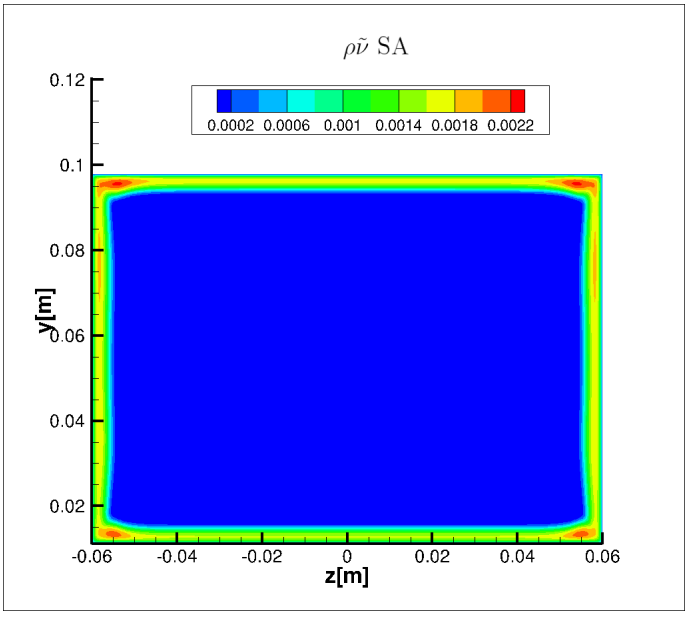

Figure II.29: Field of $\rho\tilde{\nu}$ imposed at the inlet of the mesh.

extractions. The calculations were limited to 36.5 ms due to computer time's limitation.

The calculations are processed on a NEC cluster, more precisely on 1120 cores distributed on 40 processors. It takes an equivalent of 11 200 h CPU to achieve 10 000 iterations with 4 gear sub-iterations for each.

iv Extraction

In order to describe the dynamic of the flow, several sensors have been positioned to record the pressure in the flow. Their positions are presented on Fig. II.30 and summed up in Table II.8. They are measured at a frequency of 4000 kHz.

Name	X(mm)	Z(mm)
KZ17	327.0	0.0
KZ21	340.0	0.0
KZ25	351.4	0.0
KZ27	359.5	0.0
KZ37	392.0	0.0
KZ47	424.5	0.0
KZ63	351.4	-20.0
KZ65	351.4	-40.0
KZ67	351.4	-50.0
KZ69	351.4	-60.0

Table II.8: Kulites sensors position.

Furthermore, two slices have been periodically extracted from the flow. The slice $z = 0$ mm is thought to permit comparison with precedent 2D numeric calculations and 2D measurements of experiment. The second slice is for $x = 468$ mm, this slice corresponds

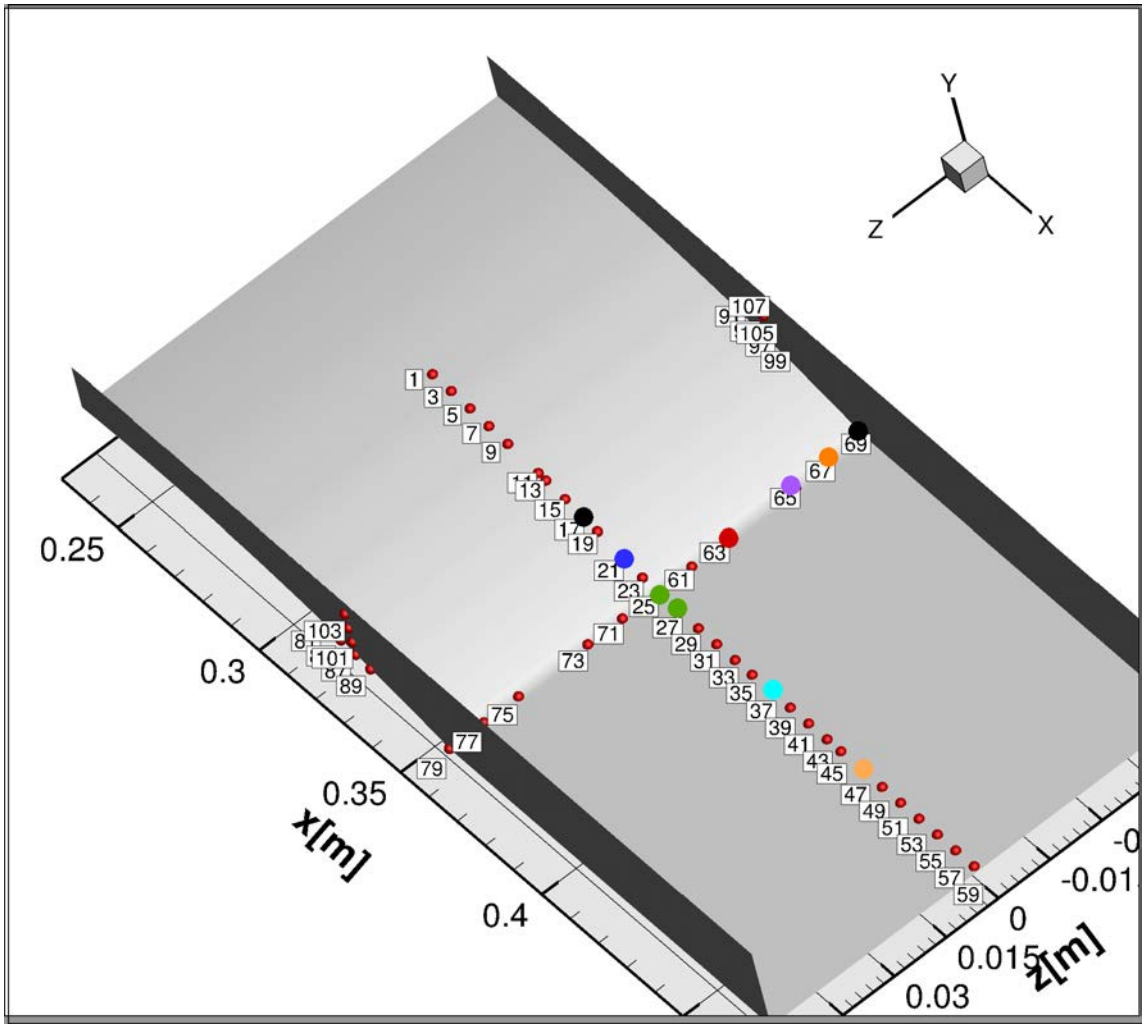

Figure II.30: Position of the different pressure sensors for the ZDES calculation.

to the plane measured experimentally with the Pitot tube rake and to the plane of the $DC50$ criterion of the optimizations in Chap. IV. These slices are extracted at a frequency of 200 kHz.

III

Validation of the RANS modeling technique for the Optimization

Science is what we understand well enough to explain to a computer. Art is everything else we do.

Donald Knuth

Objectives

This chapter is dedicated to the presentation and the study of the RANS modeling of the reference case: the uncontrolled SWBLI.

The RANS modeling is presented and validated with respect to some preceding experimental data. A more precise insight will be taken at the physical structure of the corner flow separation. A more detailed comparison to experimental data will be done in Chap. VI.

Contents

III.1 Reynolds Averaged Navier Stokes modeling

This section describes the results obtained with the numerical method described in section 3.c of Reynolds Averaged Navier Stokes modelization of the shock-wave boundary-layer interaction appearing in the S8Ch wind tunnel presented in the section II.1.

1.a General remarks

The RANS equations are closed with different turbulence models, namely the Spalart-Allmaras model with and without QCR correction and the $k-\omega$ Menter SST model. Their results are globally compared before a more detailed presentation of the most satisfying one.

i Quadratic Constitutive Relation (QCR) correction

The Spalart-Allmaras modeling has been tested with and without the Quadratic Constitutive Relation (QCR) correction presented among others in [43]. This correction adds some cross terms in the linear Reynolds stress tensor τ_t using an anti-symmetric normalized rotation tensor. These terms are added in order to improve the modeling of the corner flow's simulation as the presence of two perpendicular walls induced an anisotropy in the development of turbulence which is not taken into account by the classical Boussinesq eddy-viscosity hypothesis.

The results of the simulations clearly show far downstream of the interaction, on the slices $x = 468\,\text{mm}$ presented in Fig. III.1 that the Spalart-Allmaras model without correction displays huge non physical corner flow separations notably in the higher corner of the flow. These corner flow separations have not been observed experimentally before while the lower ones are known to appear in previous experiments (see Bur et al. [20]).

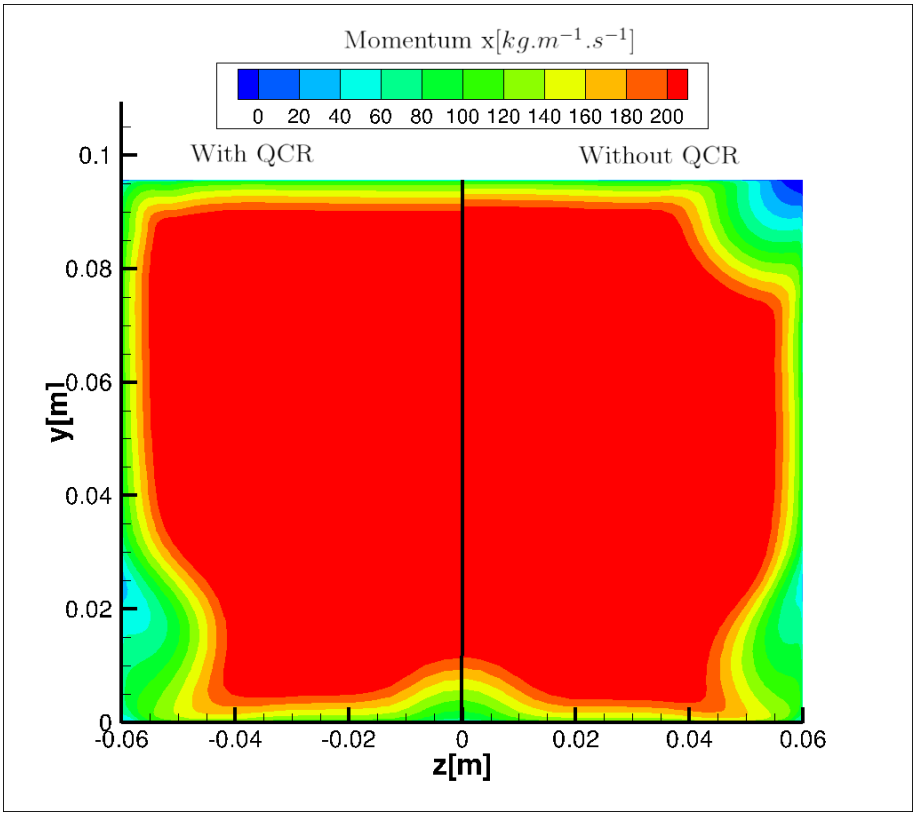

Figure III.1: Longitudinal momentum at $x = 468\,\text{mm}$ for Spalart-Allmaras with QCR correction (on left) and without QCR correction (on right).

Hence the QCR correction will be used for both models in the following comparison of

Spalart-Allmaras and $k-\omega$ Menter SST models.

ii Turbulence model choice

In order to visualize the separation zone on both the corner flow and the central flow, a colorized map of the longitudinal friction is presented on Fig. III.2. Friction lines are added in order to appreciate the size of both separation zones. The Spalart-Allmaras model produces a wider central separation zone which is closer to the results presented in Bur et al. [20]. The $k-\omega$ model, for its part displays an important corner flow separation which by its amplitude, narrows the central separation. Both models displays the two foci characteristics of a corner flow separation. Nevertheless, the Spalart-Allmaras produces a flow field closer to the experimental one and will thus be used for the optimization process presented in Chap. IV. The accordance between the Spalart-Allmaras and the experimental results will be more detailed in Chap. VI.

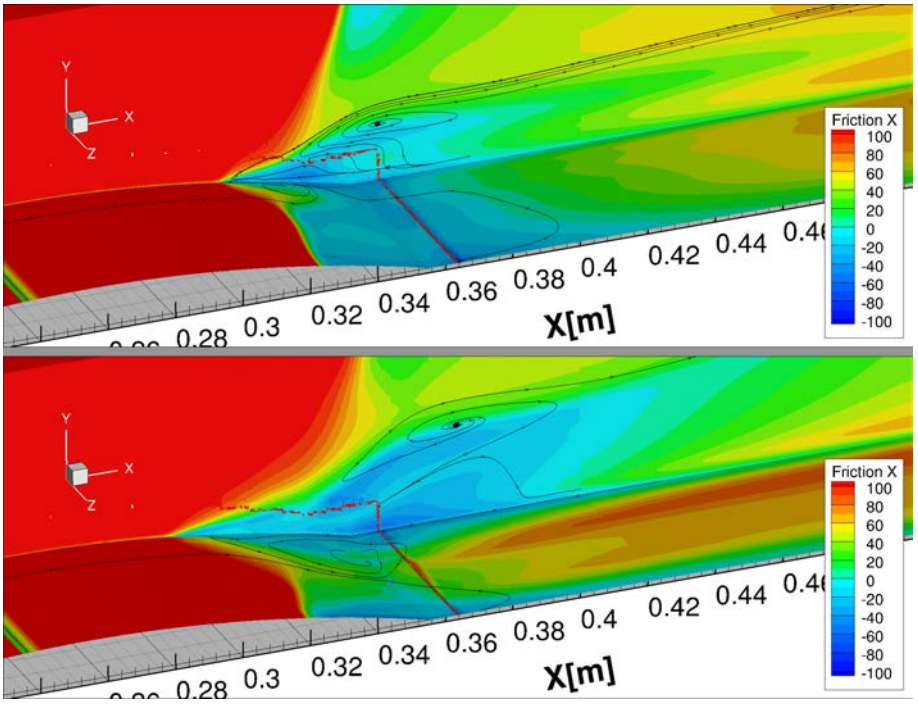

Figure III.2: Comparison of friction distribution on the half wind tunnel between Spalart-Allmaras (above) and $k-\omega$ (below) models. The streamlines correspond to friction lines.

iii Incoming Boundary-Layer

In order to validate the right development of the incoming boundary-layer, the profile of longitudinal velocity is compared to the LDV measurement by Galli et al. [71] on Fig. III.3. The general tendency and levels are well predicted. Nevertheless, there is a small discrepancy in the region close to the wall which can explain the difference between the experimental and numerical boundary-layer thicknesses, respectively $\delta = 3.9\,\text{mm}$ and $\delta = 3.3\,\text{mm}$. This difference may be due to a too low level of initial turbulence in the simulation. However, the incompressible shape parameter obtained numerically, $H_i = 1.33$

is closer to the one of a classical turbulent boundary-layer ($H_i = 1.4$) than the experimental one equal to $H_i = 1.63$. The higher value is due to the lack of LDV measurements in the vicinity of the wall and the profile is interpolated from the last measured point. Yet, this incoming velocity profile is considered satisfying for the following calculations.

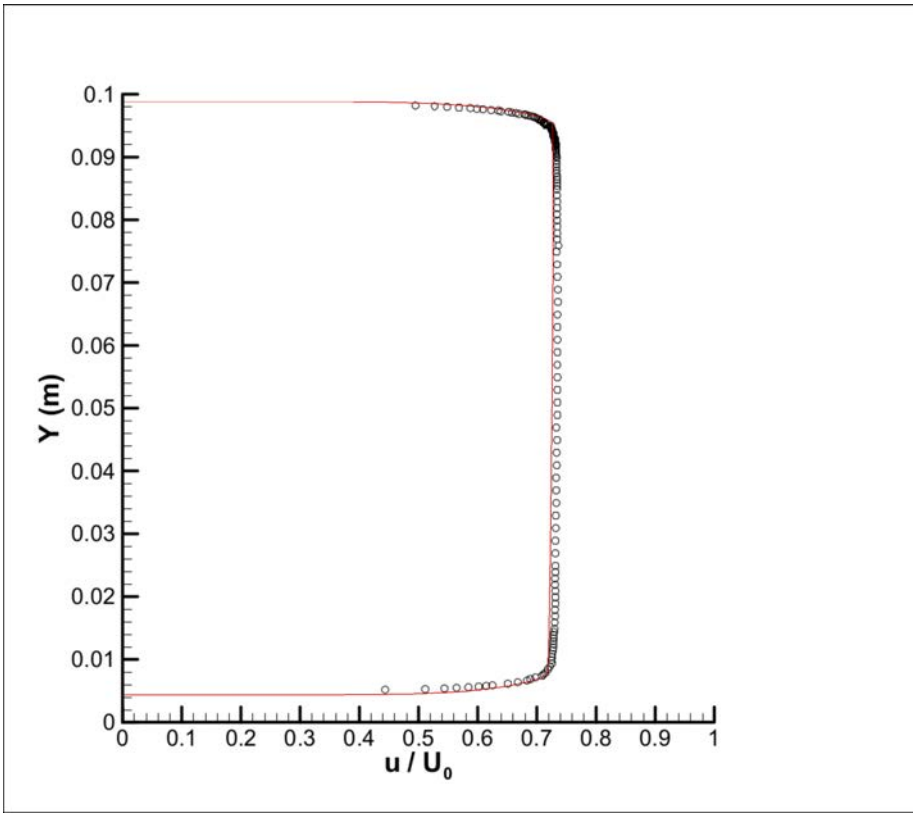

Figure III.3: Comparison of velocity distribution downstream of the interaction (at $x = 135\,\text{mm}$) between LDV measurements from Galli et al. [71] (symbol) and RANS Spalart-Allmaras QCR (line).

iv Pressure measurements

The static pressure measurement along the centerline of wind tunnel are compared to experimental measurement (from Bur et al. [20]) in Fig. III.4. The two curves present a good agreement of the pressure jump through the shock-wave pattern. The RANS calculation suggests a shock-wave located slightly upstream which generates a stiff plateau corresponding to the detachment zone. The separation zone seems to be of equivalent size since the interpolation between two experimental points leads to uncertainty on the shock intensity measurement. The re-compression is slightly quicker in the experiment but it converges toward the same level as the numerical ones at the end of the channel.

The numerical pressure field on the lower wall of the wind tunnel is compared to Pressure Sensitive Paint (PSP) measurements presented in Merienne et al. [124] on Fig. III.5. The difficulty for the comparison resides in the fact that the part of the lower wall close to the lateral walls is less effectively measured due to optical access limitation. However, the two figures exhibit coherent levels and general shapes (taking into account the different

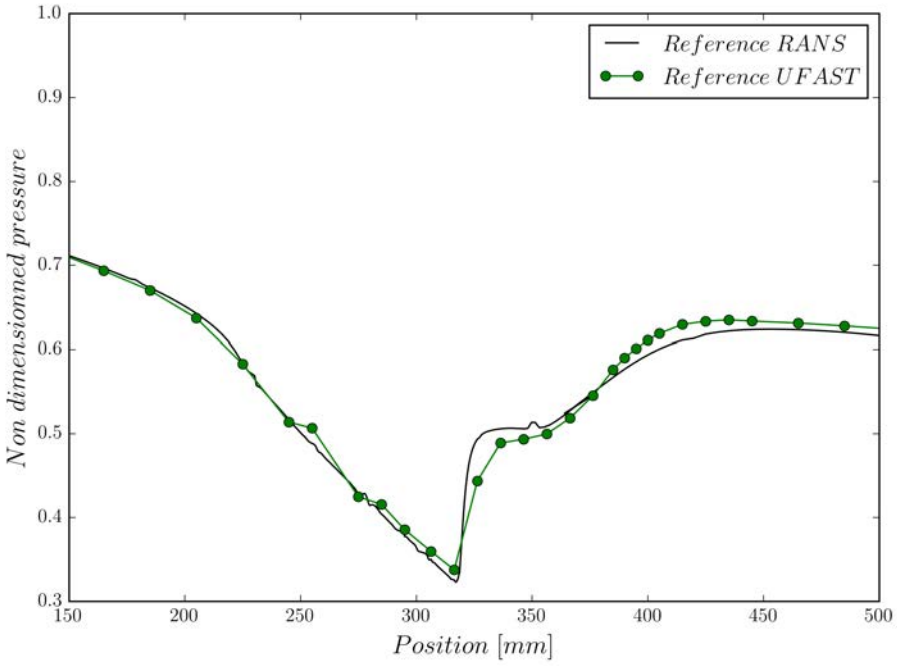

Figure III.4: Pressure distributions on the lower wall, comparison between RANS Spalart-Allmaras QCR and experimental results (Bur et al. [20]).

color bar). The beginning of the central separation, positioned on the left part of the picture is well corresponding. The end of the separation seems to correctly fit even if the end of the bump is less well measured by the PSP with an incoherent pressure increase at the limit. This non physical jump of pressure may be due to a non uniform thickness of paint at this sharp position. Nonetheless, the corner flow separation seems to be slightly over-predicted by the simulation. The position of the beginning of the corner separation, (the green triangle shape close to the lateral wall) fits well but the separation appears wider in the simulation. Yet, the PSP measurement is more noisy in this zone close to the wall.

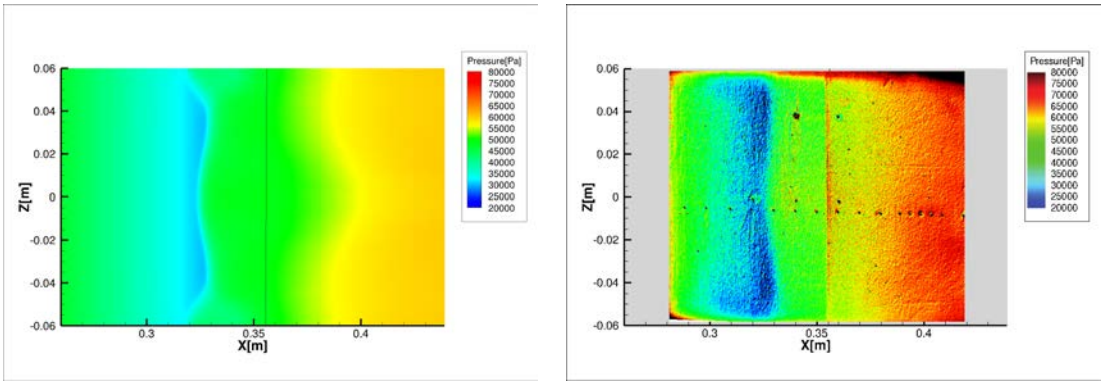

(a) RANS result

(b) Measured using PSP method from Merienne et al. [124].

Figure III.5: Pressure field on the lower wall of the wind tunnel.

1.b The central separation

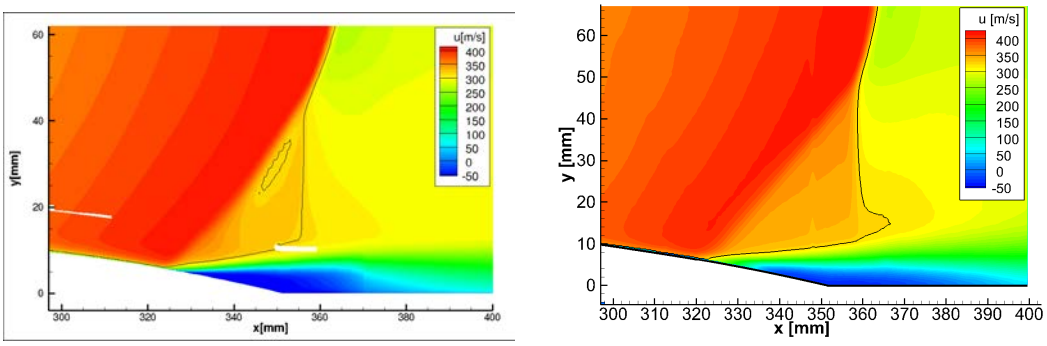

(a) RANS result

(b) measured using 2D PIV method from Sartor et al. [152].

Figure III.6: Longitudinal velocity fields at the median plane of the wind tunnel.

The computed flow field in the median plane of the wind tunnel is compared to 2D PIV results obtained by Sartor et al. [152] in Fig. III.6. The longitudinal velocity fields are well matching and the size of the separated zone in the streamwise direction is well predicted even if the height of the bubble is slightly overestimated by computation. Nota bene, the white cells in the red and blue area in Fig. III.6a are due to the blanking function used to show both fine and coarser mesh superimposed and thus do not reflect an error in the computation. The cross term of the 2D Reynolds stress tensor, $u'v'$, calculated using the Boussinesq relation, is presented on Fig. III.7a and III.7b for respectively the RANS calculation and the 2D PIV measurement. The shock-wave motion is not detected numerically due to the RANS approach. However, the shear stress distribution of the intense fluctuation zone is close to the experimental one even if the turbulence acts more strongly and in a finer zone in the RANS calculation. The RANS calculation also presents higher levels of shear stress than the experimental 2D PIV, this is not clearly visible here due to the saturation of the color map chosen by Sartor et al. [152]. Nevertheless, this last remark can be mitigated by the fact that the PIV is based on window correlation and that the window size influences the size of the smallest structures solved. This may result in lower levels than the real ones.

To conclude, the central separation is reasonably predicted by the Spalart-Allmaras RANS calculation, even if it does not completely capture the physics of the separation zone.

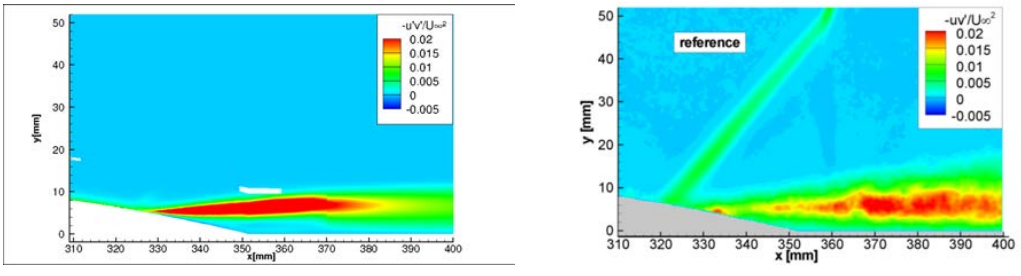

(a) RANS result

(b) measured using 2D PIV method from Sartor et al. [152].

Figure III.7: Shear stress fields at the median plane of the wind tunnel.

1.c The corner flow separation

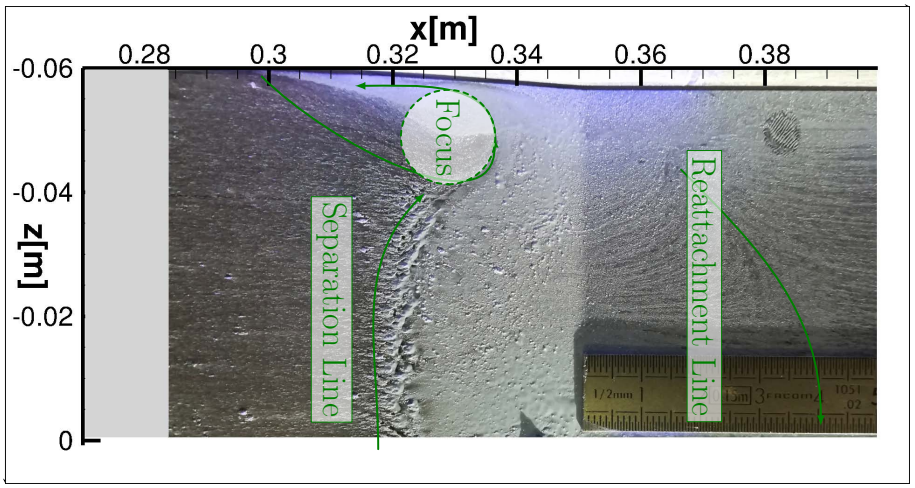

(a) Experimental.

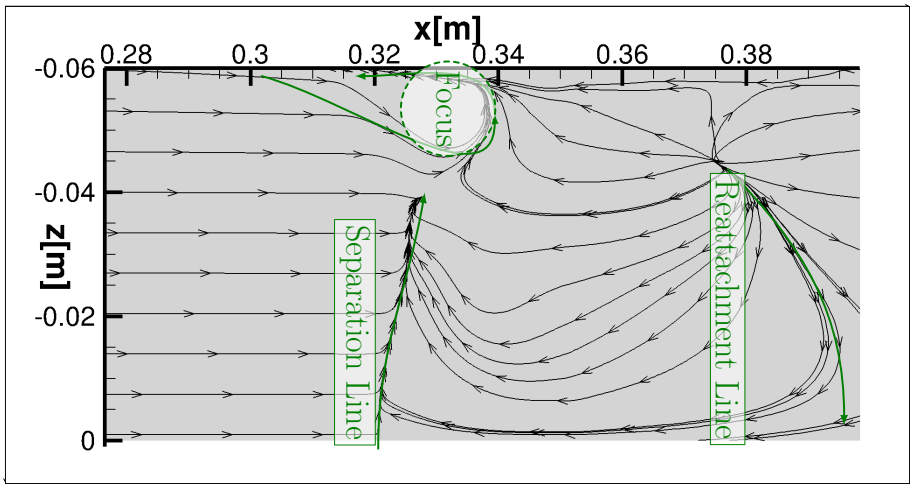

(b) RANS.

Figure III.8: Comparison between an experimental colored oil visualization and the friction lines of the RANS calculation for the corner flow separation on the lower wall.

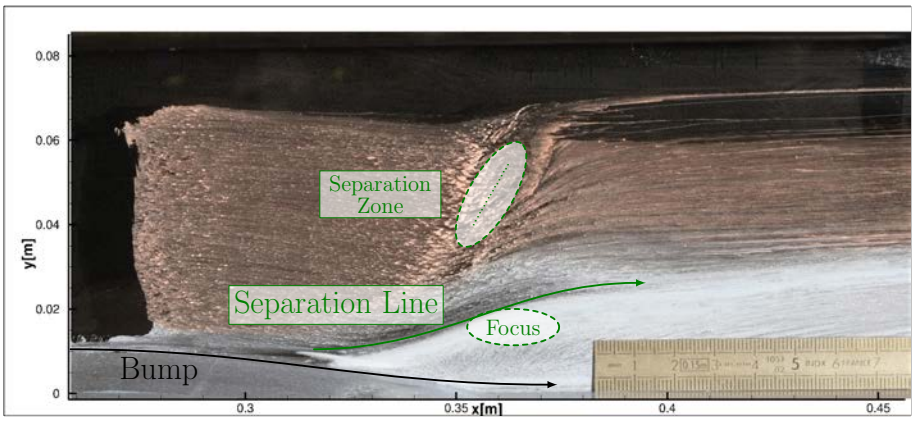

(a) Experimental.

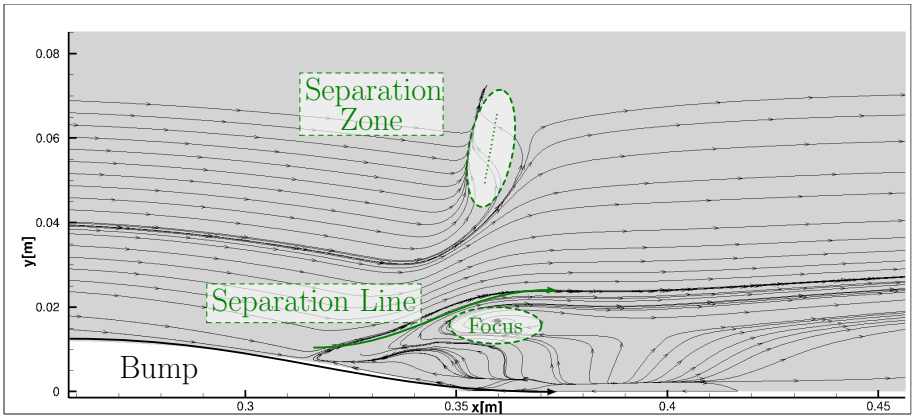

(b) RANS.

Figure III.9: Comparison between an experimental colored oil visualization and the friction lines of the RANS calculation for the corner flow separation on the lateral wall.

In order to validate the use of the QCR correction, a colored oil visualization has been performed in the wind tunnel and is compared to the friction lines of the RANS calculation for the corner flow separation on the lower and lateral walls on respectively Fig. III.8 and III.9. The position and the size of the corner flow separation at the lateral wall is well predicted numerically, which confirms the interest of the QCR correction for a fine enough mesh in a confined configuration contrary to previous results observed in Cartieri et al. [23] for a wing body separation flow. Nevertheless, once again, the corner flow separation seems to be slightly over-predicted when looking at the lower wall. On the lower wall, it is also noticeable that the beginning of the central separation is well predicted but its length is over-estimated by the RANS calculation. The node from where the friction lines diverges is closer to the wall in the experiment than in the computation.

The friction lines exhibit the two divergent foci characteristics of the corner flow separation. The two resulting vortices are presented on Fig. III.10. The first one appearing in the flow is the lower one at the end of the bump whilst the lateral one is positioned downstream and above the first one. These two vortices will have to be damped thanks to the fluidic vortex generators devices in order to mitigate their impact downstream of the interaction.

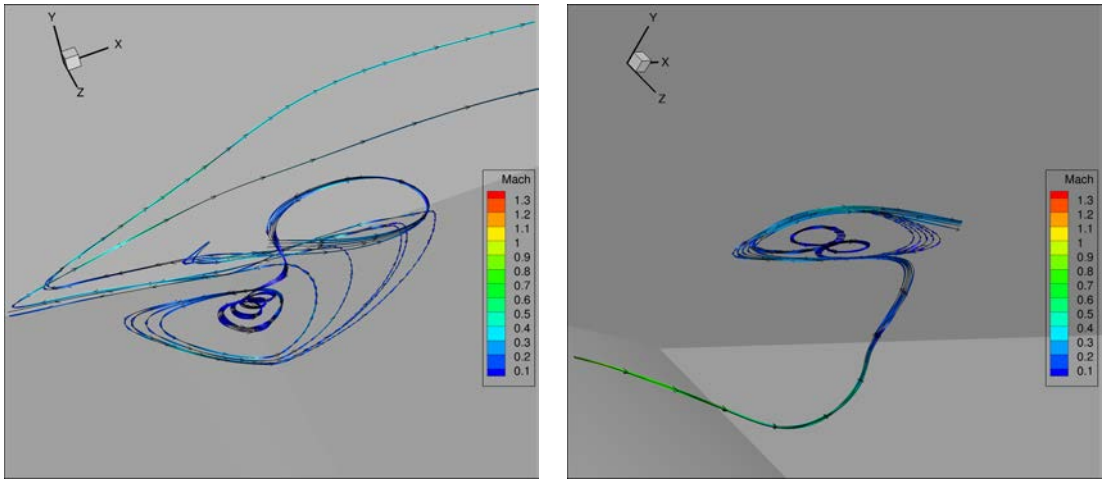

(a) Bottom vortex structure of the corner flow separation

(b) Lateral vortex structure of the corner flow separation

Figure III.10: Streamlines decomposition of the corner flow separation.

1.d Impact on far downstream flow

The zero iso-surface of vanishing longitudinal velocity is presented on a 3D view on Fig. III.11. The central separation is visible and is quite confined to the center of the channel, inducing that this interaction has a complex 3D pattern, the corners separation interacting with the central separation. The shape of the corner flow separation reflects the positions of the two vortices with the first one being positioned on the lower wall and the second one being located on the lateral wall. Far downstream of the interaction, at $x = 468\,\text{mm}$, the stagnation pressure level presents two weak zones, one corresponding to the central separation and a second wider one corresponding to the lateral part of the corner separation. This is due to the fact that the lateral corner separation spreads more downstream than the central one and has less time to be mitigated in the flow. There is also a separation at the top corner of smaller amplitude and a small separation also occurs at the top wall of the wind tunnel (not shown on Fig. III.11 for clarity purpose). The main separation zones are indicated on Fig. III.11.

1.e Conclusion

To conclude, the RANS calculation using the Spalart-Allmaras QCR turbulence model has proven its capacity to capture the principle characteristics of the flow in the S8Ch wind tunnel. It has been successfully compared to PSP measurement, static pressure measurement, colored oil flow visualization and 2D PIV for the central separation. These comparisons reveal that the separation zones are well captured along the wall of the wind tunnel even if their height amplitude may be over estimated. This study validates the use of RANS Spalart-Allmaras QCR modeling for the following process of control optimization.

The flow field presents a complex topology with six zones of separation. Two separations arise in the center of the channel on the lower and upper walls. Four others develop in corner regions, the lower ones being widely more important than the upper ones. It can be noticed that contrary to other studies on SWBLI (see Bruce et al. [16]), no separations

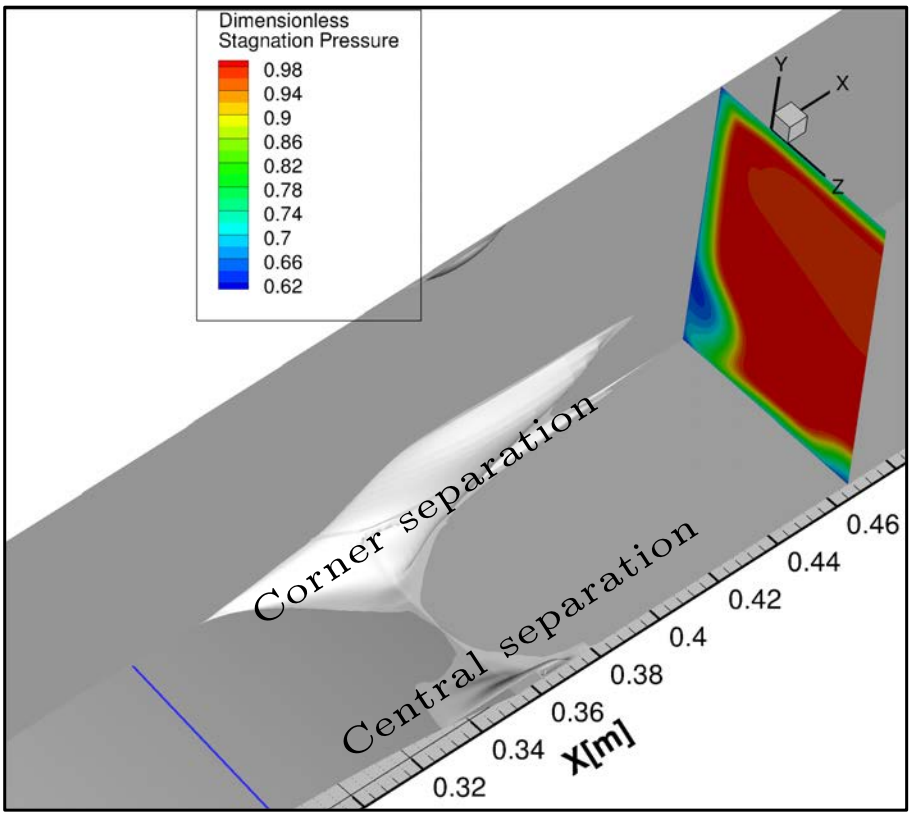

Figure III.11: Non dimensionalized stagnation pressure on the DC50 plane, volume of the reverse flow-white surface- for the RANS reference case.

along the side wall are pointed out. This may be due to the fact that the bump induces a strong pressure gradient on the lower wall which provokes strong separations, notably in the corner. The corner flow separation prevents or is merged with the lateral separations.

The RANS calculation also allows to investigate the corner flow separation zone. It has been distinctly decomposed into two vortices. The first one is slightly upstream on the lower wall and the second one is positioned on the lateral wall.

IV

Optimization Process

L'informatique, ça fait gagner beaucoup de temps... à condition d'en avoir beaucoup devant soi !

Mireille Sitbon

Objectives

The numerical modeling of the uncontrolled case being precisely described, the next stage of work is to design and optimize a control set of fluidic vortex generators using the RANS modeling.

The main idea of the work presented in this chapter is to optimize, using a Kriging based algorithm, a set of fluidic vortex generators. The optimization is conducted in two steps and spotlights two interesting configurations. These configurations are then detailed in order to try to understand how they influence the phenomena that govern the complex Shock-Wave / Boundary-Layer Interaction.

First, the concepts and the algorithm of optimization are presented on a simple example. Secondly, the parameters and the objective function for the fluidic control of the SWBLI are disclosed before the result of the optimization. Thirdly, the second step of optimization focusing on the control of the corner flow separation is detailed. And finally, a closer look is taken at the vortices structures and properties.

Contents

IV.1 Optimization Approach: a Kriging based algorithm

After a general introduction on optimization methods, the mathematical development of the Kriging model is exposed. The algorithm of optimization based on this Kriging modeling is then applied to a simple example, during which the other more trivial parts of the process are detailed.

1.a Short presentation of the wide zoology of optimization methods

Historically the optimization methods have been developed to solve two distinct kinds of problems: the combinatorial ones (the most known example being "the traveling salesman") and the continuous ones (as an example the minimization of any physical law). The studies of these two categories have resulted in exact and effective methods for simple problems (low dimension problem or linear functions). Nevertheless, for difficult optimizations, meaning high dimensions problems or non linear functions, others methods had to be developed.

The optimization methods for the non linear functions can be classified into two main categories, the local methods and the global ones. The local methods are based either on the gradient of the function such as the classical Newton method or on a random local displacement as in the Random Search Algorithm. The local methods without gradients are not really effective and can be extremely long to converge. For the gradient based methods, their drawback is that for each step of the optimization, the gradient of the implicit function should be approximated using the rate of change calculated for each dimension which can be really costly for high dimensions functions. Furthermore, these methods are heavily dependent on the first guess, they can be slow to converge and can converge toward a local minimum of the function. Furthermore as their name indicates, they are local methods meaning that they do not give information about the global tendency of the function with respect to each of the variables. And their most important disadvantage is that they cannot discriminate between local optima and the global optimum.

Due to all these reasons, global methods are more promising for the optimization of a costly numerical function. These methods can be classified between two categories, the heuristics (from the ancient greek $\epsilon\upsilon\rho\iota\sigma\kappa\omega$ meaning "find") and the metaheuristics (from ancient greek $\mu\epsilon\tau\alpha$ meaning here "above"). The heuristic name regroups the techniques designed for solving specific difficult optimizations quicker than the classical methods. They are also designed to find an approximate solution when the classical methods do not manage to find the exact solution of a specific problem. The metheuristics are heuristics

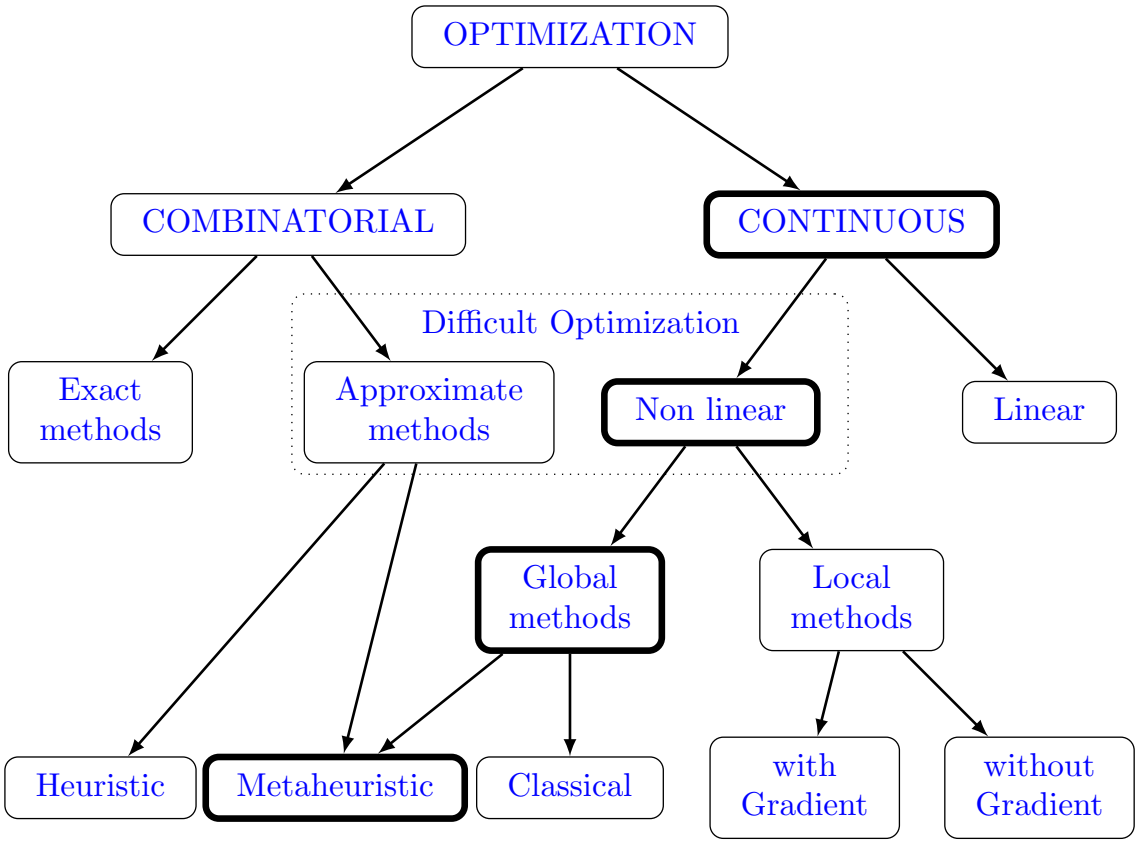

Figure IV.1: Classification of the different methods of optimization- adapted from Dréo et al. [57].

methods that are designed in order to be able to solve more diverse and generals problems, they may be a combination of different heuristics. These metaheuristics such as the particle swarm or the genetic algorithms are more adapted to a difficult optimization of a function which can present local optima. Nevertheless these methods suffer from another inconvenient, even if they do not need a lot of calculations of the local gradient, they need a huge amount of evaluation of the objective function to converge.

This classification of methods is not entirely fixed and some methods can be hybrids between two or more methods which complicate the classification. The classification adapted from Dréo et al. [57] is presented on Fig. IV.1

The main idea of the current process of optimization is to minimize a function really expensive to evaluate as each RANS calculation takes 15 hours. In order to effectively optimize a costly objective function, methods of surrogate modeling or meta-model have been developed. They are presented below.

i Meta model

In order to find the minimum of a complex objective function named f with respect to k parameters $\mathbf{x} = [x_1..x_k]$, a common idea is to build a low cost model of this function $\hat{f}$ called a surrogate model. In the current case since each RANS calculation of a control set up takes 15 hours, the surrogate model needs to be conceived using a really effective

method, meaning using a method which needs as little calls to the test function as possible.

The main idea of the use of a surrogate model is that $\hat{f}$ the model of the function will be explicitly known and thus a search of an optimum on this model can be done using more precise and more resources demanding methods. The process is summed up in Fig. IV.2.

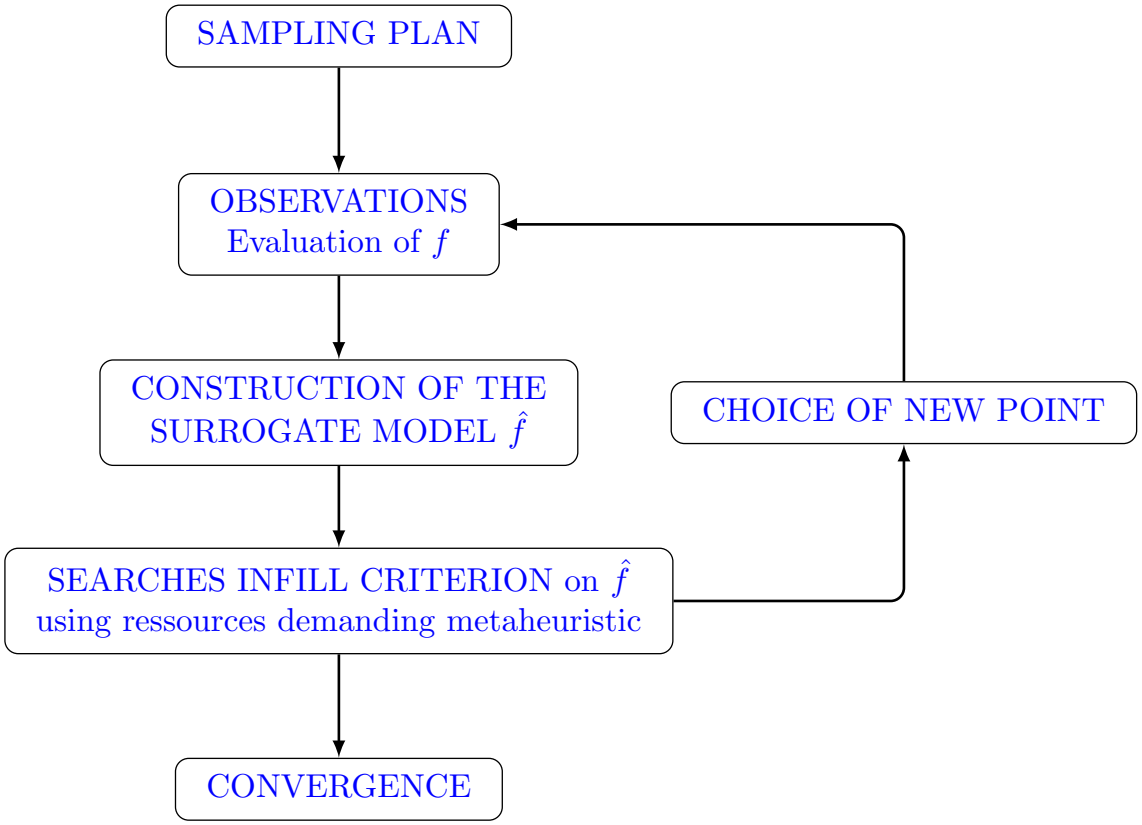

Figure IV.2: Illustration of the process of meta model based optimization.

For the current study, the meta model chosen is a Kriging model. As the phenomena of the interactions between a jet and a cross flow and between a vortex and a shock-wave can be really non linear, a Kriging algorithm is chosen.This method has been widely employed in various optimization processes, such as for example: porous media Evans et al. [62], aerodynamic design J. Toal et al. [94], fluid structure interaction Chanzy and Keane [27]. It has the advantage of not inferring the smoothness of the function. Furthermore as the objective function can be really flat with only very localized maxima, this method of search should be quicker than a conventional Newton method. Another method would have consisted in running an adjoint state method to calculate the gradient, nevertheless the size of the mesh is still a huge obstacle to its application. The Kriging model has the advantage of being able to model efficiently complex non linear functions. Furthermore, it allows the use of the Expected Improvement Function as criterion for enrichment of the model. This criterion is well adapted for the construction of surrogate models since it permits to compromise between two main kinds of enrichments: the exploration enrichment and the improving enrichment. The Kriging model theory is presented below as well as the expected improvement function.

1.b Theory of the Kriging model

i History and mathematical hypothesis

The Kriging method is named after Danie G. Krige [107]. Krige was a mining engineer which was confronted to the difficult geostatistical modeling of the gold veins in the gold deposits with the minimum number of test drilling. His method was then developed and formalized in the work of Matheron [122].

The advantages of this method is that it is adapted to really complex non linear function. It consists in the modeling of the objective function seen as a stochastic distribution function of mean μ and standard deviation σ.

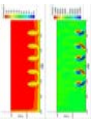

The only hypothesis is that the correlation between two points of the search space only depends on the distance between the two points. Thus this correlation will be modeled using a chosen function and from this an optimal statistic distribution model of the objective function will be derived. This way of modeling comes from the geostatistic field with a continuity of correlation along the gold deposits. It is well adapted for physical problems and is finally less assuming than other classical models of interpolation that necessitate $\mathcal{C}^2$ condition.

ii The Kriging modeling

After evaluating the sampling plan, the method called Kriging is used to construct a first model. This method is clearly explained in Forrester et al. [66] and Jones [97]. The main idea when building a model is to use a base of functions to calculate the model at each point of the parameter space.

In Kriging, the basis functions are defined in Eq. (IV.1), each i^{th} one linked to a i^{th} calculated point of the n points already measured.

$$\psi^i(x) = \exp(-\sum_{k=1}^{n} \Theta_k |x_k^i - x_k|^{p_k}) \tag{IV.1}$$

With x_k^i, x_k the coordinates in the k^{th} dimensions of respectively x^i, x, the i^{th} calculated point and the evaluation point. The Θ_k and p_k are variable parameters.

These functions are close to Gaussians with parameters Θ_k and p_k which allows to balance the influence of each sample point in every dimension in order to find the best model. These functions takes advantages of the fact that the validity of the surrogate model is more certain near to a calculated point and of the fact that the function can change more or less quickly near to each calculated point.

iii Correlation

The Kriging model comes from the notion of correlation. The correlation between two variables y_1, y_2 is usually defined as in the equation IV.2.

$$corr(y_1, y_2) = \frac{E[(y_1 - \mu_1)(y_2 - \mu_2)]}{\sigma_1 \sigma_2} \tag{IV.2}$$

Where μ_1, μ_2 and σ_1, σ_2 stand for respectively the mean and standard deviation of the variables y_1, y_2. E is the function called expectation value.

The correlation coefficient is a way to measure the dependence between two variables. Here the way of studying the variables is changed since the two variables are supposed to be linked by a correlation coefficient equal to the basis functions chosen. The new correlation coefficient is shown in the equation IV.3. This is a strong hypothesis since it supposes that the correlation between two points only depends on the distance between these two points. Nevertheless, this hypothesis is almost always verified in physical modeling and this is weaker than the ones used for others models which need conditions on the derivability and smoothness of the objective function.

$$corr(Y(x^l), Y(x^m)) = \exp\Big(-\sum_{k=1}^{n} \Theta_k |x_k^l - x_k^m|^{p_k} \Big) = \Psi_{lm} \tag{IV.3}$$

With these correlation coefficients a $n \times n$ matrix Ψ called the correlation matrix is defined.

All the measured values are grouped in a vector $n \times 1$, named $\mathbf{y}$.

$$\mathbf{y} = \begin{pmatrix} y^1 \\ ... \\ y^n \end{pmatrix} = \begin{pmatrix} Y(x^1) \\ ... \\ Y(x^n) \end{pmatrix} \tag{IV.4}$$

All these values are supposed to have the same mean μ, and the same standard deviation σ which will be specified later.

iv Likelihood

Another statistic notion is now needed, the likelihood. The likelihood function of a set of parameters here μ and σ, giving the outcome $\mathbf{y}$, is equal to the probability of those observed outcomes given the parameter values. Here as the results are supposed to follow a normal distribution with a standard deviation σ and a mean μ, for a n variables function, the likelihood L is found to be of the form:

$$L = \frac{1}{(2\pi\sigma^2)^{\frac{n}{2}} |\Psi|^{\frac{1}{2}}} \exp\Big[-\frac{(\mathbf{y} - \mu\mathbf{1})^t \Psi^{-1} (\mathbf{y} - \mu\mathbf{1})}{2\sigma^2} \Big] \tag{IV.5}$$

This likelihood would be maximized to find the best parameters. To do this more easily, the natural logarithm of the likelihood is now studied.

$$\ln(L) = -\frac{n}{2}\ln 2\pi - \frac{n}{2}\ln\sigma^2 - \frac{1}{2}\ln|\Psi| - \frac{(\mathbf{y} - \mu\mathbf{1})^t \Psi^{-1} (\mathbf{y} - \mu\mathbf{1})}{2\sigma^2} \tag{IV.6}$$

By taking derivatives of the equation IV.6 with respect to μ and σ^2 and making it equal to zero, the expressions of μ_0 and σ_0^2 which maximize the likelihood as a function of Ψ are found.

$$\mu_0 = \frac{\mathbf{1}^t \Psi^{-1} \mathbf{y}}{\mathbf{1}^t \Psi^{-1} \mathbf{1}} \tag{IV.7}$$

$$\sigma_0^2 = \frac{(\mathbf{y} - \mu_0\mathbf{1})^t \Psi^{-1} (\mathbf{y} - \mu_0\mathbf{1})}{n} \tag{IV.8}$$

These values are injected in the equation IV.6, then the constant terms are removed to find what is known as the concentrated ln-likelihood function:

$$\ln(L) = -\frac{n}{2}\ln(\sigma_0^2) - \frac{1}{2}\ln|\Psi| \tag{IV.9}$$

This function only depends on Ψ, so on the measured values and the parameters Θ and p. By maximizing this implicitly known function with respect to the parameters Θ and p, the best estimate of the objective function will be found. Nevertheless, this function cannot be derivated as for μ_0 and σ_0^2. Here, a metaheuristic algorithm is needed to maximize concentrated ln-likelihood function, such as the genetic algorithm.

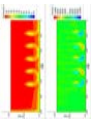

v Predictor

Once this tuning phase is done with the already measured data, it is now possible to construct the Kriging model predictor. To evaluate this model at a point x, the correlation will be used again. First the value of the model at x is named y and $\bar{\mathbf{y}} = \{\mathbf{y}^t, y\}^t$. Then the correlation vector $n \times 1$, $\psi(x)$, a function of x, is defined to complement the correlation matrix now named $\bar{\Psi}$.

$$\psi(x) = \begin{pmatrix} \psi^1(x) \\ ... \\ \psi^n(x) \end{pmatrix} \tag{IV.10}$$

$$\psi^i(x) = \exp(-\sum_{k=1}^{n} \Theta_k |x_k^i - x_k|^{p_k}) \tag{IV.11}$$

$$\bar{\Psi} = \begin{pmatrix} \Psi & \psi \\ \psi^t & 1 \end{pmatrix} \tag{IV.12}$$

It's from here that comes the definition of the basis functions presented in equation IV.1.

The new ln-likelihood is now:

$$\ln(\bar{L}) = -\frac{n}{2}\ln(2\pi) - \frac{n}{2}\ln(\sigma_0^2) - \frac{1}{2}\ln|\bar{\Psi}| - \frac{(\bar{\mathbf{y}} - \mu_0\mathbf{1})^t \bar{\Psi}^{-1}(\bar{\mathbf{y}} - \mu_0\mathbf{1})}{2\sigma_0^2} \tag{IV.13}$$

The idea is now to find y thanks to this equation. The only term which depends on y is the last one, so this term is just derivated with respect to y and using the paritioned inverse decomposition applied to $\bar{\Psi}$, putting the derivative equal to zero, this gives:

$$\left(\frac{-1}{\sigma_0^2(1 - \psi^t\Psi^{-1}\psi)}\right)(y - \mu_0) + \left(\frac{\psi^t\Psi^{-1}(\mathbf{y} - \mu_0\mathbf{1})}{\sigma_0^2(1 - \psi^t\Psi^{-1}\psi)}\right) = 0 \tag{IV.14}$$

So:

$$y(x) = \mu_0 + \psi^t\Psi^{-1}(\mathbf{y} - \mu_0\mathbf{1}) \tag{IV.15}$$

This equation shows how the radial basis function are used to calculate the response of the model thanks to the vector ψ.

vi Expected Improvement

Once the meta model is calculated thanks to our first sampling, the algorithm needs to choose a new point to calculate to try to improve the minimum of the function. In order to do this the expected improvement is now considered.

The great advantage of Kriging is that as it is a process based on Gaussian functions, an estimated error in the model can be calculated. This is going to help to know where to improve the model to find the optimum design. The mean squared error of the Kriging model is calculated as:

$$s^2(x) = \sigma^2 \left[1 - \psi^t \Psi^{-1} \psi + \frac{1 - \mathbf{1}^t \Psi^{-1} \psi}{\mathbf{1}^t \Psi^{-1} \mathbf{1}} \right] \tag{IV.16}$$

After this, $y(x)$ is again considered as a randomly distributed variable along a normal distribution, with $\hat{y}(x)$ the mean and most probable value of the function at the point x this allows to calculate the probability of an improvement $I = y_{min} - y(x)$:

$$P[I(x)] = \frac{1}{s(x)\sqrt{2\pi}} \int_{-\infty}^{0} exp\left[- \frac{(I - \hat{y}(x))^2}{2s^2(x)} \right] \mathrm{d}I \tag{IV.17}$$

A graphical interpretation of this can be seen on Fig. IV.3.

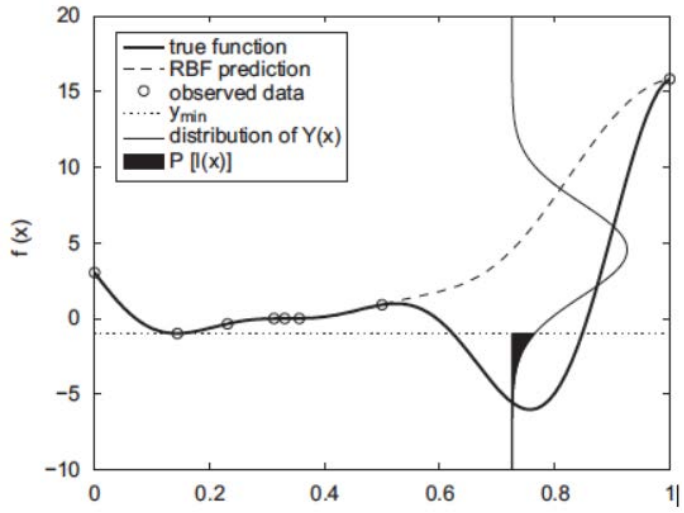

Figure IV.3: A graphical interpretation of the probability of improvement from Forrester and Keane [68].

On this figure, the supposed Gaussian distribution of the possible values of the model can be seen around the value given by the Kriging model (named Radial Basis Function here). The probability of improvement is equal to the black area.

The probability of improvement is only a measure of "is it possible to improve our design", the expected improvement function can be defined which is a measure of "how much the design can be improved". The expected improvement is equal to the expected value of the improvement:

$$E(I) = \frac{1}{s(x)\sqrt{2\pi}} \int_{I=0}^{I=\infty} I(exp\left[-\frac{(y_{min} - I - \hat{y}(x))^2}{2s^2(x)}\right])\mathrm{d}I \tag{IV.18}$$

This can be simplified by using integration by part as:

$$E(I) = \begin{cases} (y_{min} - \hat{y}(x))\Phi\left(\frac{y_{min} - \hat{y}(x)}{s(x)}\right) + s(x)\phi\left(\frac{y_{min} - \hat{y}(x)}{s(x)}\right) & \text{if } s > 0 \\ 0 & \text{if } s = 0 \end{cases} \tag{IV.19}$$

Where Φ and ϕ are the normal cumulative distribution function and density function respectively. The expected improvement function is a good criterion of enrichment since it takes into account the lowest predicted points of the model and the incertainty (and possible error) of the model which are the two main strategies of enrichment for a meta model.

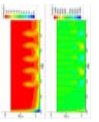

vii Regression Kriging

Due to noise in the data, simple Kriging model is not always well adapted to the problem, as it is an interpolating function. In order to take into account the noise in the data, a regression constant λ is added on the leading diagonal of Ψ. The correlation matrix becomes $\Psi + \lambda\mathbf{I}$ (with $\mathbf{I}$ the identity matrix of same size as Ψ). Using the same derivation as for the simple Kriging, the predictor function y_r becomes:

$$y_r(x) = \mu_r + \psi^t(\Psi + \lambda\mathbf{I})^{-1}(\mathbf{y} - \mu_r\mathbf{1}) \tag{IV.20}$$

With

$$\mu_r = \frac{\mathbf{1}^t(\Psi + \lambda\mathbf{I})^{-1}\mathbf{y}}{\mathbf{1}^t(\Psi + \lambda\mathbf{I})^{-1}\mathbf{1}} \tag{IV.21}$$

$$\sigma_r^2 = \frac{(\mathbf{y} - \mu_r\mathbf{1})^t(\Psi + \lambda\mathbf{I})^{-1}(\mathbf{y} - \mu_r\mathbf{1})}{n} \tag{IV.22}$$

1.c Kriging based optimization method applied to a simple 2D example

Lets take a simple example in order to clarify the explanations and make them more concrete: if you want to send a rocket of mass equal to 1000 kg to the moon, you want to minimize the attraction force to consume less fuel. Therefore, you want to minimize the weight of you rocket for a fixed mass. If you don't know the physical law behind weight for the terrestrial gravity acceleration[1], you will measure the weight of the rocket at different positions on Earth to find your optimum.

Here the two parameters of interest will be the longitude and the latitude coordinates of the point of measurement. In order to get an effective first sampling, we will use the method known as the best Latin hypercube sampling to choose the first points to measure.

[1] $g = 9{,}780\,318 \times (1 + 5{,}302\,4 \times 10^{-3} \times \sin^2(L) + 5{,}9 \times 10^{-6} \times \sin^2(2L))$ with L the latitude position.

i The Latin hypercube sampling

The Latin hypercube method is a good method to design a first sampling which explores at the maximum the variables space without privileging a direction. The method used here is the one presented by Forrester et al. [66]. This algorithm is based on the Latin hypercube method which is itself based on the Latin square. The main idea behind the Latin square is really easy to visualize in two dimensions: to ensure a vast dispersion of the sampling points, the exploration space is divided into $n \times n$ squares. Then the points are distributed in the squares, being careful that there is not two points in the same row or the same column. Two different Latin hypercube samplings for $n = 4$ are presented on Fig. IV.4: the blue and red dots correspond respectively each one to one sample.

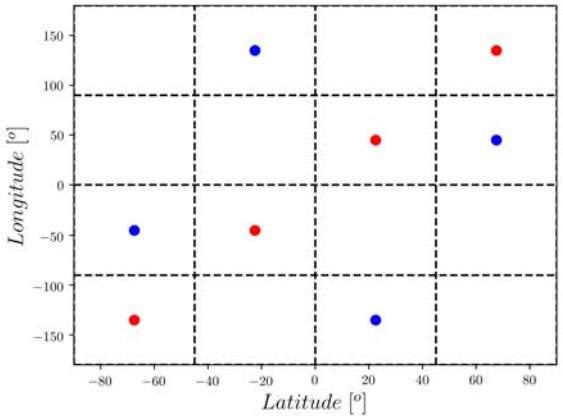

Figure IV.4: Latin hypercube sampling in 2 dimensions for 4 samplings.

As it can be seen on the Fig. IV.4, if the blue sampling seems to ensure a sampling without privileged direction, the red one is biased as it will priviledge the diagonal direction. Thus, the definition of a sampling using the Latin hypercube is not sufficient to ensure a sampling which does not priviledged a specific direction. In this example the red sampling is really not appropriate for building a surrogate model. It will not allow the model to understand easily the variation along the other diagonal axis. This is to show that the Latin hypercube method needs to be improved. This is even more true for a exploration space with more than two dimensions. So Forrester et al. [66] constructed a way to find the best Latin hypercube distribution based on a criteria function Φ defined by Morris and Mitchell [126]:

$$\Phi_q(X) = \left(\sum_{j=1}^{m} J_j d_j^{-q}\right)^{\frac{1}{q}} \tag{IV.23}$$

Where X is the vector of the sampling points coordinates, $d_1, d_2, ..., d_m$ are the rectangular distances between all the couples of sampling points and $J_1, J_2, ..., J_m$ the number of couples distant respectively of $d_1, d_2, ..., d_m$. q is varied to get several sampling plans. A genetic algorithm is then used to improve the sampling based on the criteria function. After all, the best sampling is chosen using the first but not easily applicable definition of the best space-filling sampling plan: the sampling which maximizes the smallest distance and minimizes the number of couples associated with this distance.

The best sampling plan for the actual example is the blue one. The corresponding points measured for the weight of the rocket are presented in Table IV.1.

Table IV.1: Latin hypercube sampling of the rocket's weight measurements.

Latitude (°)	Longitude (°)	Weight (kN)
-22.5	135.	9 787
-67.5	-45.	9 824
67.5	45.	9 824
22.5	-135.	9 787

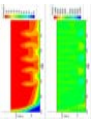

It can be noticed that in the case of the rocket's weight, the first sampling gives only two different values of weight. This sampling is intentionally biased in the case of the rocket as the function is actually 1D. Nevertheless for an hypercube sampling of 5 or more points, the function is directly very precisely modeled. In order to improve the interest of this example this biased sampling is kept for the following.

ii Genetic Algorithm

In a second step, the Kriging parameters $\Theta_{Latitude}$ and $\Theta_{Longitude}$ are tuned using a genetic algorithm in order to minimize the likelihood of the statistic function of Kriging with respect to the measured points (see iv).

The genetic algorithm was developed by Holland et al. [90]. This algorithm is based on the principle of species evolution developed by Darwin in 1859. The main idea is to effectuate crossing and mutations of the best known test points in order to find an optimal solution for the initial problem. It is one of the most used metaheuristics because it is really effective for optimal solution research in a small calculation time. It consists in placing randomly points on the search domain, (here $\Theta_{Latitude}$ and $\Theta_{Longitude}$). Then the positions are quantified by calculating the likelihood of the Kriging model. The particles having the smallest likelihood are suppressed(natural selection). New particles are then created by mixing the position of two valid particles. Some others are also randomly modified to model mutation. This process is repeated several times until the particles converge to the searched maximum.

The algorithm is briefly summarized below.

This optimization results in the values below and the Kriging model and Expected improvement function presented on Fig. IV.5.

$$\Theta^{iter1}_{Latitude} = 88.6 \tag{IV.24}$$

$$\Theta^{iter1}_{Longitude} = 81.2 \tag{IV.25}$$

It should be noticed that due to the insufficient sampling, the algorithm cannot find that the function varies only along one dimension.

Another interesting point to notice is also that the expected improvement function is a plateau with importantly restraint peaks and valley. This type of function is really harsh to optimize, that is why an algorithm of Particle Swarm Optimization is used to find its maximum.

Algorithm 1 Genetic Algorithm

1: First population randomly distributed

- Each individual is made of n bits linked to n chromosomes.

2: Evaluation

- For each individual a note is attributed to its result.

3: Selection

- Random selection of n/2 couples of individuals.
- Each individual as a chance of being selected linked to its result.

4: Crossing and mutation

- Each couple gives 2 children.
- Crossing of the genetic material.

5: Mutations of the children.

- Random change of one bit.

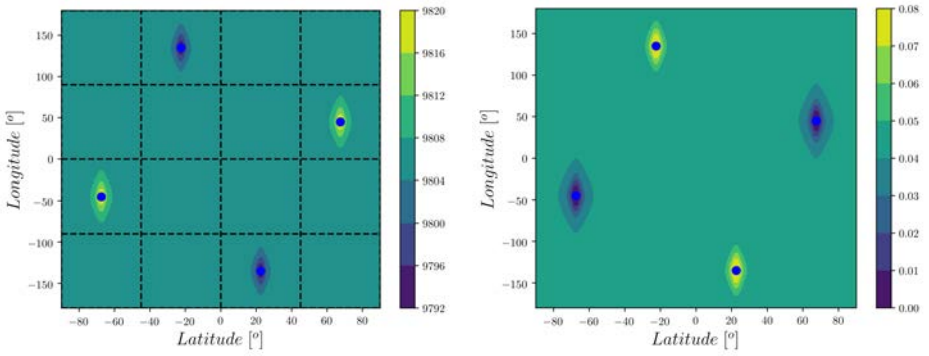

(a) Kriging model of the rocket's weight at iteration 1.

(b) Expected improvement function of the rocket's weight at iteration 1.

Figure IV.5: First iteration of the Kriging based optimization of the rocket's weight.

iii Particle Swarm Optimization

The Particle Swarm Optimization algorithm is a metaheuristic algorithm developed by Kennedy and Eberhart [101]. This metaheuristic algorithm is based on the social comportment of bees and on the concept of distributed intelligence. Its principle is the following.

Several particles are considered on the search space. These particles are going to move at each iteration of the algorithm, in function of three parameters:

- An inertial component : its current velocity $\vec{V_i}$
- A personal component : the position of its own best known position $\vec{Pbest_i}$

- A social component : the best known position obtained by the group of its neighbors $\vec{Gbest}$

The first version of this algorithm written by Kennedy and Eberhart [101] took into account an inertia coefficient for the inertial component and random coefficient for the two other components. With $\mathbf{x}_i^t$ the position of i^{th} particle at t^{th} iteration with $\mathbf{x}_i^t = [x_{i,1}^t, x_{i,2}^t, ..., x_{i,D}^t]$ and $\mathbf{v}_i^t$ the velocity of the particle at t^{th} iteration:

$$\mathbf{v}_i^{t+1} = w.\mathbf{v}_i^t + K_1.\mathbf{r}_{1,i}^t(\mathbf{Pbest}_i^t - \mathbf{x}_i^t) + K_2.\mathbf{r}_{2,i}^t(\mathbf{Gbest}^t - \mathbf{x}_i^t) \quad \text{(IV.26)}$$

$$\mathbf{x}_i^{t+1} = \mathbf{x}_i^t + \mathbf{v}_i^{t+1} \quad \text{(IV.27)}$$

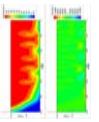

with w inertial constant
$K_1 \& K_2$ acceleration constants
$\mathbf{r}_{1,i}^t \& \mathbf{r}_{2,i}^t$ are two random vectors uniformely taken in $[0,1]^D$ at each iteration.
The algorithm is summed up in Algorithm 2.

Algorithm 2 Particle Swarm Optimization

```
Initialise randomnly N particles : position and velocity.
Evaluate the position of the particles
For each particle i, Pbest_i = x_i
Calculate Gbest
while Stop criterion is not reached do
    Move the particles
    Evaluate the positions of the particles
    Update Pbest and Gbest
end while
```

The Particle Swarm Optimization manages to find the maximum of the expected improvement function where a new point is added. Following this, the three steps -adding a new point, tuning of the Kriging parameters, and looking for the maximum of the expected improvement function- are repeated two times. The corresponding results are presented on Fig. IV.6 and on Fig. IV.7. The values of the added points and of the resulting Kriging parameters are summed up in Table IV.2.

It is noticeable that with just the addition of one point, the algorithm detects that the function is actually 1D and $\Theta_{Longitude}$ is not important anymore as it is reduced to the minimum of the search space for the Θ parameters(1.0e-05).

Another interesting fact is that the model is very well reproduced at iteration 2 and the maximum of the expected improvement is really close to the actual minimum of the function. The last added point is placed at only 0.02° of the actual minimum of the function.

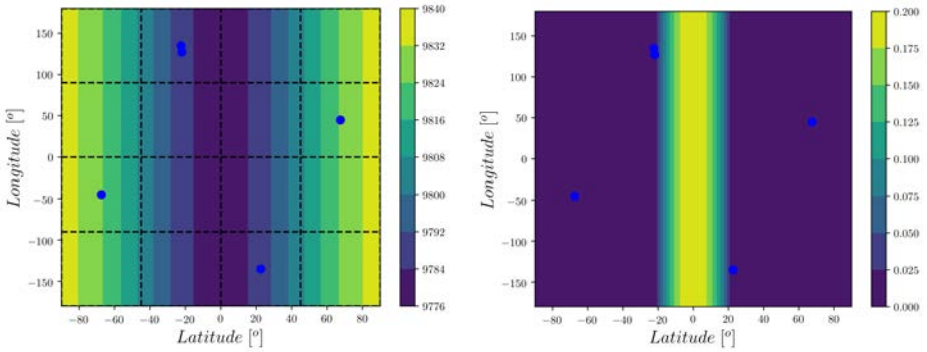

(a) Kriging model of the rocket's weight at iteration 2.

(b) Expected improvement function of the rocket's weight at iteration 2.

Figure IV.6: Second iteration of the Kriging based optimization of the rocket's weight.

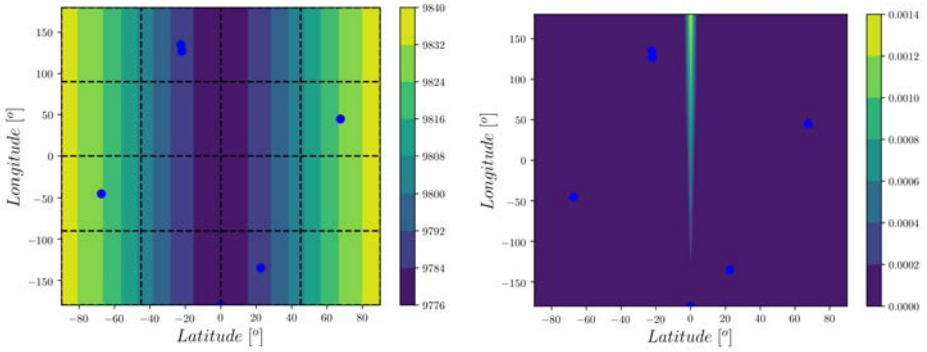

(a) Kriging model of the rocket's weight at iteration 3.

(b) Expected improvement function of the rocket's weight at iteration 3.

Figure IV.7: Third iteration of the Kriging based optimization of the rocket's weight.

Table IV.2: Points added to the Kriging model of the rocket's weight and the resulting Kriging parameters.

Added Point			Kriging parameters	
Latitude (°)	Longitude (°)	Weight (kN)	$\Theta_{Latitude}$	$\Theta_{Longitude}$
			88.6	81.2
-22.	127.1	9 787.6	5.0	1.0e-05
-0.02	-180.	9 780.3	4.3	1.0e-05

iv About the expected improvement function

In order to visualize more precisely the interest of the expected improvement function, the same study is now done with only one parameter: the latitude coordinate. The first sampling is again chosen biased in order to fault the Kriging model. Due to this ill-posed problem, the first model is far from the objective function in the central range of latitude as it can be seen on Fig. IV.8. The limits of the variance of the model are presented. The variance is equal to zero at the measured points and grows between the measured points. It should be noticed that these variance limits are not the real limits of the distribution of probability of the model. Since this probability is a Gaussian for each point of the model, it extends farther than the variance. The expected improvement is the measure of the quantity of probability times the improvement, meaning the possibility of being below the actual minimum of the test points. Once the new point is added, the model manages to predict the objective function and the new maximum of the expected improvement is close to the actual minimum of the true objective function.

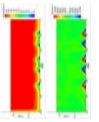

The lessons of these examples are that the first sampling is of the utmost importance in the optimization process. It should provide enough information on the whole domain and be uniformly spread out. This confirms the interest of the Latin hypercube sampling method. Furthermore, as it can be seen on Fig. IV.8 b), d) and f), the diminution of the maximum of the expected improvement is not sufficient to justify the convergence of the algorithm. The maximum of the expected improvement is around 0.04 at the first iteration and grows up to 0.7 at the second iteration before finally decreasing to 0.00025. Thus, the diminution of the Expected improvement may be a criterion of convergence only if it is correlated to the end of variation of the model with each newly added point.

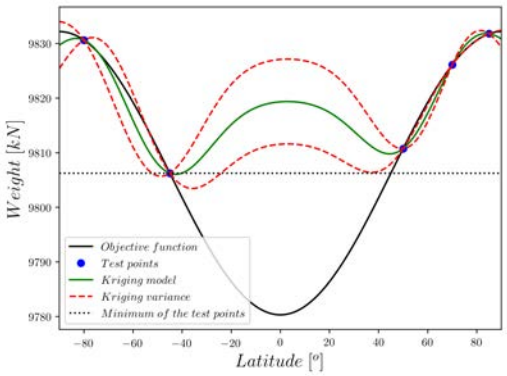

(a) 1D Kriging model of the rocket's weight at iteration 1.

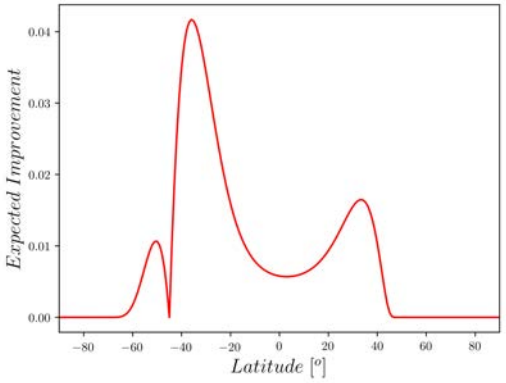

(b) 1D expected improvement function of the rocket's weight at iteration 1.

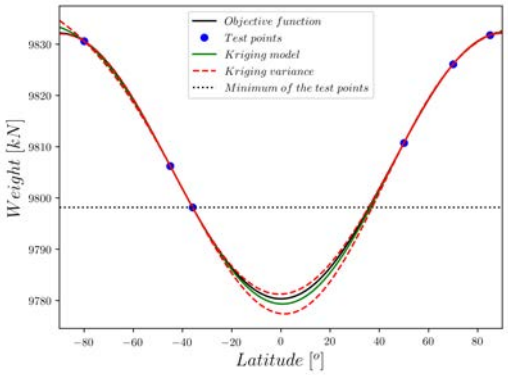

(c) 1D Kriging model of the rocket's weight at iteration 2.

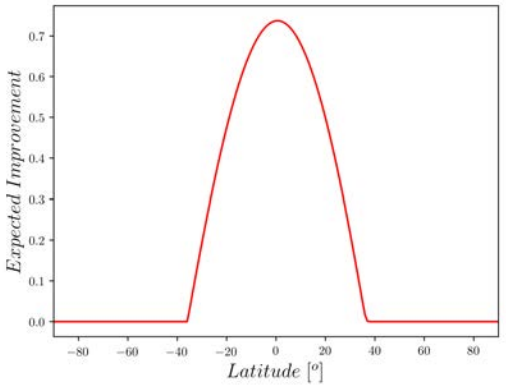

(d) 1D expected improvement function of the rocket's weight at iteration 2.

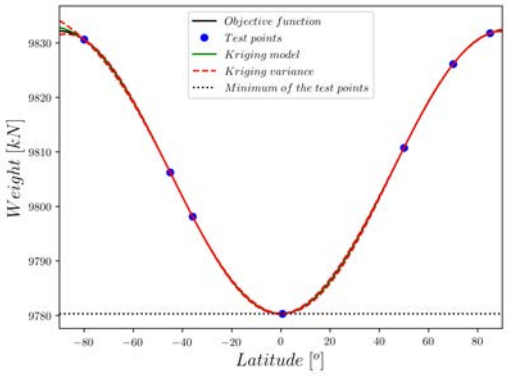

(e) 1D Kriging model of the rocket's weight at iteration 3.

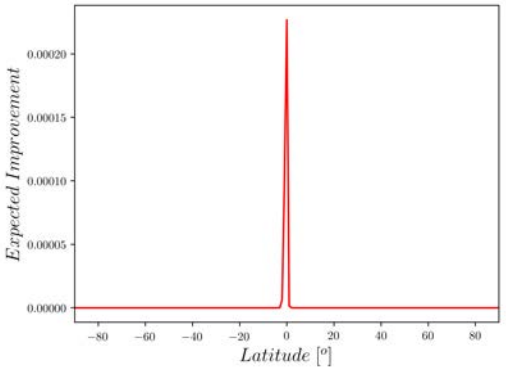

(f) 1D expected improvement function of the rocket's weight at iteration 3.

Figure IV.8: 1D Kriging based optimization of the rocket's weight.

1.d Summary of the Kriging based optimization method

In order to proceed to an optimization of several parameters of the control, an optimization method is set up. The idea is to be able to minimize an objective function described in 2.b with respect to some parameters described in 2.a and 3.a.

The different sequences of the method are described in Algorithm 3, with the parameters of the metaheuristics used within the process, presented in Table IV.3. The complete algorithm is presented on Fig. IV.9. The algorithm used for the following study is based on a modified version of the python toolbox pyKriging by Paulson [133].

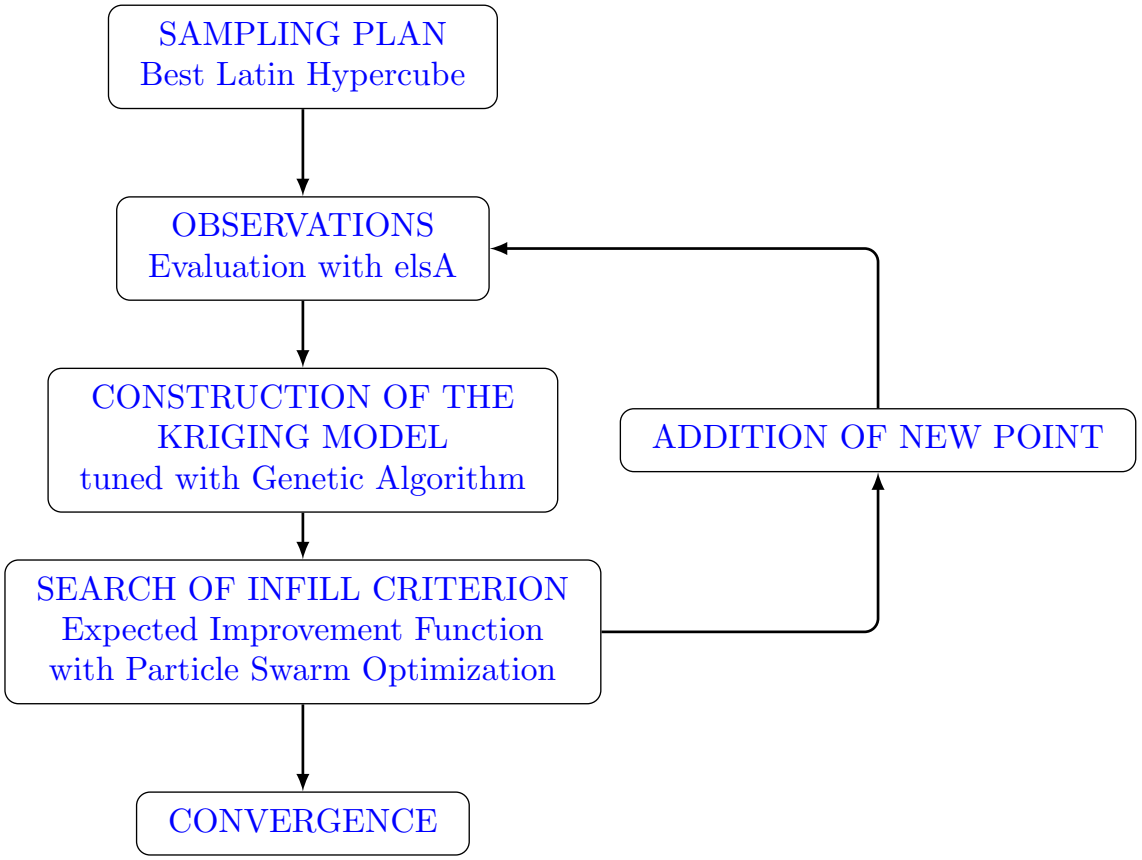

Figure IV.9: Kriging based optimization.

Algorithm 3 Kriging based optimization

1: Sampling Plan

- Generation of the initial sampling points with a Latin hypercube sampling method → Sec. 1.c i

2: Observations

- Evaluation of these designs with elsA, see 3.c

3: Construction of the Surrogate model

- Construction of a surrogate model using Kriging method → Sec. 1.b ii
- Optimization of the Θ parameters using a Genetic algorithm → Sec. 1.c ii

4: Search of the Infill Criterion

- Construction of the model of the expected improvement → Sec. 1.b vi
- Search of the maximum of the expected improvement thanks to a Particle Swarm Optimization → Sec. 1.c iii

5: Addition of a New Design

- Evaluation of the new design at the maximum of the expected improvement with elsA.
- Addition of the new design to the model then back to step 3.

Table IV.3: Parameters fo the metaheuristics used in the general optimization process.

Genetic Algorithm		Particle Swarm Optimization	
Population	50	Population	1 000
Evaluation Max	30 000	Evaluation Max	200 000
Elite	10	Neighbors	40
Mutation	0.05		

IV.2 First Optimization: separation's control

2.a Optimization Parameters

The achievement of the control depends on a wide variety of parameters: the numbers of jets, their lateral and longitudinal positions, their injection pressure, their pitch and skew angles for each of them. In order to keep the calculation time reasonable, only two parameters are optimized in a first approach: the pitch and skew angles. The others parameters are chosen thanks to some first trials and literature results on the mechanical micro VGs. The basic configuration is defined as follows: ten VGs are positioned in the

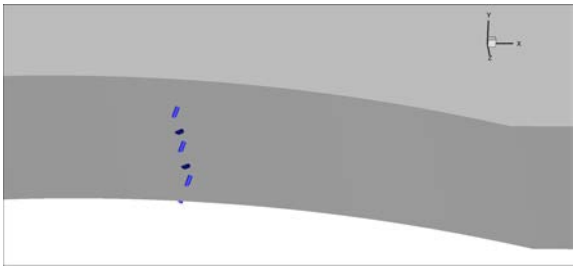

Figure IV.10: Positions of the jets.

spanwise direction, separated by 2.1 δ (with a bigger gap in the center of the channel due to the presence of a pressure sensor) and 12 δ in front of the shock-wave / boundary-layer interaction which was the best location determined in a previous study with the same interaction Bur et al. [20]. The positions of the jets can be seen on half of the wind tunnel in Fig. IV.10, it corresponds to a position of x =0.280 m. The total injection pressure is fixed to 2 bar. The jets diameters are fixed to 1 mm. This is done to ensure a small velocity ratio and a small momentum coefficient c_μ defined in Eq. (IV.28) which are main criteria of efficiency for such fluidic control devices. The velocity ratio is comprised between 1.5 and 2 for the different configurations studied. The momentum coefficient c_μ characterizes the energy of the jets compared to the one of the whole channel.

$$c_\mu = \frac{\Sigma \rho_{jet} U_{jet}^2 S_{jet}}{0.5 \rho U^2 S} \tag{IV.28}$$

It should be noticed that the real shape of the injection hole is an ellipse which varies with respect to the pitch and skew angles.

Furthermore, the VGs are chosen to be oriented in counter-rotating angles. Previous studies (as Godard and Stanislas [83] for instance) demonstrated that even if the vortices generated by a counter-rotating pair of VGs are more likely to interact and to generate a zone in between with a velocity deficiency, they sustain each other and thus generate a better mixing elsewhere. Moreover, in a rectangular channel, co-rotating VGs cause a lateral speed which strongly deteriorates corner flows.

The two angles of the jets are defined in Fig. IV.11 with respect to the local tangents. Due to physical constraints (the unfeasibility of drilling a hole of 1 mm diameter at really small angles), the α angle is only varied between 30° and 150°. The angle β is varied between 0° and 180°. Combined with the pitch rotation, this variation allows to consider all the physical configurations including the upstream blowing jets which are less tested in the literature.

2.b Objective Function: DC50 Criterion

ø ø The goal of this study is to reduce the separation zone which should improve both the homogeneity and the total internal energy of the flow downstream of the shock-wave / boundary-layer interaction. In order to quantify the improvement on both of these quantities, a one dimension function has been selected. A distorsion criterion, called $DC50$, is defined based on an existing criterion used by aircraft manufacturers: the $DC60$ criterion Goldsmith and Seddon [86], Garnier [75]. This criterion is calculated on a slice perpendicular to the flow direction placed downstream of the separation zone as it can be

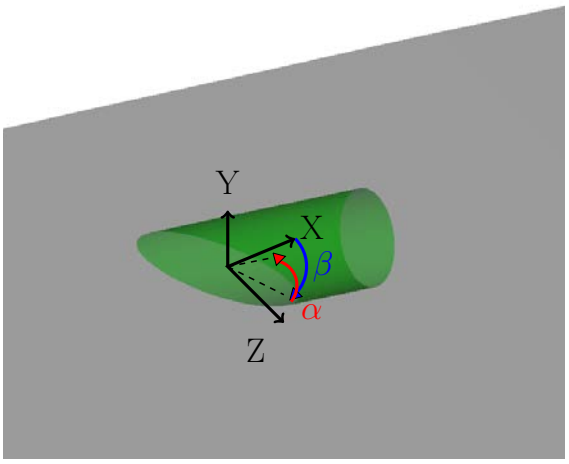

Figure IV.11: Definition of α and β, respectively pitch and skew angles in the case of the perpendicular jet producing the well known counter-rotating pair of vortices visualized on a Q criterion equal to $3 \cdot 10^8$ isosurface colorized with longitudinal vorticity.

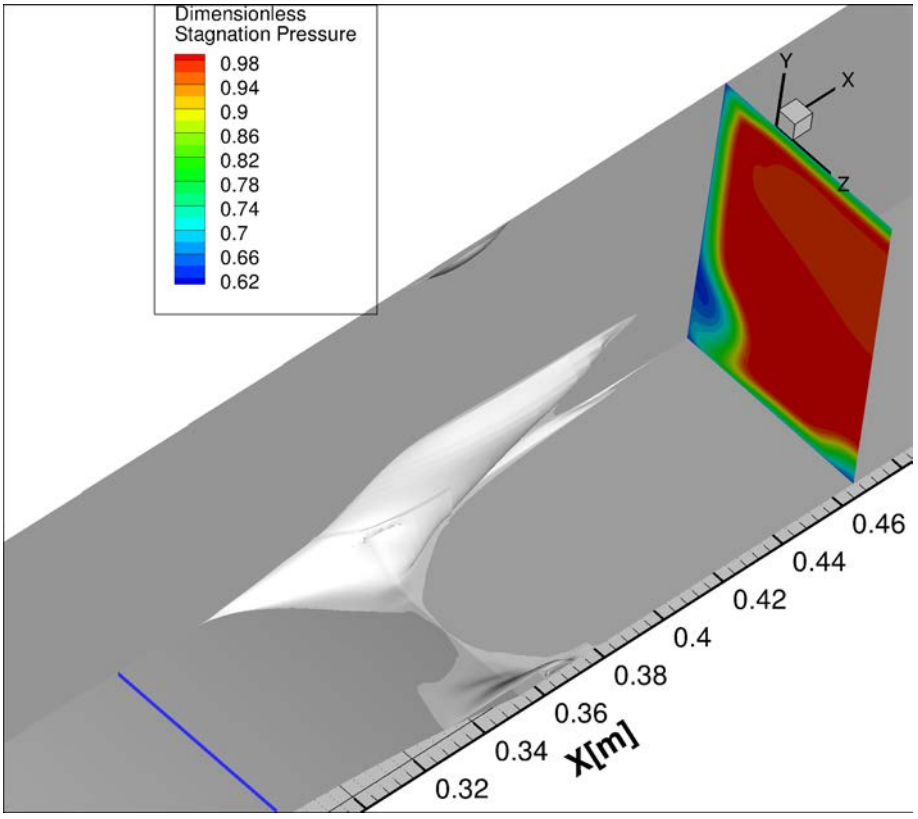

Figure IV.12: Non dimensionalized stagnation pressure on the DC50 plane, volume of the reverse flow-white surface- for the reference case (the blue line represents the position of the VGs).

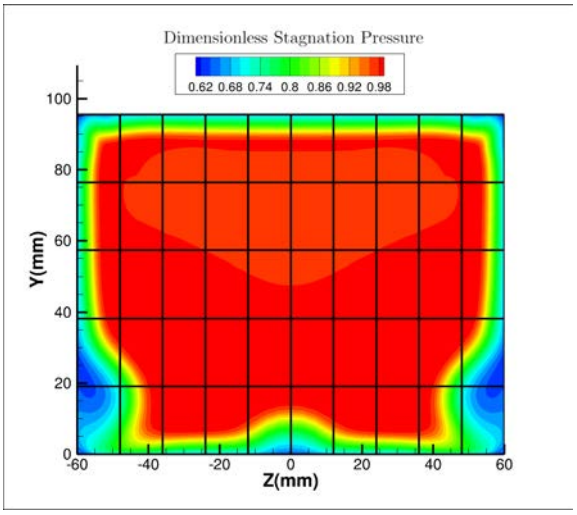

Figure IV.13: Non dimensionalized stagnation pressure on the transverse plane of the reference case used for the DC50 calculation with the 50 zones.

seen in Fig. IV.12 at x =0.468 m. This position has been chosen because it is the location of a mobile Pitot rake in the wind tunnel. The criterion consists in a comparison between the spatial mean (denoted '$< . >$') stagnation pressure Pi in the slice with the worse mean stagnation pressure in a fiftieth of the slice Pi_{zone}. This quantity is divided by the mean dynamic pressure q in the slice in order to give an information not only on the homogeneity of the flow but also on the conservation of the energy. This criterion is summed up in Eq. (IV.29). The fifty portions of the slice of the reference case (without control) are presented in Fig. IV.13. The loss of stagnation pressure due to the boundary-layer and the corner flow separation are clearly visible. The $DC50$ of the reference case is equal to 0.88. The objective of the optimization is to minimize this criterion.

$$DC50 = \frac{< Pi > -min(< Pi >_{zone})}{< q >} \tag{IV.29}$$

2.c Results

The process of optimization is illustrated in Fig. IV.14, the dots represent the calculated points. Their colors are associated with their rank in the optimization process, the 7 first sampled points are white and the dots are getting darker as the optimization progresses.

Six noticeable cases of the optimization are named in this figure with small letters from a) to e). They correspond to vertical jets, aligned downstream blowing jets, aligned upstream blowing jets, a sub optimum case, the optimum case and a case close to the configuration used in several studies $\alpha = 30°$ and $\beta = 60°$ Rao [138], Bray and Garry [15], Dandois et al. [44]. Their physical geometries are presented in Fig. IV.15 and the diverse vorticity patterns they generate are presented in Fig. IV.16. These vorticity patterns are studied more precisely in section IV.4. In order to visualize the whole diversity of vorticity patterns and the influence of each parameter on it, the vorticity patterns are integrated to the model in Appendix A.2.

What can be noticed on the model of the $DC50$, presented in Fig. IV.14, is that the

algorithm first finds a zone of interest close to the point d) where several points are added. After this, the algorithm starts a second exploration and manages to find a second zone of interest close to the point e). In a third time, after several enrichments, the algorithm starts a third period of exploration during which it does not manage to find a new interesting place even after adding three new points. Furthermore, the model is not modified any more, the calculated points having values close to the ones predicted by the model and thus the optimization is considered converged.

In order to add more physical considerations in the model and not for optimization purposes, four points are added at no additional numerical cost as they all correspond to the same configuration. Indeed, when the pitch angle is fixed to 90° the skew angle does not have a real signification as the jets remain vertical with respect to the local tangents.

The final model is presented in Fig. IV.14, it does not interpolate all the points within a 3% error margin following the philosophy of regression Kriging (the error is calculated between the value of the regression Kriging model at the calculated points and the $DC50$ criterion calculated by the RANS code).

First of all, the upper and lower limits of the model corresponding to the axis $\beta = 0°$ and $\beta = 180°$ are resembling but with reverse direction following the variation of α. Meaning that for $\beta = 0°$ the augmentation of α follows the same variation as the diminution of α for $\beta = 180°$. This is a fair result as for the jets with no lateral deviation meaning $\beta = 0°$ or $\beta = 180°$, when β is changed from 0° to 180° the jets are just directed in the opposite direction. Thus the α angle corresponds to its complementary angle to 180°. As an example the configuration $\beta = 0°$ and $\alpha = 60°$ is exactly the same as $\beta = 180°$ and $\alpha = 120°$.

Then the model presents a "quasi-central symmetry". This is coherent with the fact that the intensity and position of the vortices generated by the jets symmetric with respect to the centers of the model are symmetric along the longitudinal plane. The difference of level of $DC50$ is due to the fact that the jets close to the center and the corner of the channel interact differently and that there is an even number of jets in this configuration. The two main zones of interest in blue and green are on the upstream blowing jets zones presented which differs from the previous studies which consider that the preferential angles were $\alpha = 30°$ and $\beta = 60°$ Rao [138], Bray and Garry [15], Dandois et al. [44].

ø

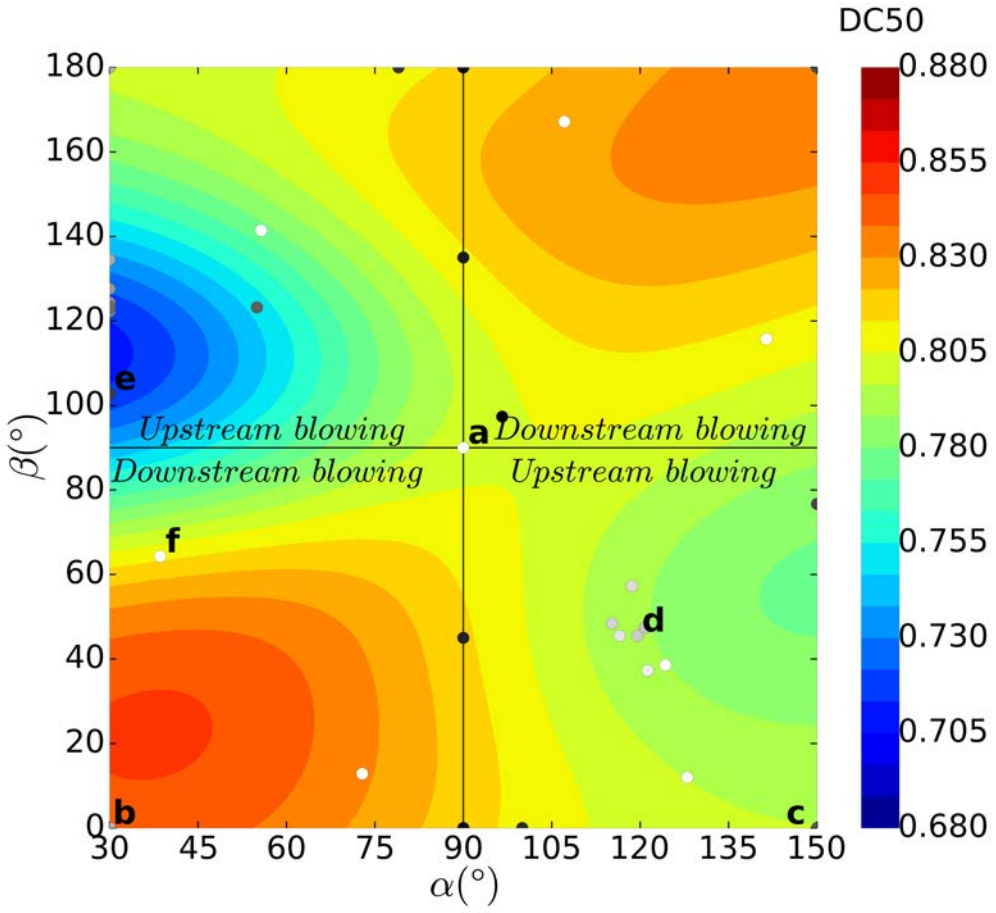

Figure IV.14: Regression Kriging model of the DC50 function with respect to the skew and pitch angles of ten VGs. The dots represent the calculated cases, the first sampled ones are white and the other ones are getting darker with respect to their order of infill.rChanger la couleur des lettres

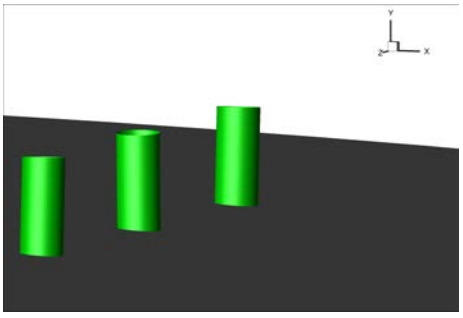

(a) Vertical jets, $(\alpha, \beta) = (90, 90)$

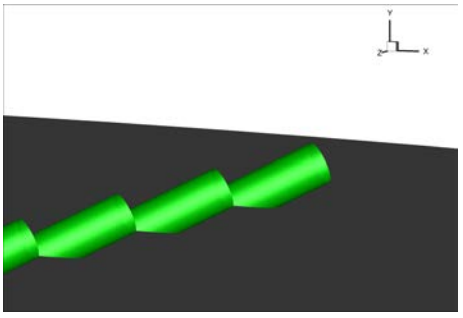

(b) Aligned downstream blowing jets, $(\alpha, \beta) = (30, 0)$

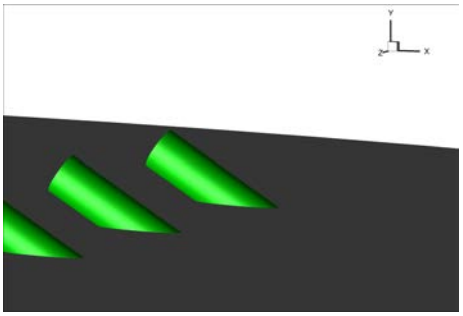

(c) Aligned upstream blowing jets, $(\alpha, \beta) = (150, 0)$

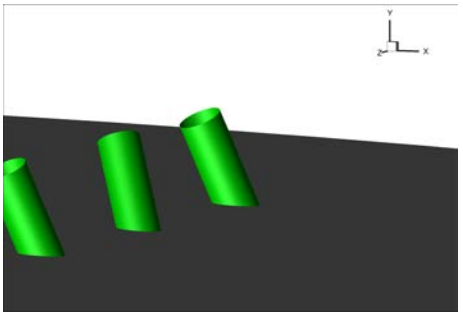

(d) Sub optimum case, $(\alpha, \beta) = (120, 45)$

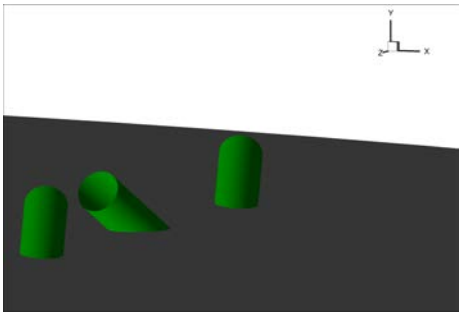

(e) Optimum case, $(\alpha, \beta) = (30, 102.8)$

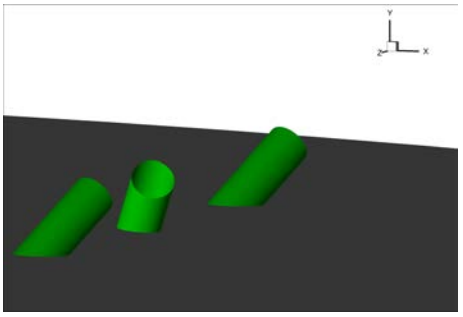

(f) Classical control, $(\alpha, \beta) = (38.6, 64.3)$

Figure IV.15: Physical geometry of jets configurations studied more precisely, the letters correspond to the one on the DC50 model Fig. IV.14

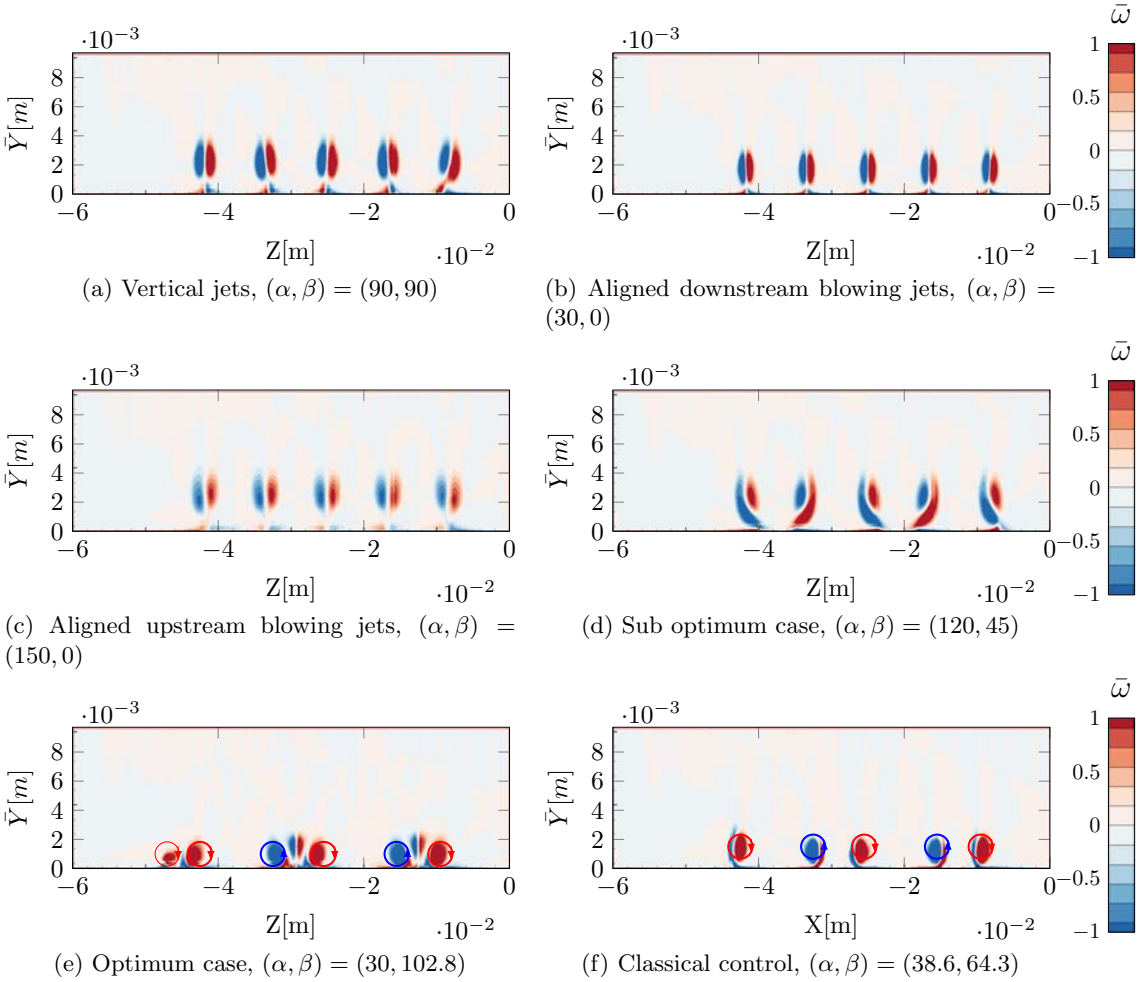

(a) Vertical jets, $(\alpha, \beta) = (90, 90)$

(b) Aligned downstream blowing jets, $(\alpha, \beta) = (30, 0)$

(c) Aligned upstream blowing jets, $(\alpha, \beta) = (150, 0)$

(d) Sub optimum case, $(\alpha, \beta) = (120, 45)$

(e) Optimum case, $(\alpha, \beta) = (30, 102.8)$

(f) Classical control, $(\alpha, \beta) = (38.6, 64.3)$

Figure IV.16: Vortices produced by the VGs' configuration on a transverse plane at x=290 mm, the letters correspond to the one on the DC50 model Fig. IV.14

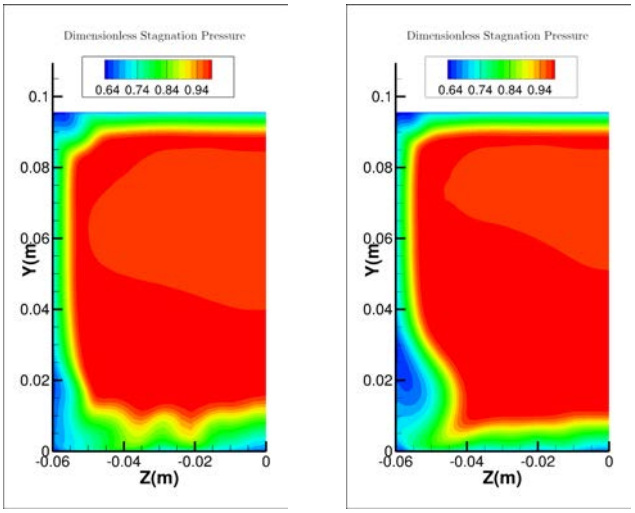

(a) Optimum case, $(\alpha, \beta) = (30, 102.8)$(case e)

(b) Sub optimum case, $(\alpha, \beta) = (120, 45)$(case d)

Figure IV.17: Non dimensionalized stagnation pressure on the transverse DC50 plane of the best controlled cases of the first optimization.

The best controlled case found is for $\alpha = 30°$ and $\beta = 102.8°$ values of angles, the objective function being equal to 0.68 which represents already an improvement of 22% with respect to the baseline case. It generates the stagnation pressure distribution presented in Fig. IV.17a and the whole flow topology is visible in Fig. IV.18. This configuration is composed of upstream blowing jets with the lateral one pointing outward at the wall. The external jet manages to reduce the impact of the corner flow by inducing a reverse flow farther from the lateral wall compared to the baseline case presented in Fig. IV.12. The corner flow presents a completely different shape and seems to be more efficiently dissipated. Due to the fact that, in this configuration, the two central jets are pointing outwards, the central separation is diminished but not completely removed. The reduction of corner flow separation however, impacts more the $DC50$ criterion.

ø

The conclusion of this first optimization is that the algorithm managed to find an optimum which reduces the value of the objective function with a configuration composed of slightly upstream blowing jets. Nevertheless, this study emphasizes the fact that the most important contribution of the control is done by the external jet which controls the corner flow separation. The corner flow separation itself is responsible for the main variations of the $DC50$. The importance of the corner flow separation has already been highlighted in Titchener and Babinsky [166], Xiang and Babinsky [178]. To further the control, a second optimization is considered with a specific jet controlling the corner flow. In order not to allow the central reverse flow to grow while the corner separation diminishes, a central control is conserved. The case chosen for this control variant is the sub optimum case with $\alpha = 120°$ and $\beta = 45°$, presented in Fig. IV.17b and Fig. IV.19. It generates a $DC50$ of 0.78 which is only a 11% of improvement with respect to the baseline case. However, it controls better the central separation and since the external jet is pointing inward, it does not interact with the new external jet, added to specifically control the corner flow separation.

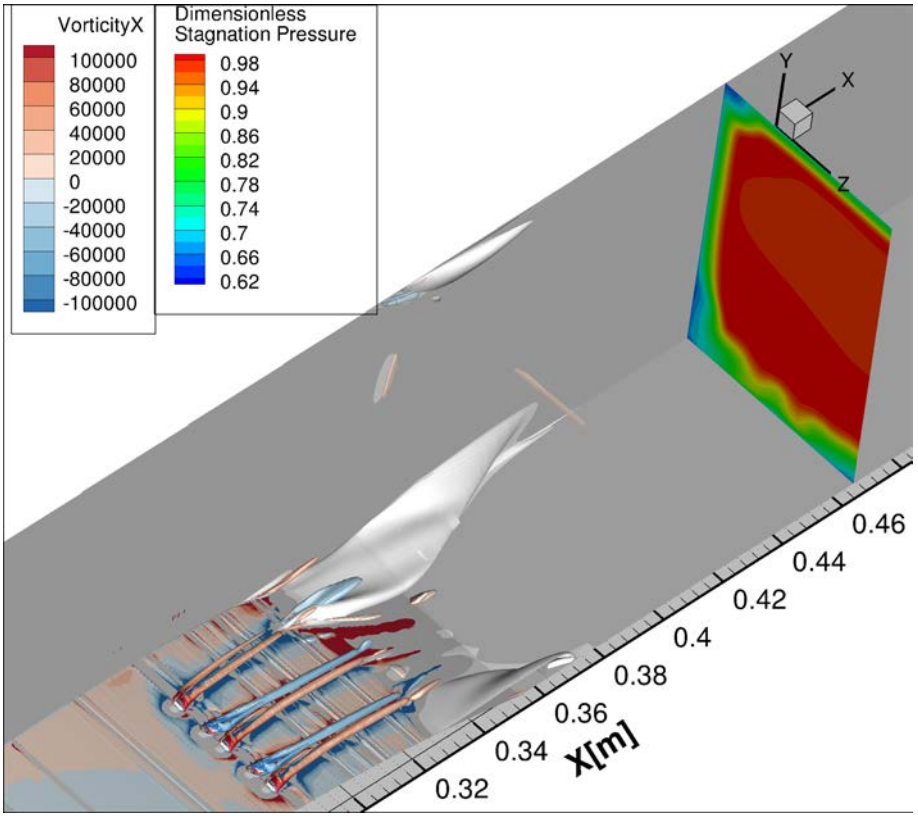

Figure IV.18: Non dimensionalized stagnation pressure on the DC50 plane, volume of the reverse flow-white surface- and Q criterion equal to $3 \cdot 10^8$ isosurface colorized with longitudinal vorticity for the optimum case e).

ø

IV.3 Second Optimization: the Corner Flow Separation's Control

3.a New Optimization Parameters

As explained above, the second optimization considers a control with 12 jets, the 10 central ones of sub optimum case with $\alpha = 120°$ and $\beta = 45°$, and an additional jet in each corner to control specifically the corner separation. The positions and orientations of the central jets can be seen in Fig. IV.15d). The new optimization takes into account two others parameters, namely the longitudinal and lateral position of the jet. The pitch and skew angles are also to be optimized. Ranges of variation of each parameter are summarized in Table IV.4.

The objective function is calculated as in the previous optimization.

The problem is of dimension four and thus the initial number of samples for the Latin hypercube sampling is increased to 15. Then, the processus of improvement is kept as before except that, in order to accelerate the convergence, the new points are calculated 3 by 3. To choose these three points, the model is updated with the predicted value of

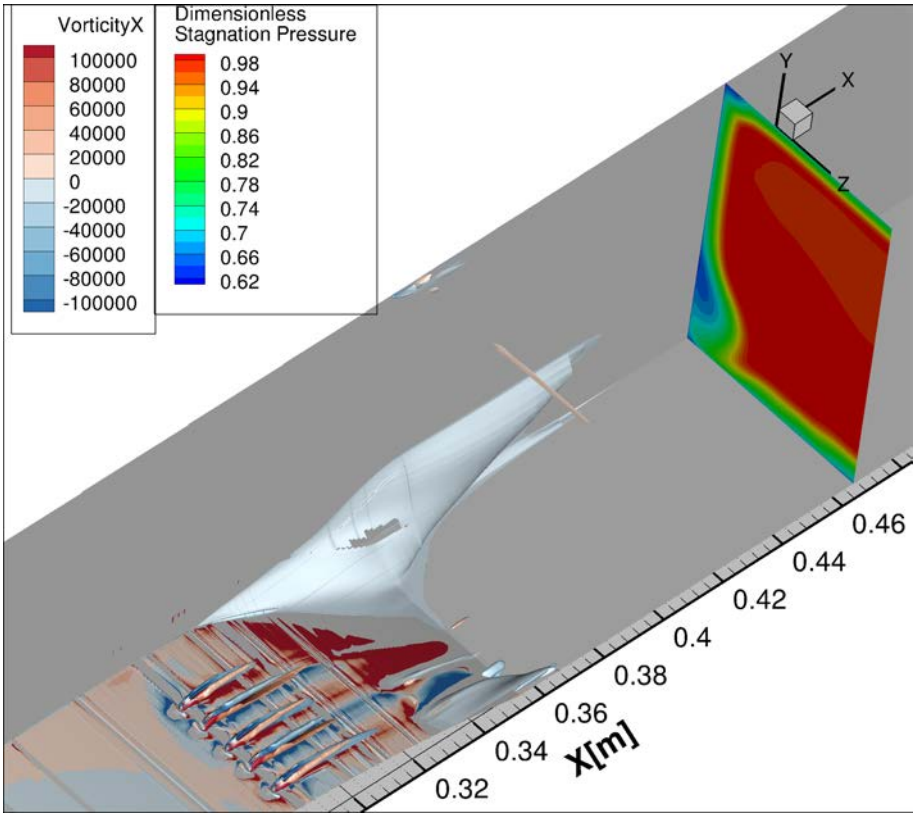

Figure IV.19: Non dimensionalized stagnation pressure on the DC50 plane, volume of the reverse flow-white surface- and Q criterion equal to $3 \cdot 10^8$ isosurface colorized with longitudinal vorticity for the sub-optimum-Case 12.

Table IV.4: Parameters' range of the external jet for the second optimization.

Parameter	Min	Max
X position (mm)	260	320
Z position (mm)	38	57.5
Pitch angle α (°)	30	150
Skew angle β (°)	0	180

the first optimum of the expected improvement and a new model is computed before a second research of the maximum expected improvement. The same technique is used for the third point. Once the three points have been calculated, their real values are added to the model of the previous step before it is tuned again.

The algorithm enriches the model reaching a total of 122 points. After a first period of exploration, the algorithm finds a zone of interest in which it keeps enriching without attempting a new phase of exploration elsewhere in the domain.

3.b Results

Overall, the model calculated is almost constant with a value of $DC50$ close to the one of the sub optimum case e) (0.78) meaning that the external jet does not improve the control.

The whole model is presented in Appendix A.3. Nonetheless, this is not true on the whole domain as the algorithm manages to find a zone of interest which is presented on a 2 dimension map which shows the dependence of the $DC50$ with respect to the longitudinal and lateral positions, α and β being respectively fixed to 30° and 106° in Fig. IV.20. In this small zone close to the lateral wall, the jet induces an important improvement of the $DC50$. The longitudinal position is less sensitive than the lateral one demonstrating that the control efficiency relies on the position of the vortex with respect to the sidewall much more than to its intensity.

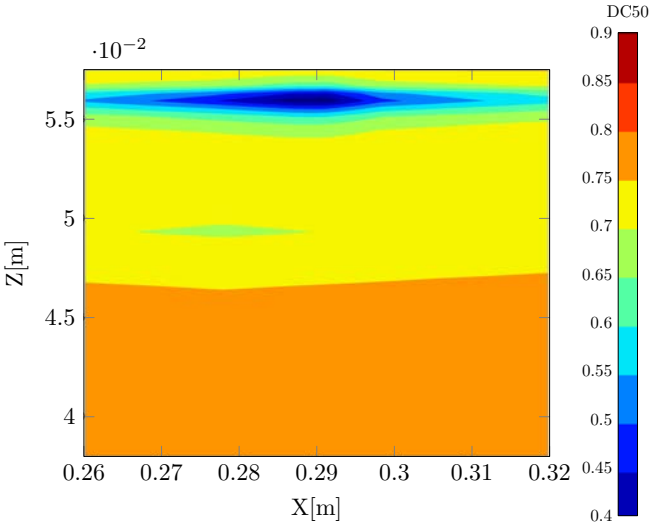

Figure IV.20: Zone of interest of the second DC50 model.

The best controlled case found is for $\alpha = 30°$ and $\beta = 106°$, the objective function falls down to 0.34 which represents an improvement of 61% of the $DC50$ with respect to the baseline case. It generates the total pressure distribution presented in Fig. IV.21 and the reverse flow visible in Fig. IV.22.

ø

ø

The corner flow separation is no longer present and is replaced by two smaller separation zones along each side of the corner as visible on Fig. IV.22. These separation zones have smaller impact on the total pressure downstream than the corner flow separation of the reference case. The description of the corner flow vortex is presented in Fig. IV.23 on transverse planes at $x = 295 - 305 - 315 - 325$ and 335 mm i.e. from the vortex formation to the beginning of the lateral separation which replaces the corner flow separation. The impact of the mixing due to the pair of co-rotating vortices is visible on the longitudinal momentum field in Fig. IV.24 and can be compared to the uncontrolled case provided in Fig. IV.25. In the uncontrolled case, the separation begins between $x = 305$ and $x = 315$ mm and is clearly interacting with both the lower and lateral walls, while in the optimal controlled case, the separation occurs between $x = 325$ and $x = 335$ mm and is reduced to a separation on the lateral wall. By being able to stick to the corner, the vortex manages to reinject energy into the boundary-layer of the corner flow and thus to prevent the separation. This result is similar to the ones found experimentally in Xiang and Babinsky [178].

Nevertheless, as it can be seen in Fig. IV.21, compared to Fig. IV.17b(case of the first

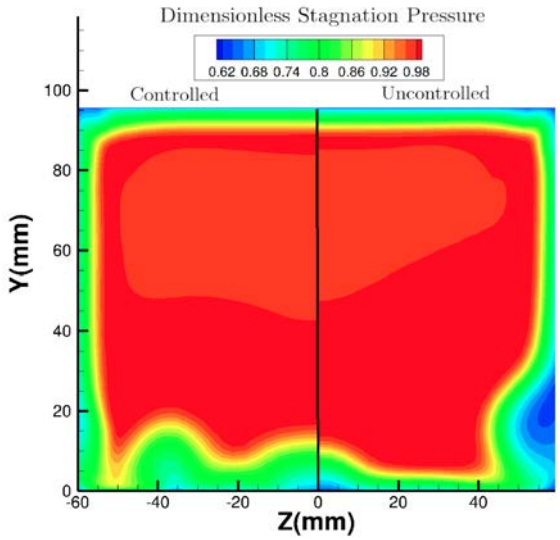

Figure IV.21: Non dimensionalized stagnation pressure on the transverse DC50 plane of the best controlled case of the second optimization-left- and uncontrolled case-right-.

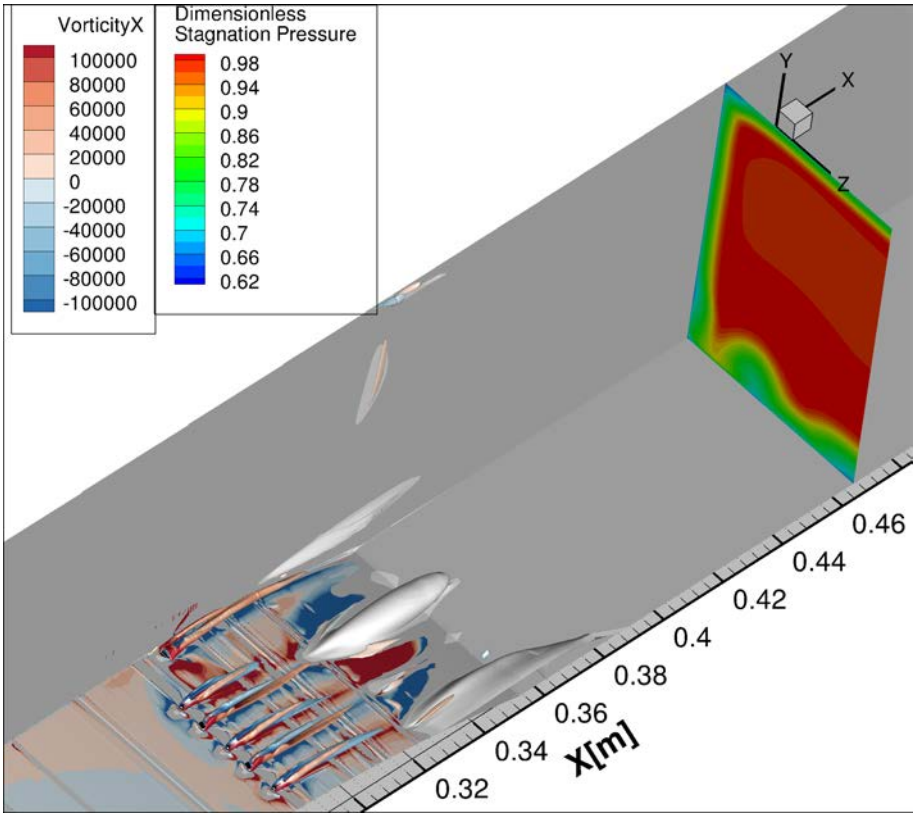

Figure IV.22: Non dimensionalized stagnation pressure on the DC50 plane, volume of the reverse flow-white surface- and Q criterion equal to $3 \cdot 10^8$ isosurface colorized with longitudinal vorticity for the optimum.

optimization corresponding to the second optimization without corner flow control) the improvement of the control on the corner flow separation deteriorates the control of the central separation. The same effect is visible on the 3D views of the separation for the optimum case in Fig. IV.22 compared to the corresponding case of the first optimization without corner control in Fig. IV.19. More generally, this confirms the interest of controlling both the boundary-layer and the corner flow separation as a global phenomenon as done in Titchener and Babinsky [166].

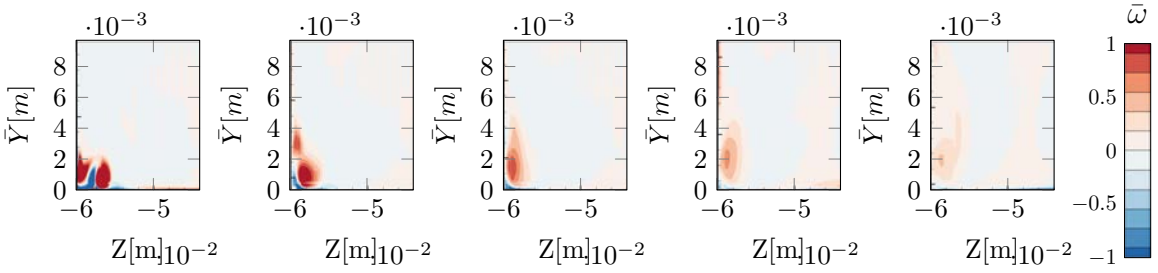

Figure IV.23: Longitudinal vorticity on five transverse planes close to the corner, along the flow at x equal 295, 305, 315, 325 and 335 mm from left to right for the optimum case of the second optimization.

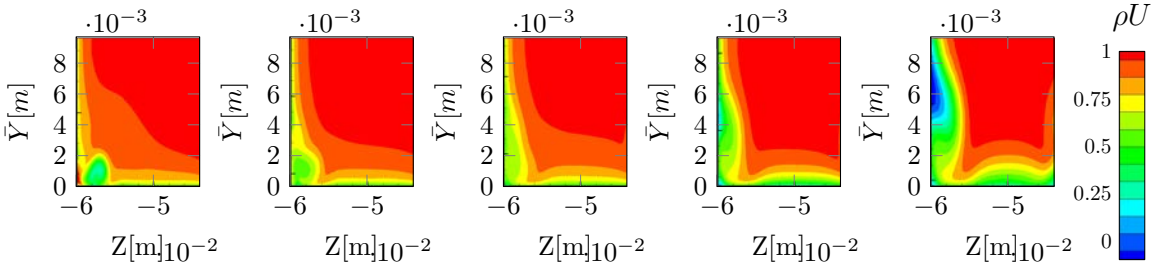

Figure IV.24: Longitudinal momentum on five transverse planes close to the corner, along the flow at x equal 295, 305, 315, 325 and 335 mm from left to right for the optimum case of the second optimization.

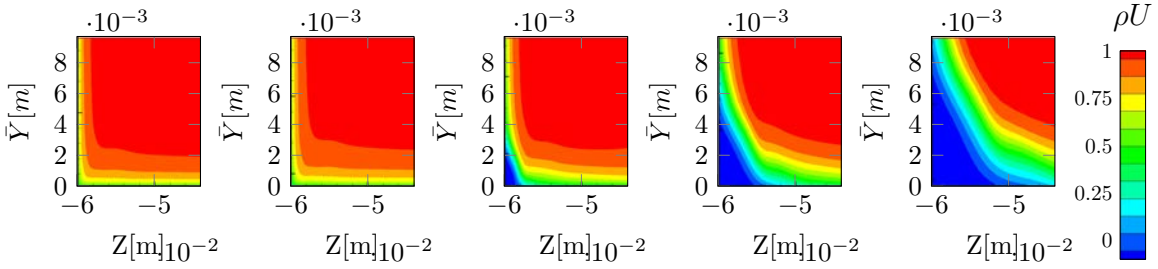

Figure IV.25: Longitudinal momentum on five transverse planes close to the corner, along the flow at x equal 295, 305, 315, 325 and 335 mm from left to right for the uncontrolled case.

IV.4 Furthers Analysis on the Vorticity Patterns Generated by Downstream and Upstream Blowing VGs

In order to further analyze the fact that the upstream blowing jets seem to generate a more effective control of the interaction, the data of the cases calculated during the first optimization in section IV.2 are used to design three models characterizing the physical properties of the vortices produced by a pitched and skewed jet: the absolute value of the streamwise vorticity ω and the vertical Y_B and lateral Z_B position of the barycentre of $||\omega||$.

Considering only one of the ten jets, the absolute value of the streamwise vorticity ω and the vertical Y_B and lateral Z_B position of the barycentre of $||\omega||$ are calculated on a plane placed at $x = 290\,\text{mm}$. This plane is positioned four δ_j $2.5\,\text{mm}$ after the jets -δ_j = being the boundary-layer physical thickness at the jets position-. This position has been chosen to be able to see the completely developed vortical structures and to stay in the region where the jet induced vortices are not yet interacting with the other vortices produced by the adjacent jet.

In order to increase the concentration of the calculated points in the models, the construction of the models takes advantage of the fact that for a single jet considered here, the absolute value of longitudinal vorticity and the vertical barycentre are even with both variables considering the point of coordinates $(90, 90)$ as the origin. This means that for any couple of angles (a, b):

$$||\omega(a,b)|| = ||\omega(90-(a-90), 90-(b-90))|| \tag{IV.30}$$

$$Y_B(a,b) = Y_B(90-(a-90), 90-(b-90)) \tag{IV.31}$$

Furthermore due to the same symmetrical reasons, the lateral position of the barycentre is odd with respect to the same origin meaning

$$Z_B(a,b) = -Z_B(90-(a-90), 90-(b-90)) \tag{IV.32}$$

This allows to construct the models only on the range $\alpha = 30 - 90°$ and $\beta = 0. - 180°$. The models constructed using the same regression Kriging method as in section IV.2 are presented in Fig. IV.26. The visualisation of the vorticity distribution for all the cases presented previously in Fig. IV.15 are added on the model of $||\omega||$.

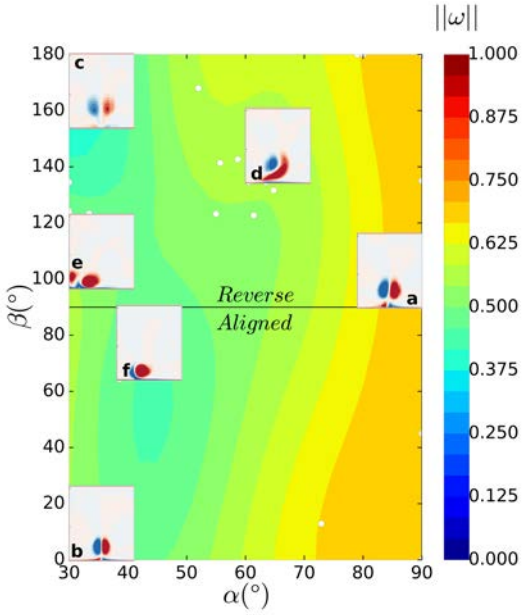

(a) Absolute value of Vorticity with the representation of the vorticity map corresponding (colormap of vorticity is the same as in Fig. IV.16).

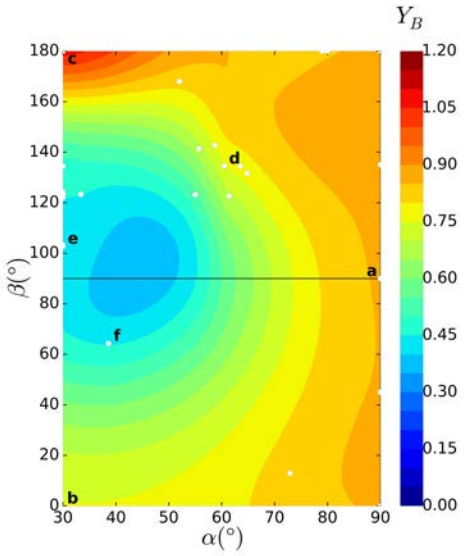

(b) Vertical position of the barycentre of absolute vorticity non dimensionalized using δ_j.

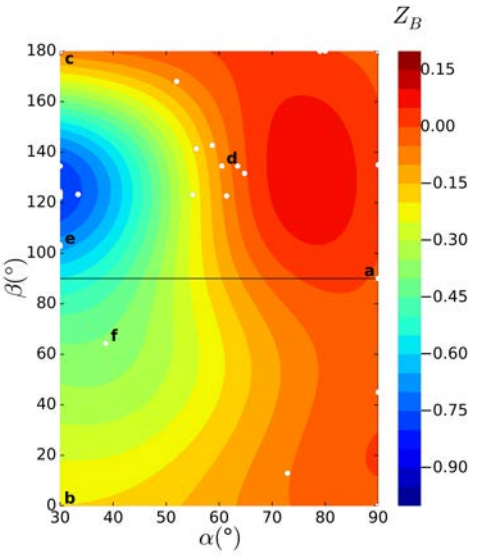

(c) Lateral position of the barycentre of absolute vorticity non dimensionalized using δ_j.

Figure IV.26: Models of functions calculated on a plane at x=290 mm for one VG, the letters correspond to the cases presented in Fig. IV.15.

The first observation is that there are different configurations of vortices. On the axis $\alpha = 90°$ the vertical configuration (a) is visible with the strong counter-rotating pair of vortices. This configuration is also visible in Fig. IV.11 and is really close to the flow topology presented by [100, 95, 121].

The second observation is about the two axes $\beta = 0°$ and $\beta = 180°$ where the jet is parallel with the flow. The structure of the vortices is the same along these axes as for the

vertical case with two counter-rotating vortices with similar shapes and intensities. For the jet blowing downstream (i.e. $\beta = 0°$) when α diminishes $||\omega||$ diminishes too and the barycentre is descending from a little above the boundary-layer to a quarter below. On the contrary for the upstream blowing jet (i.e. $\beta = 180°$), when α diminishes the barycentre is moving away from the boundary-layer up to $1.1\delta_j$ with $||\omega||$ also diminishing. This is coherent with the fact that the upstream blowing jet is turned downward during the mixing of the jet. What is important to notice here is that the vortices produced by this type of interaction (case (c)) are more spread out than in the downstream blowing case, this propriety is known and is used as a mean of enhancing mixing for scramjet development as reported by Han et al. [88].

If we now consider an axis for β =90° we confirm a result seen by Beresh et al. [13] among others, that the the total amount of streamwise vorticity diminishes with decreasing pitch angle. The structure of vorticity produced by a jet with a skew angle of 90°, transitions along its variation of pitch angle, as noticed by Feng et al. [63] from a pair of counter-rotating vortices to a strongly unbalanced pair of vortices as it is visible on case (f). The weaker vortex vanished more rapidly in the flow and thus farther downstream the vorticity patterns is reduced to a strong solitary vortex.

On the Fig. IV.26b, it can be observed that the vortices tend to be located at the height of the boundary-layer which reinforce the idea of a mixing between the boundary-layer and the fluid above it.

Another interesting point is that the vortical structure developed by an upstream blowing jet of the same sweep angle does not follow the exact same topology variation as for the downstream blowing jet. There is a transition from the case (f) to the case (d) which pass by the case (e). This specific case generates a lower vorticity but since it forms a pair of same sign vortices, this generates a strong lateral displacement as it can be seen in Fig. IV.26c. This allows the structure to have a smoother mixing on a wider extend.

Using these models, the mechanism which makes the optimum control of the first optimization can be explained as follows: this couple of angles $(\alpha, \beta) = (30, 102.8)$ generates for each jet a pair of same sign longitudinal vortices as it can be seen in Fig. IV.27a. This pair of vortices is going to generate a lateral velocity. Looking at the development of the vortices farther downstream in Fig. IV.27b, in the case of the central jets, the two vortices are going to merge when they meet the adjacent opposite vortices and form a new pair of opposite vortices that are going to sustain each other in the downstream flow direction. For the external jet, the pair of vortices is going to move closer to the wall and provokes a mixing which induces a zone of boundary-layer with a deficit of longitudinal momentum between the two vortices. This weaker zone is more sensitive to the adverse pressure gradient due to the shock and separates earlier than the corner flow separation. This modifies the shape of the corner flow separation and this new shape has a less significant impact on the stagnation pressure farther downstream.

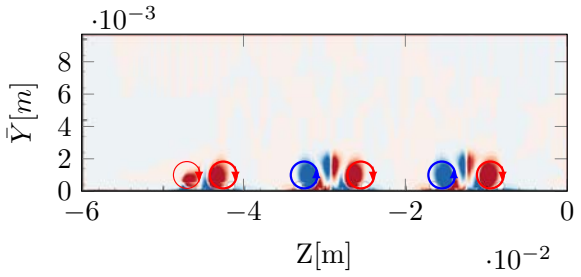

(a) Longitudinal vorticity at x=290mm-optimum case of the first optimization.

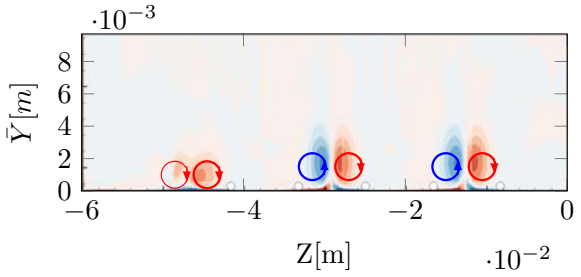

(b) Longitudinal vorticity at x=310mm-optimum case of the first optimization.

Figure IV.27: Longitudinal vorticity on two transverse planes along the flow, the white dots represent the lateral position of the jets.

IV.5 Conclusion

The optimization process based on RANS computations and Kriging meta-model turns out to be an effective process which manages to identify the optimal pitch and skew angles of ten fluidic VGs to control the Shock-Wave / Boundary-Layer Interaction. This fluidic control configuration with pitch angles equal to 30° and skew angles equal to ± 102.8°, i.e. slightly upstream blowing jets, has not been studied yet at the authors knowledge. This configuration makes the objective function, the $DC50$ criterion falling down by 22%.

In order to improve this first result, a second optimization has been implemented. This optimization focuses on the control of the corner flow separation by adding an external jet to a sub-optimal configuration of the first optimization. This added VG is optimized not only in pitch and skew angles but also in lateral and longitudinal positions. The algorithm detects a zone of interest in which the $DC50$ criterion is reduced by 61%. This configuration only requires a momentum coefficient c_μ of 0.03% which makes it an efficient control. The external jet added in the optimal configuration is again slightly blowing upstream with a pitch angle of 30° and a skew angle of 106°. This optimal control of the corner flow separation is possible in a thin lateral zone close to the lateral wall with a wider range of variation in longitudinal position.

This study highlights the interest of having a global approach for the design of a control of Shock-Wave / Boundary-Layer Interaction because the massive central separation is linked to and influenced by the corner flow separation and vice versa. These central and corner flow separations are themselves linked to the intensity and the shape of the shock-wave. All this makes this interaction a complex multi-parameters 3D phenomenon.

This study demonstrates that upstream blowing jets can be efficient to control the

flow destabilized by a strong Shock-Wave / Boundary-Layer Interaction. Compared to jets blowing downstream, they generate different vorticity structures which have different vertical and lateral velocities. Their capability to generate a pair of co-rotating vortices close to the wall allows for a larger lateral displacement of the vortices and induces a wider mixing of the boundary-layer.

Following this numerical study, the best controlled configuration will be tested in the wind tunnel in order to validate its performance.

V

Conception of the control configurations

- *Pas mal, hein? Entièrement faite à la main.*
- *En quel métal?*
- *En airain. L'airain solide, rien de tel pour réussir une chose pareille.*

Gosciny, Des Astres pour Iznogoud

Objectives

The goal of this chapter is to detail the process of conception of the control set-up. This will be done using the results of the optimization presented in the previous chapter. The results of the experimental tests will be presented in the following one.

The first section details the preliminary tests realized to chose and characterize the fluidic actuators and their ability to excite the flow up to the characteristic frequency of the shock, 300 Hz. The second section exposes the technical details of the implementation of the actuators in the wind tunnel and the resulting limitations to the choice of the control configurations to be tested. Finally, the last section describes the process of choice of the two configurations of control and their interest.

Contents

V.1 Fluidic vortex generator actuator

Fluidic actuators have been selected on their capacity to deliver a clear square signal at the characteristic frequency of the shock-wave around 300 Hz (found experimentally by Sartor [151]). Few fluidic actuators available on the market are able to achieve such high frequencies. It remains a challenge, since at this frequency the time necessary to stop the jet start to be of the same order of magnitude as the duration of a period of the signal (3 ms). Current actuators consisted into a small metallic plate which is alternately attracted and released using electromagnetic magnets. The future development of piezoelectric actuators may enable to reach higher frequencies. Three different models have been tested, namely the SMC SX12-GH, the Festo MHJ9-MF and the Festo MHE2-MS1. Only the last one has proven its capacity to deliver a clear square signal at 300 Hz and will be discussed below.

A pressure supply of 2 bar has been chosen thanks to numerical simulations which confirmed the capacity of jets supplied with 2 bar to induce vortices of the size of the boundary-layer, see Chap. IV. This choice has also been supported by previous tests performed at ONERA on fluidic control of buffet phenomena (see Dandois et al. [44]). This pressure value will be used for all the following tests of actuators.

1.a Frequency characterization

The actuator has first been linked using a first tube of 2 mm diameter and 20 mm length, linked to a connector and a second tube of 4 mm diameter and 40 mm length to a small cavity. This cavity is perforated by a 1 mm diameter vertical hole representing the hole of one jet of the VGs' control. The set-up and the main lengths are presented on Fig. V.1. The tests consisted into a measurement of velocity at the opening using an hot wire velocimetry and were done at the ONERA laboratory in Lille (see Delva [54]).

The actuators are monitored by a Pulse Width Modulation signal. The frequency of the command signal governs the frequency of the actuator and the modulation of the Duty Cycle of the signal (ratio between time of the square signal being on with respect to the total period of the signal) governs the instant when the plate closing the actuator is relieved. It has been observed that at 300 Hz, with the default 50% Duty Cycle, the signal of velocity measured 1 mm away from the hole is almost constant. Therefore, a variation of Duty Cycle has been undertaken and the results are presented on Fig. V.2.

With a Duty Cycle of 25%, the actuator manages to stop the jet and delivers a signal close to a perfect square signal with 50% of the period open and the other 50% closed. The slight distortion of the square signal is due to the closing time which is longer than the opening time. With a Duty Cycle of 50%, the actuator fails to close and reaches a limit cycle after 2 periods with seemingly attempts to stop which do not reach the zero velocity. For a duty cycle of 75%, the velocity reaches a limit cycle after 3 periods which is close to a permanent jet. It should be noticed that the Barré de Saint Venant relation used to

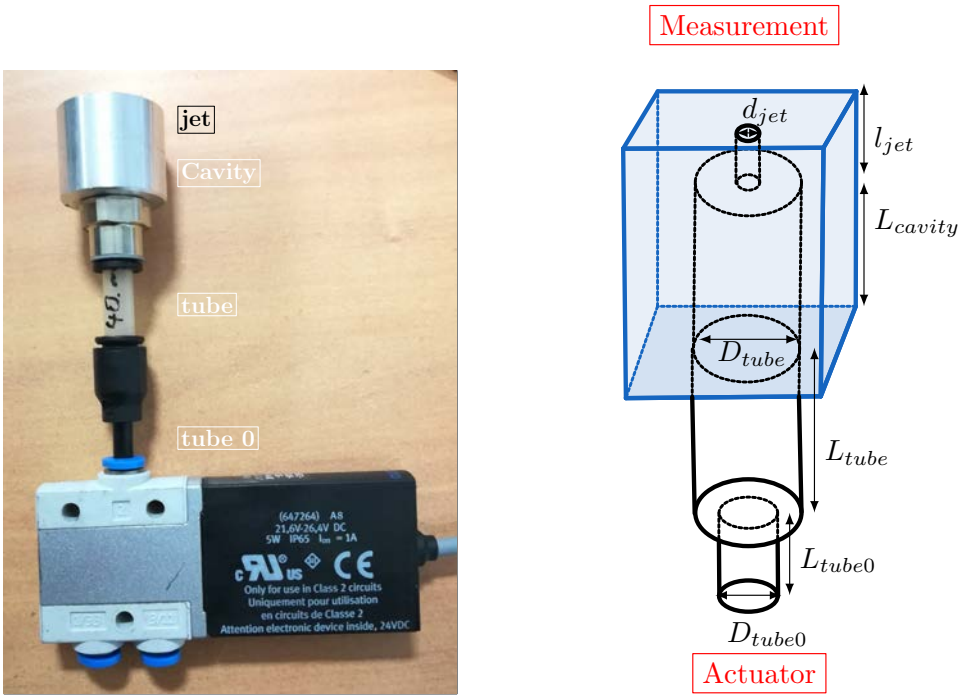

(a) Set-up used for the test of the MHE2 actuator.

(b) Definition of the characteristic lengths of the set-up.

Figure V.1: Definition of the set-up used for the preliminary tests of the MHE2 actuator.

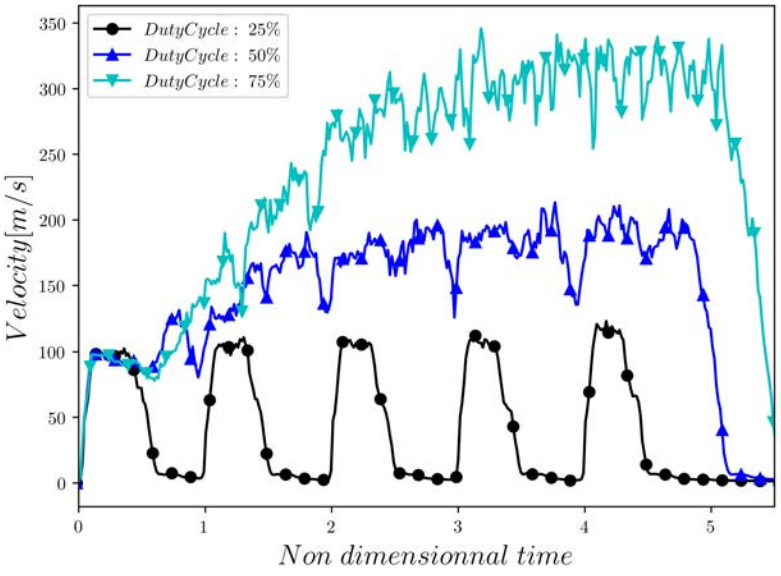

Figure V.2: Velocity measured for various of duty cycle at a frequency of 300 Hz on assembly.

calculate the velocity is not valid anymore at this higher velocity, close to Mach one, since a shock-wave occurs in front of the hot wire. Nevertheless, this maximum velocity is of no

interest for the following work.

This experiment has been settled also for lowest frequencies and has validated the use of a Duty Cycle of 50% for the frequencies lower than 200 Hz.

1.b Test of different tube lengths, close-up the influence of distance from the actuator to the ejection hole

In order to quantify the influence of the principal tube going from the actuator to the cavity on the shape of the signal, same measurements have been performed for three different length of tubes: 40 mm, 80 mm and 130 mm. This is done to know the range of length usable for the implementation of the actuators in the wind tunnel test section. The results are presented on Fig. V.3. For the two smallest lengths the shape of the signal is slightly modified. Nonetheless, the tube of length 130 mm provokes a rebound on the signal during the closing time, visible on Fig. V.3. This deformation may be due to a resonance phenomenon in the tube. Thus, the actuators need to be located close to the lower wall of the test section in order to achieve a clean signal in the wind tunnel.

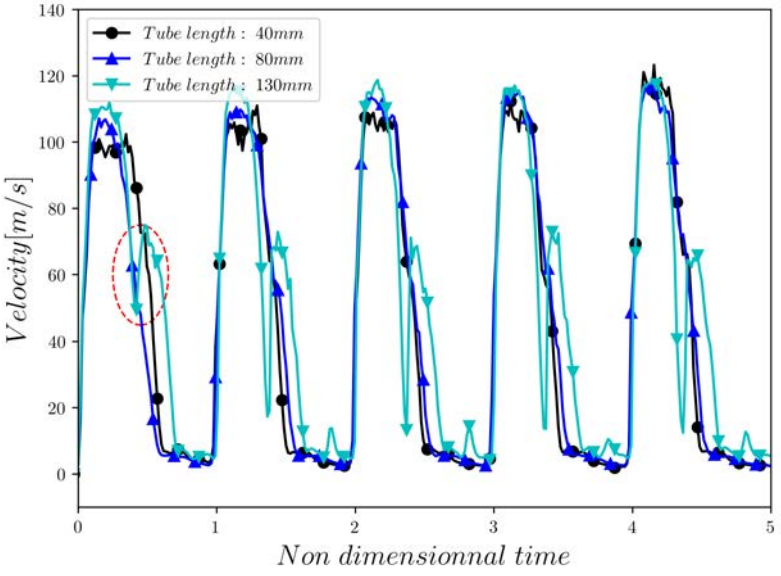

Figure V.3: Velocities measured for several tube lengths at a frequency of 300 Hz. The red ellipse highlights the rebound phenomenon observed with a tube of 130 mm.

1.c Theorical limit: Helmholtz resonance

In order to understand the limitation of the length of the tube, a modeling of the cavity as an Helmholtz resonator is undertaken (see Pamart [130] for a detailed explanation of the modeling). The idea of the Helmholtz resonator modeling is to consider the small volume of air comprised in the higher part of the set-up called jet which is presented on Fig. V.1. This volume is going to diminish the pressure of the cavity when leaving and therefore will be re-attracted into the cavity, increasing its pressure and being repulsed again. This phenomenon may impact the relaxation of the jet. Considering the air as a viscous fluid and using the first principle of dynamics applied to the volume of fluid, the

resonance frequency of this system f_r, is given by the equation V.1. The term $0.8d_{jet}$ is empirically added in the literature to take into account the viscosity effect.

$$f_r = \frac{c}{2\pi}\sqrt{\frac{S_0}{V_{tot}(l_{jet}+0.8d_{jet})}} \tag{V.1}$$

$$\text{with } V_{tot} = \frac{\pi D_{tube0}^2}{4}L_{tube0} + \frac{\pi D_{tube}^2}{4}L_{tube} + \frac{\pi D_{tube}^2}{4}L_{cavity} \tag{V.2}$$

This model gives a resonance frequency of respectively 970 Hz, 770 Hz and 630 Hz for the tubes of 40, 80 and 130 mm. The frequency of 630 Hz is close to the one of the rebound during the closing of the actuator and is close to the first harmonic of the excitation frequency of 300 Hz. This explains the default of the signal observed with the tube of 130 mm. The same phenomenon may appear for the length 40 mm but 970 Hz is close to the second harmonic which is far less energetic.

1.d Conclusion

An actuator able to excite the flow up to a frequency of 300 Hz with a clean square signal have been found and characterized. This actuator will be connected to the wind tunnel with a tube of length less than 80 mm. In order to prevent the Helmholtz resonance of the system to deteriorate the signal, the diameter of the tube will be of 2 mm all along preventing the use of the connector which may degrade the signal. A smaller diameter ensures a smaller V_{tot} and so a higher resonance frequency which prevents it to interfere with the jet signal. This study emphasizes the need to locate the actuators close to the jet in order to deliver an accurate signal. This will be a limiting parameter in the conception process of the set-up.

Furthermore, the actuator was tested in continuous flow and was able to generate a flow close to sonic velocity which is recommended to interact with a transonic transverse main flow. The velocity of the jet has not been precisely measured since the conditions of the static tests are different from the ones in the wind tunnel (transverse flow close to Mach 1 with a pressure close to 0.3 bar).

V.2 Test set-up conception

The conception process of the mechanical set-up of the control configurations is presented. The jets angles for the control configurations will be defined using the limiting parameters resulting from the mechanical conception.

2.a Physical implementation

The goal of the conception of this set-up is to design a flexible system allowing to easily modify the control configuration in the wind tunnel. Nevertheless, this system should be sufficiently resistant to endure the transonic environment and not to degrade the main flow. The main idea is to remove a strip of the lower wall of the test section which will be replaced with others strips perforated for the jets. These strips are screwed directly to the lower wall of the wind tunnel taking care of the sealing and the matching with the main part of the bump. The twelve actuators are then mounted on the strip and linked using tubes of 2 mm diameter to the twelves cavities corresponding to the twelves fluidic

actuators. The use of this set-up allows to put actuators closer to the lateral wall in order to control the corner flow. Nevertheless, due to the lateral joint and to the size of the cavity in which the tubes are sealed, the jets cannot be positioned closer than 5 mm away from the lateral wall. This differs from the limits imposed to the optimization process presented previously. The final strips are visible on Fig. V.7 in the conclusion of this chapter.

In order to ensure a constant and well distributed pressure to the actuators, a plenum chamber is added below the actuators. This tank consists into a large cavity, air supplied in the middle by a 6 mm diameter tube. This tube is linked to a manometer allowing to adjust the incoming pressure to 2 bar using the 7 bar general air circuit.

All the different components of the set-up are presented on Fig. V.4. The blueprints of the set-ups are presented in Appendix A.4.

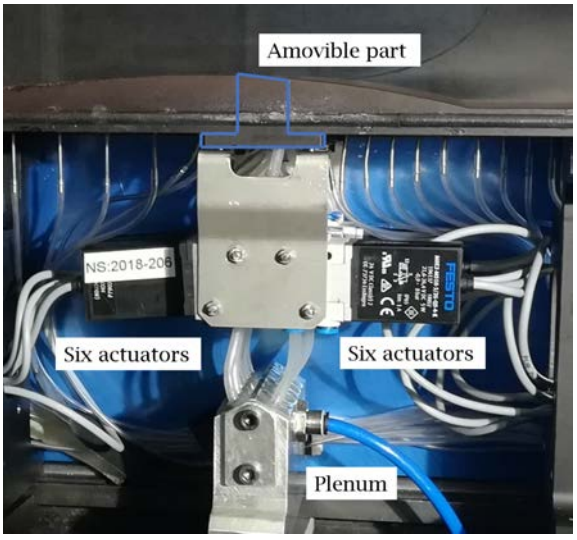

Figure V.4: Fluidic control devices mounted in the wind tunnel's test section (under the bump).

2.b Electronic implementation

The actuators are monitored using a special electric power supply of 24 V. Each actuator is linked to a command card which received a PWM signal generated by Xpert, an ONERA in house developed software. This signal is amplified by the card using the electric power supply. Indeed, the actuators require a strong peak of 4 A for the first period of the signal. This command allows to control the jets from continuous up to 300 Hz. The external jets have been linked to the same command card and can be driven independently from the central jets in order to quantify the interest of the corner flow separation control.

V.3 Choice of two control configurations

Once the actuators and the general mechanical implementation of the control are chosen, the control configuration has to be selected. This is done based on literature results and on the results of the optimization process presented in Chap. IV.

3.a Limitations due to the geometry of the wind tunnel

The optimization process has started before the choice of actuators and before the conception of the system of integration of the jets in the wind tunnel test section. Thus, some limiting parameters were not taken into account in the optimization process. The first parameter not taken into account was the fact that the central Kulite sensor was going to be removed and leave some space to the jets. As a reminder, this sensor was the reason for a bigger gap between jets in the center of the wind tunnel during the optimization process.

The second limiting parameter is the presence of a lateral joint. This lateral joint and the radius of a cavity in which a jet is pierced prevent to place the lateral jet closer than 5 mm away from the lateral wall. The result of the optimization has therefore to be adapted to these technical limitations.

3.b Adaptation of the results from optimization

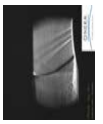

To begin with, it should be noticed that due to the time limitation of the thesis work, the second part of the optimization was not completed when the control configurations had to be chosen. Thus, the model of the $DC50$ (objective function see Chap IV section 2.b for the detail of this criterion) was not the same as the final one. The final model is presented in Appendix A.3 with a zoom on the zone of interest of the model. What is interesting to notice is that the control seems to be sensitive to the lateral positioning of the jet controlling the corner separation. Even if the longitudinal position(x) allows a wide range for the optimal control, from 260 to 310 mm, 50 mm wide, the range of lateral position(z) is very fine, about 3 mm from 56 to 59 mm. Unfortunately, this range is not achievable for the chosen set-up of control. Some adjustments on the joint along the side of the bump need to be done in future work in order to be able to test this control configuration.

In order to take into account the possibility of changing the distribution of the actuators along the span of the wind tunnel, a new distribution called "Corrected" is defined. This differs from the one used for optimization called "Optimization". The details of these two distributions are presented in Table V.1. In both configurations, the lateral jet is positioned as close as possible to the lateral wall, meaning at $z = 55$ mm, the side wall being at $z = 60$ mm. The others jets are positioned with a constant interval of 11 mm in the "Corrected" distribution and with a constant interval of 8.3 mm except for the central interval which is doubled, equal to 16.6 mm for the "Optimization" distribution. The "Corrected" distribution was supposed to allow for a more effective control.

Table V.1: Lateral distribution of jets used in the conception process (only the positive half of the wind tunnel is presented).

Distibution	Jet 1	Jet 2	Jet 3	Jet 4	Jet 5	Jet 6
Optimization z[mm]	8.3	16.6	25	33.3	41.6	55
Corrected z[mm]	5.5	16.5	27.5	38.5	49.5	55

The parameters of the five cases tested in this study for the adaptation of the result of the optimization to the experimental environment, are showed in Table V.2 with the resulting $DC50$ criterion.

The two first cases tested were defined using the Corrected distribution. The first one corresponds to a control close to the ones observed in some of the studies in the literature, with pitch and skew angles equal respectively to 30° and 60° with one jet placed close to

the wall to control the corner flow separation. The second one is close to the optimal case found by the second optimization, the central jets follows the angle found in the first optimization and the lateral one has a pitch angle equal to 60° and a skew angle of 115°. These two controls give the same $DC50$ equal to 0.69, bigger than the optimal case of the second optimization. By "re-distributing" the jets along the span, it changes the global control of the flow. The distribution along the span strongly influences the control. It can generate an improvement of the central separation which causes a degradation of the corner flow control and vice versa.

In order to improve the control deriving from the optimization process, two new configurations were tested with a lateral distribution corresponding to the optimization. These two configurations are chosen close to the optimal control of the model. The two configurations slightly improve the control with a $DC50$ equal to 0.63. Due to time limitation, the case with pitch and skew angles of the lateral jet equal to 50° and 105° is chosen for the tests. This configuration is also tested with a "Corrected" distribution which gives a $DC50$ equal to 0.70, confirming the interest of keeping the "Optimization" distribution.

Thus, the two configurations chosen for the experimental tests are the number 3 called "Control 1" which is close to the best case of the optimization process taking into account the physical limitations and the number 1 called "Control 2" which is close to a more classical control.

Table V.2: Characteristics of the cases tested for the choice of control configurations tested experimentally.

Num.	Name	Distribution	$\alpha_{center}[^\circ]$	$\beta_{center}[^\circ]$	$\alpha_{corner}[^\circ]$	$\beta_{corner}[^\circ]$	$DC50$
1	Control 2	Corrected	30	±60	30	±60	0.69
2	-	Corrected	60	±135	50	±115	0.69
3	Control 1	Optimization	60	±135	50	±105	0.63
4	-	Optimization	60	±135	30	±100	0.63
5	-	Corrected	60	±135	50	±105	0.70

3.c RANS results of the tested control configurations

The two tested control configurations, Control 1 and Control 2 are presented on Fig. V.5. The first control used jets slightly reverse and will allow to test a result of the optimization process. The second one is closer to more classical control configurations with jets along the main flow direction. It will allow to compare to fluidic and mechanical literature cases.

The non dimensionalized stagnation pressure far downstream of the interaction, on the plane $x = 468\,\text{mm}$, resulting from the RANS calculations of the reference case and the two control configurations are presented on Fig. V.6. Both Control 1 and Control 2 do not completely erase the corner flow separation, contrary to the optimum of the second optimization, even if they diminish it. This is due to the lateral limitation to the jet's location. Nevertheless, the corner flow separation impact is reduced compared to the reference case.

Moreover, a central separation remains for both controls, even for the Control 2 which has a smaller gap at its center distribution. This is coherent with the goal of this study, the decreasing of the $DC50$ criterion, an homogeneity criterion, being strongly linked to the size of the most important separation, the corner flow separation. Furthermore, both

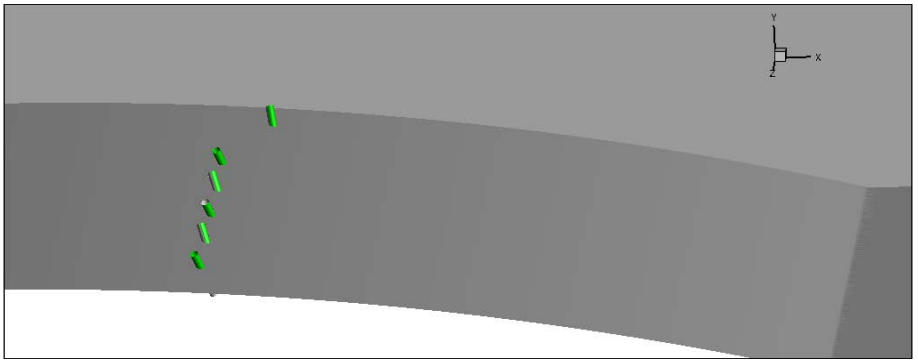

(a) Control 1

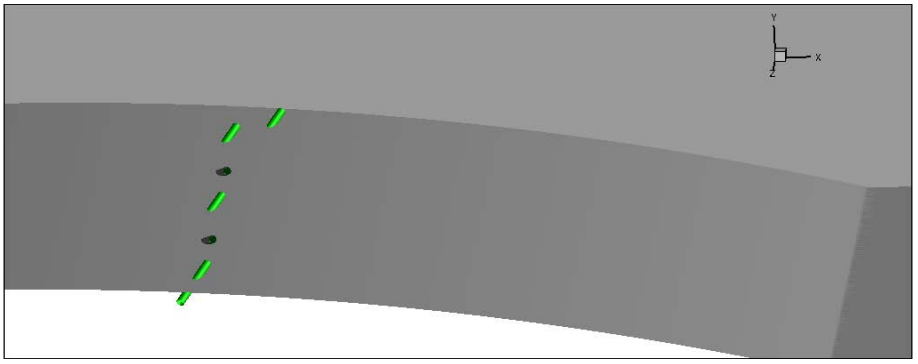

(b) Control 2

Figure V.5: Physical positions and angles of the jets of the two control configurations chosen for the experimental tests (only half of the wind tunnel presented).

controls thicken the boundary-layer outside of the separation zones. This is a logical consequence of the mixing between the main flow and the boundary-layer by the vortices.

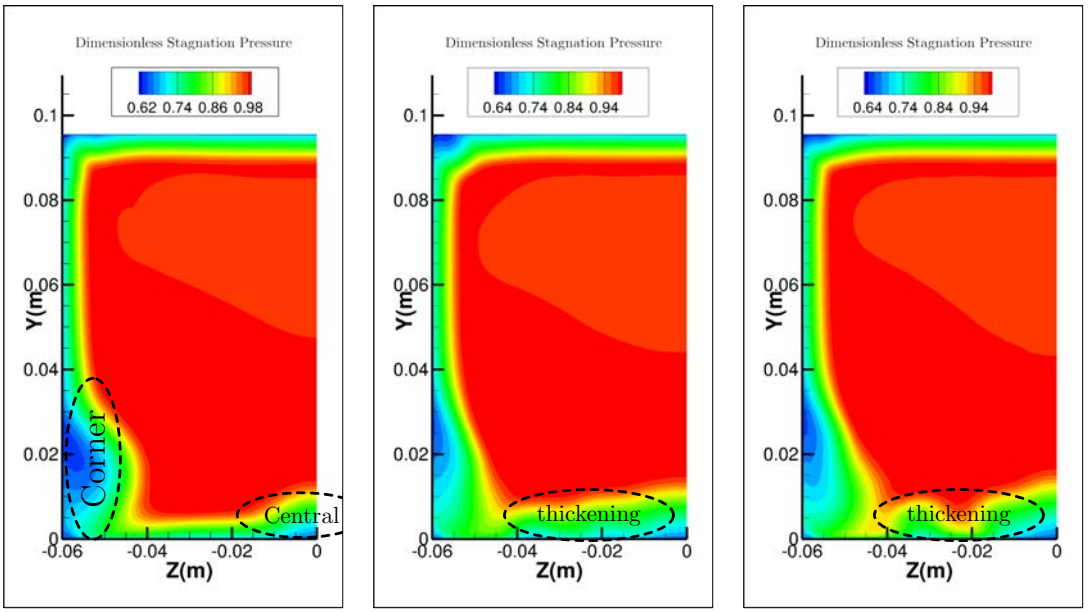

(a) Reference cas (b) Control 1 (c) Control 2

Figure V.6: Dimensionless stagnation pressure far downstream of the interaction on the plane $x = 468\,\text{mm}$, from RANS calculations for the three cases tested experimentally.

V.4 Conclusion

The process of development of experimental control configurations has been presented. The first part is the choice and qualification of actuators able to achieve fluidic control at the characteristic frequency of the shock-wave(300 Hz). Once the actuators are chosen, their characteristics give the main physical limitations to the integration of the actuators in the wind tunnel test section. Notably, the removal of the central sensor originally placed between the jets and the minimum gap of 5 mm with the lateral wall are the main constraints. A set-up with removable strips is then conceived in order to easily and efficiently change the control configuration. The three strips used for the tests are presented on Fig. V.7.

Two control configurations are chosen following results provided by RANS calculation. This numerical work highlights the difficulty to conceive a strongly effective control with fluidic jets (VGs). In order to take full advantage of the optimization process, due to the extreme sensitivity of this control set-up, all the limiting physical parameters should be taken into account in the optimization process. The time limitation of the thesis work did not permit to make a perfect use of the optimization process in the conception of the control set-up. Nevertheless, the two configurations chosen for the tests will give information on the accuracy of the RANS results and the efficiency of the two control methods, the one resulting from an adaptation of the optimization called "Control 1" and the other one closer to classical control called "Control 2". Both control configurations will be compared to fluidic and mechanical controls from the literature.

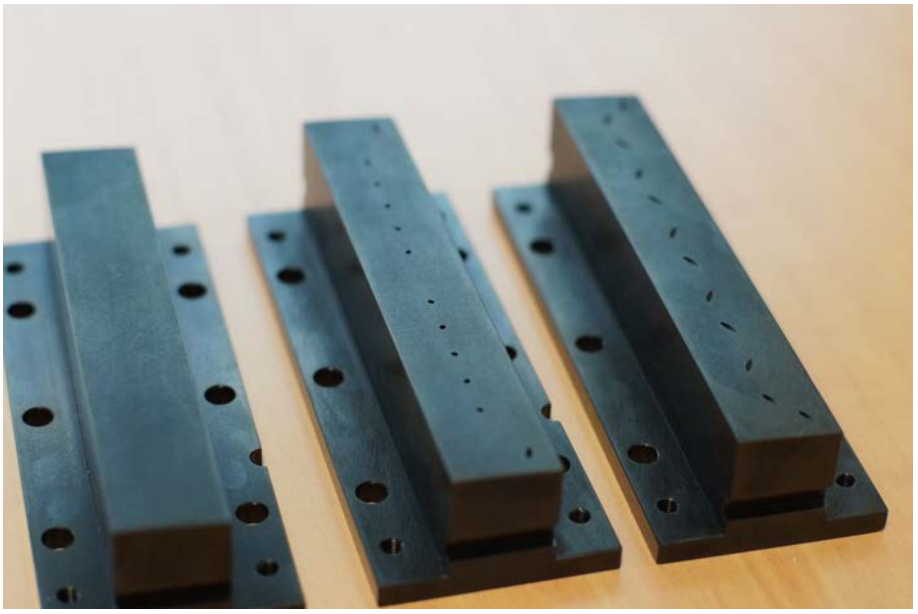

Figure V.7: Three removable parts of the control devices designed for the tests, from left to right: without control, Control 1 and Control 2.

VI

Characterization of the reference case

- *Rater son avion, ce n'est pas si grave que ça.*
- *Sauf*
- *Quand on est l'ingénieur qui l'a conçu.*

Geluck, Le chat

Objectives

The results of the tests are displayed in this chapter, the reference case is characterized and compared to numerical results from RANS and ZDES modeling.

The tomographic PIV method is then validated with respect to previous 2D PIV and LDV studies.

The lateral variations of the central separation are then investigated.

The dynamical aspects of the SWBLI is finally presented and compared to the ZDES modeling.

Contents

VI.1 Reference case characterization

1.a General aspect of the separation zones

In order to have in mind the general aspect of the 3D Shock-Wave / Boundary-Layer Interaction, the separation zones calculated using RANS model (see Chap. III) and ZDES model (see Chap. II), are presented on Fig. VI.1 and Fig. VI.2 respectively for half of the wind tunnel. The current experimental study is focused on the central separation appearing on the lower wall of the wind tunnel and on the corner flow separation which takes place between the lower and the lateral wall. The other separations are smaller.

The first thing to notice is that the separation zones have really different shapes in the two numerical modelings. In the RANS modeling, the central separation, visible on the right side of the half wind tunnel is of restricted width and important height whereas in the ZDES modeling the central separation is more spread in the lateral direction. As the size of the central separation influences the other parts of the flow by modifying the shape of the shock-wave, the size of the corner flow separation is linked to the one of the central separation. Thus, the corner flow separation is far bigger in the RANS modeling than in the ZDES modeling.

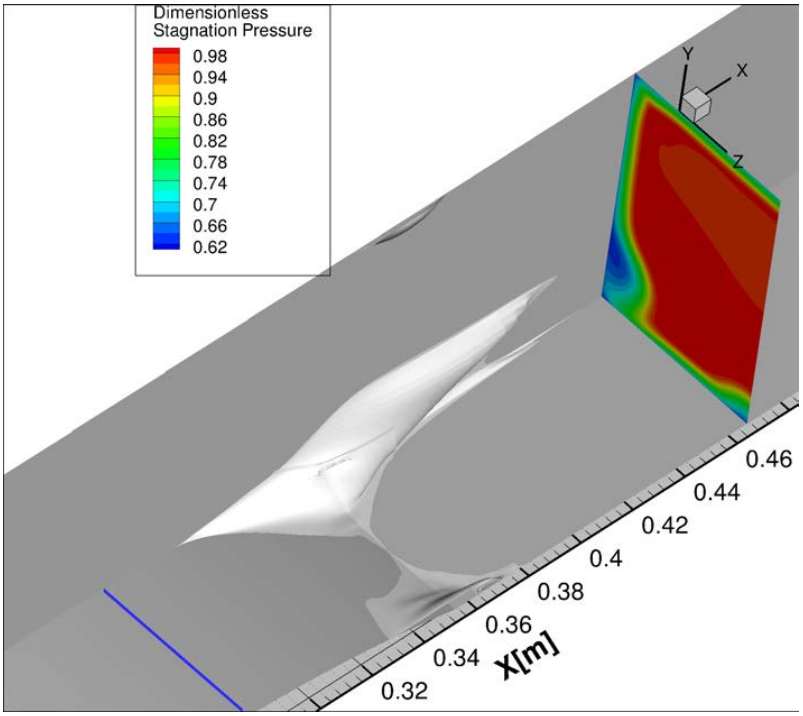

Figure VI.1: Non dimensionalized stagnation pressure on the DC50 plane, volume of the reverse flow-white surface- for the uncontrolled case RANS.

In order to visualize the impact of these separation zones on the downstream flow, visualizations of the stagnation pressure non dimensionalized (using the reference stagnation pressure equal to 96 000 Pa) on the plane x =468 mm are also presented on Fig. VI.1 and Fig. VI.2. The usual pressure loss through the normal shock-wave at Mach 1.4 is of 5% and is visible in the central orangey-red region. Losses are smaller in the regions where the flow pass through the oblique shock-waves and bigger in the regions impacted by the

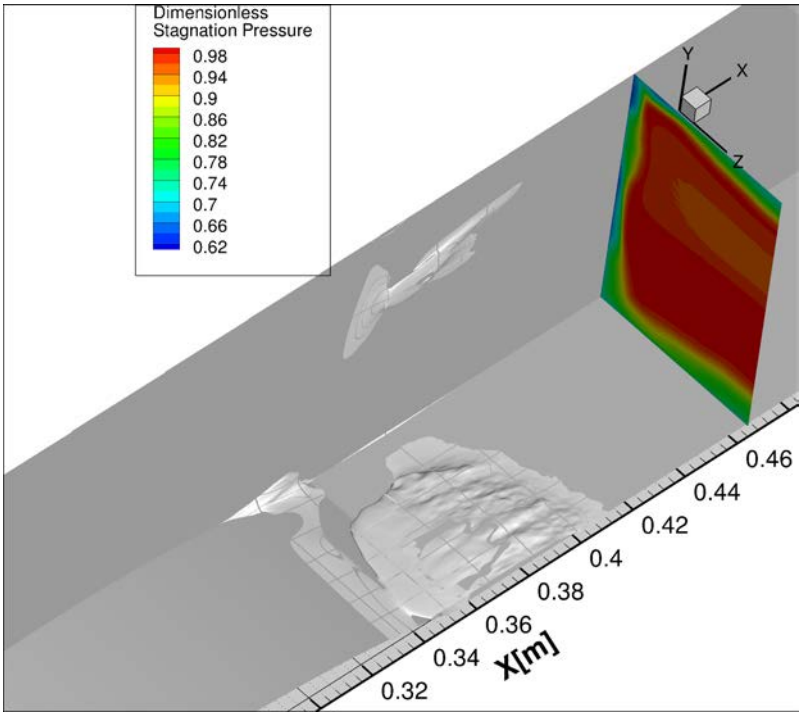

Figure VI.2: Non dimensionalized stagnation pressure on the DC50 plane, volume of the reverse flow-white surface- for the uncontrolled case ZDES.

boundary-layer and the separated zones.

In the ZDES calculation, the impact of separated zones on the downstream pressure is more limited than the one in the RANS calculation. This is due to the fact that the amplitude in height of the corner and central separation zones are smaller in ZDES and so their losses are more quickly and efficiently mitigated in the flow. It can be noticed that the central separation is divided in two parts in the ZDES modeling but not on the entire wind tunnel spanwise extent. The smaller size of the corner separation zone is linked to a lateral separation visible on th lateral wall higher and more downstream than the two main separations, the central one and the corner one. It should be noticed that separation zones on the upper wall have been blanked in the ZDES modeling in order to visualize the flow. Nevertheless, they exist and their impact is visible far downstream on the stagnation pressure plane.

1.b Schlieren visualizations

A visualization of the vertical density gradient of the uncontrolled Shock-Wave / Boundary-Layer Interaction is presented on Fig. VI.3 for the experiment and the ZDES model. For the ZDES, 11 planes regularly disposed in the width of the wind tunnel are used to calculated the mean of vertical density gradient along the width of the wind tunnel. The λ shock structure is clearly visible as well as the development of turbulent structures due the Kelvin-Helmholtz instability in the mixing layer above the separation zone.

The boundary-layers on the lower and upper walls present opposite colors, the lighter one and darker one correspond respectively to positive and negative vertical density gradient. The shock-wave is mainly dark as it corresponds to an abrupt increase of pressure

along a diagonal feature, thus presenting a positive density gradient. The upper part of the shock-wave is lighter as the first leg of the small λ shock-wave on the upper wall is oriented on the opposite diagonal as the one of the λ shock-wave on the lower wall.

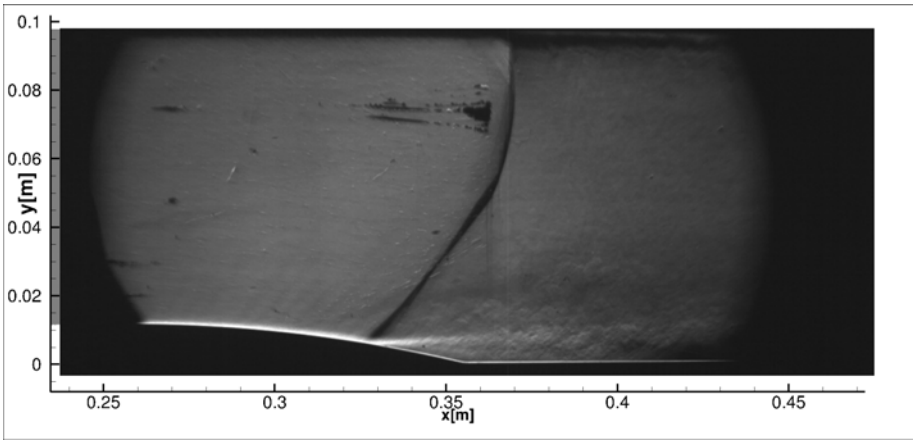

(a) Schlieren visualization in the S8Ch test section.

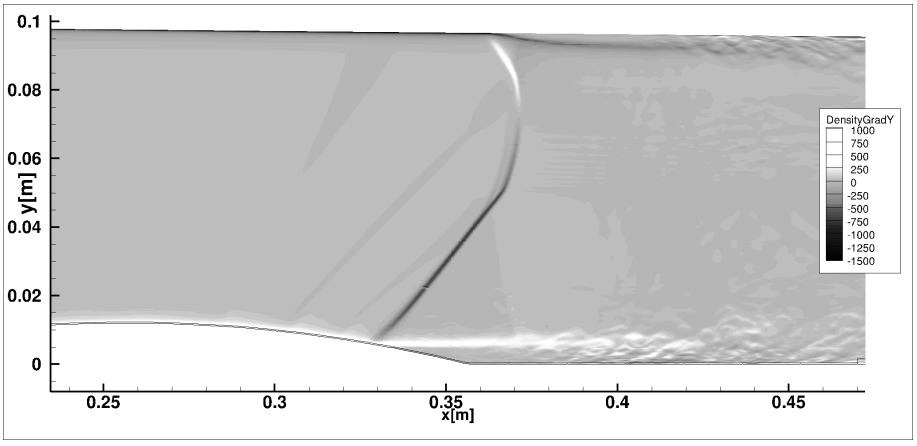

(b) ZDES numerical Schlieren.

Figure VI.3: Vertical density gradient of the SWBLI interaction obtained with Schlieren visualization.

Due to the fact that the light goes through the whole width of the channel, the resulting picture is the integration of the 3D field of density gradient. The fact the λ shock-wave undergoes a lateral curvature is noticeable thanks to the wide thickness of the shock-wave at the feet at the upstream leg of the λ shock structure. More variations of the shock-wave shape can be visualized in Appendix A.5.

The black horizontal lines upstream of the shock-wave on the experimental data denoted the presence of scratches on the windows of the wind tunnel, this has to be noticed as it will be detrimental to the following tomographic PIV measurements.

The instantaneous position of the clearly visible λ shock-wave is well predicted by the ZDES. The shape only differs a bit at the top of the wind tunnel, the upper λ shock is more marked in the ZDES calculation. This may be a clue for an overestimated separation zone. Nevertheless, the fact that this is only an instantaneous visualization does not invalidate the modelization and a study of the mean flow will give more pieces of information.

Turbulence development In order to highlight the development of large turbulent structures, iso-surfaces of the instantaneous Q criterion colorized with Mach number have been plotted on Fig. VI.4. First of all, the large turbulent structures are well positioned at the level of the SWBLI, they develop on the four walls of the wind tunnel along the λ shock-wave. Hairpin structures are then transformed into elongated structures visible at the end of the wind tunnel, due to the acceleration around the second throat. The two black squares on Fig. VI.4 are zones which are reproduced zoomed on Fig. VI.5. On the first one, the central separation is presented. It can be seen that this separation is linked to the development of transverse structures characteristic of the Kelvin Helmholtz instability which then turn into hairpin structures. On the second sub-figure, the corner flow separation is presented. The hairpin structures appearing first on the lower wall seems to be then deported on the lateral wall. This may explain the position of the two vortices observed in the RANS calculation. The back flow corresponds to the center of the hairpin developed here. The hairpins are moved away due to the development of the central separation. All this confirms the strong correlation between the two separation zones. It can be noticed that this corner flow separation differs from the one calculated for a straight shock-wave in Wang et al. [175], maybe due to the difference of pressure gradient in the corner resulting from the geometry of the channel. The corner flow structure found in the LES work by Wang et al. [175] is closer to the one of the present upper corners, with less pressure gradient, which are more limited in spanwise extent.

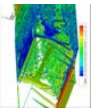

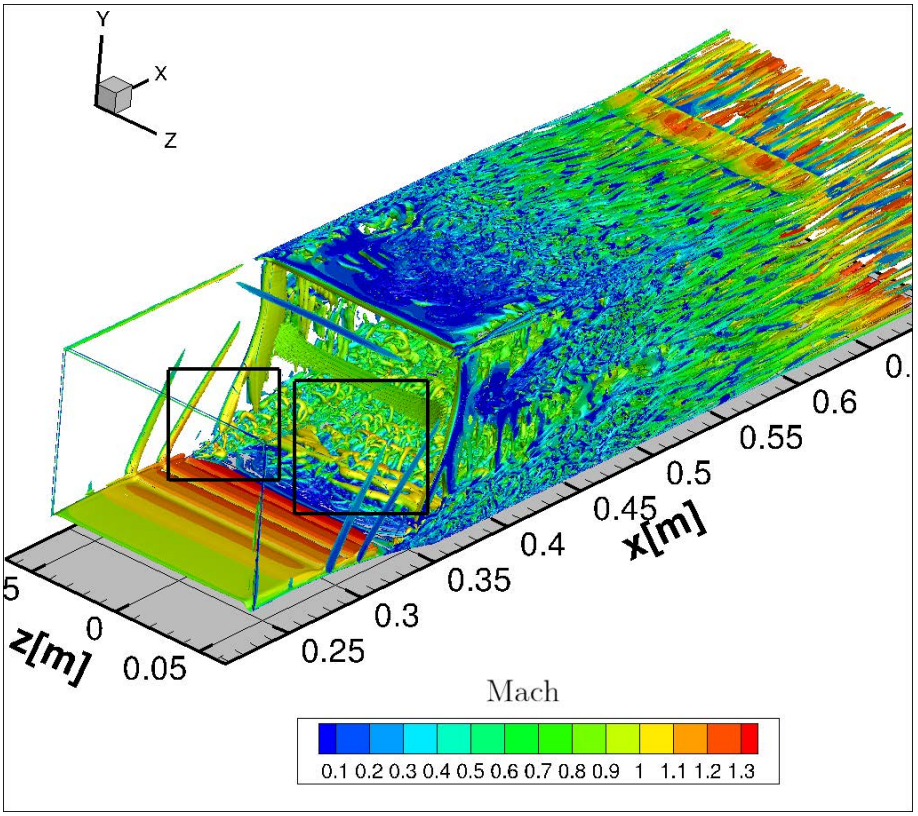

Figure VI.4: Iso-surface of Q criterion equal to $3 \cdot 10^6$ colorized with Mach number.

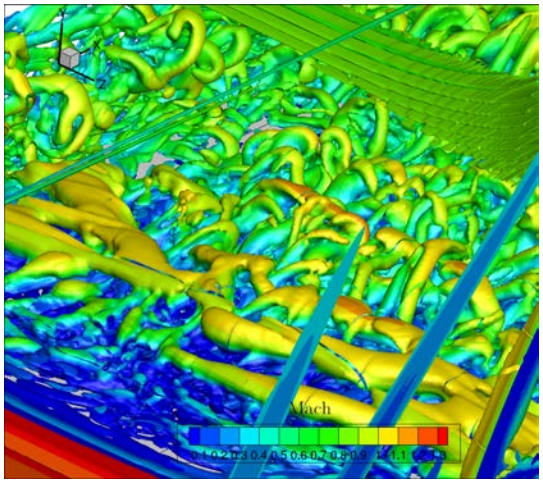

(a) Iso-surface of Q criterion equal to $3 \cdot 10^6$ colorized with Mach number, zoom on the central separation.

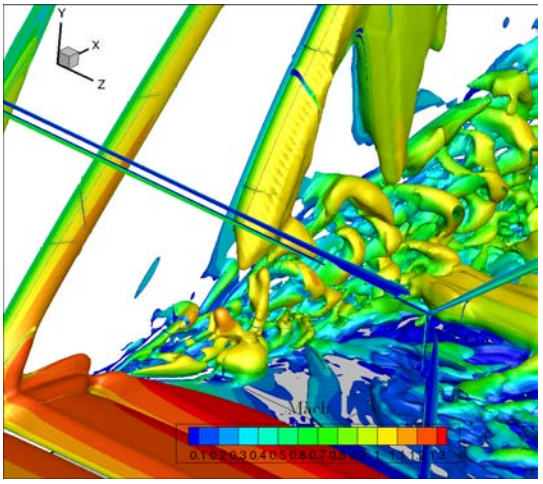

(b) Iso-surface of Q criterion equal to $3 \cdot 10^6$ colorized with Mach number, zoom on the corner flow separation.

Figure VI.5: Iso-surface of Q criterion equal to $3 \cdot 10^6$ colorized with Mach number, zoom of Fig. VI.4.

1.c Friction lines

The friction lines on the lower wall measured experimentally using oil flow visualization and calculated using RANS and ZDES are presented on Fig. VI.6, for the ZDES only the lower half is represented. The numerical results, even if they do not completely follow the experimental results, are a useful tool to understand the direction of the friction lines obtained experimentally.

On this figure, the positions of the experimental and numerical unsteady pressure sensors used in subsection i are indicated using colored circles. The three green lines correspond to the position of the median planes of the three volumes studied using tomographic PIV in subsection 1.e.

The central separation on the median line starts close to $x = 320\,\text{mm}$ and ends close to $x = 380\,\text{mm}$. The separation presents a 2D aspect only on half of the whole wind tunnel width (between $z = -30\,\text{mm}$ and $z = 30\,\text{mm}$). On the exterior part, the central separation is strongly influenced by the corner flow separation which starts upstream than the central separation, around $x = 295\,\text{mm}$.

The lateral friction lines close to the corner flow separation are presented on Fig. VI.7. It is important to notice that only orange oil was deposited on the lateral wall, the white part of the oil in the corner comes from the lower wall. This confirms a strong interaction between the separation appearing on the lateral and on the lower wall. Due to the fact that the photographs are taken after the wind tunnel is shut down, the oil is a little washed by the flow and the focus pattern is not clearly identified. Nevertheless, it seems to be close to the RANS calculations since the part above the ruler presents more paint than the lower part where the friction lines are more separated. It can be noticed that a small separation seems to take place in the middle of the lateral wall.

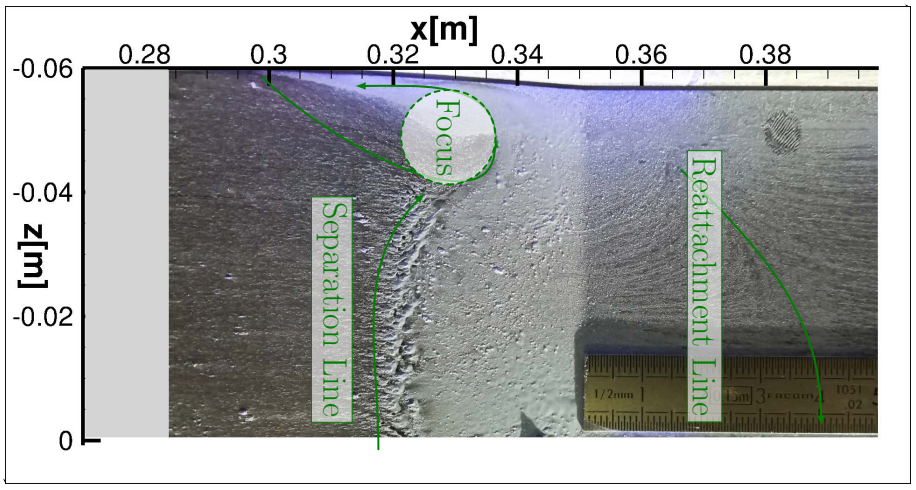

(a) Experimental.

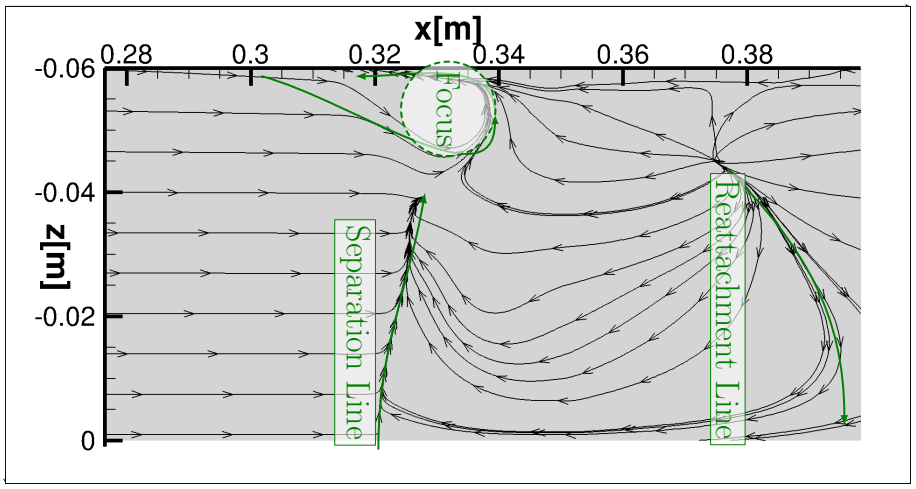

(b) RANS.

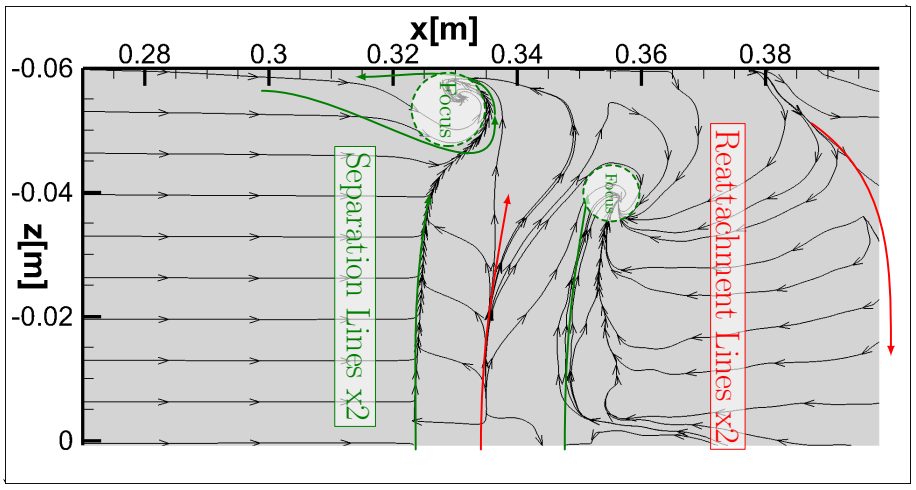

(c) ZDES.

Figure VI.6: Friction lines of experimental tests, RANS and ZDES on the lower wall of the wind tunnel presenting the focus of the corner flow separation and the separation and reattachment lines of the central separation.

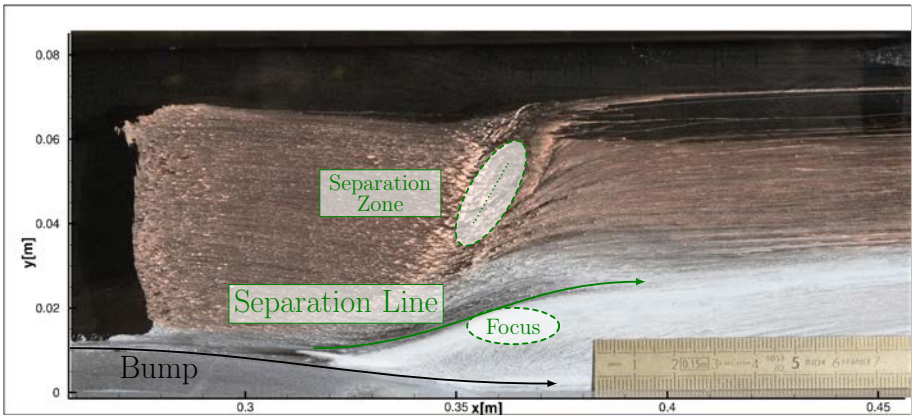

(a) Experimental.

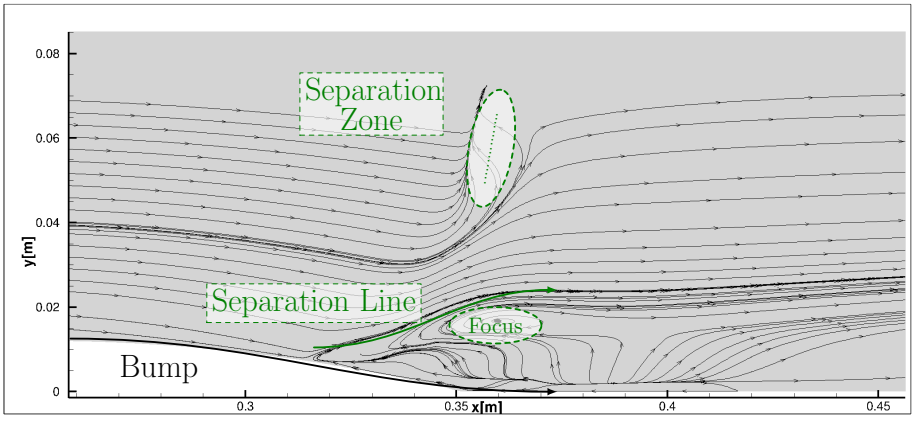

(b) RANS.

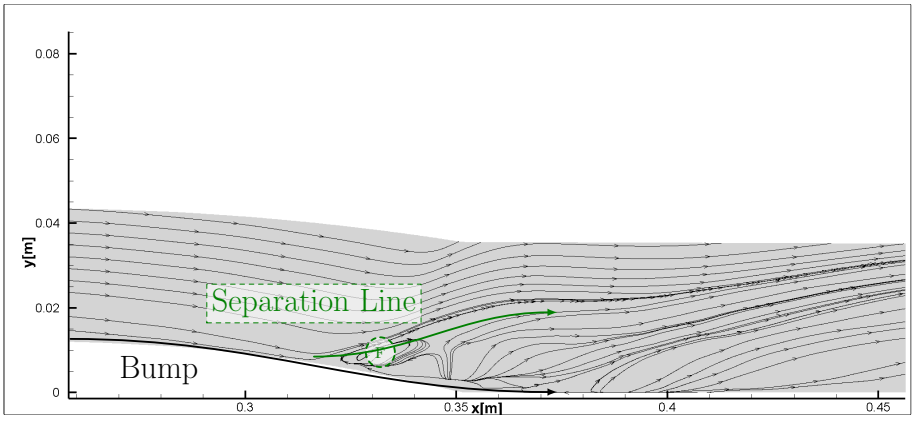

(c) ZDES only lower half.

Figure VI.7: Friction lines of experimental, RANS and ZDES calculation for the corner flow separation on the lateral wall.

For the ZDES calculation, even if the corner separation is well predicted on the lower wall, on the lateral visualization of the corner flow presented on Fig. VI.7c, the size of the re-circulation zone indicated by the letter F in a circle, is reduced compared to the experimental one, visible thanks to the accumulation of paint. Some colored oil flow visu-

alization should be done in order to determine more accurately the size of the longitudinal vortex. Due to movement of oil during the stop of the wind tunnel, its size is not precisely measured. Nevertheless, it appears to be smaller on the ZDES modeling. This may be due to the over-predicted size of the central separation.

It can be noticed that a lateral separation zone appears in RANS, and ZDES (not visible on this image due to extraction limitations during the ZDES calculation but visible on Fig. VI.2) above the corner flow separation. This separation is not clearly visible on the oil visualization and should be confirmed in future experiments. It can be due to the small size of the corner flow separation.

1.d Static pressure distribution

The static pressure distribution measured on the median line of the wind tunnel is presented on Fig. VI.8 within the height of the bump. The lack of data close to $x = 300\,\text{mm}$ is due to the presence of the removable strip were the fluidic control is mounted. In the first part of the curve, the flow undergoes an expansion phase following the bump, before a strong compression due to the shock-wave. Then, a small plateau denotes the presence of the separation zone. This plateau is slightly smoothed, probably by the fact that the shock-wave is moving due to the inherent instability while the plot of pressure represents a mean over time of the different positions of the shock-wave. The separation zone ended close to $x = 380\,\text{mm}$ which is coherent with the oil flow visualization presented above. The flow then relaxes with a compression occurring before the second throat.

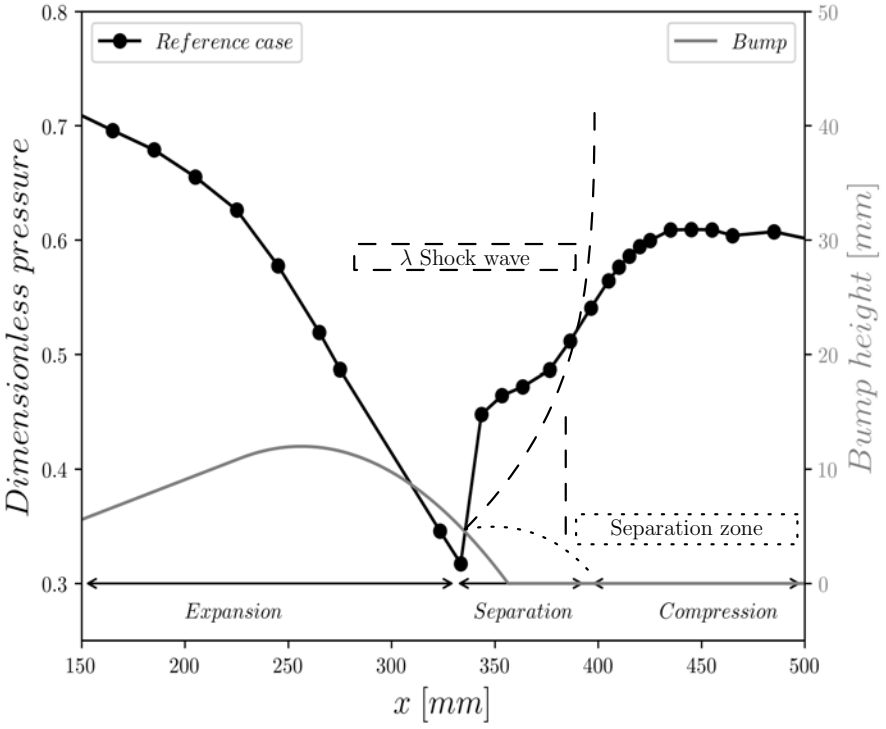

Figure VI.8: Static pressure distribution on the median line of the lower wall for the reference case(normalized by the flow stagnation pressure, equal to 96 000 Pa).

The static pressure distribution in the median line of the lower wall from the ZDES and

RANS calculations are compared to experimental data from Bur et al. [20] on Fig. VI.9. The position of the shock-wave, characterized by the rapid pressure increase around 320 mm is really close to the experimental data for both computations. Nevertheless, if the RANS curve follows well the experimental data, taking into account the interpolation, the ZDES distribution presents a plateau corresponding to the first part of the separation zone almost two times longer than the experimental one. However, the expansion region (between 150 mm and 320 mm) and the flow recompression behind the interaction (after 450 mm) are well predicted.

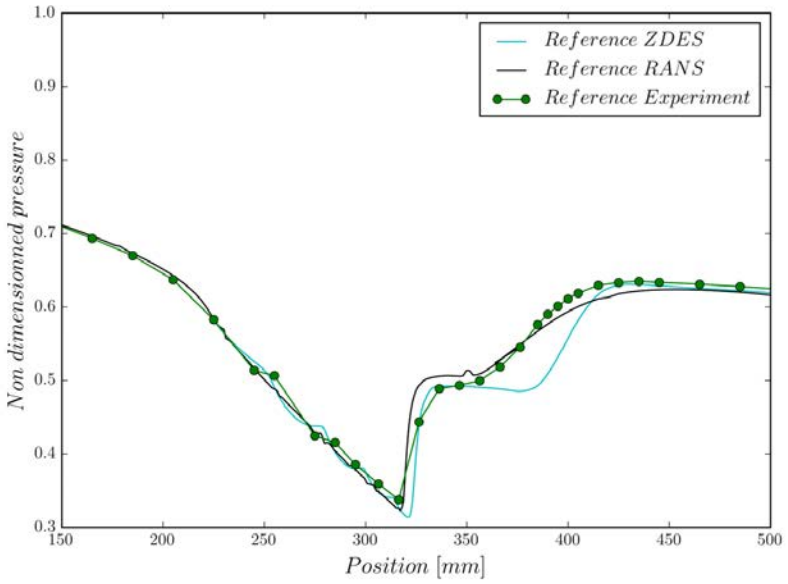

Figure VI.9: Pressure distributions on the lower wall, comparison between ZDES, RANS Spalart-Allmaras QCR and experimental results (Bur et al. [20]).

1.e PIV measurements

i Comparison to previous 2D PIV measurements

The RANS and ZDES mean flow on the median plane of the wind tunnel are compared to the the 2D PIV measurement from Sartor et al. [152]. The maps of longitudinal velocity and shear stress, $u'v'$ are plotted on Fig. VI.10.

As seen before in Chap. III, the RANS modeling on the median plane is close to the experimentally measured data, the size of the separation zone is well predicted even if the amplitude of the separation is slightly over predicted. The "dissipation" of the separation zone occurs slightly earlier than in the PIV data, this is visible on the shear stress tensor. Nevertheless, this may also be due to a limitation of the 2D PIV measurement interrogation window size.

On the other hand, for the ZDES, the first thing to notice is that the central separation zone is far too long. This may be due to the fact that the beginning of the separation is not well modeled. Indeed, it can be seen that there is a small zone, close to the wall where the flow is not reversed any more. This was visible on the friction lines on Fig. VI.6c. This prevents the Kelvin Helmholtz instabilities from starting closer to the foot shock.

Due to time limitation, the field of $u'v'$ presented for the ZDES only displays the non modeled part of the Reynolds stress tensor. The part modeled by the RANS technique at the beginning of the separation zone is missing. However, it can be seen that the height of the non null cross term of the Reynolds stress tensor is close to the experimental one with a middle part with too high level compared to the PIV data. This is due to the delay in the starting of the Kelvin Helmholtz instability. This longer separation zone generates a longer supersonic tongue above the end of the separation zone and it has also an impact on the lateral separation zones.

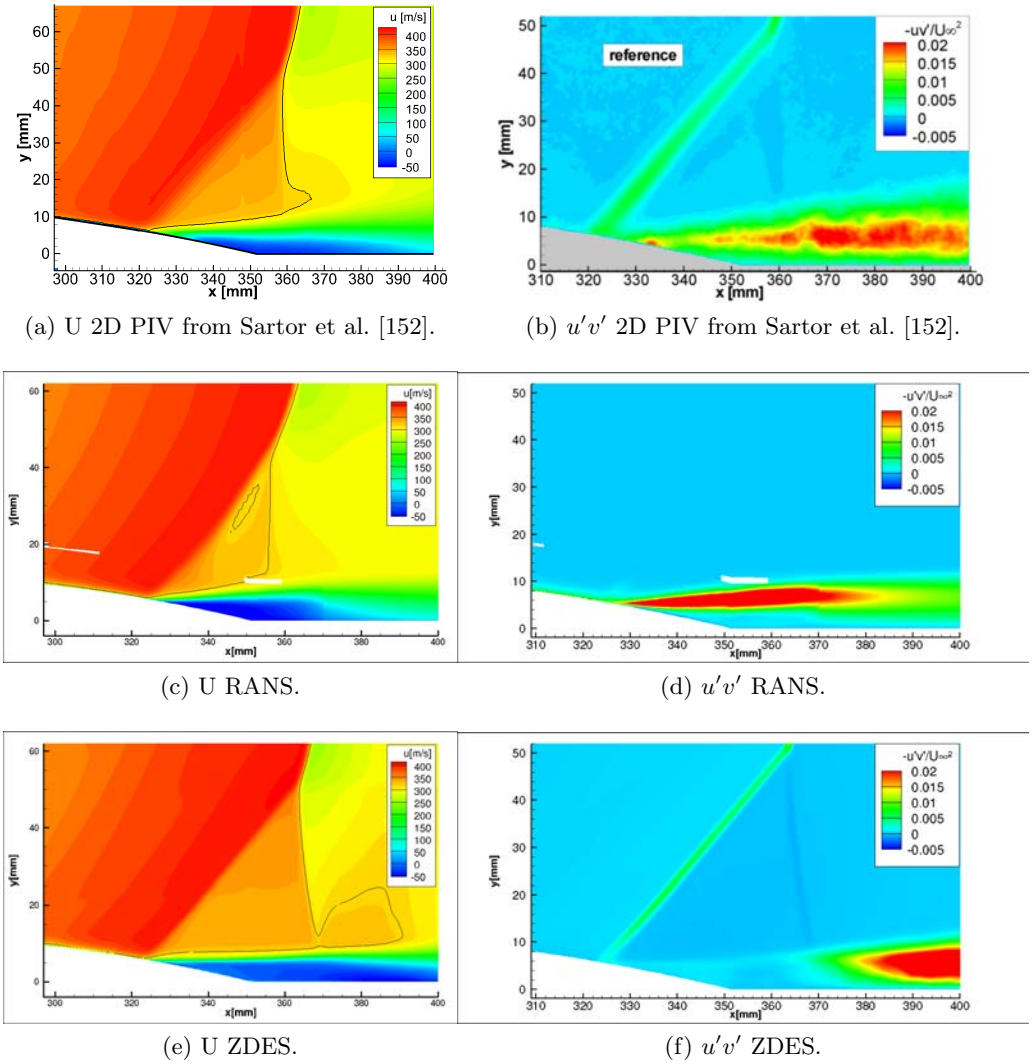

(a) U 2D PIV from Sartor et al. [152].

(b) $u'v'$ 2D PIV from Sartor et al. [152].

(c) U RANS.

(d) $u'v'$ RANS.

(e) U ZDES.

(f) $u'v'$ ZDES.

Figure VI.10: Comparison of longitudinal velocity and shear stress fields on the median plane, between 2D PIV, RANS and ZDES.

ii Validation of tomographic PIV measurements

In order to validate the results obtained by tomographic PIV, these last ones are compared thereafter to previous results obtained by Délery [49] using Laser Doppler Velocimetry

(LDV) and Sartor et al. [152] using 2D PIV. Then the results of the current study will be presented.

The 2D PIV measurements of the longitudinal velocity on the median plane of the wind tunnel done by Sartor et al. [152] is compared to the present tomographic PIV results on Fig. VI.11. It should be noticed that the two measured surfaces do not completely match, the tomographic PIV being placed more downstream than the 2D PIV. The small discontinuity around $y = 25\,\text{mm}$ for the tomographic PIV is due to the fact that the lower part is reconstructed using only 2 cameras, while the upper part is reconstructed using 4 cameras. This was done to improve the measurements in the separation zone after the bump as the two cameras placed upstream of the interaction where blinded by the reflection of the laser on the lower wall (see Chap. II section II.2 for a more detailed explanation of the reconstruction method). The discontinuity between the two reconstructions is due to the fact that by doing the reconstruction on a part only of the lighted volume, some particles illuminated by the laser volume are seen by each camera in the reconstructed volume while they are just above. This generates noise in the upper part of the reconstructed volume. The gray parts presented on the tomographic PIV represents the part of the flow which are invalidated when compared precisely to LDV and 2D PIV velocity profile. This will be detailed just after.

The two measurement techniques display a good agreement on the general velocity field. The 2D PIV is more precise in the vicinity of the shock-wave, this is due to the fact that the radius of the interrogation window used is 0.85 mm while the radius of the interrogation volume for tomographic PIV is almost two times bigger, $r = 1.55\,\text{mm}$. This provokes a small smoothing of the sharp gradient. It can be noticed that the 2D PIV presents a discontinuity of velocity close to $x = 348\,\text{mm}$ which is not physical and is not retrieved in tomographic PIV.

Six profiles of longitudinal velocity distributions are measured along the x axis on the median plane. They are reproduced on Fig. VI.12 with the measurements of LDV from Délery [49], and 2D PIV from Sartor et al. [152]. The velocity profiles are made dimensionless, following the recommendations of Piponniau et al. [136], using the formula $(u-U_2)/(U_1-U_2)$ with U_1 and U_2 respectively the outer velocity and the highest negative velocity inside the re-circulation bubble for each profile. These values are taken from the 2D PIV profiles. This formula is necessary to confront the LDV results as, contrary to the 2D PIV measurements, the LDV measurements were done with a slightly different Mach number and thus a different size of separation zone.

The three measurements techniques exhibit a good agreement in the upper part of the flow. However, the tomographic PIV measurements differ from the two others in a zone close to the wall. This is due to the fact that in order to remove the reflection of the laser on the pictures taken by the two lower cameras, the cameras are placed at grazing angle, sightly lower than the wall. This provokes a small blind zone close to the wall. This zone is of around 2.5 mm height on the plane area and of around 3 mm height on the bump. The larger blind zone on the bump is due to the fact that the camera is at grazing angle of the plane surface. The part on the bump is thus more masked by the height of the bump. This limitation is known for tomographic PIV measurements, the strong intensity of the laser volume provokes intense reflections which generate noise on the images and thus measurements. The current configuration is highly complicated to measure as it displays a separation zone of small height and furthermore, the geometry of the wall is curved and thus generates reflections in a larger number of directions. However, the technique has

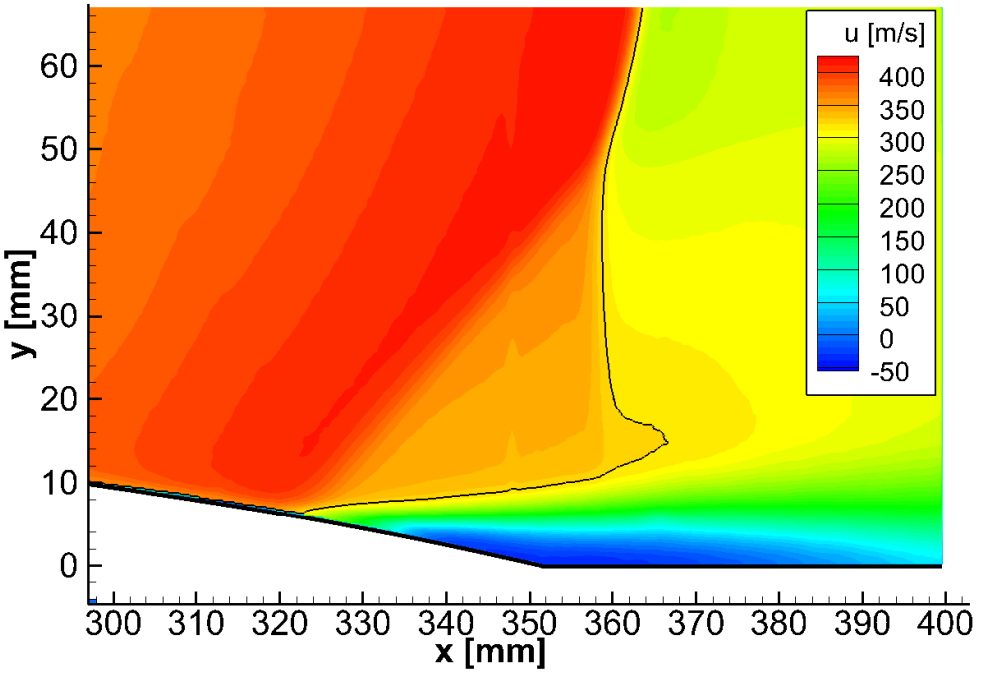

(a) 2D PIV from Sartor et al. [152].

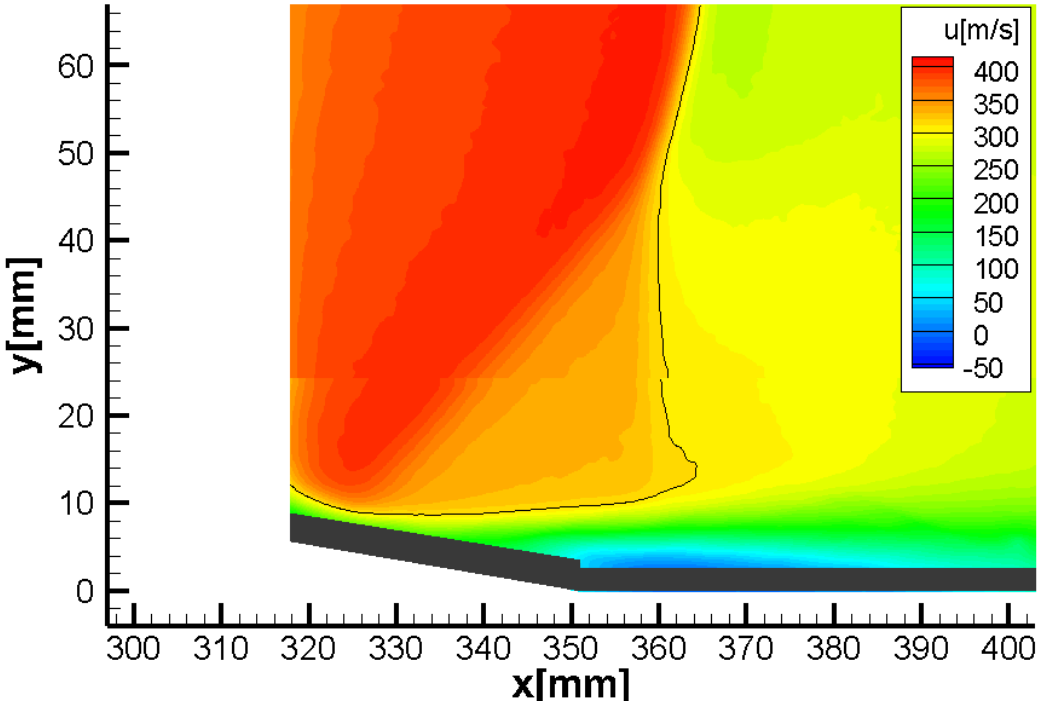

(b) Tomographic PIV.

Figure VI.11: Comparison of longitudinal velocity fields on the plane $z = 0\,\text{mm}$ between 2D PIV from Sartor et al. [152] and tomographic PIV.

the advantage of permitting to easily measure 3D variations of the flow field. This may be interesting for the controlled cases and the part of the reference case where the flow is

not 2D anymore.

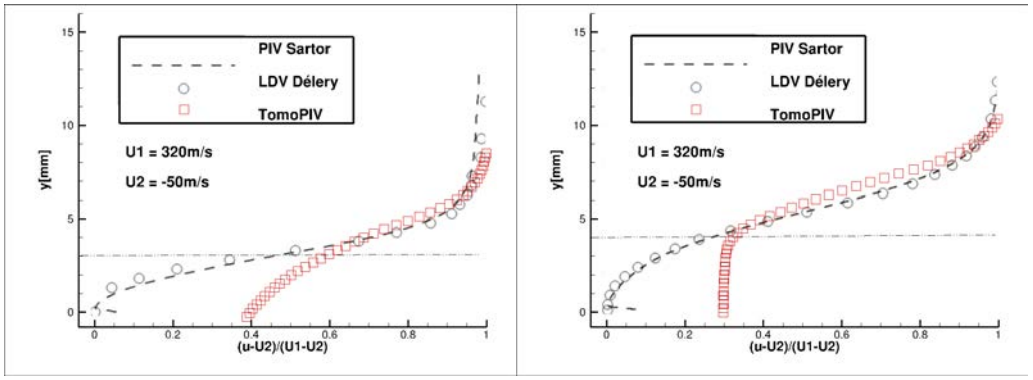

(a) $x = 340\,\text{mm}$

(b) $x = 350\,\text{mm}$

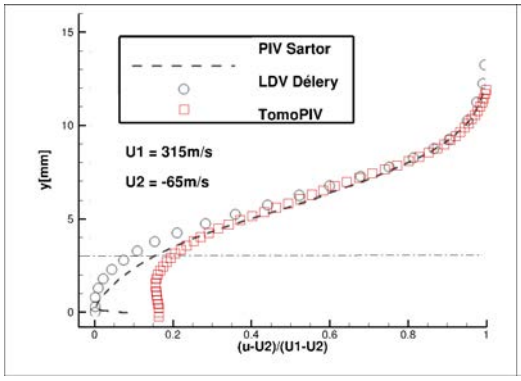

(c) $x = 360\,\text{mm}$

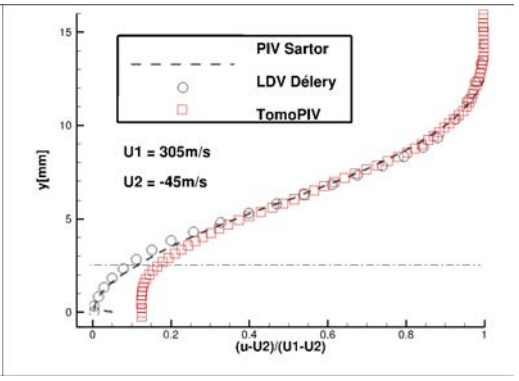

(d) $x = 370\,\text{mm}$

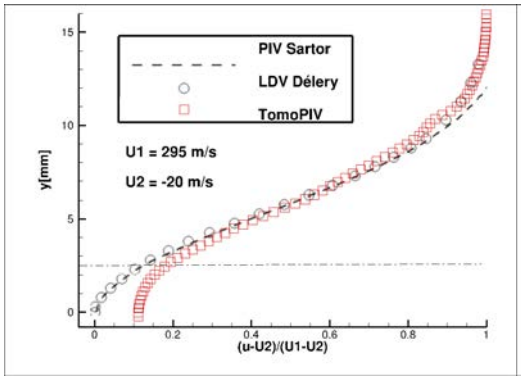

(e) $x = 380\,\text{mm}$

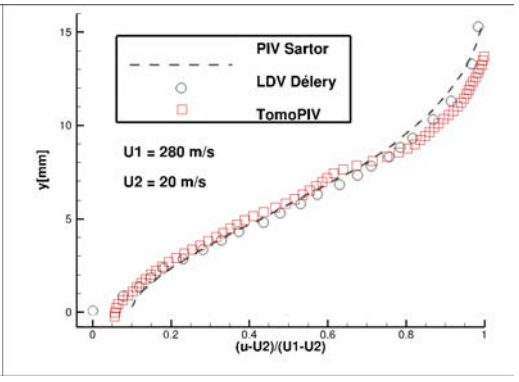

(f) $x = 390\,\text{mm}$

Figure VI.12: Comparison of longitudinal velocity profiles at various x positions on the median plane, between LDV from Délery [49] , 2D PIV from Sartor et al. [152], and 3D PIV (current study).

The turbulent quantities measured are compared to the one obtained by Sartor et al. [152] using 2D PIV on Fig. VI.13. It is important to notice that the measurement of Sartor et al. [152] of the separation zone were done using a telecentric lens. Thus the magnification ratio is around 37 pixels/mm for the 2D PIV measurement while the magnification ratio of the current study is of 16 pixels/mm. This discrepancy will influence the quality of the

results. The 2D PIV being able to capture smaller structures than the tomographic PIV.

First the r.m.s. of the longitudinal and vertical velocities are presented. The general pattern of the r.m.s. of the longitudinal velocity is well retrieved. Nevertheless, the maximum level is lower for the tomographic PIV (0.35 instead of 0.4), because the interrogation volume of tomographic PIV has a larger radius than the interrogation windows of 2D PIV. The small circle on the plots of tomographic PIV is a visualization of the size of the interrogation volume. Furthermore, as for tomographic PIV a wide band (around 2 cm) is illuminated, a smaller number of particles per pixel is mandatory in order to reduce the number of ghost particles (particles detected by the volume reconstruction algorithm at a position where no particle takes place). This claims for larger interrogation volumes but also for a more noisy result due to the remaining of ghost particles.

The same phenomenon is visible for r.m.s. of the vertical velocity fields. The global idea is retrieved, nevertheless, the gradient is more diffused and the higher level is not reached.

For both physic quantities, the shock-wave which is subject to a cyclic movement due to the SWBLI instability leaves a trace on the r.m.s. field.

In order to characterize the mixing layer, the 2D turbulent kinetic energy, $k = \sqrt{u'^2 + v'^2}$ is then plotted on Fig. VI.13(c) and Fig. VI.13(d) respectively for tomographic PIV and 2D PIV. It shows as for the 2D PIV measurements, a peak which corresponds to the end of the separation zone. Indeed, in the first part of the Kelvin Helmholtz instability developing on the mixing layer between the separation zone and the main flow, the turbulent energy is anisotropic with a stronger r.m.s. in longitudinal velocity. Then, the development of turbulent structures is going to redistribute the energy between stream wise, vertical and transverse velocities and turbulence is closer to an isotropic distribution.

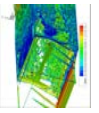

Then, considering that the change of density across the dissipative layer is small, the term $-u'v'/U^2$ is considered as a dimensionless Reynolds shear stress and is plotted also on Fig. VI.13. Once again, the classical value of 2% measured by LDV (see Bur et al. [19], Délery and Marvin [53]) in a similar configuration, is not retrieved, even if the main pattern, blurred, is retrieved. The maximum of the Reynolds shear stress is positioned downstream of the end of the re-circulation zone. The peak of shear stress implies the existence of a large-scale eddies developing after the separation zone.

This comparison validates the tomographic PIV for mean flows 3 mm away from the wall. It also validates the capability of tomographic PIV to retrieve the general topologies of turbulent quantities even if a stronger magnification may be needed for a more accurate measurement of these quantities. Nevertheless, these capacities will be sufficient to compare the efficiency and the 3D aspect of the fluidic VGs control.

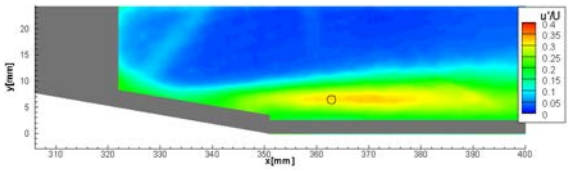

(a) Tomographic PIV: r.m.s. longitudinal velocity

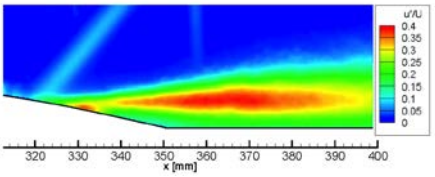

(b) 2D PIV: r.m.s. longitudinal velocity

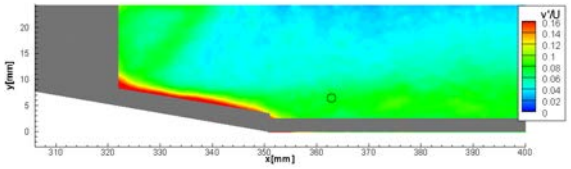

(c) Tomographic PIV: r.m.s. vertical velocity

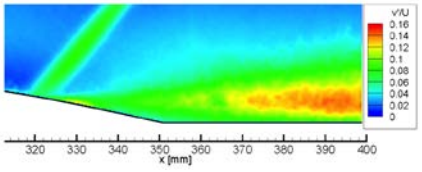

(d) 2D PIV: r.m.s. vertical velocity

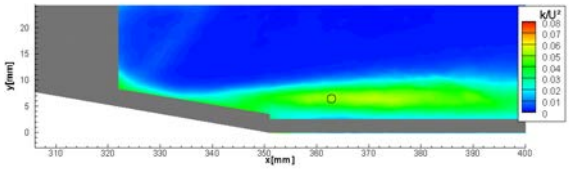

(e) Tomographic PIV: turbulent kinetic energy.

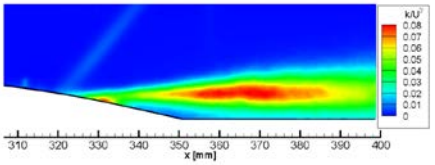

(f) 2D PIV: turbulent kinetic energy.

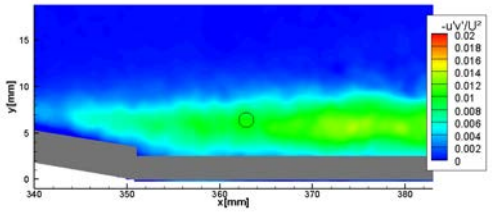

(g) Tomographic PIV: 2D Reynolds shear stress.

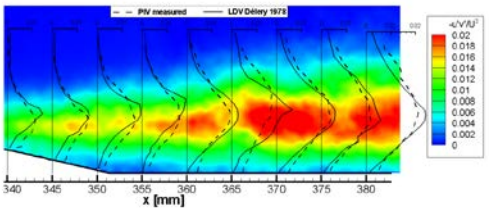

(h) 2D PIV: 2D Reynolds shear stress.

Figure VI.13: Comparison between tomographic PIV and 2D PIV from Sartor et al. [152], respectively left and right, of the 2D turbulent quantities in the lower mixing layer. The circle on left plots is an example of interrogation volume.

iii Tomographic PIV compared to RANS

In order to quantify the 3D topology of the reference case flow, the velocity fields of the median planes of the three volumes measured (visible on Fig. VI.14) are now presented on Fig. VI.15 and Fig. VI.16 for the tomographic PIV and the RANS calculation.

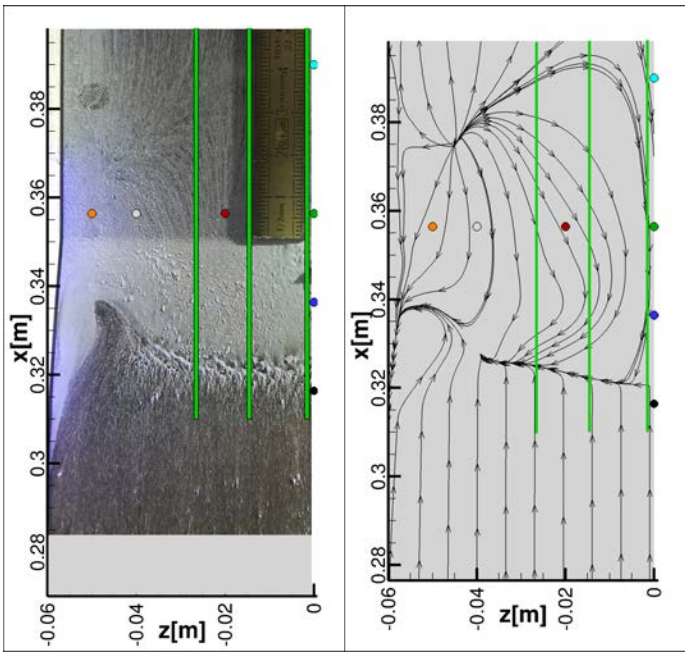

(a) Experimental. (b) RANS calculation.

Figure VI.14: Position of the three median planes of the volumes measured using tomographic PIV (green rectangles) presented on the friction lines of the Reference case.

For the tomographic PIV, first thing to notice is the presence of a diagonal ray on the measurement on the plane $z = -26\,\text{mm}$, close to at $x = 390\,\text{mm}$. Indeed, when displacing the illuminated volume closer to the windows of the wind tunnel, these latter ones are more illuminated due to the reflection on the lower wall. A scratch on the window provoked this defect on the reconstructed volume.

Considering the longitudinal and vertical mean velocities presented on Fig. VI.15, for RANS and tomographic PIV, the separation zone diminishes when the plane considered is displaced laterally. Indeed, the mixing layer is already reduced at $z = -14\,\text{mm}$ and the separation zone height is divided by two at $z = -26\,\text{mm}$ on the experimental data. This is also visible on the vertical velocity distribution. As a matter of fact, the positive vertical velocity after the shock-wave is due to the separation zone. Thus, on the plane at $z = -26\,\text{mm}$, the strong reduction of the vertical velocity after the shock, is a consequence of the reduction of the separation height.

Reference U | Reference V

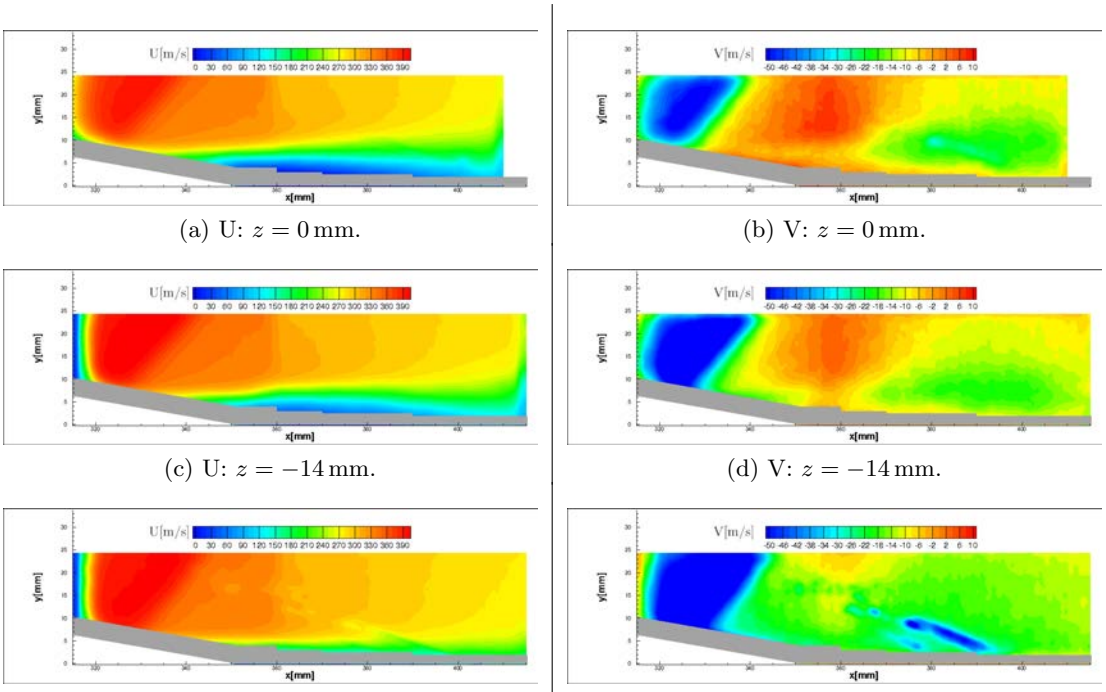

(a) U: $z = 0\,\text{mm}$. (b) V: $z = 0\,\text{mm}$.

(c) U: $z = -14\,\text{mm}$. (d) V: $z = -14\,\text{mm}$.

(e) U: $z = -26\,\text{mm}$. (f) V: $z = -26\,\text{mm}$.

Tomographic PIV

RANS

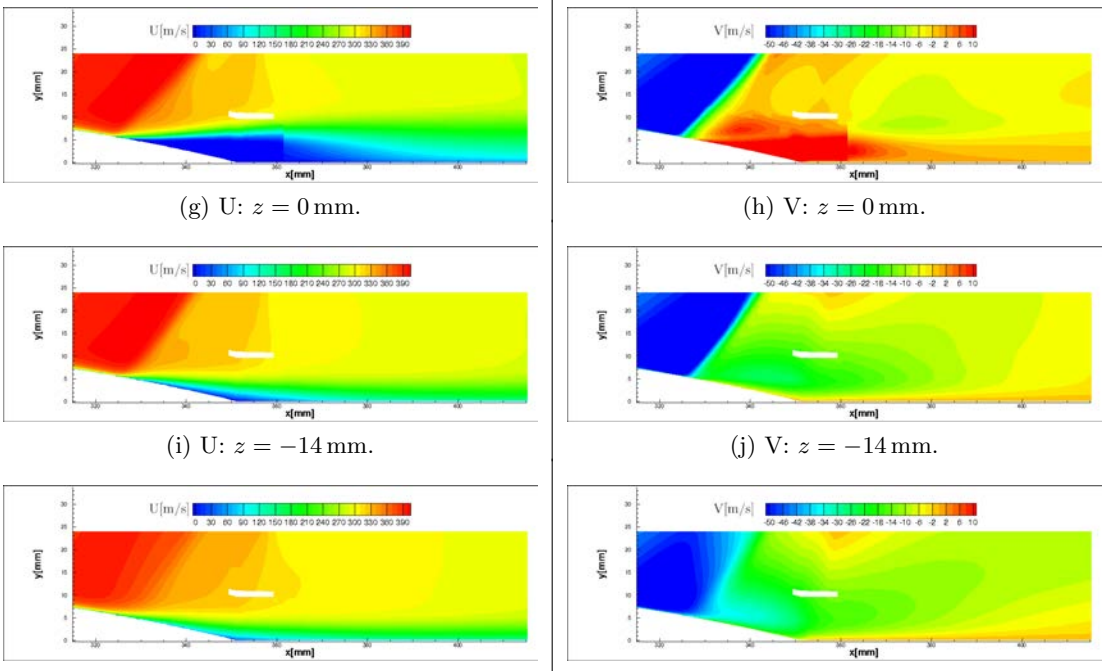

(g) U: $z = 0\,\text{mm}$. (h) V: $z = 0\,\text{mm}$.

(i) U: $z = -14\,\text{mm}$. (j) V: $z = -14\,\text{mm}$.

(k) U: $z = -26\,\text{mm}$. (l) V: $z = -26\,\text{mm}$.

Reference U | Reference V

Figure VI.15: Comparison of longitudinal and vertical velocity fields (respectively left and right) given by the tomographic PIV and RANS modeling (respectively up and down) for the reference case, at three different lateral planes.

Reference W | Reference u'v'

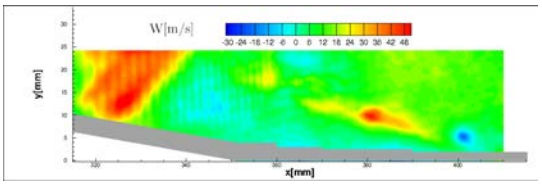

(a) W: $z = 0\,\mathrm{mm}$.

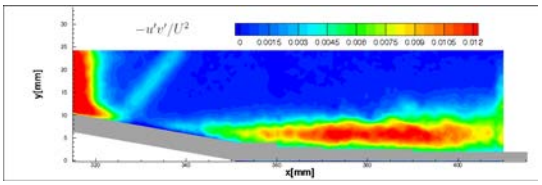

(b) u'v': $z = 0\,\mathrm{mm}$.

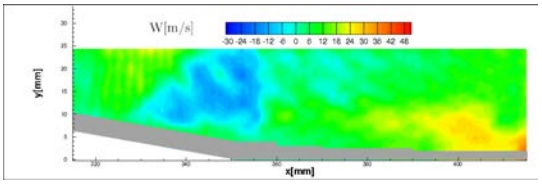

(c) W: $z = -14\,\mathrm{mm}$.

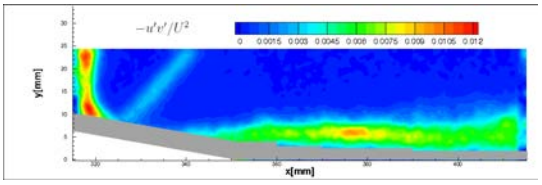

(d) u'v': $z = -14\,\mathrm{mm}$.

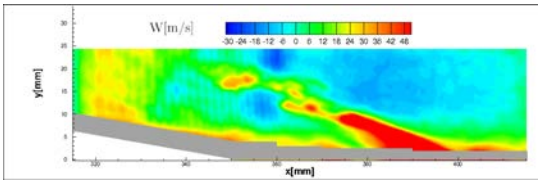

(e) W: $z = -26\,\mathrm{mm}$.

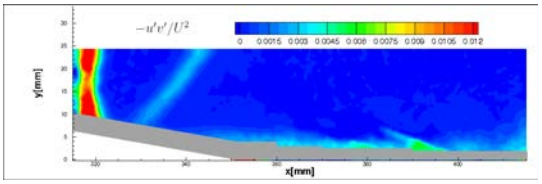

(f) u'v': $z = -26\,\mathrm{mm}$.

Tomographic PIV

RANS

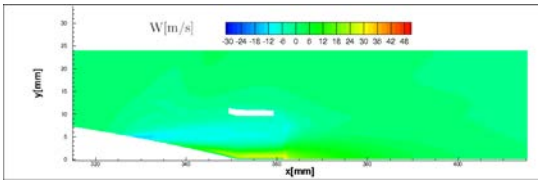

(g) W: $z = 0\,\mathrm{mm}$.

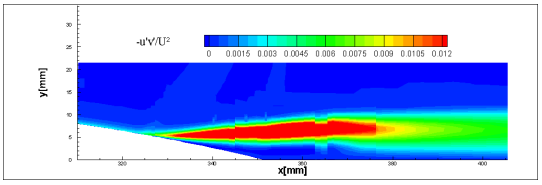

(h) u'v': $z = 0\,\mathrm{mm}$.

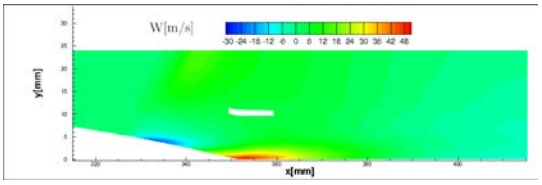

(i) W: $z = -14\,\mathrm{mm}$.

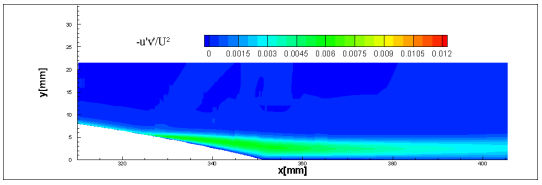

(j) u'v': $z = -14\,\mathrm{mm}$.

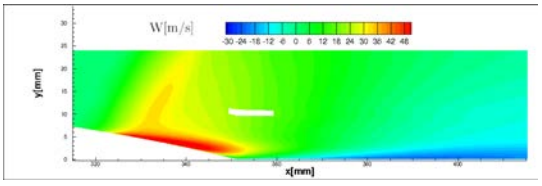

(k) W: $z = -26\,\mathrm{mm}$.

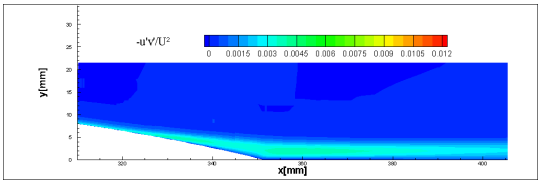

(l) u'v': $z = -26\,\mathrm{mm}$.

Reference W | Reference u'v'

Figure VI.16: Comparison of transverse velocity and dimensionless Reynolds shear stress fields (respectively left and right) given by the tomographic PIV and the RANS calculation (respectively up and down) for the reference case, at three different lateral planes.

Considering the RANS planes, the separation zone diminishes quicker than in the experimental data. Indeed, even if the central separation is more important on the plane $z = 0\,\text{mm}$ in RANS than on PIV, the height is smaller on plane $z = -14\,\text{mm}$ in RANS than in PIV. This may be linked to the shape of the corner flow separation which is predicted with a large amplitude by the RANS calculation even with the QCR correction. The vertical velocity map is globally of the same order of magnitude. It can be noticed that the vertical velocity value after the shock, above the separation zone is logically, strongly linked to the height of the separation zone.

The transverse velocity and the dimensionless Reynolds shear stress for the three planes, are displayed on Fig. VI.16 for the tomographic PIV and the RANS results.

Considering the experimental data, on the transverse velocity map, it can be seen that the wind tunnel is not completely symmetric, as the transverse velocity is not zero on the central plane. It can also be seen that the magnitude of transverse velocity after the shock-wave increases when leaving the central zone which is coherent with the increase of transverse velocity seen on the oil flow visualization. For the Reynolds shear stress, the maximum value is pulled up on the plane $z = -14\,\text{mm}$ compared to the plane $z = 0\,\text{mm}$, this can be correlated to the fact that the separation zone is smaller in length. The maximum value is lower on this plane because the separation zone is lower and thus develops smaller eddy vorticies.

For the RANS transverse velocities presented below the experimental data, the median plane is close to zero everywhere (it is not zero exactly as the plane is taken at $z = -0.01\,\text{mm}$). The plane $z = -14\,\text{mm}$ is coherent with the shape of the friction lines presented on Fig VI.6b. On the contrary, the last plane differs from the friction lines, indicating that the friction at the wall is due to a separation zone of really small height while the flow above is already influenced by the vortex of the corner flow separation which turns in the opposite direction. This was not retrieved in the tomographic PIV data, indicating a smaller corner flow separation in the experiment.

The variation of longitudinal velocity distribution along the transverse direction is also visible on the plane $x = 370\,\text{mm}$, plotted on Fig. VI.17 for tomographic PIV and RANS. The variation is quite rapid along the transverse direction as the boundary-layer is divided by two from the center to the first quarter of the test section. The SWBLI is two dimensional only on the 10 mm width in the center of the test section. The RANS separation is more peaked at its center than the tomographic PIV data. This is coherent with the previous remarks.

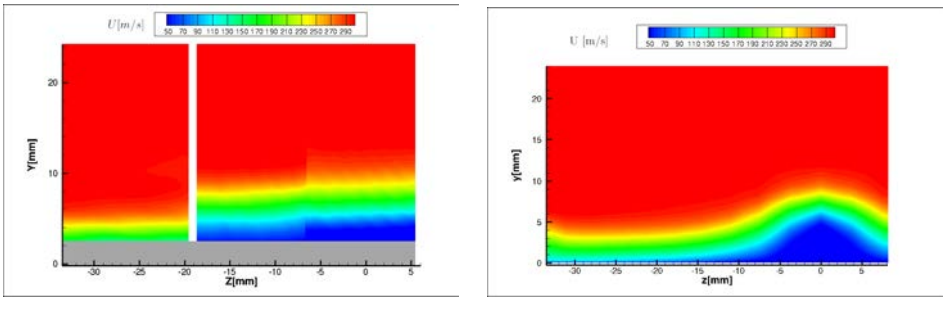

(a) Experiment. (b) RANS.

Figure VI.17: Lateral distribution of longitudinal velocity on the plane $x = 370\,\text{mm}$.

The advantage of tomographic PIV is that it also permits a more global view of the mean flow. For this purpose, two velocity iso-surfaces, allowing to distinguished the shock-wave and the separated zones, are plotted on Fig. VI.18. The black parts represent the zones where the tomographic PIV is not validated.

The spatial evolution of the supersonic tongue and the corresponding separation zone along the width of the wind is clearly visible.

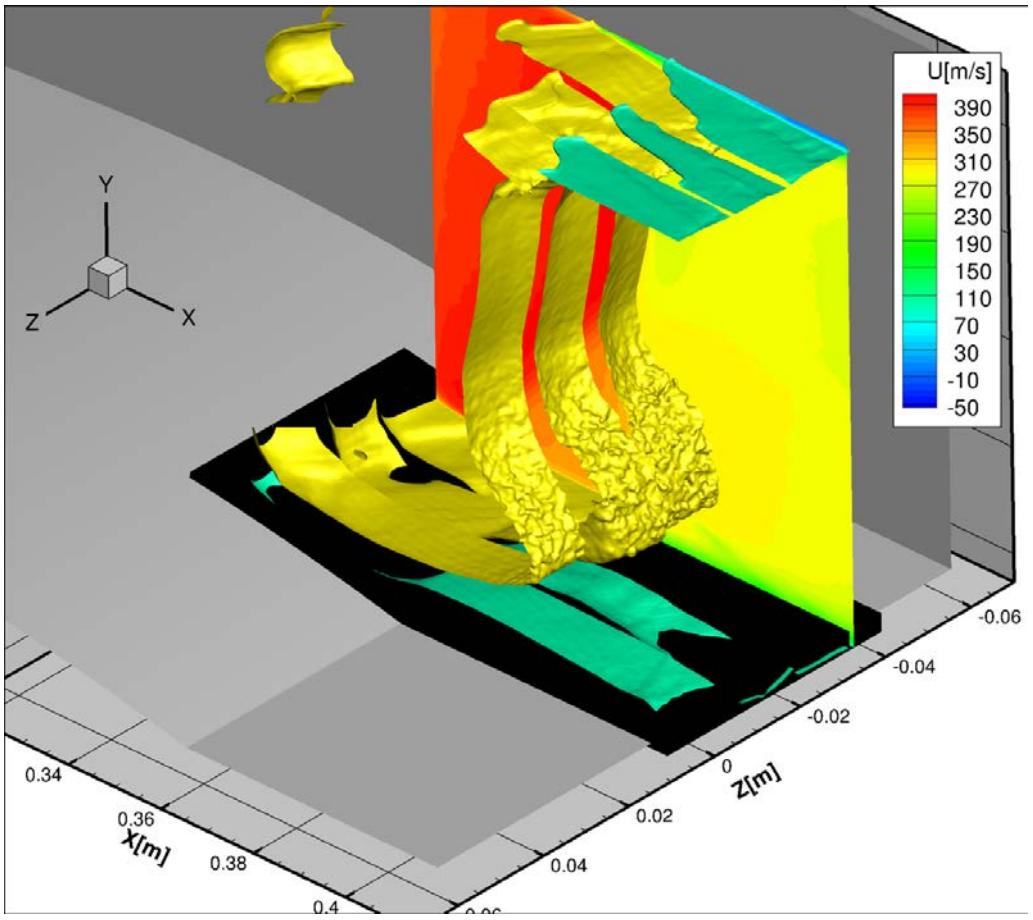

Figure VI.18: 3D visualisation of the SWBLI in the reference case, two iso-surfaces for $u = 300\,\mathrm{m\,s^{-1}}$ (yellow) and $u = 100\,\mathrm{m\,s^{-1}}$ (green). The plane $z = -40\,\mathrm{mm}$ is also represented. The black region represents the zone where the tomographic PIV is blinded due to reflection.

1.f Total pressure losses

The Pitot rake presented in Chap. II, has been used to measure the total pressure distribution far downstream of the interaction, on the plane $x = 468\,\text{mm}$. This measurement is compared to an interpolation on the same mesh of the RANS results on Fig. VI.19. The main levels are well retrieved, with only the lowest level not measured because the Pitot tube makes a small lateral integration contrary to the computations which are truly punctual and closer to the wall.

The impact of the central and corner flow separations on the downstream flow is confirmed. The impact of the central separation seems to be slightly underestimated by the RANS computation. On the contrary, the impact of the corner separation seems to be slightly over-predicted by the simulation.

These discrepancies may also be due to the presence of the Pitot rake in the subsonic region which may prevent the flow to be completely symmetrical.

The static pressure distribution is also compared to ZDES results on Fig. VI.19c. Again, the levels are comparable, but in this case, the corner flow separation is underestimated by the numerical model. This may be linked to the fact that this separation was found to be reduced due to a larger central separation. Nevertheless, the computed central separation is smaller than the measured one. This may be due to experimental modifications induced by the Pitot rake.

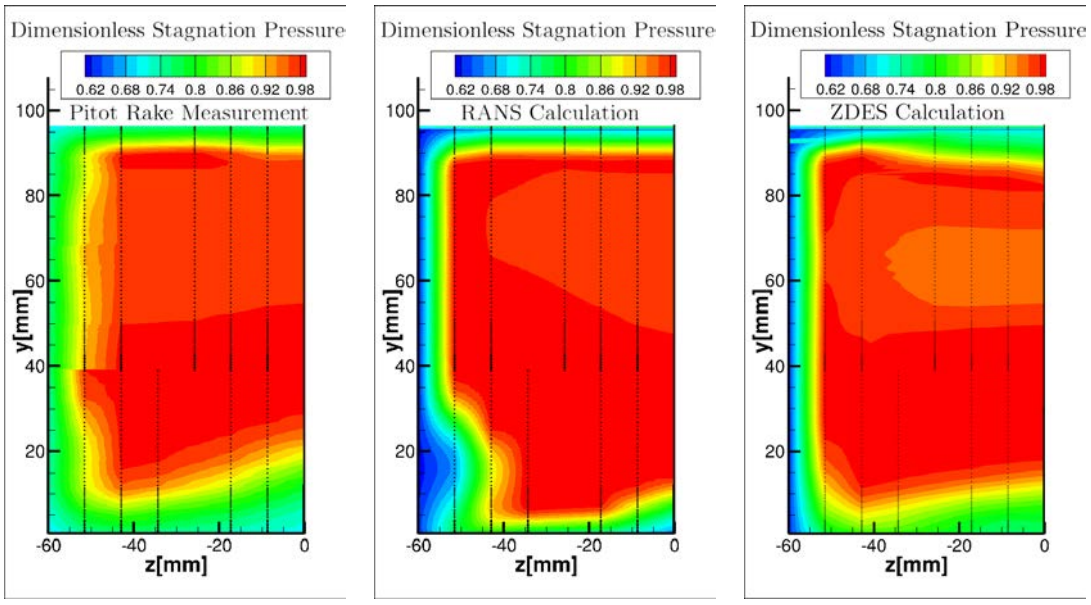

(a) Experimental. (b) RANS. (c) ZDES.

Figure VI.19: Comparison of total pressure distributions on the plane $x = 468\,\text{mm}$ for experimental, RANS and ZDES calculations.

Remark The Pitot rake took finally more space in the wind tunnel than predicted, notably due to the wake generated which induces flow perturbations. When the rake was high in the wind tunnel, the second throat had to be adapted in order to maintain the shock-wave at the same position. Moreover, at some point, a little mass flow rate needed to be removed using a auxiliary pump. Unfortunately, this pump was damaged during the

tests and not replaced before the end of the current work, preventing the Pitot rake to be used for the controlled cases.

1.g Flow Unsteadiness

i Pressure fluctuations measurements

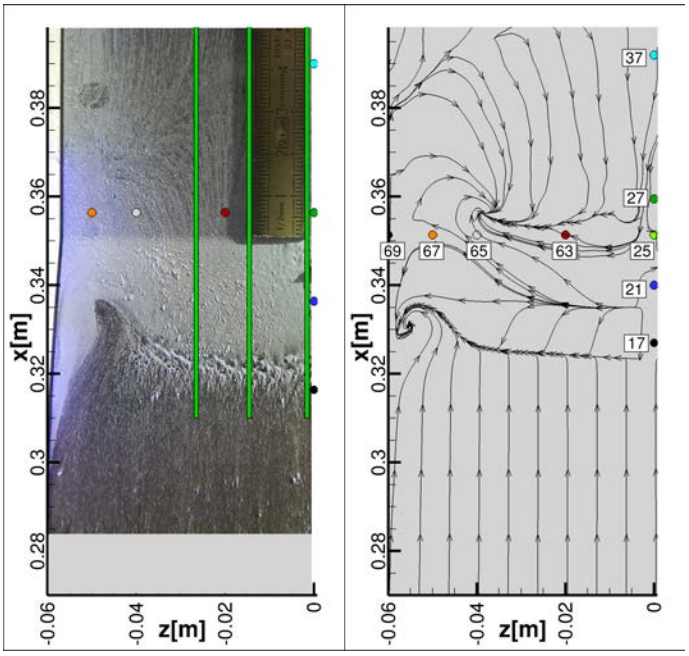

(a) Experimental. (b) ZDES calculation.

Figure VI.20: Position of the pressure sensors (colored circles) used to measure the pressure fluctuations presented on the friction lines of the Reference case.

In order to analyze the dynamic of the flow, the signals of the Kulite sensors have been post treated using fast FFT method. The power spectral density of the signal is calculated using 32000 samples long Hanning windows with 50% of overlapping, this gives a resolution of 2Hz for the spectrum as the acquisition frequency was of 100kHz. The pre-multiplied spectra obtained by both the longitudinal and lateral sensors are presented on Fig. VI.21 as well as the pre-multiplied spectrum of the sensors in the ZDES. The reader can refer to the oil flow visualization on Fig. VI.20 for a better understanding of the interpretation of the signals, the colors of the sensors correspond to the colors of the curves of the spectra.

First of all, the two main characteristic frequencies found by Sartor [151] are well retrieved. The sensor placed at $x = 316.4\,\text{mm}$, close to the shock-wave foot, has a principle peak close to 300Hz. The next sensor which is placed in the beginning of the separation zone as it is visible on the oil flow visualization on Fig. VI.6a, sees less intensively the characteristic frequency of the shock-wave but also starts to register the characteristic frequency of the Kelvin Helmholtz instability, 4kHz. The following sensor, placed at $x = 356.4\,\text{mm}$, is in the middle of the separation zone close to the position where the height of the separation is at its maximum. There, the structures convected above have a smaller impact and its spectrum is flat.

Central Lateral

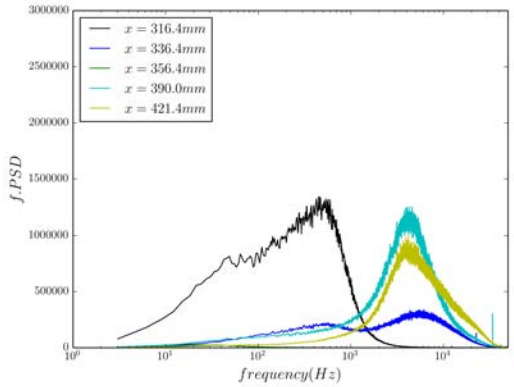

(a) $z = 0.0\,\text{mm}$

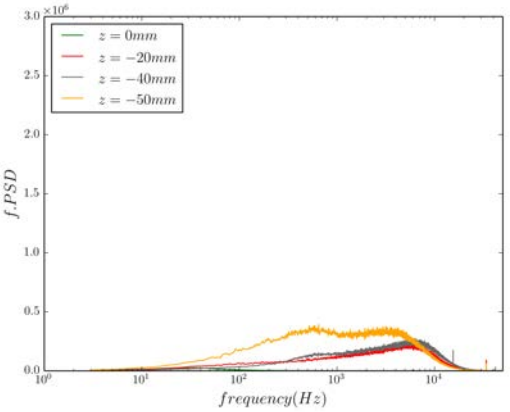

(b) $x = 356.4\,\text{mm}$

Experimental

ZDES

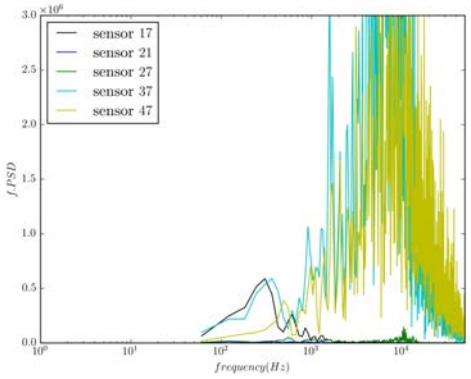

(c) $z = 0.0\,\text{mm}$ resolution 60Hz.

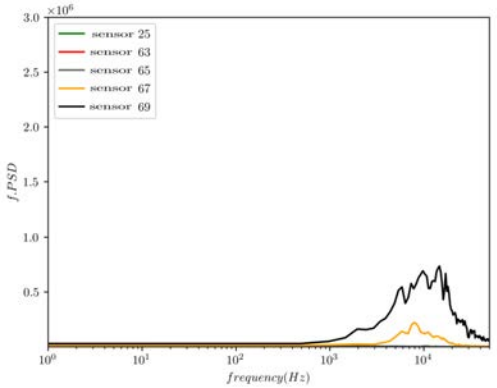

(d) ZDES $x = 351.4\,\text{mm}$

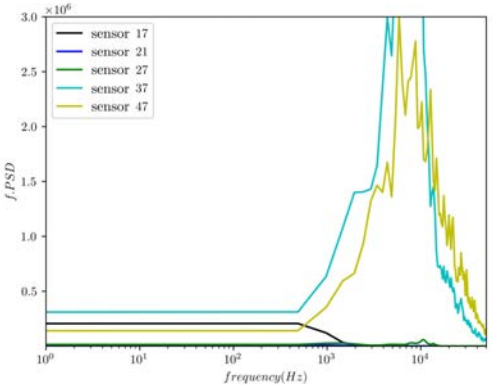

(e) $z = 0.0\,\text{mm}$ resolution 480Hz.

Central Lateral

Figure VI.21: Pre-multiplied spectra obtained by the sensors in the streamwise and spanwise directions for the reference case.

The next sensor, placed close to the end of the separation zone at $x = 390\,\text{mm}$, sees strongly the impact of the structures developing along the mixing layer at the characteristic frequency of the Kelvin Helmholtz instability. The energy in these structures is then reduced while the flow goes on as it can be seen on the last sensor placed farther downstream at $x = 421.4\,\text{mm}$, with a displacement of the spectrum to higher frequencies which is common in the case of the development of a Kelvin Helmholtz instability.

For the lateral variation of the unsteadiness, the sensor placed at $z = -20\,\text{mm}$ already sees more the frequency characteristic of the Kelvin Helmholtz instability, slightly shifted up to 6kHz, than the central sensor. This can be linked to the variation of separation thickness disclosed by the tomographic PIV. Indeed, the next sensor placed $z = -40\,\text{mm}$, also managed to measure the 6kHz. The shift in frequency can be linked to the fact that the height of the bubble is reduced on this line and thus, considering that the phenomenon is linked to a precise Strouhal number, the frequency has to increase. The lateral variation of intensity of the shock-wave frequency is coherent with the results found in Rabey et al. [137], where they found a weighted power spectral density more important in the center and quickly diminishing along the transverse direction.

The last sensor is placed very close to the lateral wall and is in a zone located just after the separation corner flow as it can be seen on the oil flow visualization displayed on Fig. VI.6a. The sensors measures two more important frequencies on a wide band phenomenon, one close to the Kelvin Helmholtz frequency and another one close to 600Hz. It seems that this sensor measures the impact of the shock oscillation in the corner.

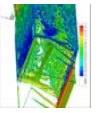

Even if the flow physics are not completely retrieved, the advantage of the ZDES simulation is that it gives information on the dynamics of the flow contrary to RANS.

The pressure fluctuations are measured by sensors positioned close to the one mounted on the wind tunnel. The ones considered here are presented on Fig. VI.6c, their exact position is given in Chap. II in Table II.8. The pressure signals are post-treated using the Welch's average periodogram method with Hanning windowing. The frequency of acquisition allows to have a maximum frequency of 200kHz but the duration of the simulation only allows a resolution of 60Hz and the signal is noisy at high frequency due to the fact that with fifty percent of overlapping, only 7 blocks are calculated before averaging. In order to improve the readability of the spectrum at high frequencies,the pre-multiplied spectrum has also been calculated using a resolution of 480Hz with 28 blocks. The pre-multiplied spectrum of the sensors positioned along the central line of the lower wall are presented on Fig. VI.21. The sensor 17 is positioned closed to the separation point and presents a bump at 300Hz which is close to the frequency found experimentally by Sartor et al. [152] for the shock-wave instability. The sensors 21 and 27 which are in the separation zone, do not capture any significant fluctuation. The following one sensor 37 is close to the end of the separation zone. It captures the frequency of the shock instability but also higher frequencies with a pick close to 4kHz which is the one found experimentally by Sartor et al. [152]. And the final one, number 47 captures only the higher frequencies characteristic of the Kelvin Helmholtz instability present in the mixing layer.

For the sensors located in the spanwise direction, the first one, on the central line, number 25 presents no signal as it is positioned in the separation zone. The same remark is valid for the two following sensors. The two last ones are positioned downstream of the corner separation zone. They reveals higher frequencies, with a peak close to 10kHz. The number 69, on the axis of the corner separation seeing more energy than the number 67.

ii Modal decomposition of the flow in the median plane

The median plane of the channel have been extracted at a frequency equal to 200kHz. This allows to identify some temporal and spatial coherent structures in the flow. The method chosen to do so is the Spectral Proper Orthogonal Decomposition (SPOD) (see Taira et al. [164], Towne et al. [169]). It consists into a Proper Orthogonal Decomposition of a matrix composed of several Fourier components modes of the flow. It decomposes the flow into coherent and orthogonal spatial modes for each frequency of the Fourier decomposition. Unfortunately, due to the small amount of time calculated and to the low frequencies investigated, the SPOD decomposes the Fourier components into only seven modes which does not ensure a proper convergence of the SPOD modes. Nevertheless, the first and most energetic modes of the flow for the known characteristic frequencies of the flow are presented on Fig. VI.22 for 292 Hz, and on Fig. VI.23 for 3.9 kHz.

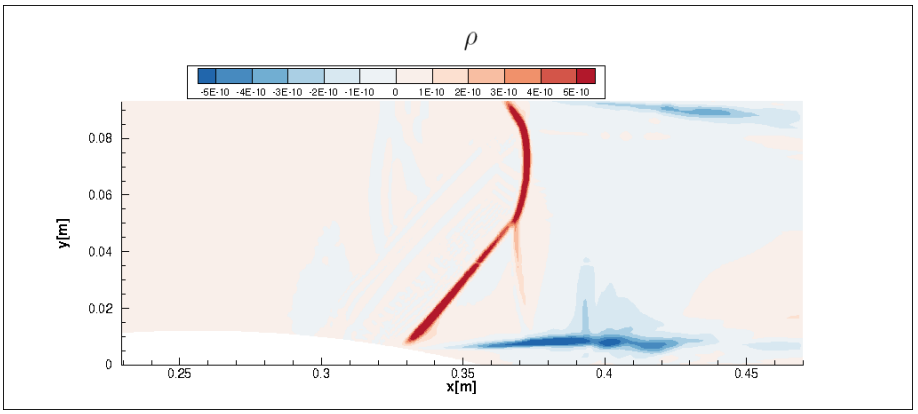

Figure VI.22: Mode 1 of density for the frequency 292Hz (67% of energy).

The dominant mode at 292Hz presents the characteristic of the interaction between the two mixing layers (top and bottom) and the main shock-wave of the lambda with a small distance between the mixing layer and the λ shape, certainly due to the slow development of the turbulent structures behind the interaction.

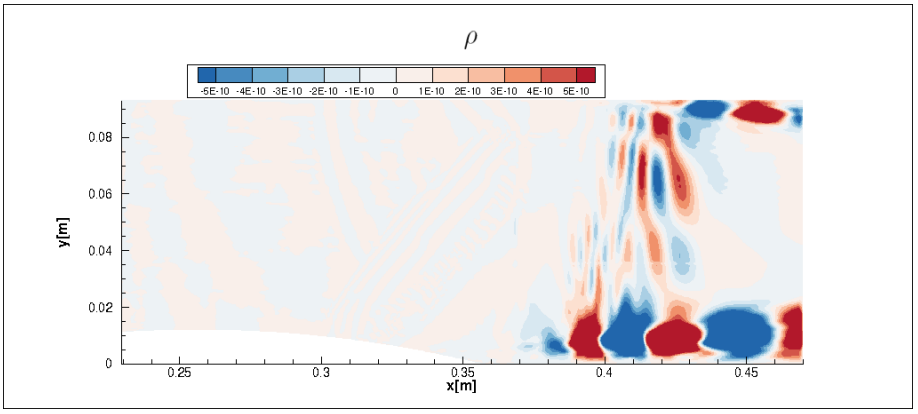

Figure VI.23: Mode 1 of density for the frequency 3,9kHz (59% of energy).

At 3.9 kHz, the structures of the mode develop along the upper and lower separation zones with a trace of interaction between both. This shape is characteristic of Kelvin

Helmholtz instability in the mixing layer.

These modes can be compared to the experimental Fourier modes found by Sartor et al. [154] using high speed Schlieren visualizations. These modes are therefore calculated for the vertical and longitudinal density gradients with respect to the direction of the knifes used for the Schlieren visualizations. The absolute values of the longitudinal and vertical density gradient of the SPOD modes are presented on Fig. VI.24 and Fig. VI.25. The structure corresponds well for the 300Hz mode. The only differences are due to the size of the lower separation zone and to saturated zones in the Schlieren visualization on the λ shock structure and on the upper wall on Fig. VI.24c, provoking the non consistent white zones in the left part of the λ shock.

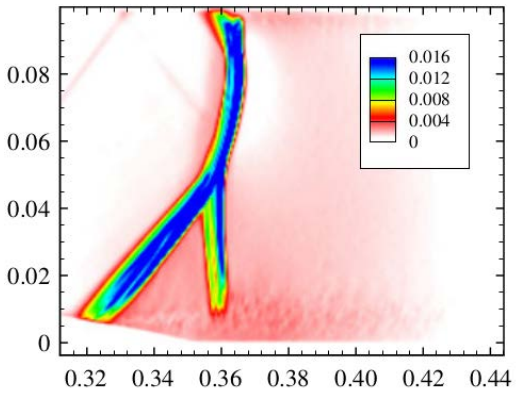

(a) Fourier mode of the longitudinal density gradient from Sartor et al. [154].

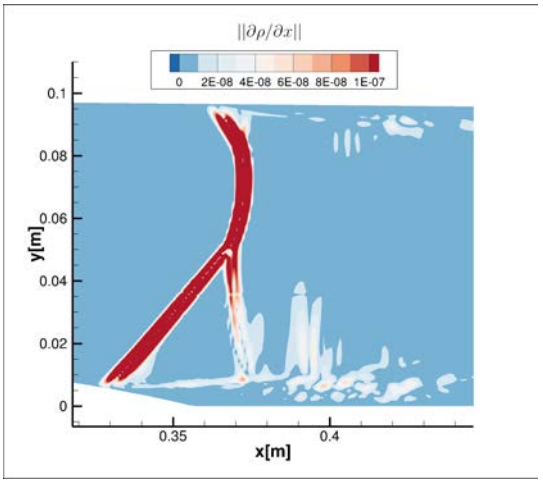

(b) SPOD mode of the longitudinal density gradient.

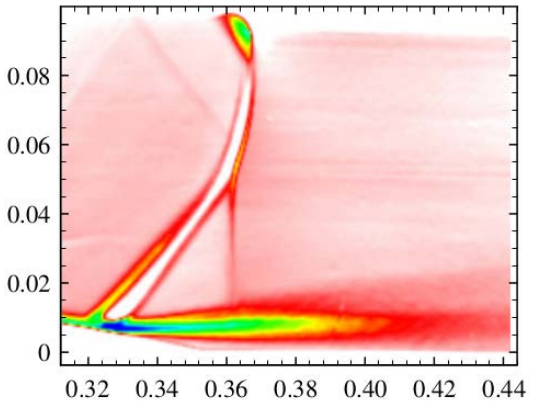

(c) Fourier mode of the vertical density gradient from Sartor et al. [154].

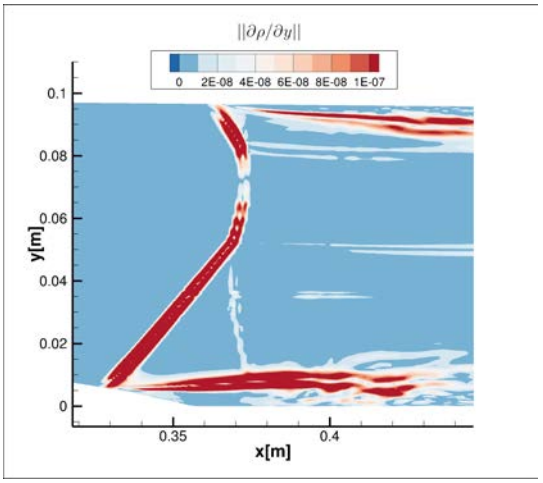

(d) SPOD mode of the vertical density gradient.

Figure VI.24: Comparison between Schlieren Fourier modes and ZDES SPOD modes of density at 292Hz (67% of energy).

For the 4kHz modes, discrepancies between experiments and numerics are more relevant. The gap between the shock-wave and the mixing layer induces variations on the general flow dynamic. The structures between the two mixing layers are more present on

Fig. VI.25b than on Fig. VI.25a.

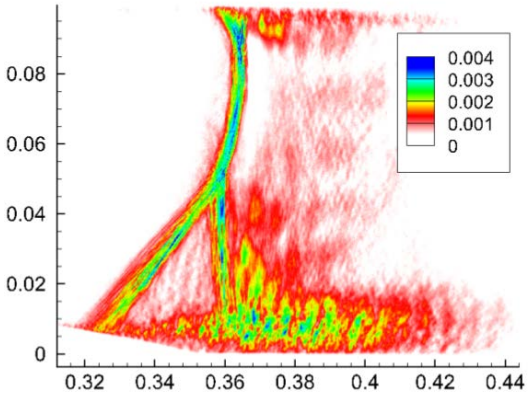

(a) Fourier mode of the longitudinal density gradient from Sartor et al. [154].

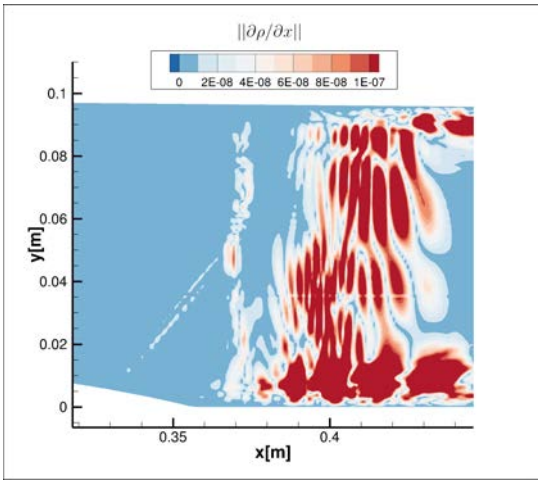

(b) SPOD mode of the longitudinal density gradient.

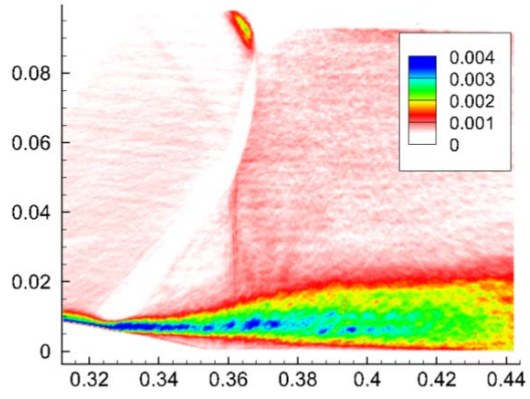

(c) Fourier mode of the vertical density gradient from Sartor et al. [154].

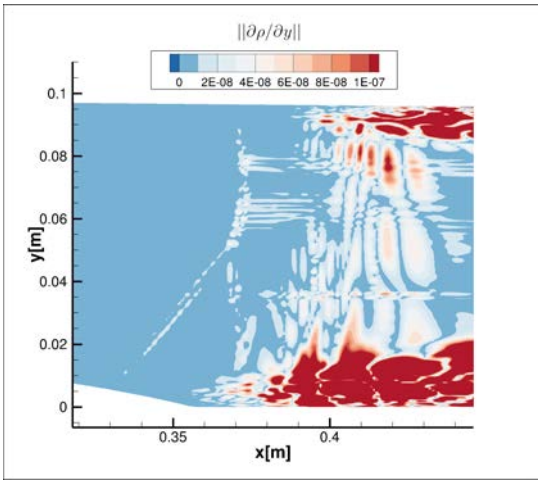

(d) SPOD mode of the vertical density gradient.

Figure VI.25: Comparison between Schlieren Fourier modes and ZDES SPOD modes of density at 3906Hz (59% of energy).

VI.2 Conclusion

The RANS model has proven its capacity to capture the principle characteristics of the flow in the S8Ch wind tunnel. It has been successfully compared to PSP and static pressure measurements, colored oil flow visualization and 2D PIV for the central separation. These comparison reveal that the separation zones are well captured along the wall of the wind tunnel even if their height amplitude may be over estimated.

The tomographic PIV method has been compared to previous 2D PIV and LDV results. It showed satisfying results down to 2.5 mm above the lower wall of the test section. It has allowed to measure 3D variations of the SWBLI. This method is promising even if the results obtained are perfectible due technical limitations in the boundary-layer and the corner region.

The Zonal Detached Eddy Simulation has failed to completely capture the exact physics of the flow observed in the wind tunnel with a main default on the development of turbulence at the beginning of the central separation zone. This may be due to the mesh being too coarse close to the mixing layer which is situated above the highly refined zone associated with the boundary-layer. This default may also be due to the fact that the height of the separation zone is close to the the size of the incoming boundary-layer. A ZDES mode 3 should be tested on this configuration. This more complex modeling uses LES down to around 10% of the boundary-layer and synthetic turbulence injection in the interface between URANS and LES. It enables the flow to develop more rapidly turbulent structures.

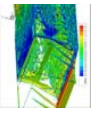

The massive central separation predicted by the ZDES modeling seems to feedback the corner flow separation and to reduced its size. Nevertheless, even with all the defaults pointed out before, this modeling allows to capture the main dynamic of the flow. The local pressure sensors capture the same characteristic frequencies as the previous experimental studies: 300Hz for the shock-wave unsteadiness and 4kHz for the Kelvin Helmholtz instability developing in the mixing layer.

The modeling of a transonic Shock-Wave / Boundary-Layer Interaction with the four walls in experimental conditions remains a challenge due to the wide range of frequency involved and to the intense interaction between all the different separation zones.

The total pressure losses in the far downstream flow, have confirmed the presence of the three main separation zones, the central one and the two corner ones. Even if the levels are globally comparable, the RANS calculation seems to slightly overpredict the corner flow separation. Nevertheless, the RANS calculations and the tomographic PIV measurements are in good agreement on the two median planes of the most centered volumes.

VII

Characterization of the controlled cases

Depuis que l'avion s'est envolé sans la permission des théoriciens, les techniciens se moquent des théoriciens.
Alain

Objectives

The results of the experimental tests of the two control cases presented in Chap. V are presented and compared to the uncontrolled case. The numerical modeling of controlled and uncontrolled cases are also compared to validate the interest of RANS modeling.

The Control 1 case is first detailed as well as different variations of the control method (frequency variation and with or without corner control). The Control 2 is then presented following the same order. In a conclusion, the different measurements performed are summed up and compared to other control configurations.

Contents

VII.1 The Control 1 test case

The characterization of the Control 1 case is now presented. The reader is referred to Chap. V for a detailed presentation of the characteristics of the control. The positions and angles of the jets are summed up in Table V.2. The Control 1 configuration results from an adaptation of the optimal configuration found by the optimization process presented in Chap. IV. The jets are slightly reverse with respect to the main flow.

1.a Recall of the RANS results

In order to visualize the main flowfield of the controlled case, the result of the RANS calculation is presented on Fig. VII.1. The reversed flows are delimited by the white surfaces and the vorticies developed by the jets are shown colorized with the longitudinal vorticity. The slightly reversed jets produced counter-rotating vorticies which impact the SWBLI.

It can be seen that a central separation remains smaller than in the uncontrolled case and some other small separations zones appear along the width of the test section. The corner flow separation is also modified with respect to the reference case.

The impact of the control is also represented on the downstream plane displaying the stagnation pressure losses. This general pattern will now be studied more precisely.

1.b Laser sheet visualizations

In order to verify the capacity of the fluidic VGs to generate vortices and in order to study the structure of these vorticies, laser sheet visualizations have been performed. The flow is saturated with synthetic smoke (Pro-Smoke Super Fluid containing polyglycols) and a thin laser sheet is placed perpendicularly to the flow in order to illuminate it. Due to their density, the particles are naturally shifted away from the zones of strong vorticity. This allows to observe the presence of the vortices generated by the angled jets / cross flow interaction.

The camera placed on the opposite side of the wind tunnel captures the trace of the vortices presented on Fig. VII.2.

The plane considered here is placed 20 mm downstream of the fluidic VGs. The vorticies are qualitatively compared to the vorticity levels computed with the RANS calculations. A good global agreement is found with structures located slightly away from the lower wall except in the corner where the vorticies are placed lower because the jet controlling the corner separation is placed more downstream than the central VGs. The RANS calculation

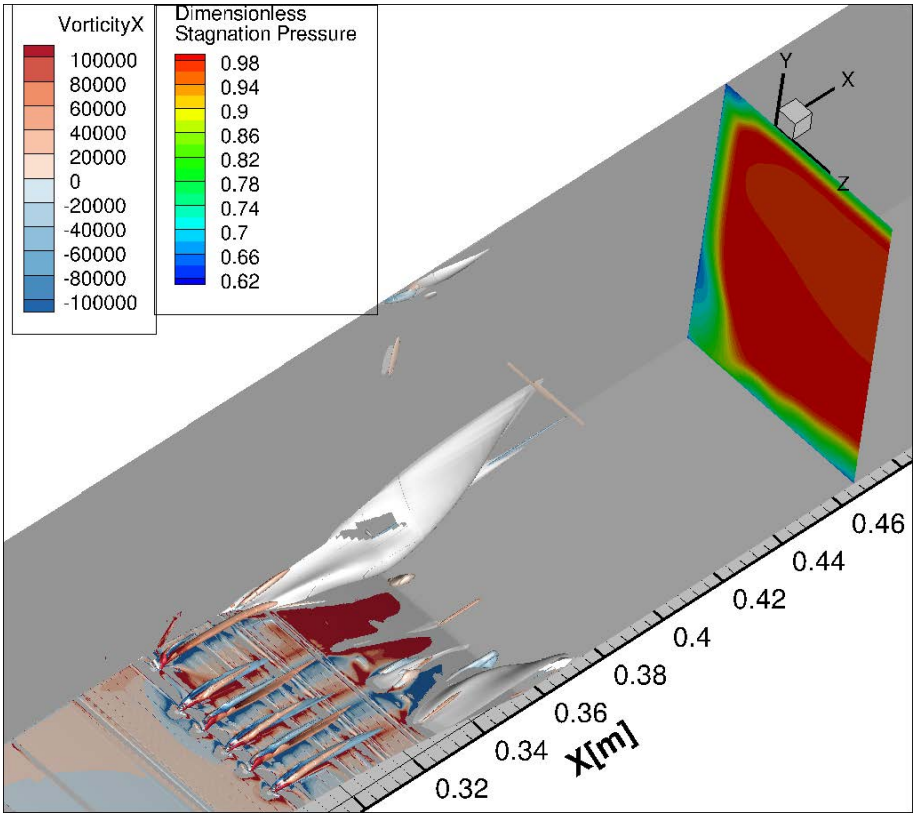

Figure VII.1: Non dimensionalized stagnation pressure on the DC50 plane, volume of the reverse flow-white surface- and Q criterion equal to $3 \cdot 10^8$ isosurface colorized with longitudinal vorticity for the Control 1 case.

manages to predict efficiently the interaction between the jets and the main flow. These vorticies need to be measured using hot wire or Pitot probe in order to validate more quantitatively their structures. This confirms that the incoming flow before the SWBLI is similar between numerical and experimental data.

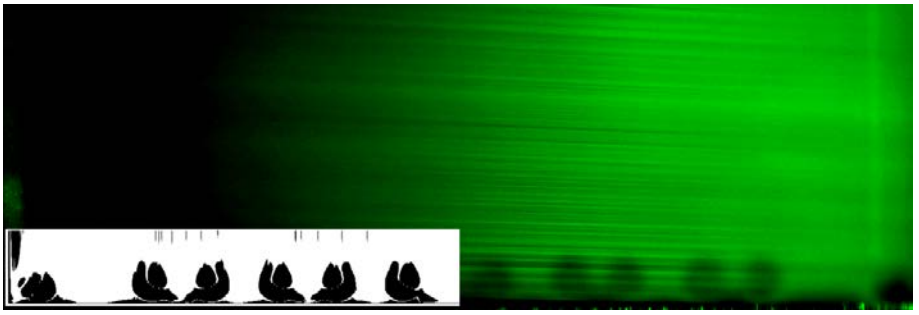

Figure VII.2: Laser sheet visualization of the vorticies generated by the jets of the Control 1 compared to the $30\,000\,\mathrm{s}^{-1}$ vorticity level from RANS calculations- in black and white- in the plane $x = 300\,\mathrm{mm}$.

1.c Schlieren visualizations

In order to establish the impact of the control, the Schlieren visualization of the controlled interaction is presented on Fig. VII.3a) and compared to reference case on Fig. VII.3b) using a superposition of the two Schlieren visualizations. It can be seen that the shock-wave is strongly impacted by the control. The front leg of the λ shock-wave is slightly pulled up and the upper part of the shock is rectified.

This phenomenon may be linked to the reduction of the central separation zone. Indeed, the flow rate being fixed by the second throat, the reduction of the separation zone generates a larger area available for the inviscid flow. In order to conserve the mass flow rate, the velocity needs to be reduced and thus, the shock-wave needs to be stronger. The shock-wave is consequently moved up and intensified.

The advantage of the use of fluidic VGs is that they can be activated once the exact uncontrolled configuration has been retrieved. This allows to ensure that the controlled configuration can be compared to the uncontrolled configuration. The global pressure loss is conserved as the stagnation and the exhaust pressures are keep constant (since the stagnation pressure injected by the jets is negligible). However, the measure of stagnation pressure just after the SWBLI in the RANS calculation and in the experiment allows to measure the variation of pressure losses only in the SWBLI and to separate it from the rest of the losses (for example, the boundary-layer development after the interaction).

The small variation of the shock position is also confirmed by the position of the separation lines on the oil flow visualizations.

Three small compression waves occurring in front of the SWBLI can also be noticed. The evanescent middle one is due to the jets and the two other ones are due to marginal steps at the border of the control strip. Nonetheless, these small steps do not modify the main flow as they are of negligible height with respect to the boundary-layer.

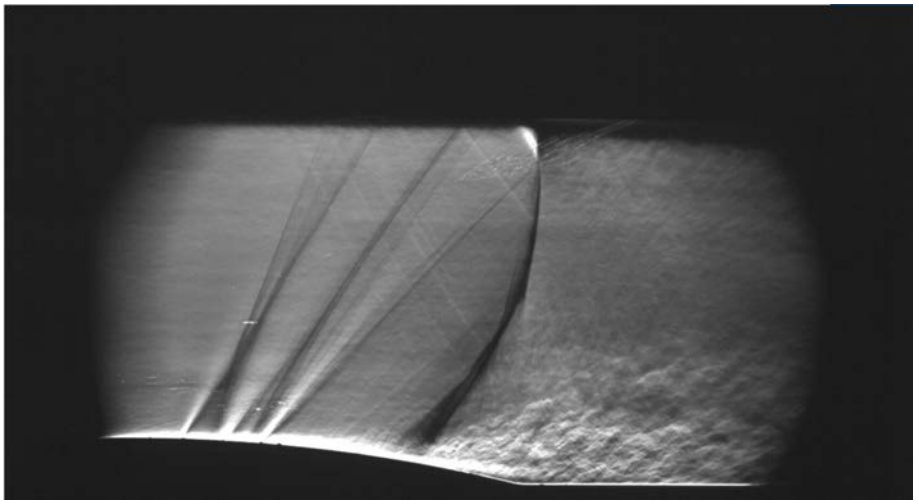

(a) Control 1

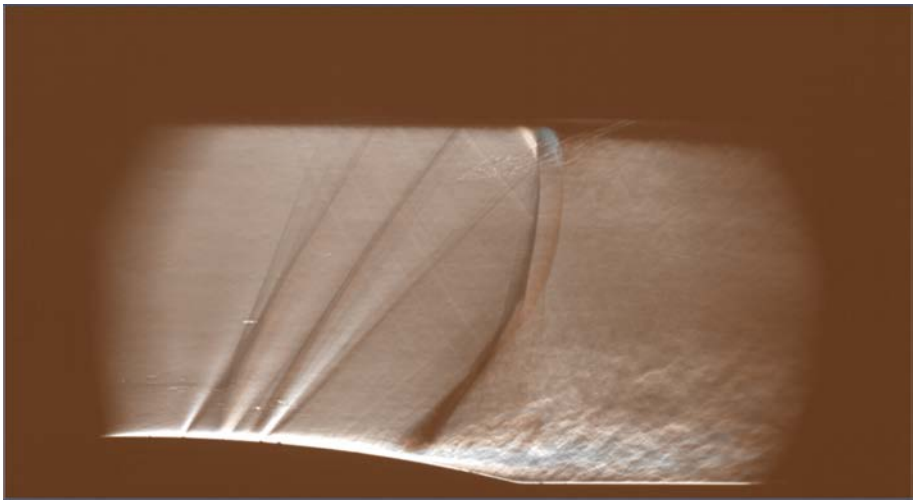

(b) Superposition of Control 1 and reference case.

Figure VII.3: Schlieren visualizations using horizontally oriented knife edge.

1.d Friction lines

The oil flow visualization on the lower wall is compared to the uncontrolled case on Fig. VII.4. The similar comparison between the friction lines of the RANS calculation for controlled and uncontrolled cases is presented on Fig. VII.5. The positions of the Kulite sensors and the tomographic PIV are again displayed to ease the understanding and the interpretation of these measurements.

The controlled flow becomes really complex and 3D. The separation line is not straight anymore, and the large separation zone is replaced by several foci. One large pair of foci generates what can be seen as the central separation. This separation is strongly reduced compared to the uncontrolled case, it only takes place between $x = 320\,\text{mm}$ and $x = 360\,\text{mm}$ (compared to $x = 320\,\text{mm}$ and $x = 380\,\text{mm}$ and between $z = \pm 10\,\text{mm}$. One other pair of foci is placed at the quarter of the test section. This separation zone is really small compared to the central one. Finally, the corner flow separation is strongly reduced.

It is divided by two in width and starts later than the one of the uncontrolled case.

It can be seen that the RANS calculation manages to capture the variation of the shock shape but as for the reference case, it overestimates the length of the separation zones. Furthermore, in this complex 3D flow pattern, the pair of foci close to the corner flow separation is not well predicted.

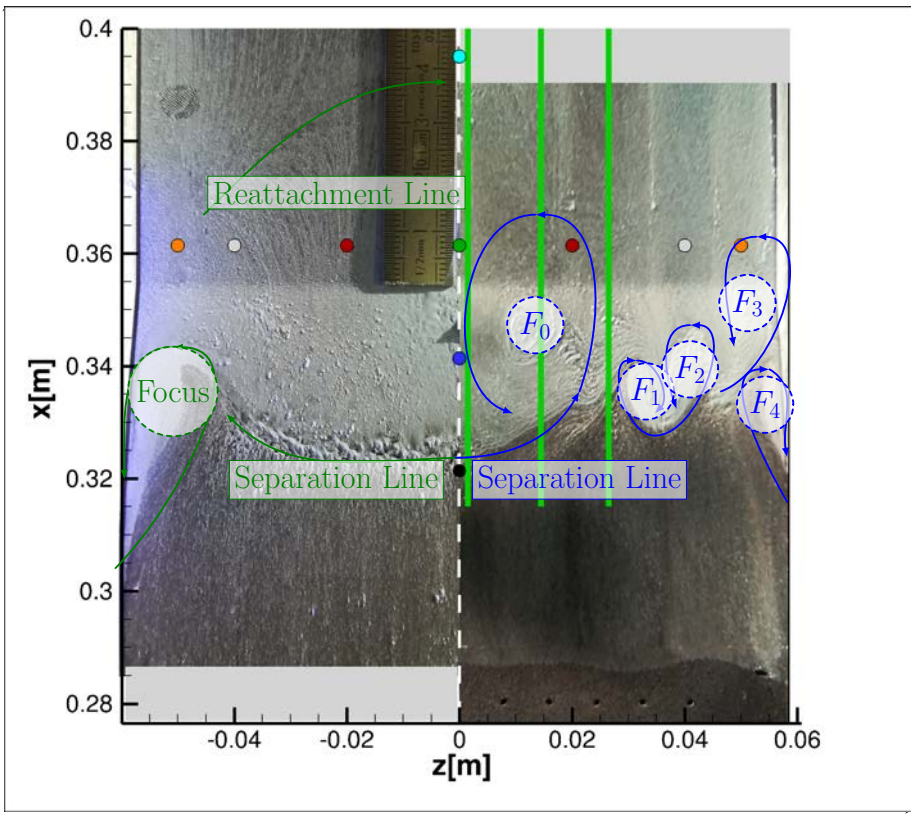

Figure VII.4: Experimental friction lines on the lower wall of the wind tunnel, comparison between uncontrolled and Control 1 respectively left and right. The dots correspond to Kulite sensors positions, their colors match the ones of the pre-multiplied spectra presented in subsection 1.g. The three green lines correspond to the median planes positions of the three PIV volumes.

The lateral wall friction lines of the RANS calculation and of oil flow visualization of uncontrolled and controlled cases are presented on Fig. VII.6. The separation on the lateral wall is well predicted by the RANS calculation. The corner separation of the reference case is shifted away from the corner and takes the place of the small lateral separation which was appearing in the reference case. The smaller amount of white oil is also an hint of a smaller interaction with the lower wall corner separation. In this case, the lateral jet slightly reverse, seems to be effective to control the corner flow separation as predicted by the optimization process presented in Chap. IV. This kind of control with a corner flow separation becoming a smaller lateral separation agrees with the effective mechanical VGs control presented in Koike and Babinsky [103].

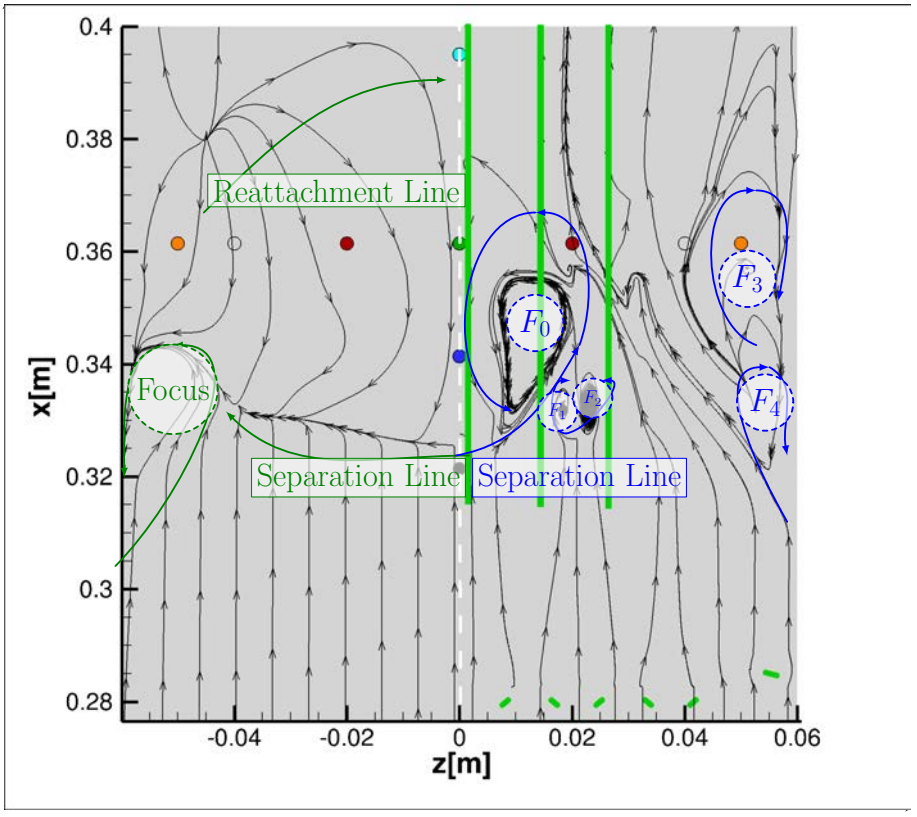

Figure VII.5: RANS friction lines on the lower wall of the wind tunnel, comparison between uncontrolled and Control 1 respectively left and right. The dots correspond to experimental Kulite sensors positions, their colors match the ones of the pre-multiplied spectra presented in subsection 1.g. The three green lines correspond to the median planes positions of the three PIV volumes.

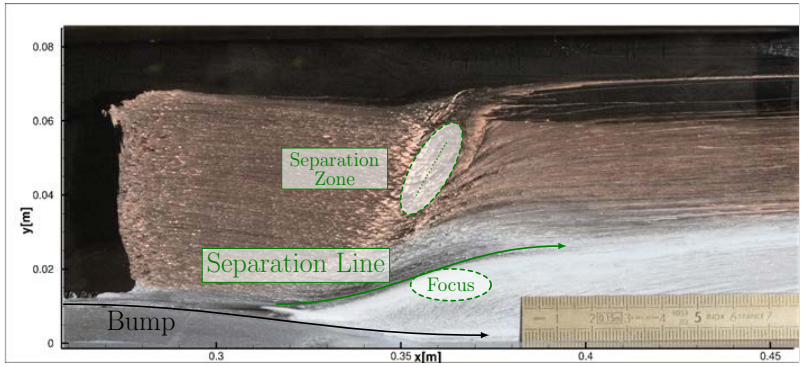

(a) Experiment uncontrolled.

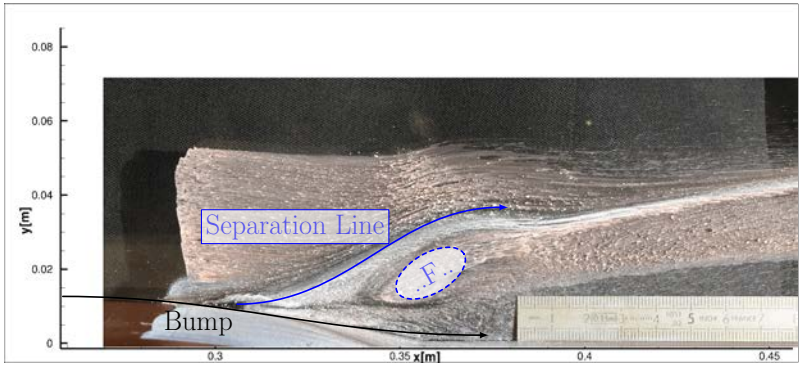

(b) Experiment Control 1.

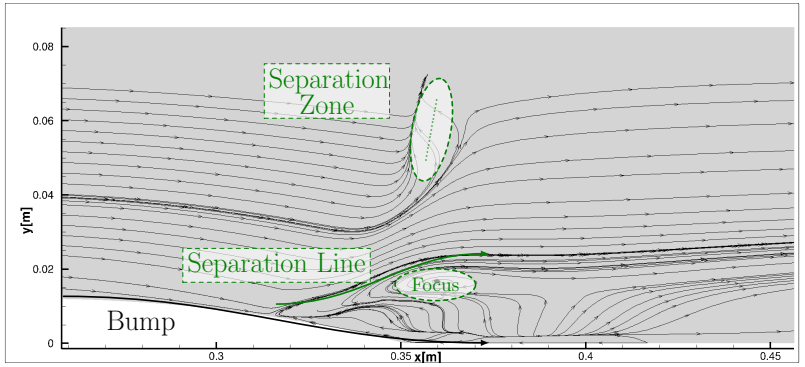

(c) RANS uncontrolled.

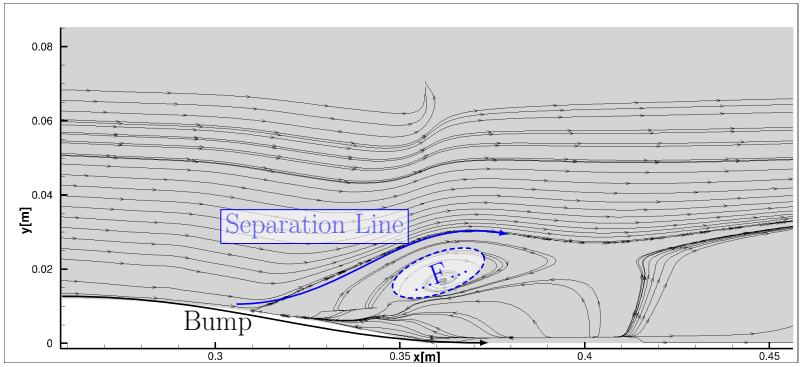

(d) RANS Control 1.

Figure VII.6: Friction lines of experimental and RANS on the lateral wall, respectively below and above for reference and Control 1 case respectively left and right.

1.e Static pressure distribution

The static pressure distribution measured along the median line of the wind tunnel for the Control 1 case is presented on Fig. VII.7. It is important to notice that this curve only characterizes the small central separation zone. Once again, the reduction of the central separation is confirmed with a pressure plateau smaller than in the reference case.

The same observation can be made with the pressure calculated using RANS presented on Fig. VII.8. The advantage of RANS is that it confirms the existence of a compression wave occurring in front of the VGs. This latter one was not noticed in the experimental data due to the lack of sensors in this region.

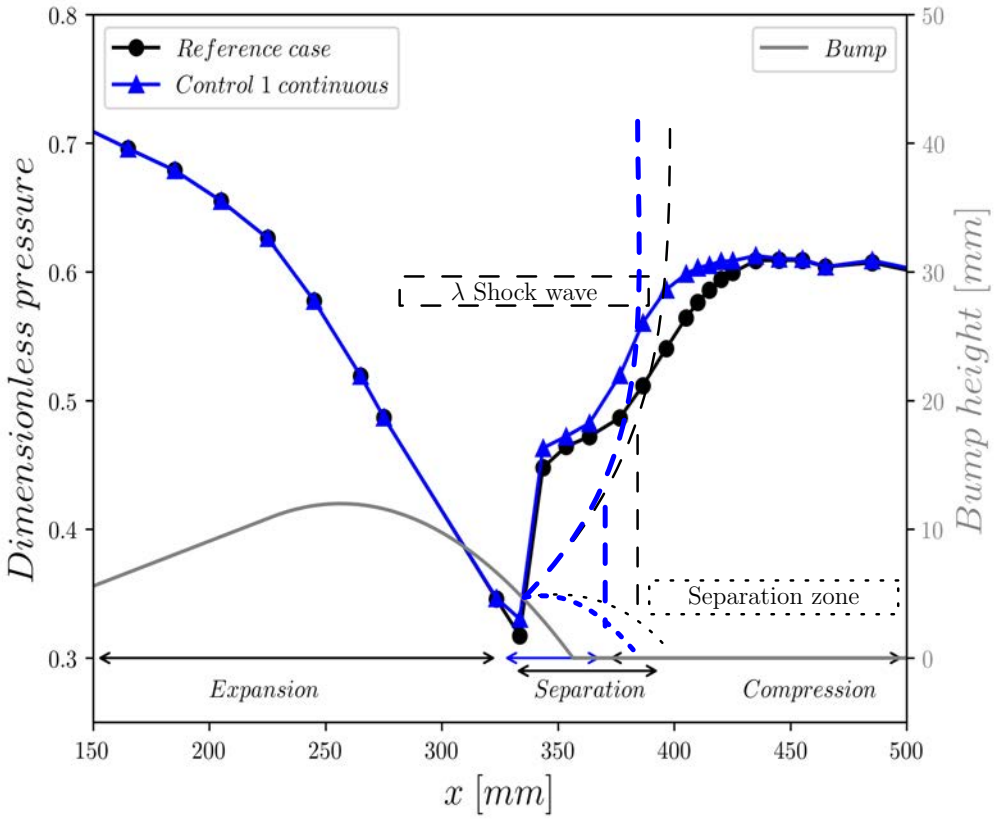

Figure VII.7: Experimental static pressure distribution in the median plane for the Control 1 case, compared to the reference case.

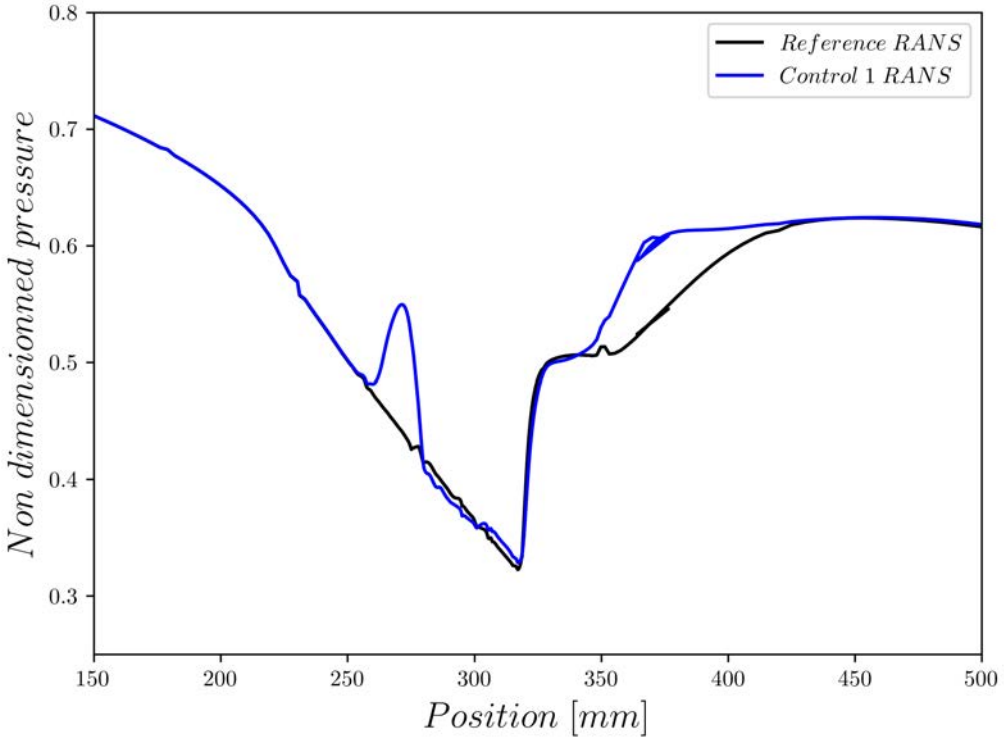

Figure VII.8: RANS static pressure distribution in the median plane for the Control 1 case, compared to the reference case.

1.f PIV measurements

The mean longitudinal and vertical velocities on the three planes presented on Fig. VII.4 for the Reference case and the Control 1 case are displayed using tomographic PIV and RANS calculations on Fig. 1.f and Fig. 1.f respectively. The white rectangles on the RANS maps are the rest interpolation zones which are blanked for better readability. The separation occurring in the central plane is of higher amplitude in height than the one occurring in the reference case. Nevertheless, the separation is smaller in length, as it is observed on the oil flow visualization. Moreover, this separation is smaller in width as it is not anymore visible on the two other lateral planes. This is well retrieved on the RANS calculations.

As before, on the central plane, the vertical velocity is going downward before the shock and is slightly going upward after the shock due to the separation zone. However, on the two lateral planes, in the absence of reverse flow, after the shock-wave, the flow is still directed downward. This is indicative of smaller influence of the lateral foci visible on the friction lines. The RANS calculations are really coherent on this point. This explains the difficulty to find precisely the position of the stronger foci in these lateral zones.

Reference Control 1

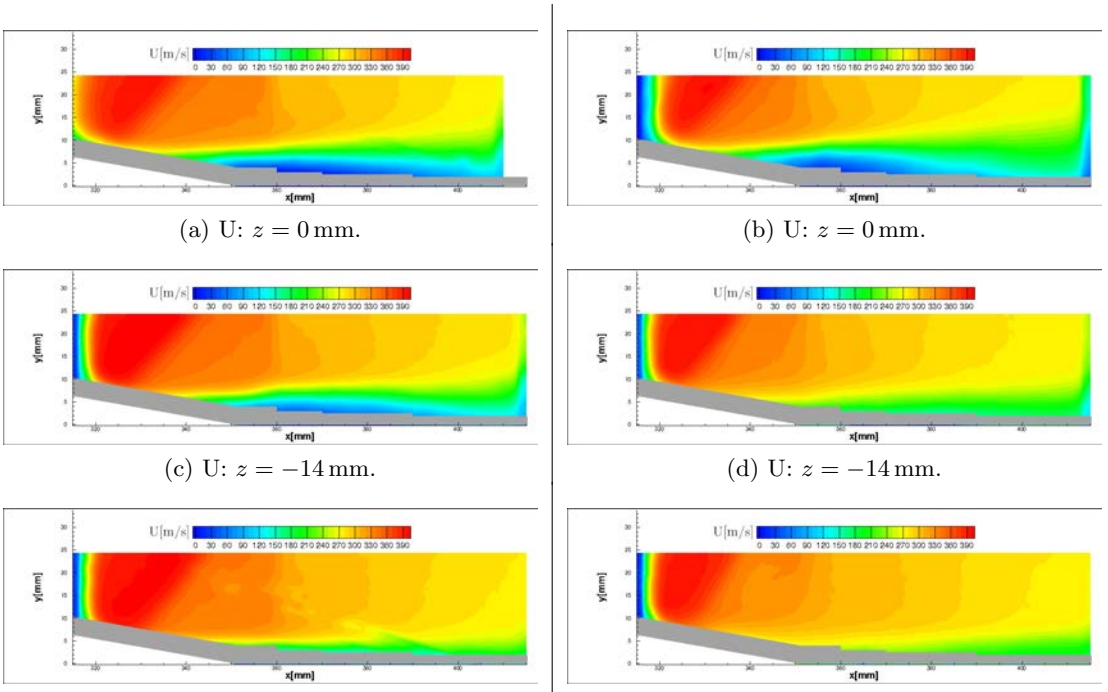

(a) U: $z = 0\,\text{mm}$. (b) U: $z = 0\,\text{mm}$.

(c) U: $z = -14\,\text{mm}$. (d) U: $z = -14\,\text{mm}$.

(e) U: $z = -26\,\text{mm}$. (f) U: $z = -26\,\text{mm}$.

Tomographic PIV

RANS

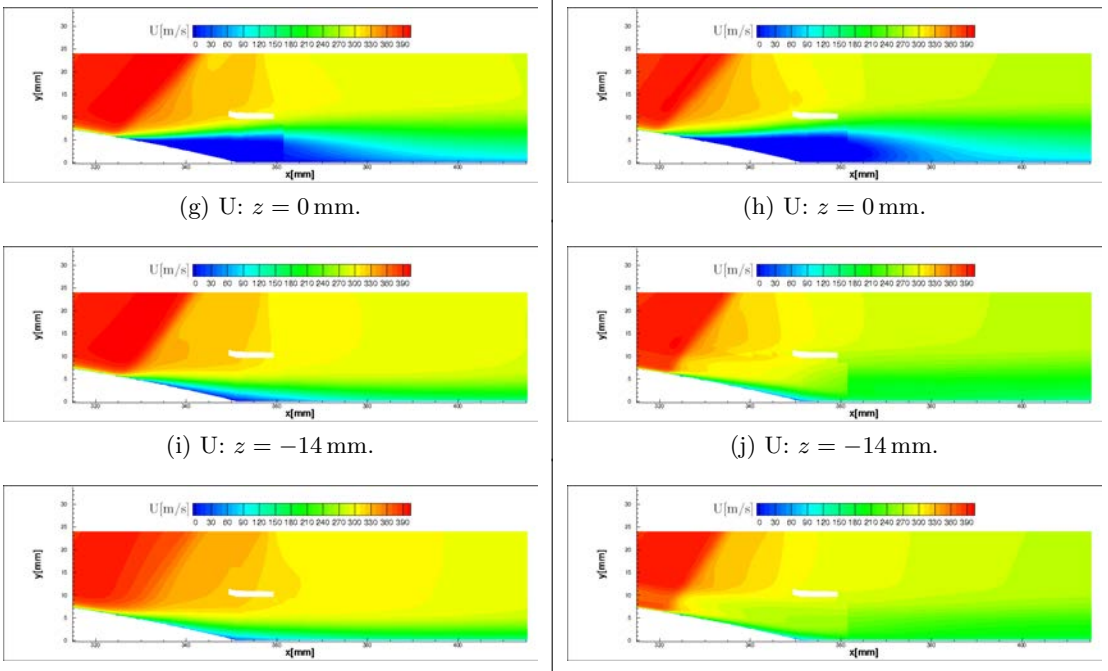

(g) U: $z = 0\,\text{mm}$. (h) U: $z = 0\,\text{mm}$.

(i) U: $z = -14\,\text{mm}$. (j) U: $z = -14\,\text{mm}$.

(k) U: $z = -26\,\text{mm}$. (l) U: $z = -26\,\text{mm}$.

Reference Control 1

Figure VII.9: Comparison of longitudinal velocity fields given by the tomographic PIV and RANS modeling (respectively up and down) for the reference and Control 1 cases(respectively left and right), at three different lateral planes.

Reference | Control 1

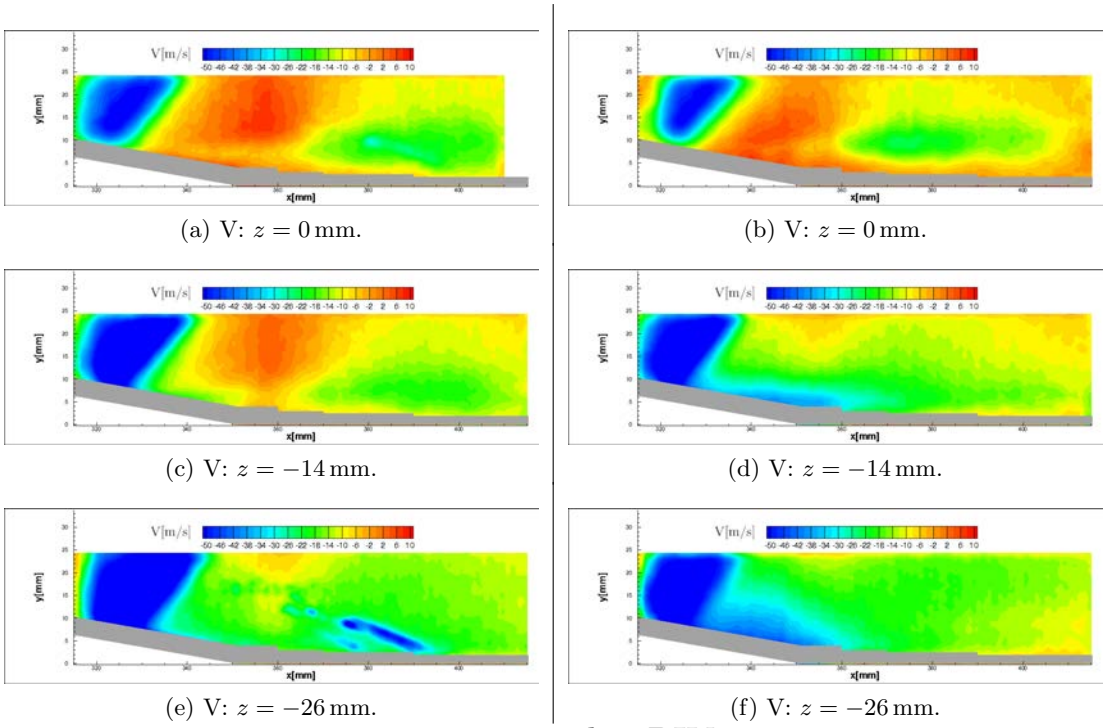

(a) V: $z = 0\,\text{mm}$. (b) V: $z = 0\,\text{mm}$.

(c) V: $z = -14\,\text{mm}$. (d) V: $z = -14\,\text{mm}$.

(e) V: $z = -26\,\text{mm}$. (f) V: $z = -26\,\text{mm}$.

Tomographic PIV

RANS

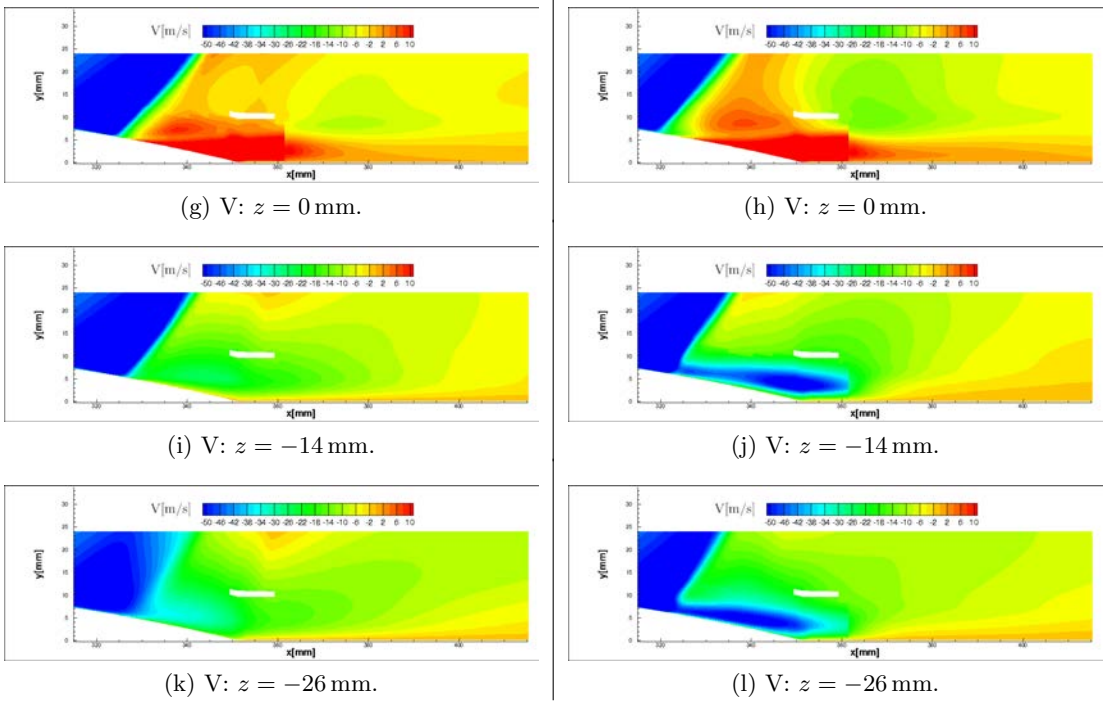

(g) V: $z = 0\,\text{mm}$. (h) V: $z = 0\,\text{mm}$.

(i) V: $z = -14\,\text{mm}$. (j) V: $z = -14\,\text{mm}$.

(k) V: $z = -26\,\text{mm}$. (l) V: $z = -26\,\text{mm}$.

Reference | Control 1

Figure VII.10: Comparison of longitudinal velocity fields given by the tomographic PIV and RANS modeling (respectively up and down) for the reference and Control 1 cases (respectively left and right), at three different lateral planes.

The transverse velocity of the three planes studied, are presented for the reference case and the Control 1 case are presented on Fig. 1.f. The 2D Reynold shear stress measured using tomographic PIV is presented on Fig. reffig:uvCont1. It can be seen that for the transverse velocity, the distribution differs from the reference case and the direction matches the one of the experimental friction lines. The RANS agrees with the tomographic PIV on this case.

For the Reynolds shear stress, the global level in the controlled case is strongly reduced compared to the uncontrolled case, even for the central plane. On this latter one, the peak of Reynolds shear stress appears earlier than in the reference case, confirming that the separation is smaller in length. Besides, the shear layer is placed higher in the controlled case. This may be due to the shock-wave appearing earlier and thus higher on the bump. This also reveals the presence of larger eddies at higher wall distance in the control case. This is confirmed by the Schlieren visualizations of the reference case and controlled case (see Fig. VII.3).

Reference | Control 1

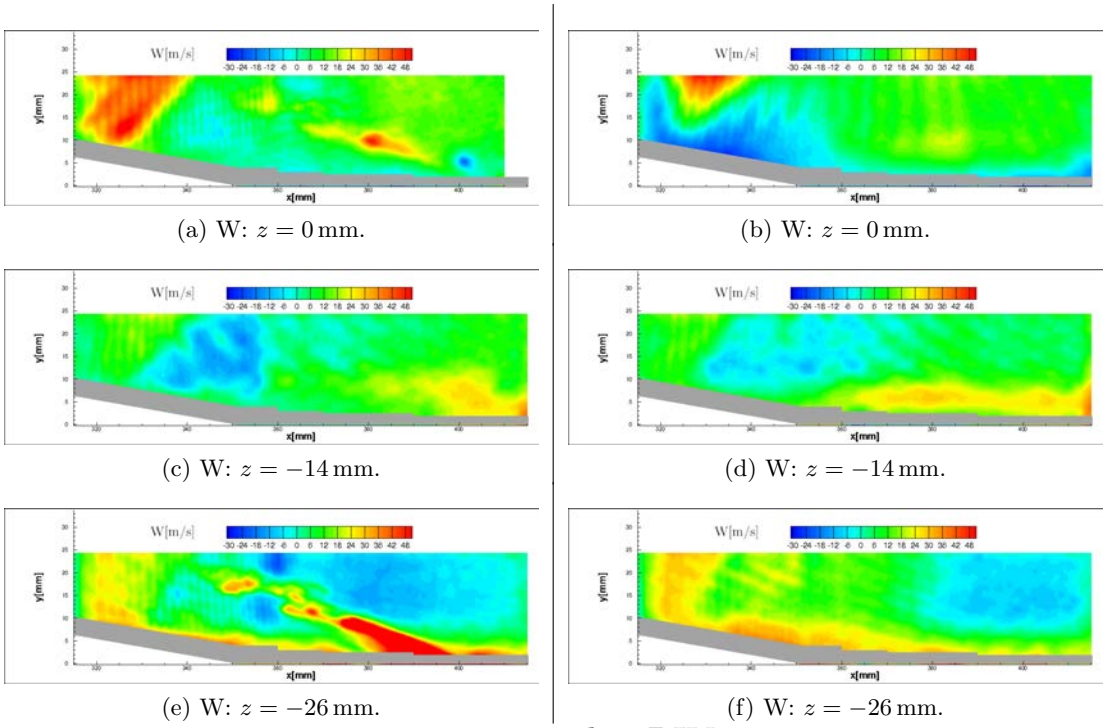

(a) W: $z = 0\,\text{mm}$. (b) W: $z = 0\,\text{mm}$.

(c) W: $z = -14\,\text{mm}$. (d) W: $z = -14\,\text{mm}$.

(e) W: $z = -26\,\text{mm}$. (f) W: $z = -26\,\text{mm}$.

Tomographic PIV

RANS

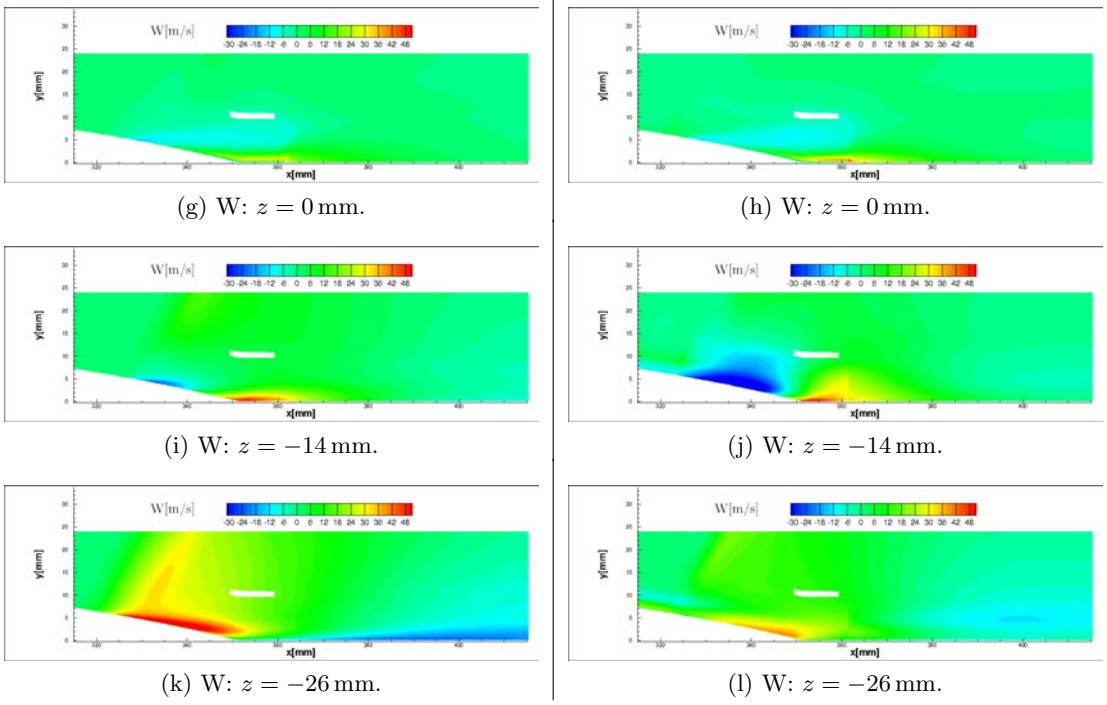

(g) W: $z = 0\,\text{mm}$. (h) W: $z = 0\,\text{mm}$.

(i) W: $z = -14\,\text{mm}$. (j) W: $z = -14\,\text{mm}$.

(k) W: $z = -26\,\text{mm}$. (l) W: $z = -26\,\text{mm}$.

Reference | Control 1

Figure VII.11: Comparison of transverse velocity fields given by the tomographic PIV and RANS modeling (respectively up and down) for the reference and Control 1 cases (respectively left and right), at three different lateral planes.

Reference | Control 1

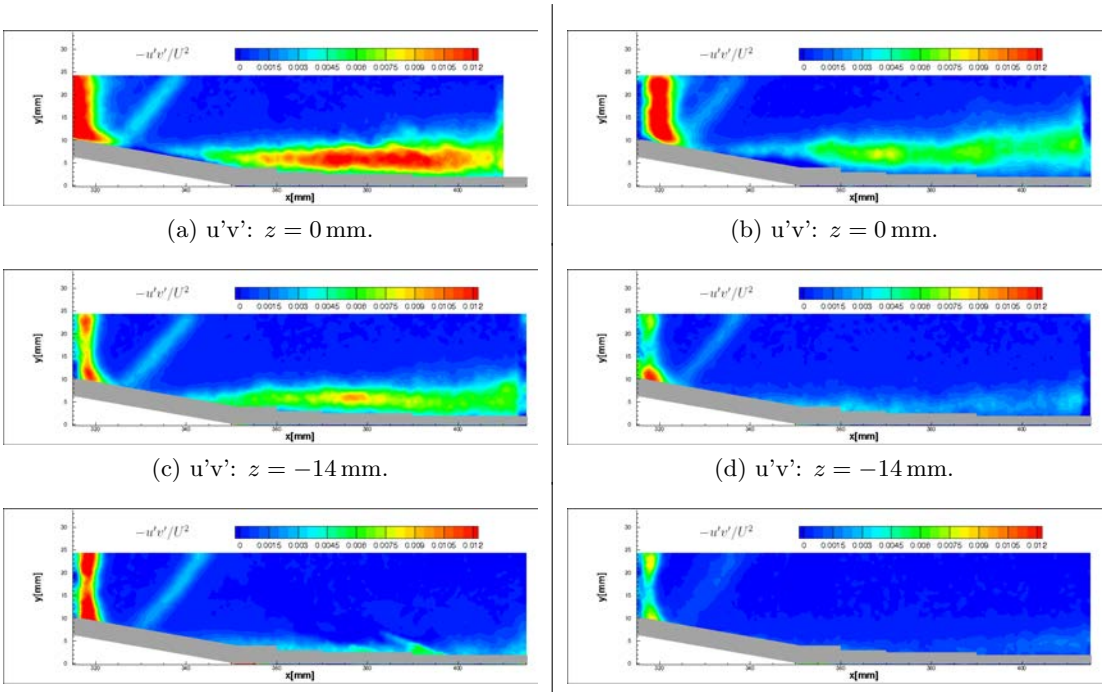

(a) u'v': $z = 0\,\text{mm}$. (b) u'v': $z = 0\,\text{mm}$.

(c) u'v': $z = -14\,\text{mm}$. (d) u'v': $z = -14\,\text{mm}$.

(e) u'v': $z = -26\,\text{mm}$. (f) u'v': $z = -26\,\text{mm}$.

Tomographic PIV

Figure VII.12: Comparison of longitudinal velocity fields given by the tomographic PIV for the reference and Control 1 cases (respectively left and right), at three different lateral planes.

The longitudinal velocity distribution in the plane $x = 370\,\mathrm{mm}$ is presented on Fig. VII.13 for RANS and tomographic PIV. The impact of the control on the flow is clearly visible. The velocities lower than $100\,\mathrm{m\,s^{-1}}$ are only displayed in the central volume. It can be noticed that the tomographic PIV has trouble to measure the rapidly changing velocity distribution on the sides of the volumes, provoking a discontinuity between the central and the first lateral volume and a large uncertainty on measurements far from the median plane of the test section..

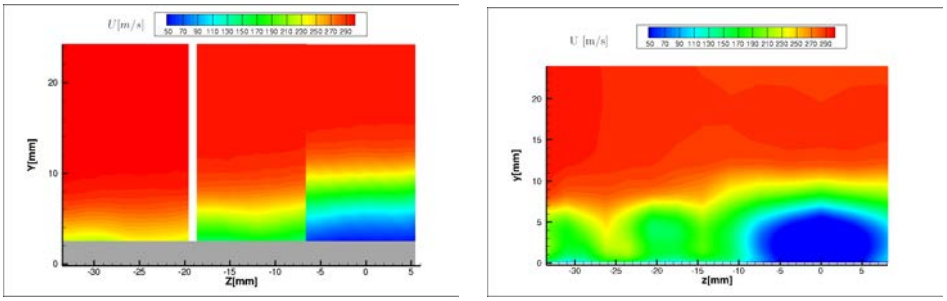

(a) Experiment. (b) RANS.

Figure VII.13: Lateral distribution of longitudinal velocity in the plane $x = 370\,\mathrm{mm}$ for the Control 1 case.

Finally, the same 3D visualization as the one presented for the reference case on Fig. VI.18 is presented for the Control 1 case on Fig. VII.14. The impact of the control is clearly visible, an iso-surface of $u = 100\,\mathrm{m\,s^{-1}}$ is now only visible on the center volume. Furthermore, the supersonic tongue varies in length along the volumes more quickly than in the reference case and the shock-wave is displaced upstream and rectified.

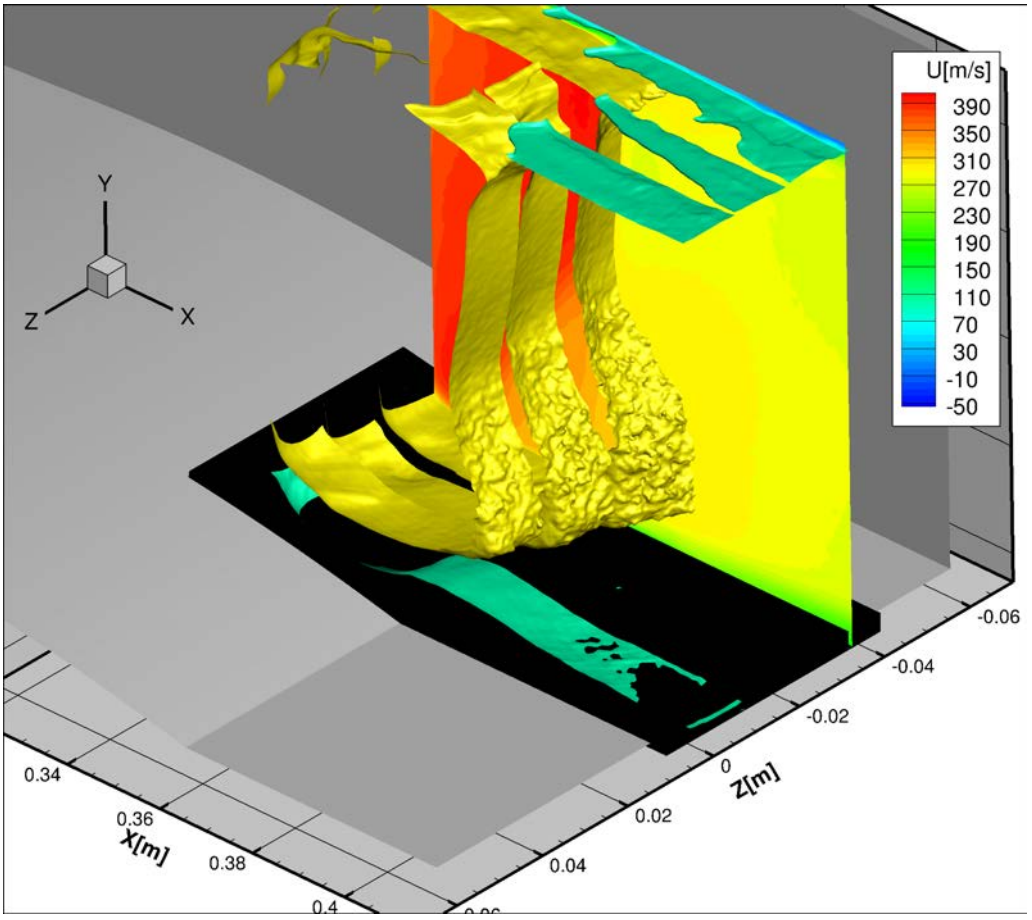

Figure VII.14: 3D visualisation of the SWBLI in the Control 1 case, two iso-surfaces for $u = 300\,\mathrm{m\,s^{-1}}$ (yellow) and $u = 100\,\mathrm{m\,s^{-1}}$ (green). The plane $z = -40\,\mathrm{mm}$ is also represented.

1.g Pressure fluctuations measurements

The pre-multiplied spectra of the longitudinal and lateral sensors are presented on Fig. 1.g. First, the same distribution pattern as for the reference case is observed. Two distinct frequencies impact the flow. In this case, the lower frequency on the central sensors is more than double, with a peak close to 800Hz. The higher one being kept at 4kHz. It can be noticed that the energy in the first sensor positioned at $x = 316.4\,\mathrm{mm}$ is far higher than previously because the shock-wave is shifted by the control and is really closer to this sensor as it can be seen on Fig. VII.4. A study of variations of the shock-wave position in the main direction, presented in Appendix A.6 shows that the intensity measured by this sensor is rather sensitive to the shock position. On the contrary, the downstream sensors capturing the Kelvin Helmholtz frequency are not sensitive to the shock position. Indeed, the lowering of the peaks of the downstream sensors in the controlled case is not linked to the shift in position of the shock-wave but either to the reduction of the separation zone.

With respect to the lateral sensors, a strong modification is visible. This is linked to the modification of the pattern of the separation zone which was mostly 2D and becomes strongly 3D. Thus, the two sensors close to the lateral wall are strongly modified while

the central ones, still placed downstream of the central separation zone are kept still. The sensor placed at $z = -40\,\text{mm}$, a bit behind a small zone of separation with two foci, sees both the shock-wave frequency, even if attenuated at 800Hz and the Kelvin Helmholtz frequency observed in the reference case for the lateral sensors at 6kHz.

The last sensor, placed at $z = -50\,\text{mm}$, behind the corner flow separation sees more strongly, the shock frequency and the Kelvin Helmholtz frequency which is slightly shifted to 3kHz. This was already visible in the reference case on Fig. VI.21. This may be due to an anisotropic development of eddy structures in the corner. The increase of energy in this region may be due to the fact that the corner separation is shifted downstream in the control case and thus the sensor is closer to the end of the separation zone as it can be seen on Fig. VII.4.

Reference Control 1

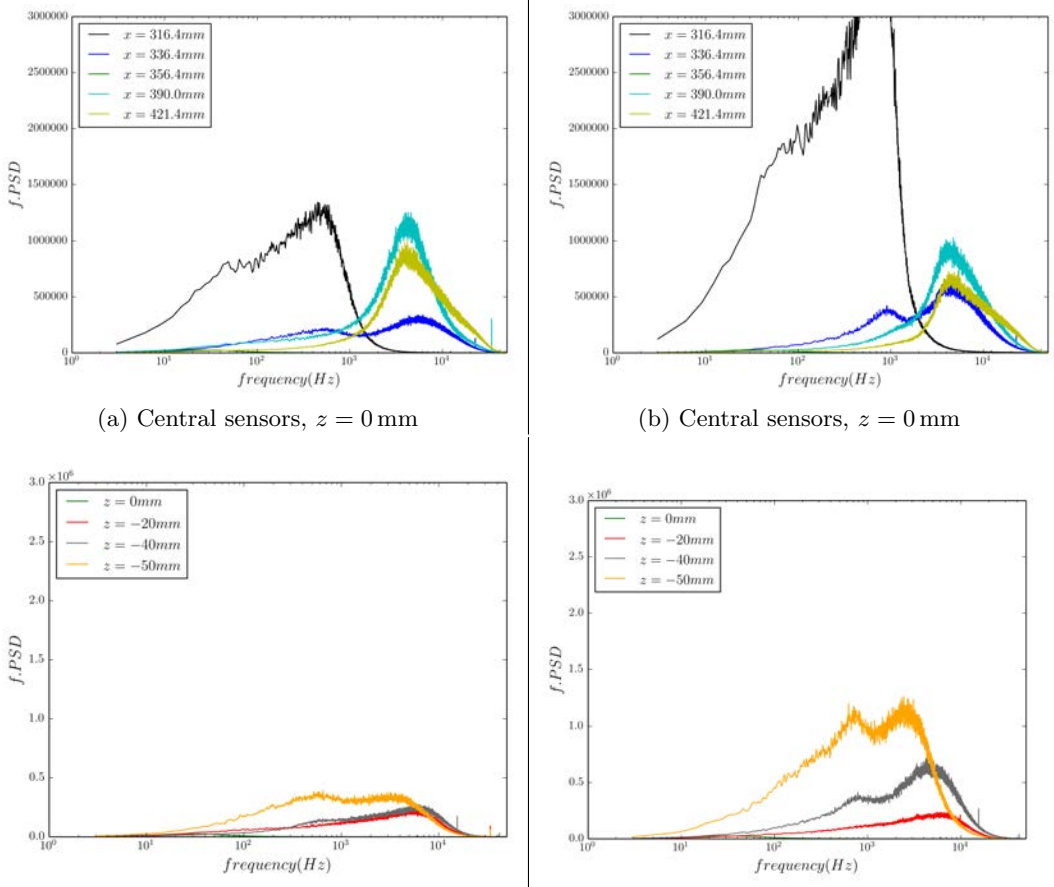

(a) Central sensors, $z = 0\,\text{mm}$

(b) Central sensors, $z = 0\,\text{mm}$

(c) Lateral sensors, $x = 356.4\,\text{mm}$

(d) Lateral sensors, $x = 356.4\,\text{mm}$

Figure VII.15: Pre-multiplied spectra obtained by the Kulite sensors for the Reference case and the Control 1 case (respectively left and right).

To conclude, the control of the interaction changes the frequency of the shock. This is coherent with the fact that this frequency is linked to the size of the separation zone (see Souverein and Debiève [159]). The new shock frequency close to 800Hz seems to be identical along the width of the shock-wave even if several separation zones of different size coexist on the lower wall. The frequency linked to the Kelvin Helmholtz is, as for the reference case, not constant along the width of the wind tunnel.

The energy in the eddies, downstream of the interaction is reduced on the median line of the wind tunnel and increased in the corner.

1.h Variation of control parameters

Several variations of the Control 1 are presented. First some tests on the interest of the corner flow control are presented and then the tests of pulsed actuators are displayed.

Corner flow control tests Two different tests are performed. First, the two external jets, controlling the corner flow separation are activated alone and then all the VGs are activated except the two external ones. The static pressures of the different cases are reported on Fig. VII.16 and the pre-multiplied spectra of the two new cases are reported on Fig. VII.17.

In the case of the corner control alone, the static pressure distribution on the median plane is quite close to the uncontrolled case. Nevertheless, an impact is visible on the position of the shock-wave which is slightly moved upstream (the plateau starting earlier and the point before the shock being higher). This is confirmed by the modification of intensity seen by the Kulite sensor positioned at $x = 316.4\,\text{mm}$ when compared to the reference case on Fig. VI.21. The other only modification is the shift on the lower frequency seen by the sensor close to the wall. In the controlled case, this sensor sees two frequencies 1 and 3kHz close to the Kelvin Helmholtz frequency.

In the case where only the center VGs are activated, the static pressure distribution is similar to the case where all the VGs are activated. Thus, in the controlled case, the addition of corner control has little impact on the topology of the flow on the median line. On the flow unsteadiness, the same impact is seen as for the case where all the control is activated, except on the external sensor which sees less intensity than in the full control case. This may be due to a modification of the length of the corner flow separation.

These variations of control allow to validate that the corner VGs have a strong impact on the corner flow separation, with or without the central VGs. An oil flow visualization may allow to quantify the impact of these jets alone on the corner flow separation.

Control by pulsed jets The full control is now activated at different frequencies from 100Hz to 600Hz with two different Duty Cycles (DC): 50% and 25%. The capacity of the actuator to produce clear square signal has been validated up to 300Hz in Chap. V. Furthermore, the length of the tubes going from the actuators to the jets is small enough to allow testing some higher frequencies. The use of a Duty Cycle of 25% ensures a full closure of the actuators at higher frequencies.

The static pressure distributions of the different cases are showed on Fig. VII.18 and on Fig. VII.19. The main result is that all the pulsed controls are situated between the full control and the reference case. The main parameter governing the efficiency of the control is not linked to the frequency but rather to the Duty Cycle. Indeed, all the control cases with a Duty Cycle of 50% are superimposed and closer to the continuous control than the cases with a Duty Cycle of 25%. This suggests that the main efficiency of the control is only linked to its time of activation over a period.

A small variation is however seen at 600Hz with respect to 300, 400 and 500Hz, indeed the control is less efficient. This may be due to the fact that the actuators have more difficulties to close at this frequency.

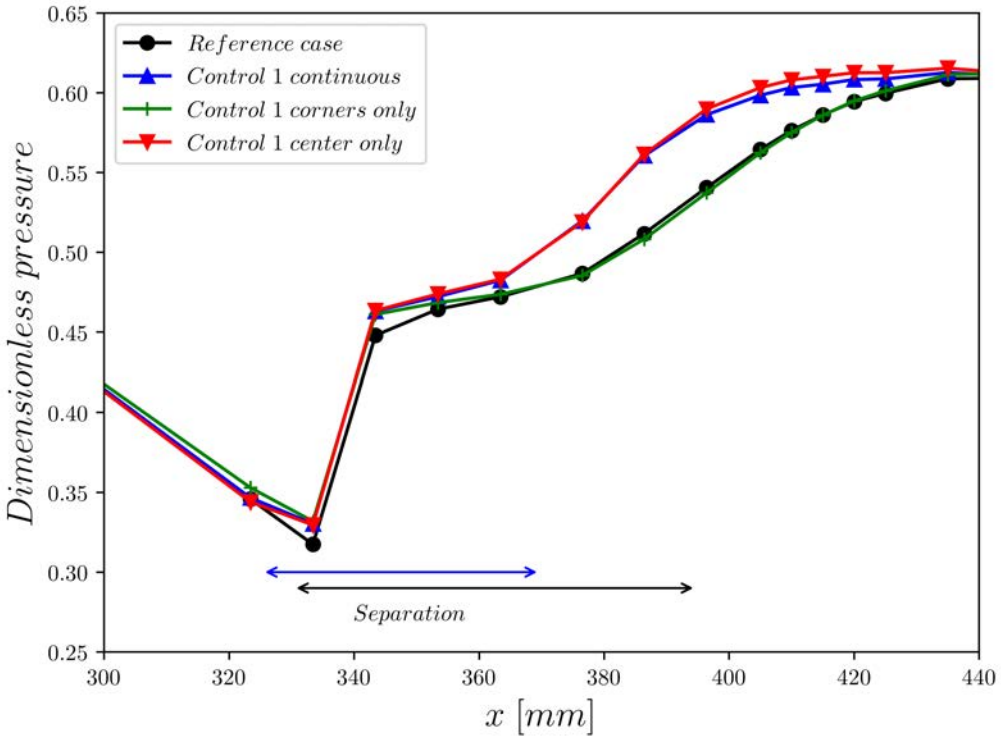

Figure VII.16: Static pressure distribution in the median plane for the Control 1 case, with full control, corners only and center only.

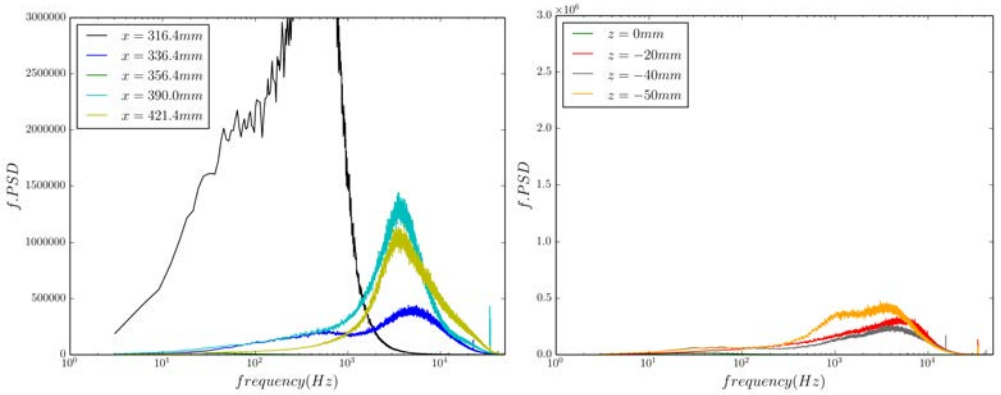

(a) Central sensors Control 1 Corners only

(b) Lateral sensors Control 1 Corners only

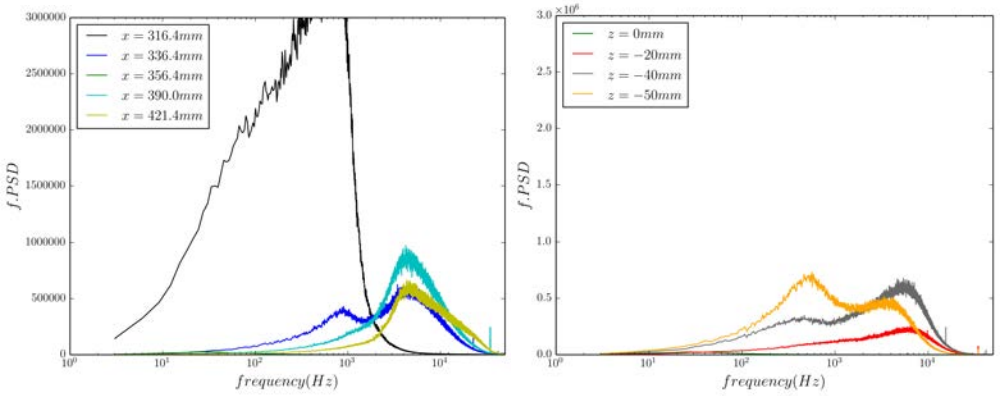

(c) Central sensors Control 1 Center only

(d) Lateral sensors Control 1 Center only

Figure VII.17: Pre-multiplied spectra obtained by the Kulite sensors of variation of continuous control of the case Control 1

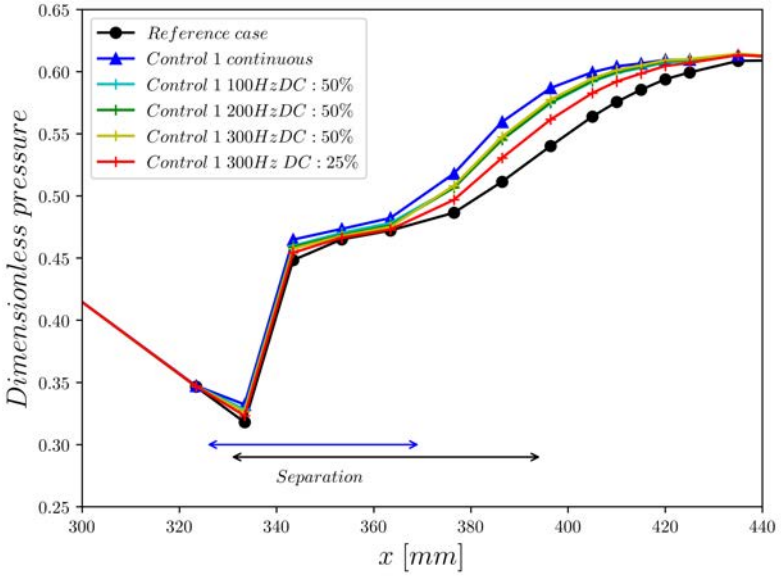

Figure VII.18: Static pressure distributions in the median plane for the Control 1 case with various frequencies compared to the reference case. Part 1

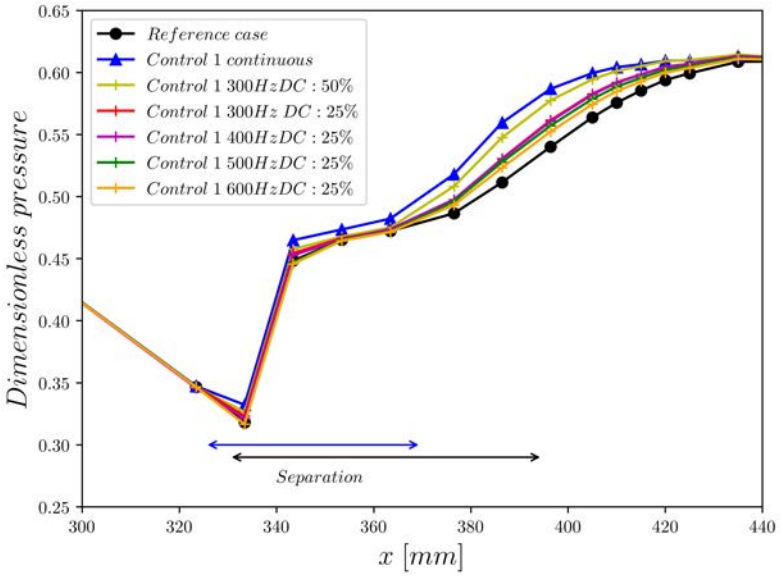

Figure VII.19: Static pressure distributions in the median plane for the Control 1 case with various frequencies compared to the reference case. Part 2

The same tendencies are visible in the dynamics of the flow. Some pre-multiplied spectra of the cases tested are presented on Fig. VII.20. The dominant frequency of the shock-wave is slightly influenced by the variation of frequency between the cases 100Hz, DC 50% and 300Hz DC 50%. On the contrary, the change of Duty Cycle between the cases 300Hz, DC 50% and 300Hz, DC 25% modifies more strongly the intensity seen by the upstream sensor and thus the mean position of the shock-wave. The shock-wave frequency is also shifted from 800Hz of the continuous controlled case to 600Hz. This is coherent

with an increase of the mean separation zone size. The frequency is getting closer to the uncontrolled case with a frequency of 300Hz. For the last case, at 600Hz and DC 25%, the shock-wave is shifted downstream, this may be linked to a limitation of the actuators which are not delivering a clear square signal.

The pulsed jets have proven to be efficient to control the separation zone, they may be interesting as they need a less important mass flow rate than the continuous ones. Nevertheless, this advantage needs to exceed the drawback of the added mass on an airplane to be useful in practice. The change of frequency does not strongly modify the dynamic response of the flow. However, the change of Duty Cycle allows to tune the efficiency of the control and to modify the frequency of the shock-wave between the frequency of the uncontrolled case and the fully controlled case.

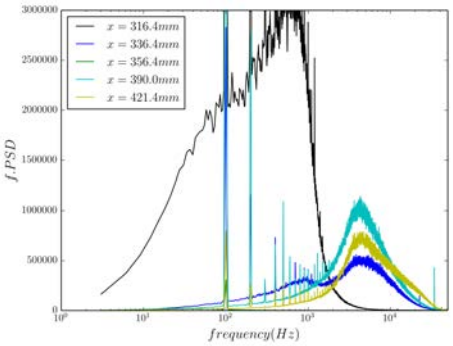

(a) Central sensors 100Hz DC: 50%

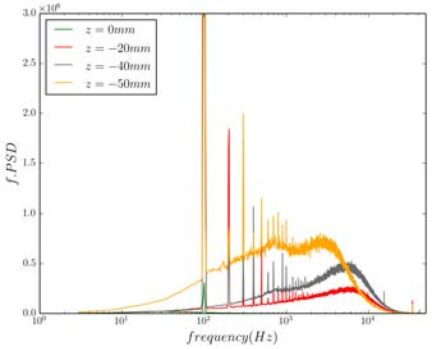

(b) Lateral sensors 100Hz DC: 50%

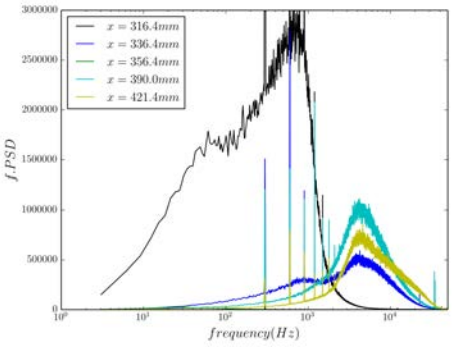

(c) Central sensors 300Hz DC: 50%

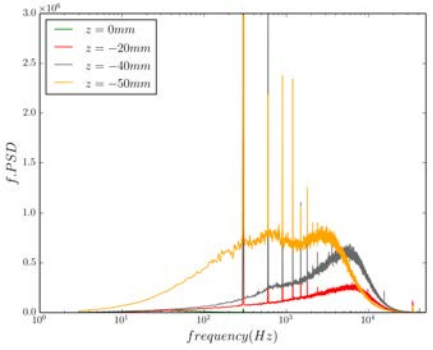

(d) Lateral sensors 300Hz DC: 50%

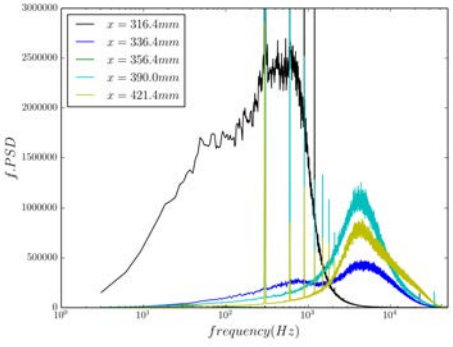

(e) Central sensors 300Hz DC: 25%

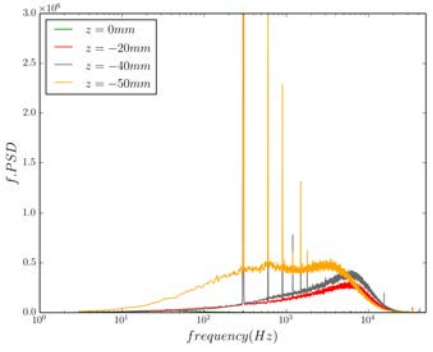

(f) Lateral sensors 300Hz DC: 25%

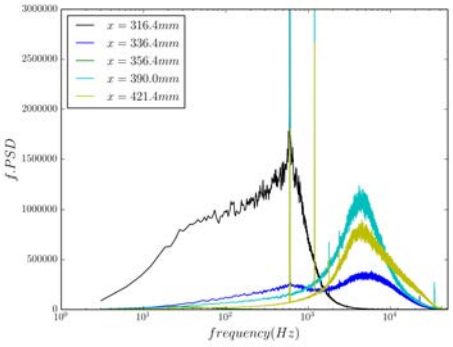

(g) Central sensors 600Hz DC: 25%

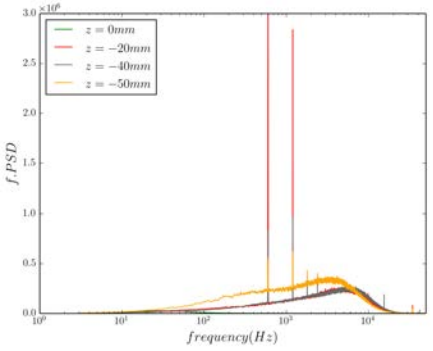

(h) Lateral sensors 600Hz DC: 25%

Figure VII.20: Pre-multiplied spectra obtained by the Kulite sensors for the Control 1 case with various frequencies and Duty Cycles.

VII.2 The Control 2 test case

The characterization of the Control 2 case is now presented. The reader is referred to Chap. V for a detailed presentation of the characteristics of the control. The positions and angles of the jets are summed up in Table V.2. In this case, the jet are oriented downstream with pitch and skew angles equal to respectively 30° and 60°.

2.a Recall of the RANS results

As for the Control 1 case, in order to visualize the global aspect of the control case, the result of the RANS result is presented on Fig. VII.21. In this case, the jet are oriented downstream with pitch and skew angles equal to respectively 30° and 60°. It should be noticed that the distribution of the jets along the width of the wind tunnel differs slightly from the Control 1 case, the central separation between the two center VGs is smaller.

As for the Control 1 case, a separation zone smaller than in the reference case occurs on the lower wall of the test section and another one more restraint in amplitude takes place on the corner. Contrary to Control 1 no separation is visible at the quarter of the width of the test section.

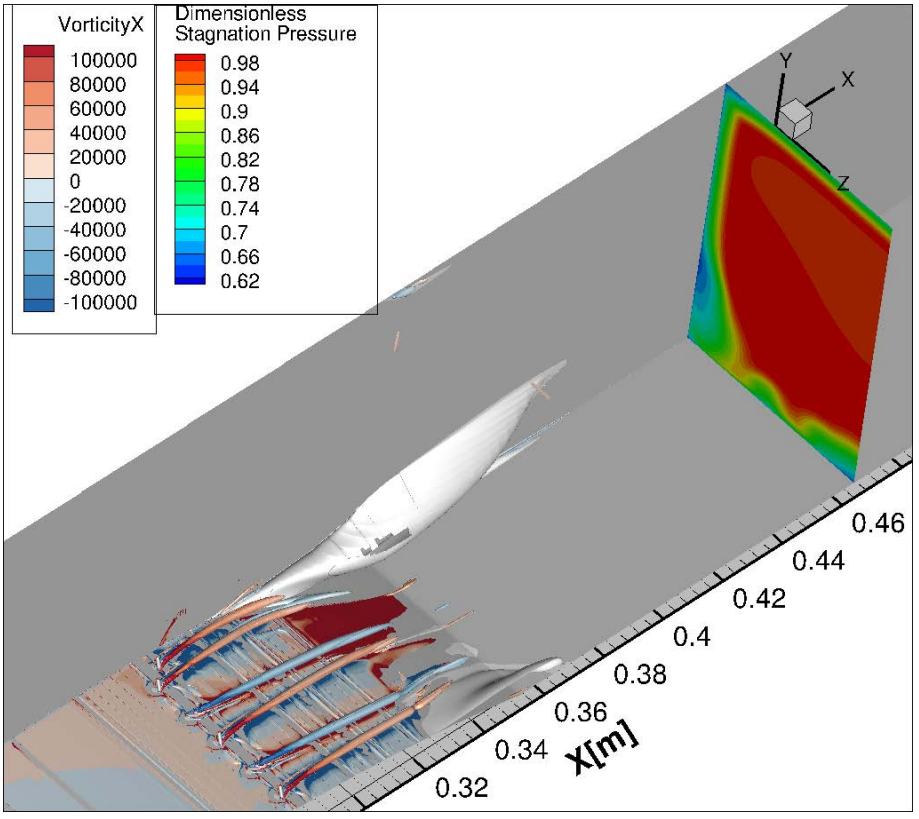

Figure VII.21: Non dimensionalized stagnation pressure on the DC50 plane, volume of the reverse flow-white surface- and Q criterion equal to $3 \cdot 10^8$ isosurface colorized with longitudinal vorticity for the Control 2 case.

2.b Laser sheet visualizations

The laser sheet visualization of the vorticies developed by the jets is compared to numerical contours of vorticity with the same levels as in the Control 1 case on Fig. VII.22. Even if less clearly visible due to their smaller height than in the Control 1 case, the six vorticies are retrieved with the two vorticies of the corner close to each other. The vorticies are closer to the lower wall than in the Control 1 case with slightly reversed jets, this is coherent with the numerical study of Chap. IV. This confirms again that the RANS modeling handles well the interaction between an angled jet and a cross flow. Once again, a more precise study using other tools is necessary to validate the modeling precisely. Nevertheless, the modeling of the impact of the jets on the close flow is qualitatively confirmed.

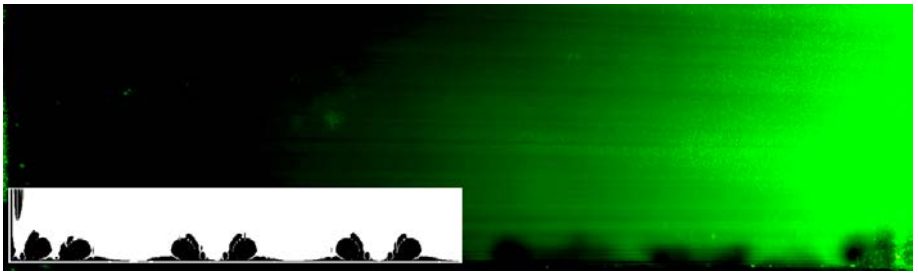

Figure VII.22: Laser sheet visualization of the vorticies generated by the jets of the Control 1 compared to the $30\,000\,\mathrm{s}^{-1}$ vorticity level from RANS calculations- in black and white- in the plane $x = 300\,\mathrm{mm}$.

2.c Schlieren visualizations

The Schlieren visualization of the controlled interaction is presented on Fig. VII.23a) and compared to reference case on Fig. VII.23b) using a superposition of two Schlieren visualizations. It can be seen that the shock-wave is, as for Control 1, impacted by the control. However, in this case, the displacement of the front leg is less important than in Control 1. The shock is also rectified surely for the same reasons as in the Control 1 case, the diminution of the separation zone causes an increase of the shock intensity.

As for the Control 1 case, compression waves are visible at the position of the jets and of the limit of the control strip.

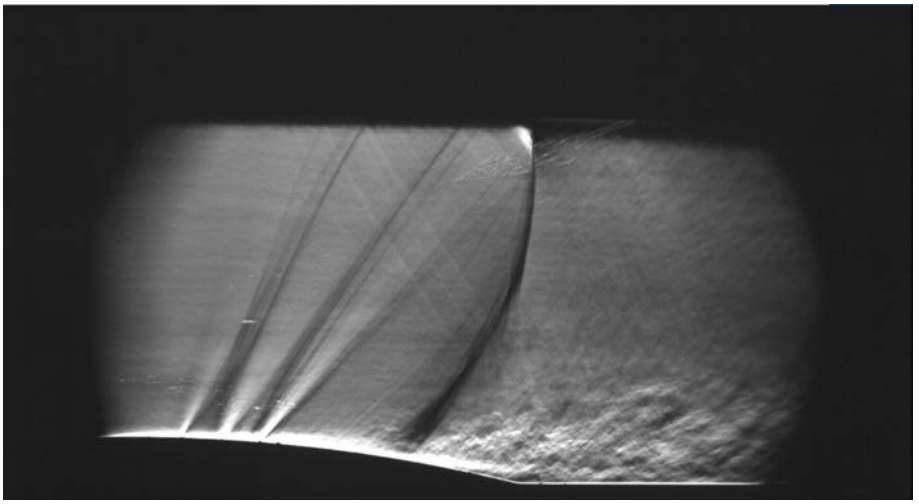

(a) Control 2

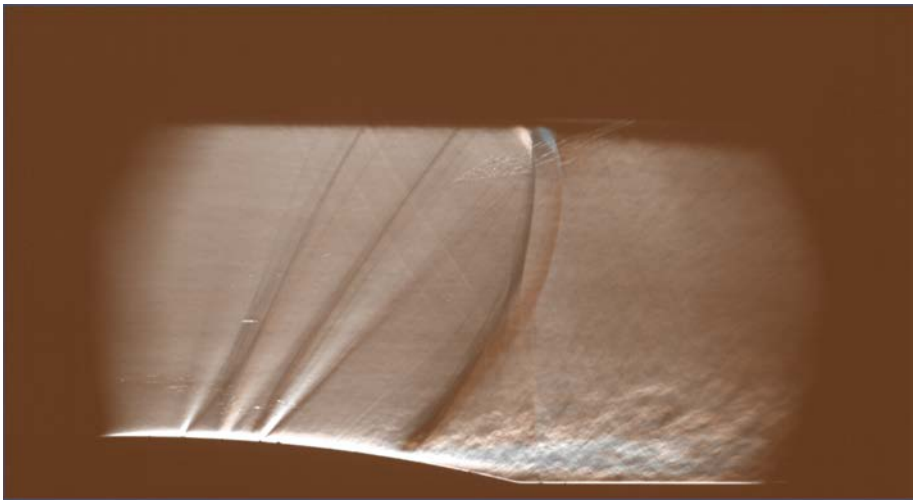

(b) Superposition of Control 2 and reference case.

Figure VII.23: Schlieren visualizations using horizontally oriented knife edge.

2.d Friction lines

The oil flow visualization of the lower wall is compared to the uncontrolled case on Fig. VII.24. The similar comparison between the friction lines of the RANS calculation for controlled and uncontrolled cases is presented on Fig. VII.25. The positions of the Kulite sensors and the tomographic PIV are again displayed to ease the understanding and the interpretation of their measurements.

Again, the controlled case becomes strongly 3D. Two important separation zones are visible, the central one and the corner one. Really small separations also occur between these. As for the Control 1, several pairs of counter rotating foci take place with the strongest one in the center. In this case, the focus is more complex, with a shape more pointy in its upstream part. On the median line, the separation is reduced, it takes place between $x = 335\,\text{mm}$ and $x = 355\,\text{mm}$. It is however slightly larger in width than in the Control 1 case.

It can also be noticed that the corner flow separation is increased in width with respect to the reference case contrary to Control 1 which was able to reduced its size.

The position of the shock-wave linked to the beginning of the separation zones is closer to the uncontrolled case than what the Schlieren visualization suggests. This may be due to the fact that the Schlieren visualization is an instantaneous observation of the flow while the oil flow visualization is a mean over time. The fact that the shock-wave is moving may explain the discrepancy. Furthermore, the Schlieren visualization is a mean over the width of the wind tunnel and thus does not give a precise information on the position of the shock-wave on the median line.

Even if the RANS calculation predicts the complex shape of the central separation zone, its position is found upstream than in experimental tests. The corner flow separation is also slightly over predicted.

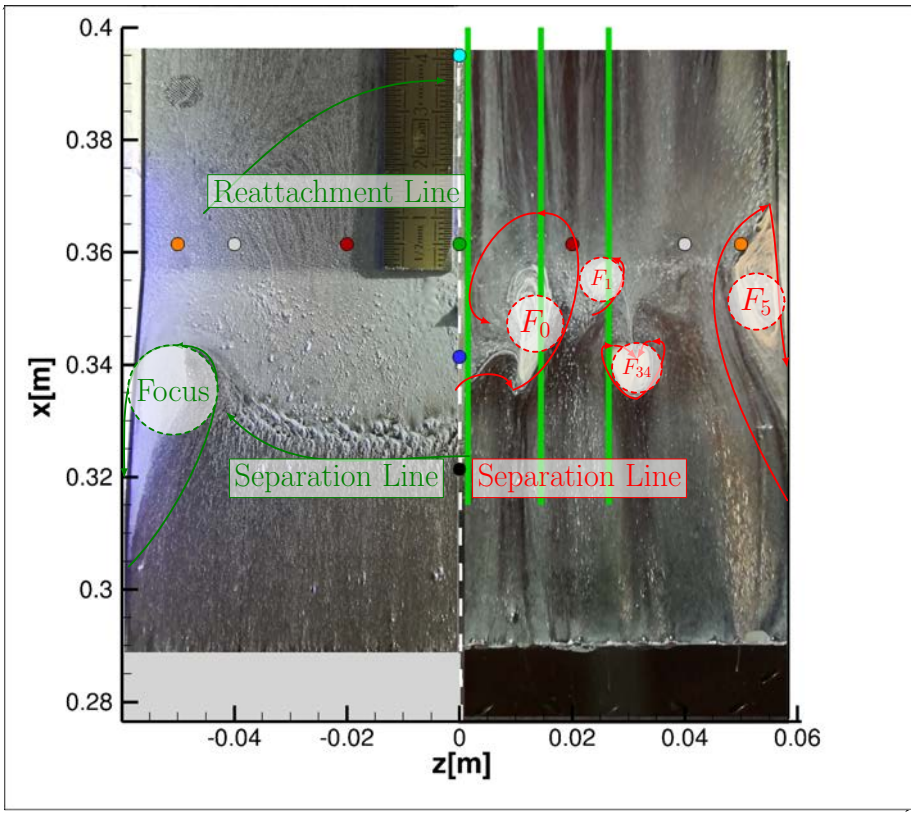

Figure VII.24: Experimental friction lines on the lower wall of the wind tunnel, comparison between uncontrolled and Control 2 respectively left and right. The dots correspond to Kulite sensors position, their colors match the ones of the pre-multiplied spectra presented in subsection 2.g. The three green lines correspond to the median planes positions of the three PIV volumes.

Overall, the control strongly reduced the total separation with respect to the reference case.

The lateral friction lines of the RANS calculation and of oil flow visualization are presented on Fig. VII.26. It can be seen that the shape of the separation is changed, a focus is not clearly visible anymore.

In this case, stronger differences are displayed between RANS and oil flow visualization

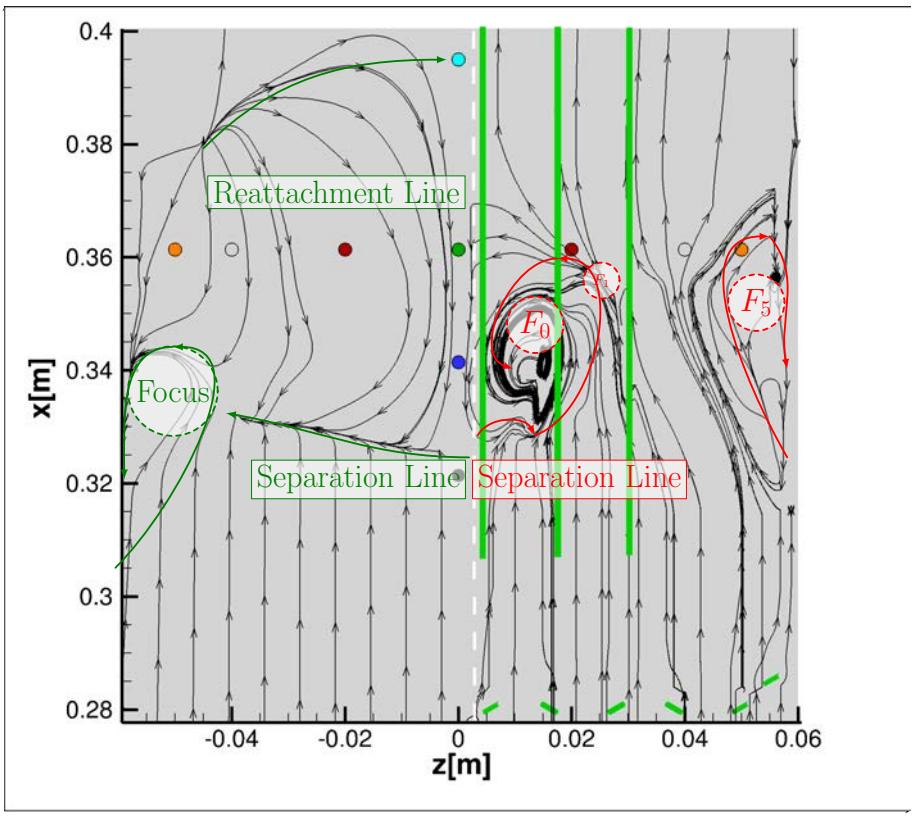

Figure VII.25: RANS friction lines on the lower wall of the wind tunnel, comparison between uncontrolled and Control 2 respectively left and right. The dots correspond to experimental Kulite sensors position, their colors match the ones of the pre-multiplied spectra presented in subsection 2.g. The three green lines correspond to the median planes positions of the three PIV volumes.

confirming the difficulty of modeling the corner flow separation. More precise experimental studies of the friction lines may be useful for a better comprehension of the topology of the separation. It should be nonetheless noticed that this confrontation is really discriminating as all the friction lines are displayed on the numerical results while the experimental ones are also limited by the intensity of the friction, meaning that the paint is not driven on friction lines of too small intensity.

Nevertheless, both results show a modification of the separation topology with no clear focus anymore.

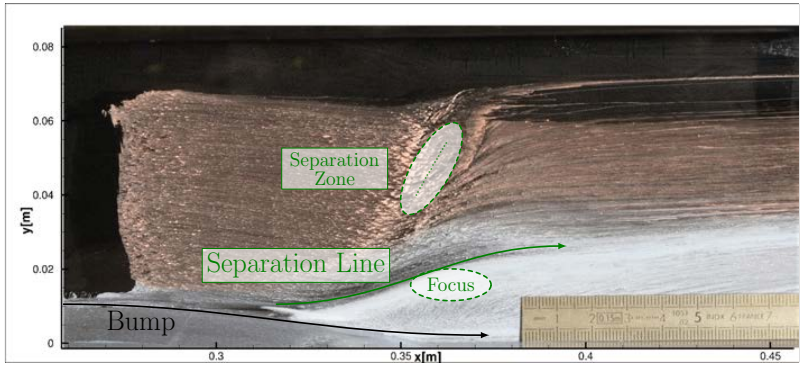

(a) Experiment uncontrolled.

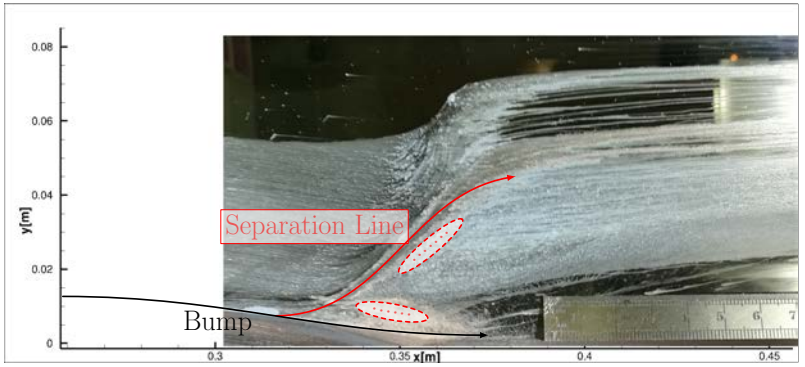

(b) Experiment Control 2.

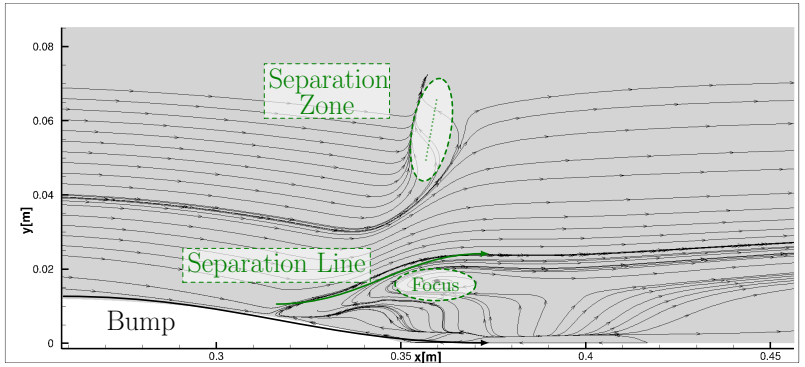

(c) RANS uncontrolled.

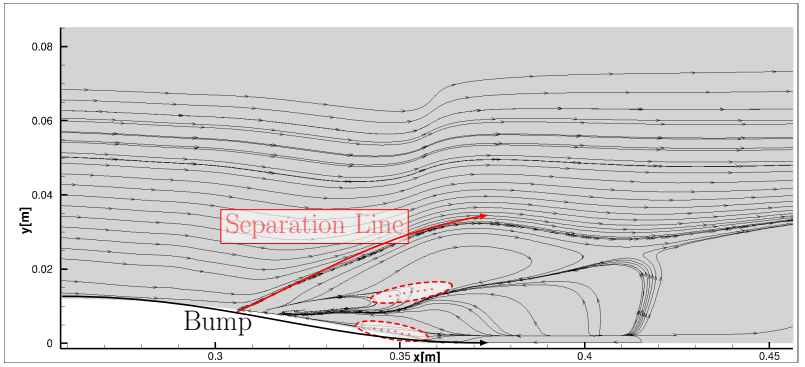

(d) RANS Control 2.

Figure VII.26: Friction lines of experimental and RANS on the lateral wall, respectively below and above for reference and Control 2 case respectively left and right.

2.e Static pressure distribution

The static pressure distribution measured along the median line of the wind tunnel for the Control 2 case is presented on Fig. VII.27. In accordance with the oil flow visualization, the static pressure suggests that the shock-wave is not strongly moved by the control and the central separation zone is well reduced by the control with a plateau not really visible anymore due to a lack of sensor in the separation region.

The static pressure evolution calculated using RANS for the uncontrolled and controlled cases are presented on Fig. VII.28. The same modification as in the experimental case is retrieved. The RANS calculation displays a small plateau which is not visible on experimental data. It also displays the compression wave in front of the control followed by an expansion wave which was not visible in the previous control.

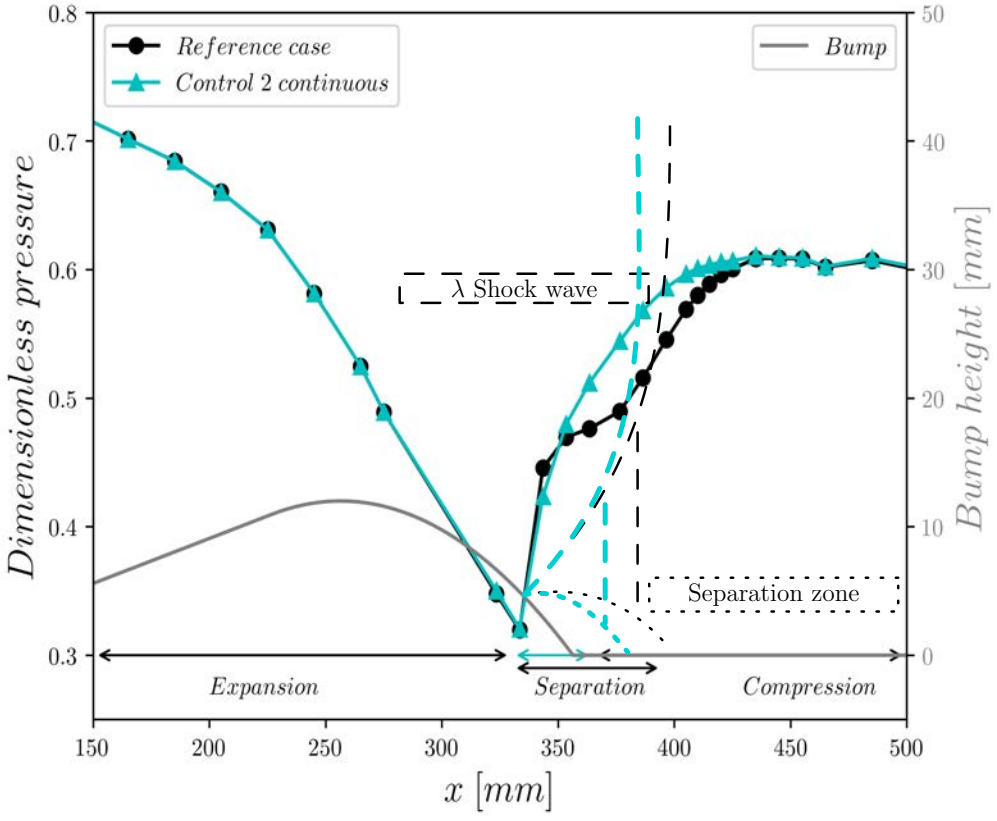

Figure VII.27: Experimental static pressure distribution in the median plane for the Control 2 case, compared to the reference case.

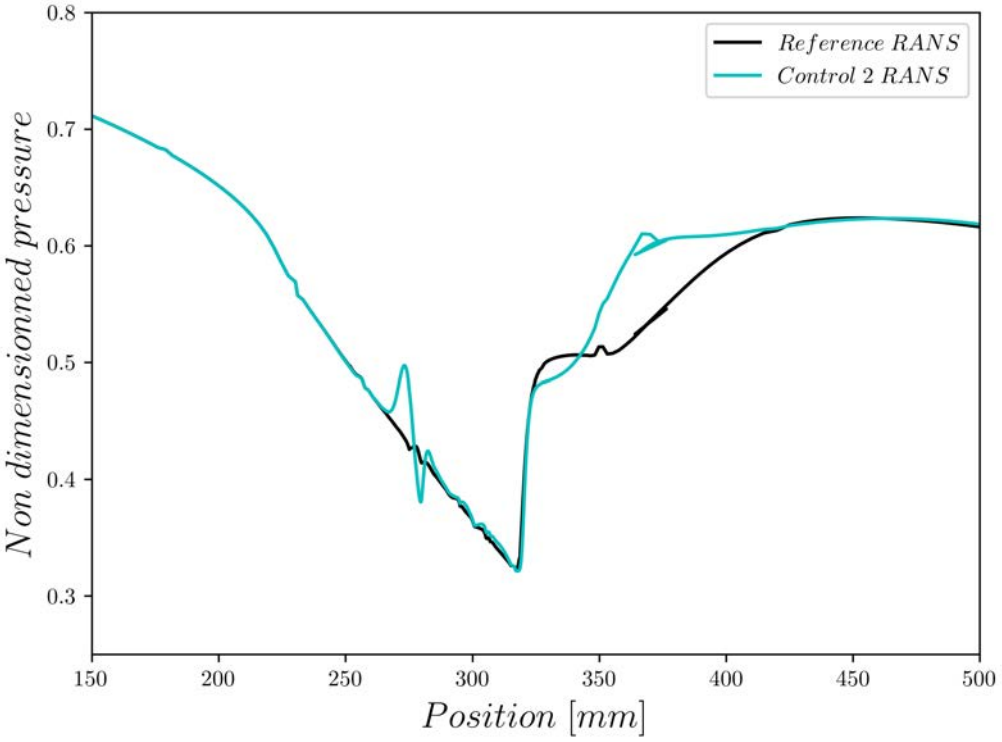

Figure VII.28: RANS static pressure distribution in the median plane for the Control 2 case, compared to the reference case.

2.f PIV measurements

The mean longitudinal and vertical velocity on the three planes presented on Fig. VII.24 are compared to the Reference case using tomographic PIV and RANS calculations on Fig. 2.f and on Fig. 2.f respectively. It shows that there still is a separation close to the center of the wind tunnel. This separation is smaller in height as it is less visible than in the Reference and Control 1 cases (see Fig. 1.f and Fig. 1.f). This separation is overestimated by RANS calculation. The separation is more complex on the second plane as it can be seen that there is a "bump" in the longitudinal velocity distribution close to $x = 340\,\text{mm}$. This is due to the fact that the plane is situated close to the focus of the central separation

The presence of the separation is again confirmed by the positive vertical velocity after the shock for the first two planes. On the last one, on contrast, no separation is visible anymore which is coherent with the oil flow visualization on Fig. VII.24. The RANS calculation find as well a positive vertical velocity after the shock-wave on the two first planes and a negative velocity on the last one which is in agreement with the tomographic PIV, characterizing a separation present on the two first planes.

Reference Control 2

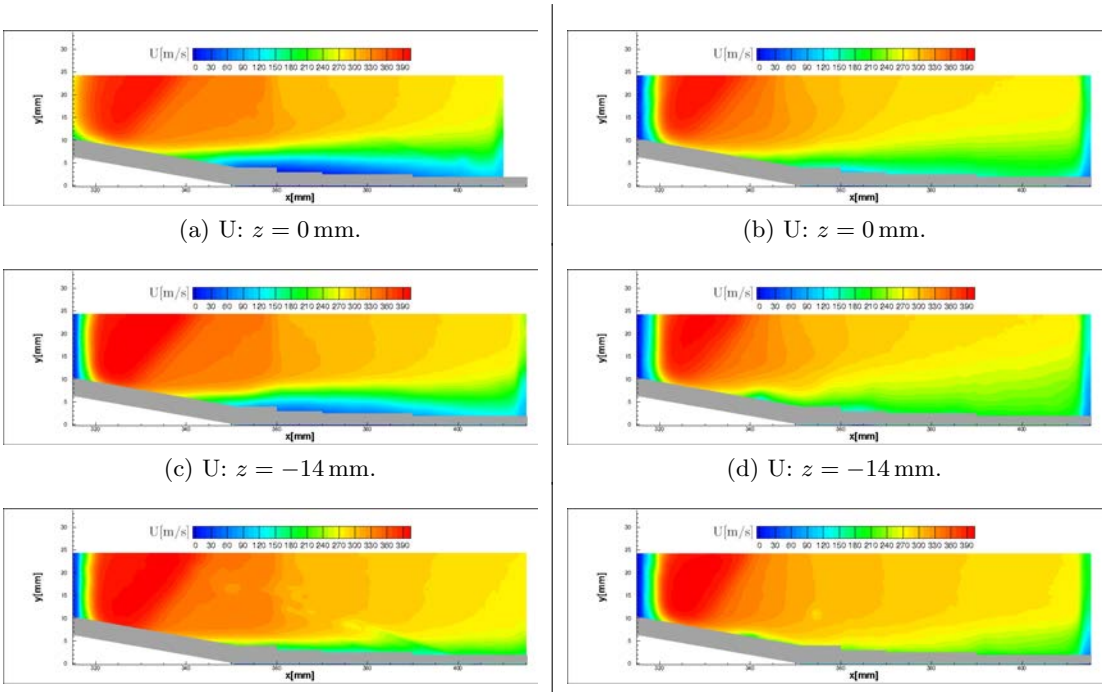

(a) U: $z = 0\,\text{mm}$. (b) U: $z = 0\,\text{mm}$.

(c) U: $z = -14\,\text{mm}$. (d) U: $z = -14\,\text{mm}$.

(e) U: $z = -26\,\text{mm}$. (f) U: $z = -26\,\text{mm}$.

Tomographic PIV

RANS

(g) U: $z = 0\,\text{mm}$. (h) U: $z = 0\,\text{mm}$.

(i) U: $z = -14\,\text{mm}$. (j) U: $z = -14\,\text{mm}$.

(k) U: $z = -26\,\text{mm}$. (l) U: $z = -26\,\text{mm}$.

Reference Control 2

Figure VII.29: Comparison of longitudinal velocity fields given by the tomographic PIV and RANS modeling (respectively up and down) for the reference and Control 2 cases (respectively left and right), at three different lateral planes.

Reference Control 2

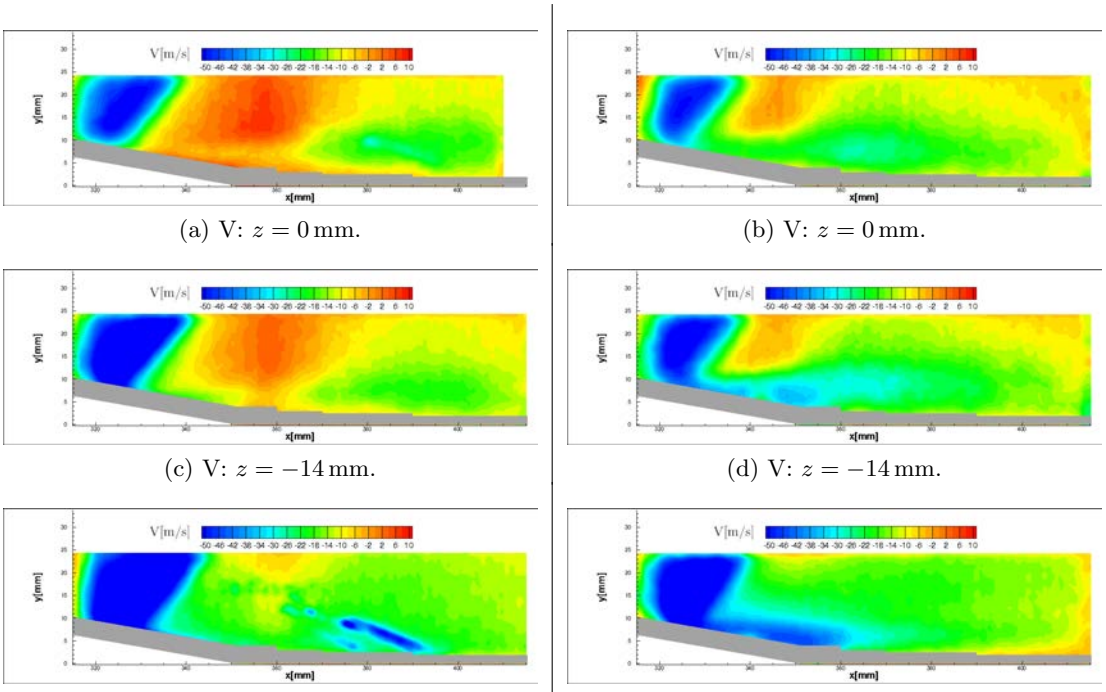

(a) V: $z = 0\,\text{mm}$. (b) V: $z = 0\,\text{mm}$.

(c) V: $z = -14\,\text{mm}$. (d) V: $z = -14\,\text{mm}$.

(e) V: $z = -26\,\text{mm}$. (f) V: $z = -26\,\text{mm}$.

Tomographic PIV

RANS

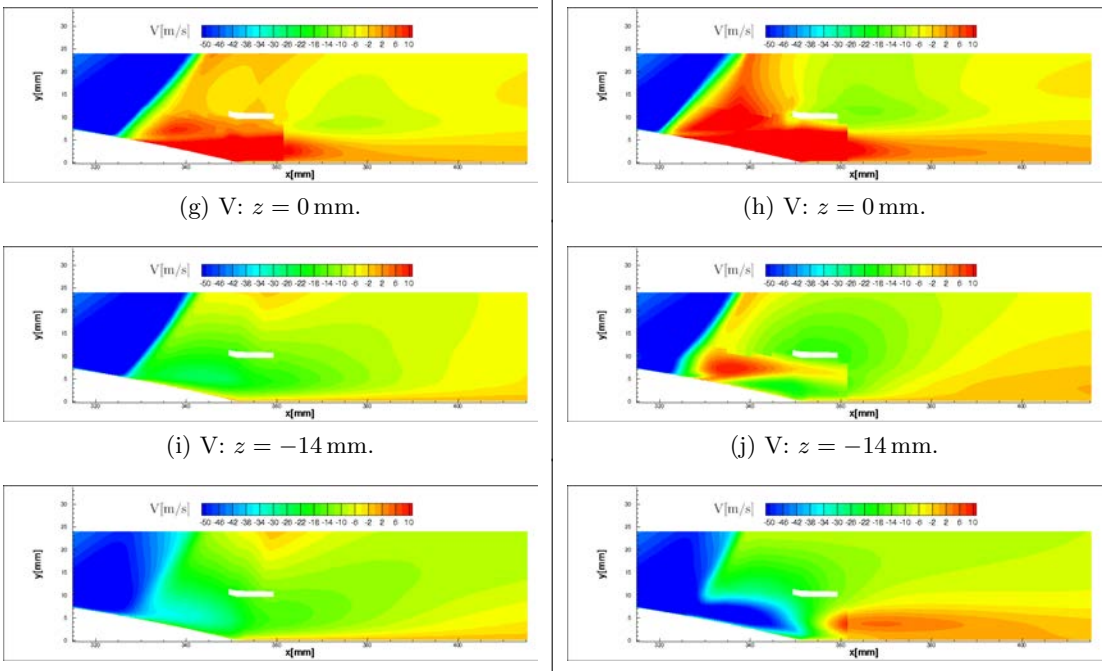

(g) V: $z = 0\,\text{mm}$. (h) V: $z = 0\,\text{mm}$.

(i) V: $z = -14\,\text{mm}$. (j) V: $z = -14\,\text{mm}$.

(k) V: $z = -26\,\text{mm}$. (l) V: $z = -26\,\text{mm}$.

Reference Control 2

Figure VII.30: Comparison of longitudinal velocity fields given by the tomographic PIV and RANS modeling (respectively up and down) for the reference and Control 2 cases (respectively left and right), at three different lateral planes.

The transverse velocity and the dimensionless Reynolds shear stress of the three planes studied, are presented on Fig. 2.f and Fig. reffig:uvCont2 for tomographic PIV and RANS calculations. It can be seen that for the transverse velocity, the distribution differs from the reference case and matches the direction suggested by the friction lines. The transverse velocity is maximum in the plane $z = -14\,\text{mm}$, which is the one closer to a focus and so where the transverse velocity is maximum. Less transverse velocity is seen in the plane $z = -26\,\text{mm}$ which is not in a separation zone. The distribution of positive and negative velocity calculated using the RANS model reveals a global agreement on the positive and negative zones of the transverse velocity with differences on the exact distribution of velocity.

For the Reynolds shear stress, it can be seen that the global level is strongly reduced. Furthermore, due to the fact that the separation zones are smaller than in the two previous cases, the Reynolds shear stress is dissipated quicker than in the previous cases.

Reference | Control 2

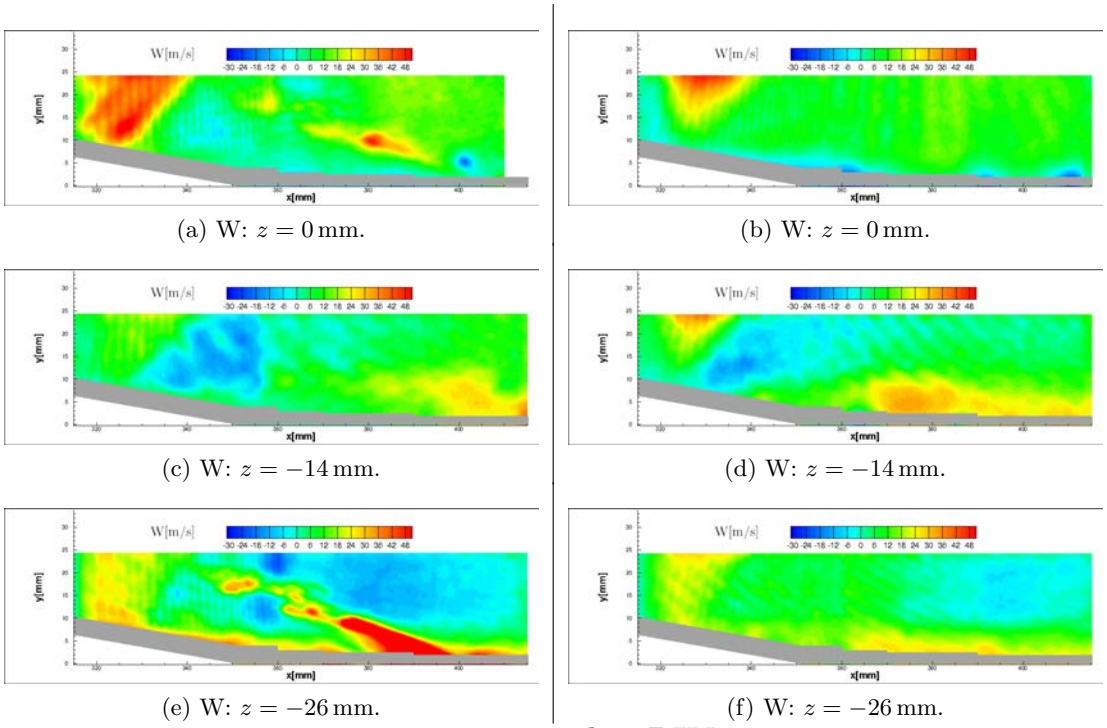

(a) W: $z = 0\,\text{mm}$. (b) W: $z = 0\,\text{mm}$.

(c) W: $z = -14\,\text{mm}$. (d) W: $z = -14\,\text{mm}$.

(e) W: $z = -26\,\text{mm}$. (f) W: $z = -26\,\text{mm}$.

Tomographic PIV

RANS

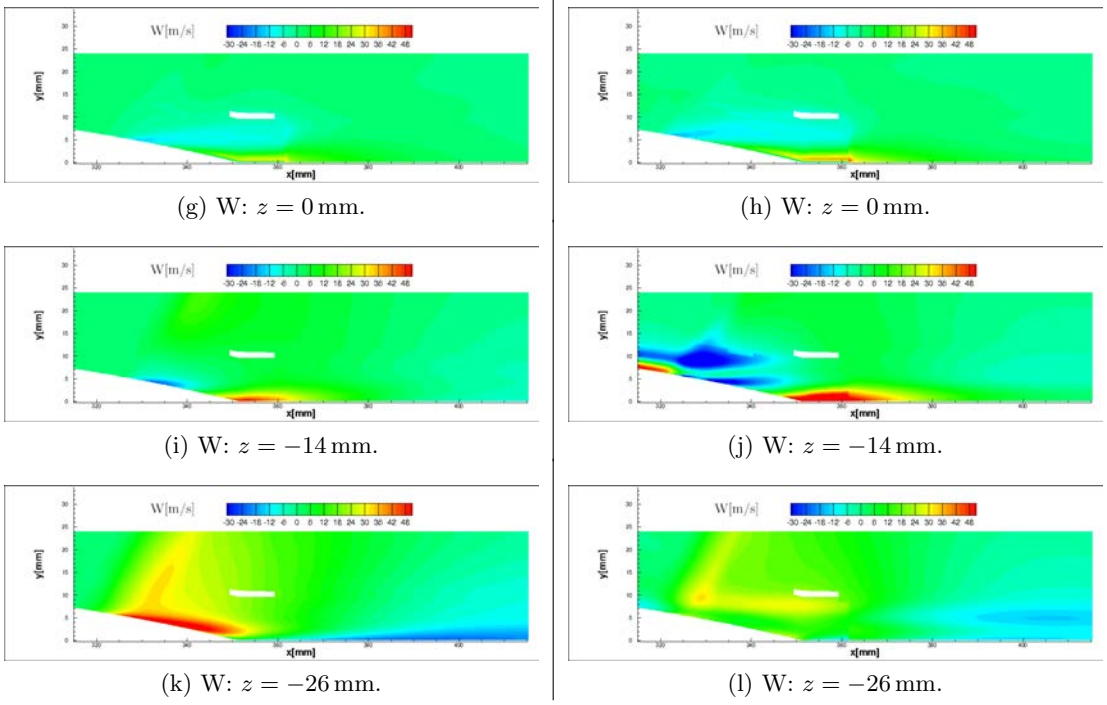

(g) W: $z = 0\,\text{mm}$. (h) W: $z = 0\,\text{mm}$.

(i) W: $z = -14\,\text{mm}$. (j) W: $z = -14\,\text{mm}$.

(k) W: $z = -26\,\text{mm}$. (l) W: $z = -26\,\text{mm}$.

Reference | Control 2

Figure VII.31: Comparison of transverse velocity fields given by the tomographic PIV and RANS modeling (respectively up and down) for the reference and Control 2 cases (respectively left and right), at three different lateral planes.

Reference | Control 2

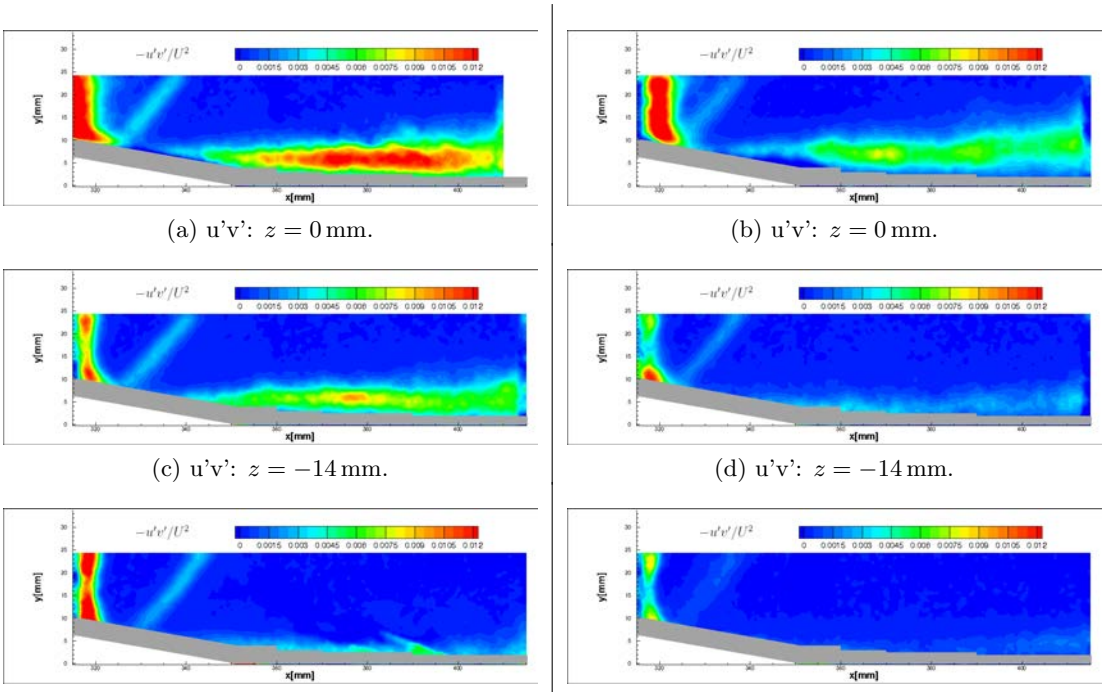

(a) u'v': $z = 0\,\mathrm{mm}$. (b) u'v': $z = 0\,\mathrm{mm}$.

(c) u'v': $z = -14\,\mathrm{mm}$. (d) u'v': $z = -14\,\mathrm{mm}$.

(e) u'v': $z = -26\,\mathrm{mm}$. (f) u'v': $z = -26\,\mathrm{mm}$.

Tomographic PIV

Figure VII.32: Comparison of longitudinal velocity fields given by the tomographic PIV for the reference and Control 1 cases (respectively left and right), at three different lateral planes.

The longitudinal velocity distribution in the plane $x = 370\,\text{mm}$ for the RANS and tomographic PIV results, are presented on Fig. VII.33. Compared to Fig. VI.17 and Fig. VII.13, no velocity under $100\,\text{m}\,\text{s}^{-1}$ is visible anymore on tomographic PIV. The impact of the separation is visible on the two volumes close to the center of the test section. This figures highlights the fact that the separation is higher and thinner in the Control 1 compared to Control 2. In this case, tomographic PIV manages to capture the variation of velocity along the width of the wind tunnel more precisely. This may be due to the fact that the variation is smoother. Nevertheless, the RANS and tomographic PIV differ in the outer part, the RANS predicts the trace of a vortex while the tomographic PIV does not detect it.

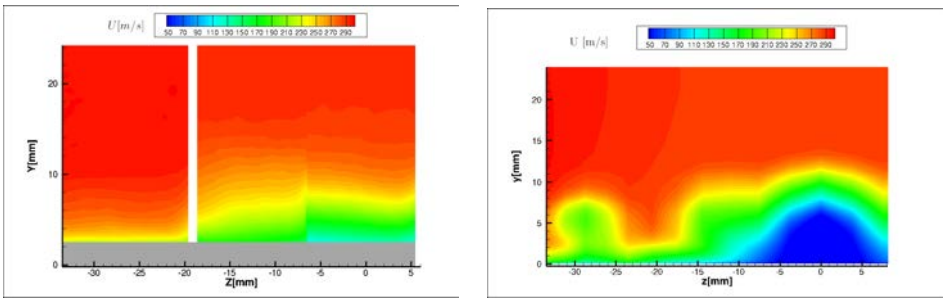

(a) Experiment. (b) RANS.

Figure VII.33: Lateral distribution of longitudinal velocity in the plane $x = 370\,\text{mm}$ for the Control 2 case.

Finally, the same 3D visualization as the one presented for the reference case on Fig. VI.18 and the Control 1 case on Fig. VII.14 is presented for the Control 2 case on Fig. VII.34. The variation of the supersonic tongue along the width is again visible, this latter one follows the existence of the separation zones. The absence of separation zone visible in the central volume is also noticeable, this is due to the limitation in close wall measurement of the current tomographic PIV.

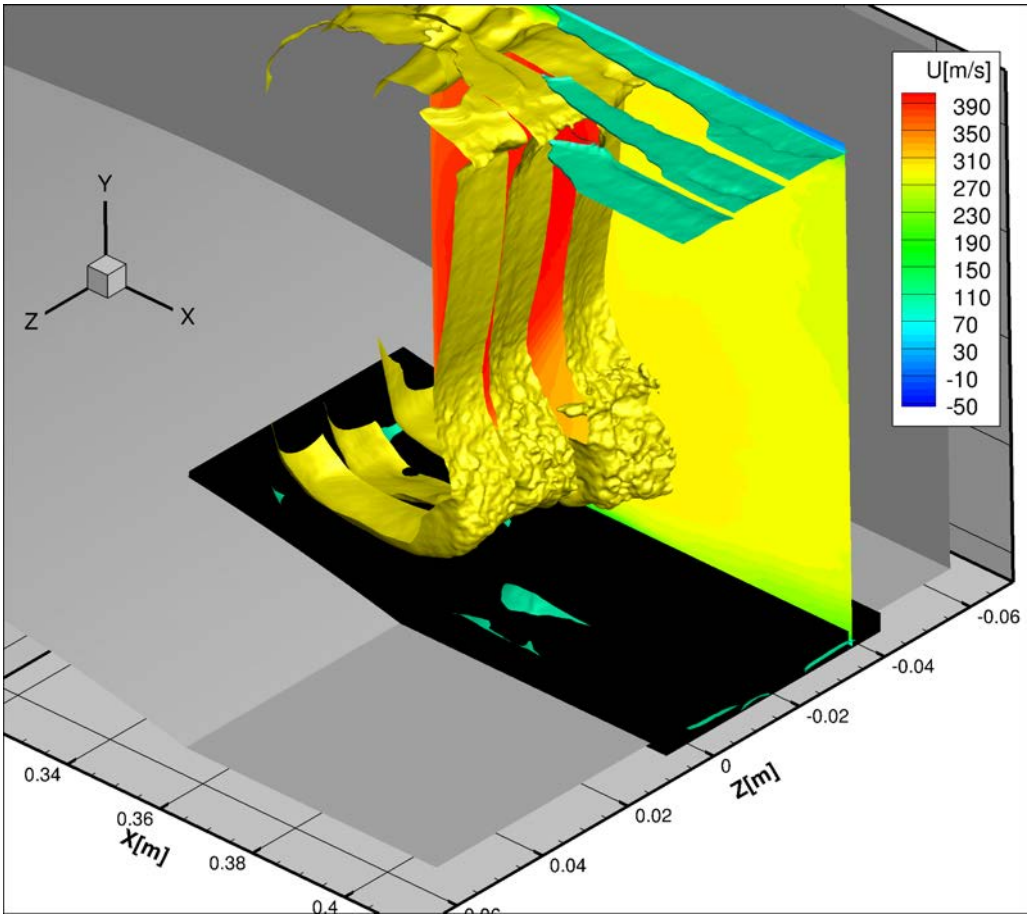

Figure VII.34: 3D visualisation of the SWBLI in the Control 2 case, two iso-surfaces for $u = 300\,\mathrm{m\,s^{-1}}$ (yellow) and $u = 100\,\mathrm{m\,s^{-1}}$ (green). The plane $z = -40\,\mathrm{mm}$ is also represented.

2.g Pressure fluctuations measurements

The pre-multiplied spectra of the longitudinal and lateral sensors are presented on Fig. 2.g. It displays a reduction in intensity on the first central sensor. This is linked to the small distancing of the shock-wave on the median line. As for the Control 1 case, the frequency of the shock-wave seems to be shifted higher, close to 800Hz. However, due to the absence of energy on the first sensor, the frequency is not clearly defined on this relatively flat spectrum. For the first time, the sensor positioned at $x = 356.4\,\mathrm{mm}$ on the median line is able to measure a signal. This may be due to the reduction in height of the separation zone which places the sensor closer to the eddies. Nevertheless, the frequency disclosed does not correspond to any other one found in the flow. This is not well understood. The other sensors see the frequency characteristic of the Kelvin Helmholtz instability. It can be noticed that its intensity diminish quicker than in the two other cases. This is coherent with the field of Reynolds shear stress displayed by the tomographic PIV.

With respect to the lateral sensors, the sensor placed at $z = -20\,\mathrm{mm}$ measures the Kelvin Helmholtz frequency may be due to a small separation present in front of it. The Kulite placed at $z = -40\,\mathrm{mm}$ sees the frequencies with less intensity as it is placed in a

zone with no reversed flow. Finally, the sensor placed close to the corner flow separation measures the same frequencies as in the Control 1 case even if the structure of the corner separation differs. It presents a peak at 800Hz, the shock frequency and a peak at 3kHz maybe linked to the development of eddies in the corner.

Reference Control 2

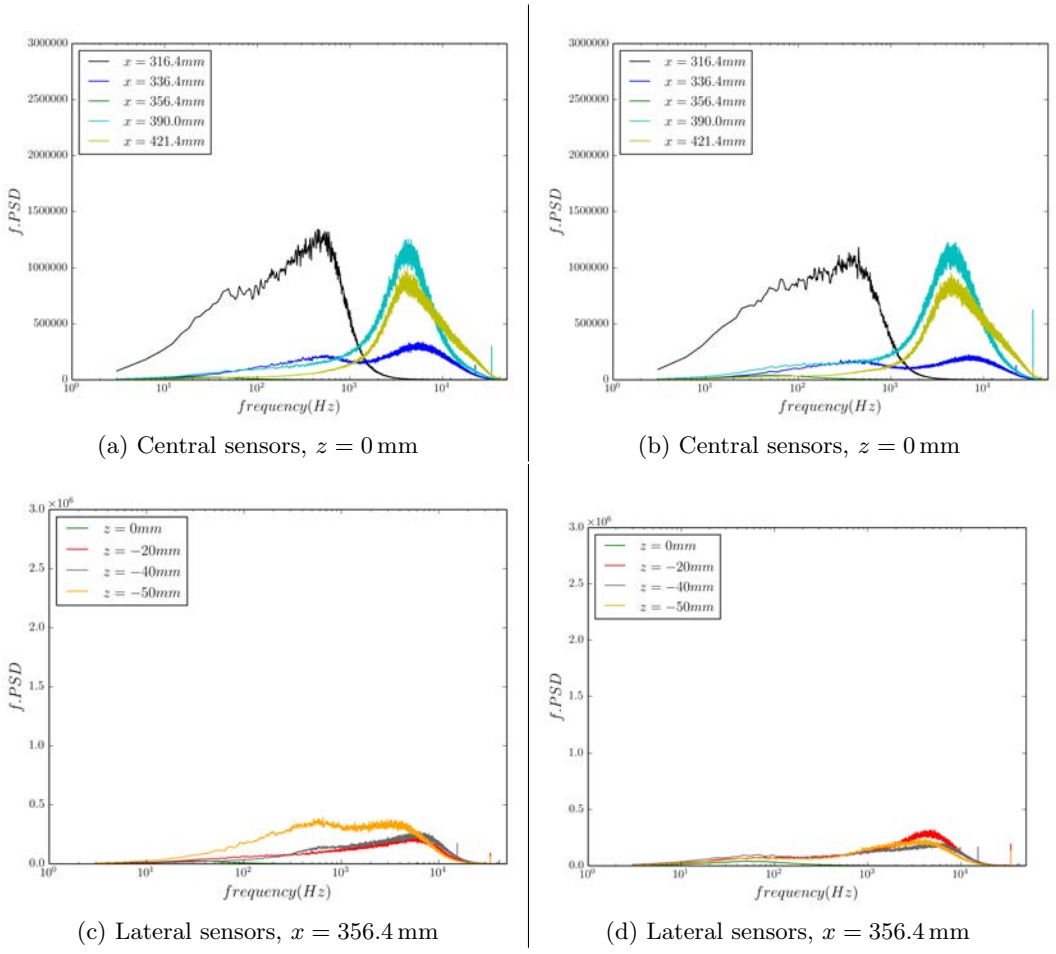

(a) Central sensors, $z = 0\,\text{mm}$

(b) Central sensors, $z = 0\,\text{mm}$

(c) Lateral sensors, $x = 356.4\,\text{mm}$

(d) Lateral sensors, $x = 356.4\,\text{mm}$

Figure VII.35: Pre-multiplied spectra obtained by the Kulite sensors for the Reference case and the Control 2 case (respectively left and right).

2.h Variation of control parameters

Some variations of the Control 2 parameters are presented. First some tests on the interest of the corner flow control are presented and then the tests of pulsed actuators are displayed.

Corner flow control tests As for the Control 1 case, two different tests are performed, one with only the 10 centers jets and one with only the two external jets. The static pressure distributions of the different cases are reported on Fig. VII.36 and the pre-multiplied spectra of the two new cases are reported on Fig. VII.37.

For the static pressure distributions, as for the Control 1 case, the case only controlled by the center VGs is close to the full control and the case with only the corner jets is closed to the uncontrolled case. They differ slightly from these, but the use of only the

static pressure does not allow to understand these variations.

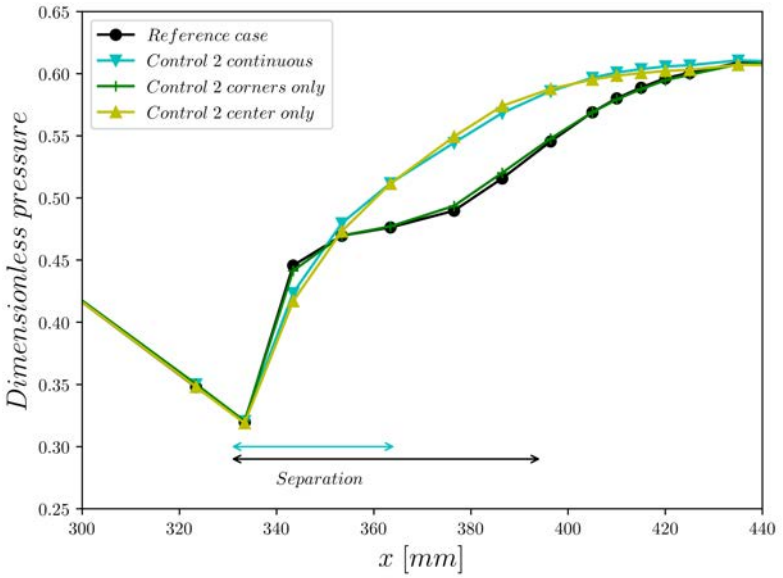

Figure VII.36: Static pressure distribution in the median plane for the Control 2 with full control, corners only and center only

When only the corner controls are activated, no significant modification of the central sensors is observed (the variation of the first Kulite is due to a shock-wave slightly shifted in the uncontrolled case before the activation of the control). However, for the lateral sensor, the use of the corner control, diminishes the intensity seen by the most external sensor compared to the reference case (see Fig. VI.21). This behavior differs from the Control 1 with only the lateral jets, which amplifies the intensity. Once again an oil flow visualization of the flow may help to better understand this case.

For the case with only the central jets, the central sensors deliver a signal close to the full control case, however, the lateral sensors differ strongly proving the importance of the external jets for the control of the 3D interaction.

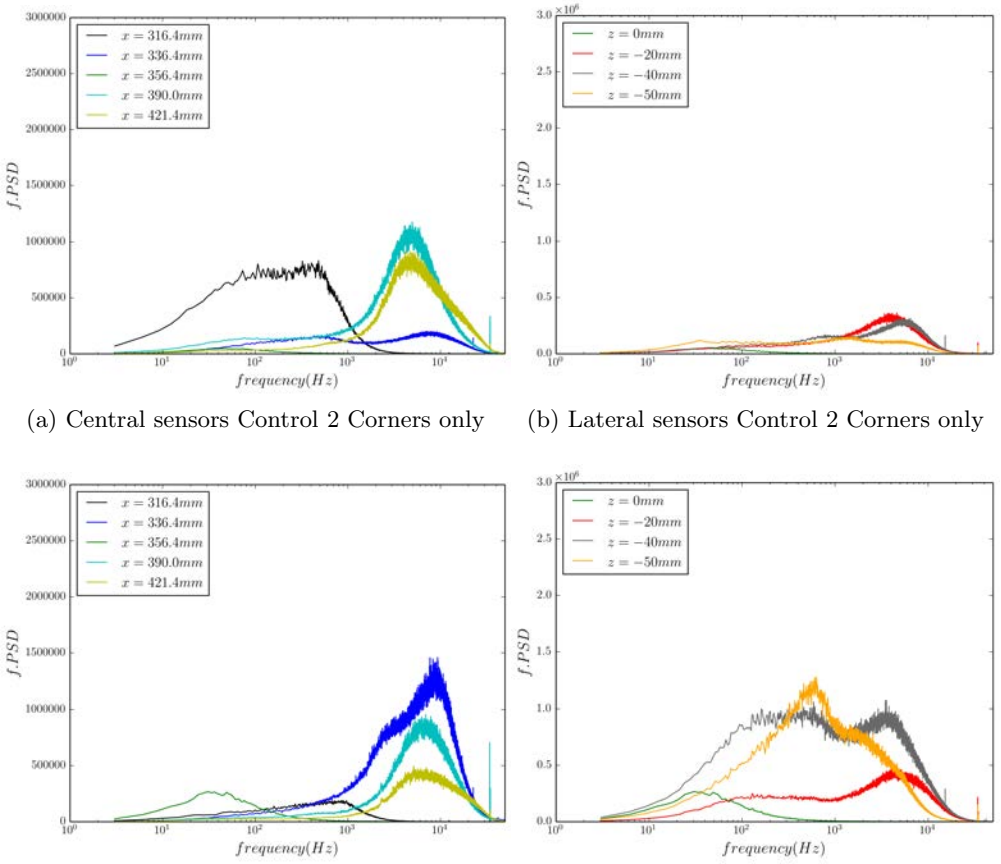

(a) Central sensors Control 2 Corners only

(b) Lateral sensors Control 2 Corners only

(c) Central sensors Control Center only

(d) Lateral sensors Control 2 Center only

Figure VII.37: Pre-multiplied spectra obtained by the Kulite sensors for variations of continuous control of the case Control 2.

Control by pulsed jets The full control is now activated at different frequencies from 100Hz to 600Hz with two different Duty Cycles (DC): 50% and 25%.

The static pressure of the different cases is shown in Fig. VII.38 and in Fig. VII.39.

As for the Control 1, it can be seen that the pulsating of the jets modifies the control, with curves placed between the full continuous control and the uncontrolled case. Once again, the Duty Cycle seems to be the dominant parameter, with two different curves for the two different Duty Cycles. Nevertheless, on this case, more differences are visible between the different frequencies at a Duty Cycle of 25%. It remains of small importance with respect to the impact of the Duty Cycle.

Considering the unsteadiness study on Fig. VII.40, it can be seen that except for the position of the shock-wave, the change of frequency does not impact strongly the general distribution of energy.

On the contrary, the modification of Duty Cycle changes more the general pattern with the lateral sensors getting close to the uncontrolled case.

It can also be seen that the reversed jets are more efficient to impose a more intense energy on the harmonic frequencies of activation as for the Control 1 case, at 600Hz, almost no intensity is visible on the spectra at 600Hz.

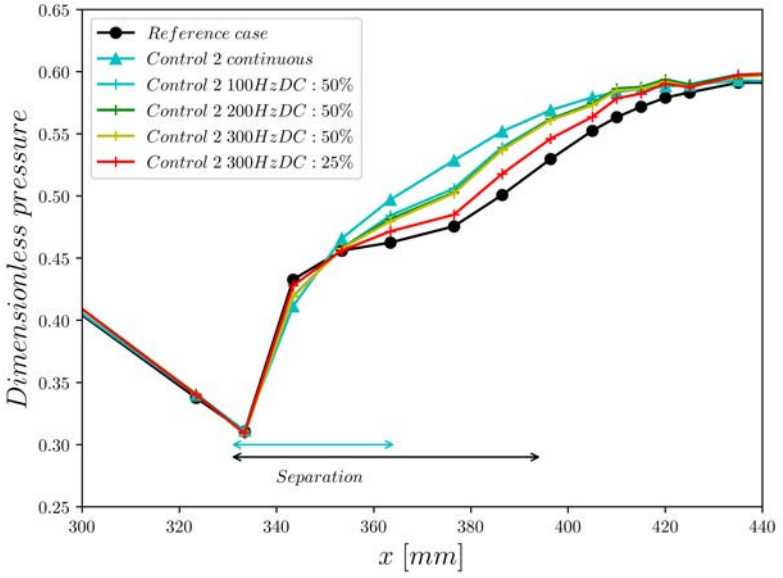

Figure VII.38: Static pressure distributions in the median plane for the Control 2 case with various frequencies compared to the reference case. Part 1

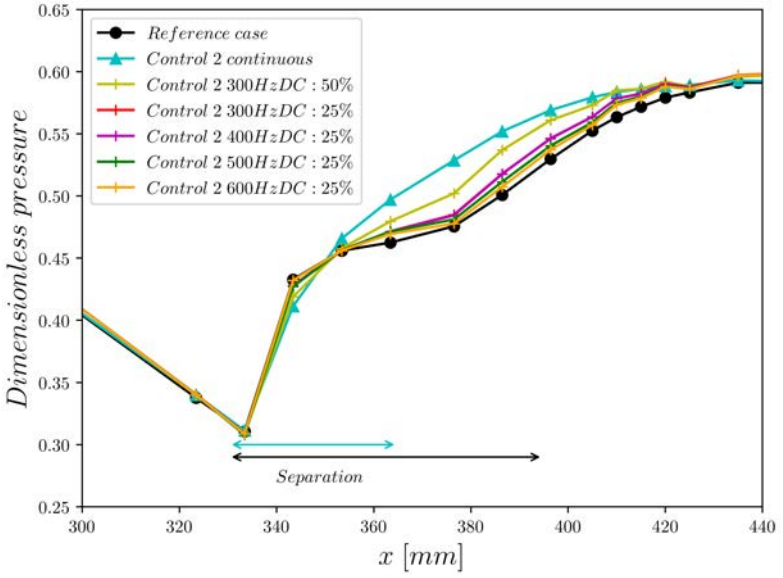

Figure VII.39: Static pressure distributions in the median plane for the Control 2 case with various frequencies compared to the reference case. Part 2

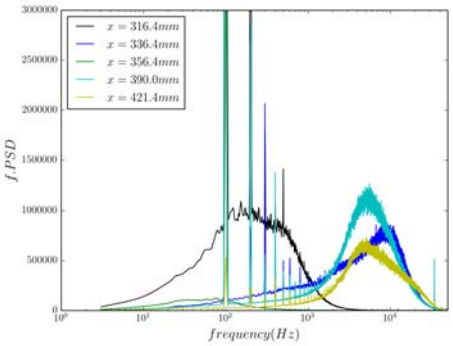

(a) Central sensors 100Hz DC: 50%

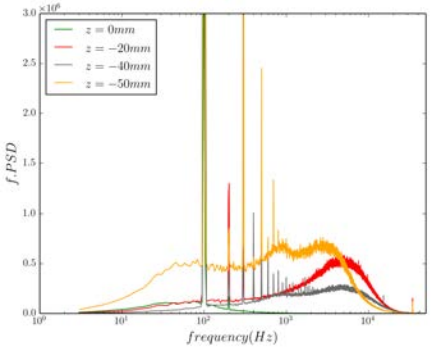

(b) Lateral sensors 100Hz DC: 50%

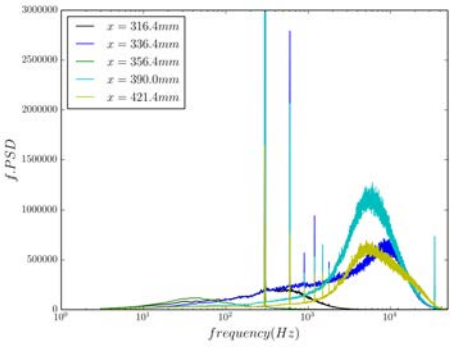

(c) Central sensors 300Hz DC: 50%

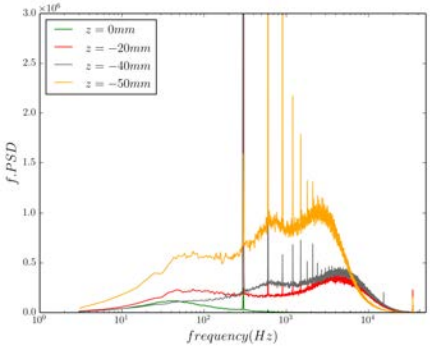

(d) Lateral sensors 300Hz DC: 50%

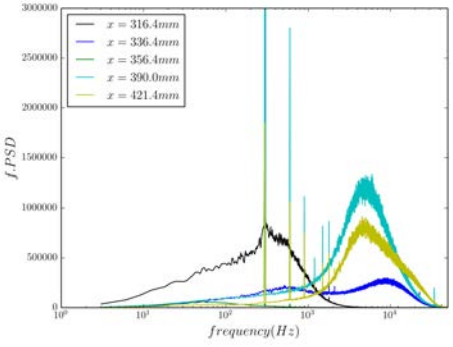

(e) Central sensors 300Hz DC: 25%

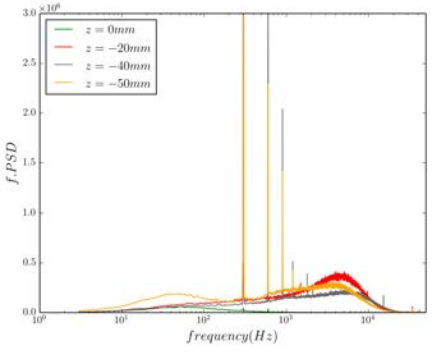

(f) Lateral sensors 300Hz DC: 25%

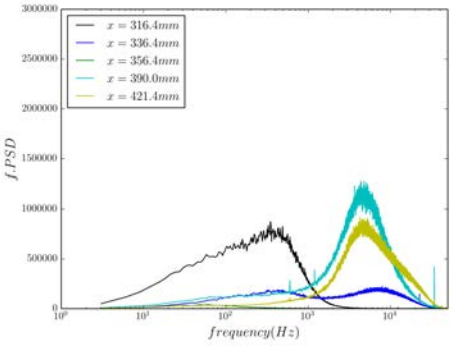

(g) Central sensors 600Hz DC: 25%

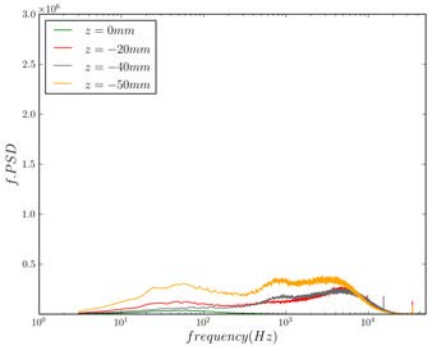

(h) Lateral sensors 600Hz DC: 25%

Figure VII.40: Pre-multiplied spectra obtained by the Kulite sensors for the Control 2 case with various frequencies and Duty Cycles.

VII.3 Conclusion

On the efficiency of the control methods Two different sets of control have been tested experimentally. They both manage to reduce the size of the central separation, developing complex 3D patterns with structures of coupled foci. The most important structure is the one in the middle of the test section in both cases with smaller, less intense structures developing on the lower wall. In the Control 1 case, the central separation is higher but less extended in width than in the Control 2.

The impact of the VGs on the central separation has been determined using notably tomographic PIV. Tomographic PIV has proven to be an interesting measurement technique even if the limitations on the measurement close to the wall are penalizing in this particular case where the separations occur in the vicinity of the wall. However, although tomographic PIV was not able to accurately described the flow at less than 2 mm from the wall, it was able to measure the modifications on the main flow which reflect the state of the boundary-layer.

The two control devices also enable a modification of the corner flow separation, with the Control 1 controlling more intensely the part of the corner separation on the lower wall than Control 2. Indeed, Control 2 is not capable to restrain the strong corner flow separation appearing due to the control of the central separation. The reverse jets of the Control 1 are thus confirmed to be more efficient in the control of corner flow separation.

Considering flow unsteadiness, the controls strongly modify the lateral distribution of energy on the main frequencies. On the central line, the major modification observed is the modification of the frequency characteristic of the shock-wave which is shifted from 300Hz to 800Hz. This is coherent with a modification of the length of the separation length for a constant Strouhal number for the SWBL interaction. It can also be noticed that in the corner, the control amplifies two frequencies intensity, the shock-wave frequency at 800Hz and a Kelvin Helmholtz frequency shifted from 4kHz to 3kHz.

The use of corner flow separation control has proven to have an impact of the whole flow, with variations of static and dynamic pressure distributions when only the central actuators are used. More investigations are needed to clearly understand these variations of control.

On another note, the two control set-ups have proven to be efficient for pulsed jets. Nevertheless, the pulsed control is only a mix between continuous control and uncontrolled case. The dominant parameter of the efficiency of the control is the Duty Cycle and thus the total time of activation over a period. This parameter allows to adjust the level of control wished. No prominent variation of controls have been noticed for various frequencies. However, only frequencies below the characteristic frequency of the controlled shock-wave have been tested.

Mechanical vs fluidic VGs In order to compare the capacity of fluidic VGs to mechanical VGs, the static pressure distributions on the median line of the wind tunnel have been plotted on Fig. VII.41 and Fig. VII.42 for the two fluidic control cases and the cases C2 and S1 from Bur et al. [20]. The C2 and S1 cases correspond to five pairs of counter rotating VGs, whose heights correspond to boundary-layer physical thickness for the C2 case

and half of thickness for the case S1 respectively. These cases are the tests of mechanical VGs which come closest to the fluidic cases considered here.

The vane-type VGs and fluidic control 2 VGs have a similar effect on pressure distribution. Furthermore, they also present a corner flow separation worsen with respect to the uncontrolled case as visible in Bur et al. [20].

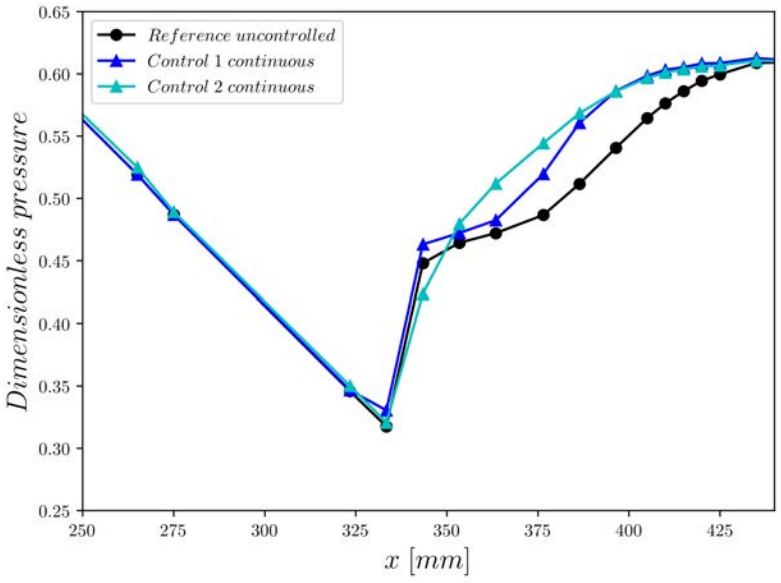

Figure VII.41: Static pressure distributions in the median plane for the Control 1 and Control 2 cases compared to the reference case.

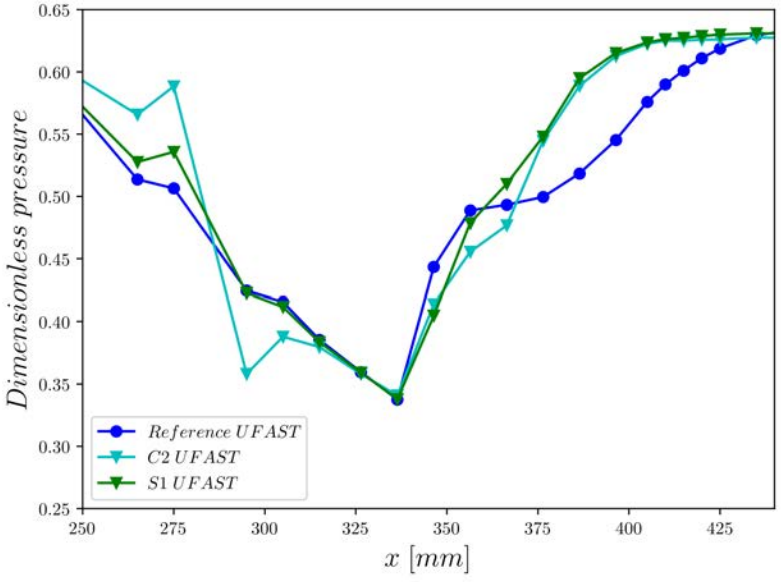

Figure VII.42: Static pressure distributions in the median plane for the mechanical VGs C1 and S2 cases compared to the reference case. Bur et al. [20]

On the experimental method This study allows demonstrates the application of tomographic PIV method to complex 3D configurations and important variations of velocity. Even if the result suffers from limitations close to the wall, it remains a promising method which has to be adapted in order to be able to tackle all situations.

Regrettably, the tomographic PIV measurements of volumes closer to the lateral wall have been found too noisy due to strong reflection on the lateral wall to be exploited. To some extent, the use of LDV measurements may be a solution to measure the flow in the corner.

On the comparison between RANS and experiments This study allows to compare globally coherent friction lines and vorticity development in the angled jet / cross flow interaction. Unfortunately, technical limitations prevent a comparison of the stagnation pressure distribution on a plane far downstream of the interaction for the controlled case. The measurement in the uncontrolled case confirms the presence of the two main separation zones, the central one and the corner one. Even if the levels are globally comparable, the RANS calculation seems to slightly overpredict the corner flow separation. Nevertheless, the RANS calculations and the tomographic PIV measurements are in good agreement on the two median planes of the most centered volumes.

VIII

Conclusions and perspectives

We wouldn't learn anything if we didn't have problems; that's basic in engineering training.
Eugene Schult

VIII.1 Synthesis

The studies performed during this thesis are dedicated to the fluidic control of the Shock-Wave / Boundary-Layer Interaction (SWBLI). After a recall of the different critical parameters of the SWBLI, the deleterious consequences of this interaction have been detailed in the context of transonic air inlets. Due to the separation zones inherent to these interactions, losses, inhomogeneities and unsteadiness are observed in the downstream part of transonic air inlets. The main goal of this thesis was to develop an optimized fluidic control device to operate in the S8Ch wind tunnel. This wind tunnel equipped with the configuration called Délery bump generates a λ shaped pattern shock-wave at Mach 1.4 with a massive separation of the turbulent boundary-layer.

Flow control context The bibliographic study on flow control techniques in Chap. I has presented different methods of control, with notably mechanical VGs which have been proven to be efficient in the control of the SWBLI. The principle of these devices is to generate vortices along the wall, which mix the inviscid upper flow with the boundary-layer, thus re-injecting energy in this last one in order to prevent it from separating when encountering the pressure gradient associated to the shock-wave. Another promising method of control is the use of fluidic Vortex Generators, indeed, these last ones can be easily turned off during the flight phases when they are not necessary.

The presentation of several studies on the interaction between a pitched and skewed jet and a transverse flow has brought to the fore the fact that different configurations of vorticity distribution are found depending on the pitch and skew angles. The whole diversity of structures has not been completely described, notably few works are found on jets pointing upward the main flow. The fluidic VGs have proven their efficiency on subsonic configurations and on wing in buffet condition. In a channel, the problem differs as studies notably described the impact of corner and thus corner flow separation on the main flow. Hence, the control set-up needs to be optimized as a whole.

Consequently, a global optimization of fluidic control configuration has been carried out.

Means of investigation A presentation of the different tools used in this study was displayed in Chap. II, with notably for the experimental part the tomographic PIV method and for the numerical part the RANS and ZDES modeling. In Chap. III, the results of the RANS calculation of the flow in the S8Ch wind tunnel have been satisfyingly confronted to the results of previous experiments. An algorithm of optimization based on the Kriging meta model has then been performed on a set-up of 10 fluidic VGs. The parameters chosen for the optimization where the pitch and skew angles. The jets were oriented in counter-rotating pairs. The objective function of this process was a criterion of homogeneity called $DC50$. A second optimization has been implemented which focuses on the control of the corner flow separation by optimizing an added external jet in pitch and skew angles, and in lateral and longitudinal positions. The optimum fluidic control configuration found, called "Control 1", has been adapted to transonic test section as well as a more common control configuration called "Control 2", where the jets are oriented in the main flow direction. The process of conception has been detailed in Chap. V. RANS and ZDES modelings have been confronted to experimental results such as oil flow and Schlieren visualizations and pressure distribution measurements in Chap.VI for the reference case and in Chap.VII for the two controlled cases.

VIII.2 Conclusions

Optimization The optimization was carried out using a Kriging based algorithm. An important part of the work was to implement an entirely automate calculation chain going from meshing to RANS resolution. This tool was operated to compute the data used to construct and enrich the meta model.

The first step of optimization, has resulted in a first optimal control configuration with pitch angles equal to 30° and skew angles equal to ±102.8° , i.e. slightly upstream blowing jets, not studied before to the author knowledge. This configuration reduces the objective function, the DC50 criterion (based on pressure losses) by 22%. The second step of the optimization consisted in the research of a new configuration, derived from an optimal of the first optimization, in which a jet is added and optimized in angles an position. The algorithm has detected a zone of interest in which the DC50 criterion is reduced by 61%. This configuration only requires a low momentum coefficient c_μ of 0.03% which makes it an efficient control. The external jet added in the optimal configuration is again slightly blowing upstream with a pitch angle of 30° and a skew angle of 106°. The optimized position of this added fluidic VG is found especially close to the lateral wall with more latitude on the longitudinal position. This highlighted the interest of having a global approach for the design of a control of SWBLI. The massive central separation is linked to and influenced by the corner flow separation and vice versa.

This study has demonstrated that upstream blowing jets can be efficient to control a normal SWBLI. Compared to jets blowing downstream, they generate different vortical structures which have different vertical and lateral velocities. Their capability to generate a pair of co-rotating vortices close to the wall allows for a larger lateral displacement of the vortices and induces a wider mixing of the boundary-layer. Kriging optimization is

now a common tool in the literature but few studies go as far as implementing and testing experimentally the numerical optimization.

Numerical modeling of SWBLI: RANS The RANS model is found quite satisfyingly precise on the central separation zone and the friction lines in the corner separation. It has allowed to characterize a complex topology with six zones of separation. Two separations arise in the center of the channel on the lower and upper walls. Four others develop in corner regions, the lower ones being widely more important than the upper ones.

The RANS calculation has also allowed to investigate the corner flow separation zone. It has been distinctly decomposed into two vortices. The first one is slightly upstream on the lower wall and the second one is positioned on the lateral wall.

For the controlled cases, this study has allowed to compare globally coherent friction lines and vorticity development in the angled jet / cross flow interaction. Taking into account the control did not deteriorate the quality of the agreement between RANS and experimental results. RANS modeling is thus considered a sufficiently accurate tool to design and optimize a control set-up.

For the clean, no-control case, the total pressure measurement in the far downstream flow, have confirmed the presence of the three main separation zones, the central one and the two corner ones. Unfortunately, technical limitations prevented a comparison of the stagnation pressure distribution on a plane far downstream of the interaction for the controlled cases. Even if the levels are globally comparable, the RANS calculation seems to slightly overpredict the corner flow separation. Nevertheless, the RANS calculations and the tomographic PIV measurements are in good agreement on the two median planes of the most centered volumes.

Numerical modeling of SWBLI: ZDES The Zonal Detached Eddy Simulation has failed to completely capture the exact physics of the flow observed in the wind tunnel with a main discrepancy at the beginning of the central separation zone. This may be due to a too coarse mesh close to the mixing layer which is situated above the zone of high grid points clustering in the wall vicinity. The scatter on the central separation estimation seems to feedback the corner flow separation and to reduce its size. Nevertheless, this modeling has allowed to capture the main unsteadiness of the flow. The local pressure sensors capture the same characteristic frequencies as the previous experimental studies: 300Hz for the shock-wave boundary-layer interaction and 4kHz for the Kelvin Helmholtz instability developing on the mixing layer.

The modeling of a transonic Shock-Wave / Boundary-Layer Interaction with the four walls in experimental conditions remains a challenge due to the wide range of frequency involved and to the intense interaction between all the different separation zones.

Implementation of fluidic VGs in a transonic wind tunnel Two fluidic control configurations have been successfully implemented in the transonic wind tunnel allowing to reduce the size of the central separation, developing complex 3D patterns with structures of coupled foci. The most important structure is the central one in both cases with smaller, less intense structures developing on the lower wall. In the Control 1 case, the central separation is higher but less extended in width than in the Control 2.

The two control devices have also allowed to modify the corner flow separation, with the Control 1 controlling more intensely the separation on the lower wall than Control 2.

Indeed, Control 2 is not capable to restrain the strong corner flow separation appearing due to the control of the central separation. The reverse jets are thus confirmed to be more efficient in the control of corner flow separation.

On the unsteadiness point of view, the control methods strongly modify the lateral distribution of energy on the main frequencies. On the central line, the major modifications observed are: the modification of the shock position which changes the intensity seen by the sensors, and the modification of the frequency characteristic of the shock-wave which is shifted from 300Hz to 800Hz. This is coherent with a modification of the length of the separation length for a constant Strouhal number for the SWBLI. It can also be noticed that in the corner, the control is modifying both frequency levels: the shock-wave frequency at 800Hz and a Kelvin Helmholtz frequency shifted from 4kHz to 3kHz.

The fluidic VGs have been compared to previous studies using mechanical VGs. They have proven to be as efficient as these latter. In particular the Control 2 has similar impact as the mechanical VGs on the central pressure distribution.

On another note, the two control devices have proven to be efficient for pulsed jets. Nevertheless, the pulsed control has an efficiency which is below the continuous control and above the uncontrolled case. The dominant parameter of the efficiency of the control is the Duty Cycle and thus, the total time of activation over a period. This parameter allows to adjust the level of control wished. No prominent variation of controls has been noticed for various frequencies. However, only frequencies below the characteristic frequency of the controlled shock-wave have been tested.

Tomographic PIV The tomographic PIV measurement technique has been validated using previous 2D PIV and LDV results for a transonic configuration.

It has allowed to measure 3D flow features of the SWBLI. The impact of the VGs on the central separation have been accurately described using notably tomographic PIV. Tomographic PIV has proven to be an interesting measurement technique even if the limitations on the measurement close to the wall are penalizing in this particular case where the separations occur really close to the wall. However, if tomographic PIV was not able to accurately describe the flow at less than 2mm from the wall, it was able to measure the modifications on the main flow which reflect the state of the boundary-layer.

VIII.3 Perspectives

Optimization process Once a reference case has been managed using ZDES modeling, an idea to improve the optimization process, could be to use co-Kriging to improve the reliability of the prediction of the model. The idea behind co-Kriging is to use more precise results such as ZDES calculations or experimental measurements to correct the Kriging meta model. Indeed, using points calculated using both RANS and ZDES, an error function can be defined and used to correct the Kriging model (for more detailed see Forrester et al. [67]). This will allow to have a more precise prediction of the capacity of each configuration of control parameters.

Another avenue for improvement could be to use the tomographic PIV measurements performed in the current study to compare to other RANS models in order to improve the coherence of the RANS and experiments farther from the central plane.

ZDES In order to improve the results obtained by the ZDES calculation, a refinement in the mixing layer may help the development of turbulent structures to happen earlier.

Another point which may be responsible for the slow development of turbulent structures is the fact that the height of the separation zone is close to the size of the incoming boundary-layer. A test of the ZDES mode 3 should be performed on this configuration. This more complex modeling uses LES down to around 10% of the boundary-layer and synthetic turbulence injection in the interface between URANS and LES. It enables the flow to develop more rapidly turbulent structures.

Experiments On the experimental point of view, several improvements may be considered. First, the use of a transparent lower wall will reduce the reflection on this latter and allow to place cameras at positions where they will have less blind spots troubles. This and the use of lateral windows exempt from scratches and with lower reflection, may allow to perform tomographic PIV measurement closer to the lateral wall in order to better describe the corner flow separation.

In order to improve the tomographic PIV results in terms of shear stress precision notably, the use of anisotropic interrogation volumes may be of great help. Indeed, the recent developments made on the Onera's in house software of correlation have considerably improve the description of re-circulation zone in a different configuration.

In a more promising way, the use of LDV measurements may be a solution to accurately measure the flow in the corner.

Another avenue for research could be the use of piezoelectric actuators in order to reach higher frequencies of actuation and try to modify the natural frequency of the Kelvin Helmholtz interaction and thus, maybe to improve the control efficiency.

A

Appendix

Contents

A.1 Résumé en français

1.a Introduction: l'interaction onde de choc / couche limite

L'interaction entre une onde de choc et une couche limite est une problématique essentielle dans la conception d'une prise d'air pour l'ensemble des véhicules supersoniques et

hypersoniques. En effet, le fort gradient de pression généré par l'onde de choc va provoquer un décollement de la couche limite à la paroi qui nuit à l'efficacité de l'entrée d'air. La topologie de cette interaction dans le cas d'une conduite rectangulaire est présentée sur la FigureA.1. La structure des chocs est en forme de λ, avec un choc oblique et un choc quasi-normal qui se rejoignent au point triple d'où part le choc droit à travers le canal. Le saut de pression à travers le choc de tête (oblique) conduit au décollement de la couche limite avec la présence d'une zone de recirculation. Cette zone de recirculation provoque des hétérogénéités, des pertes de pression totale ainsi que des instabilités qui peuvent s'avérer dangereuses pour le véhicule.

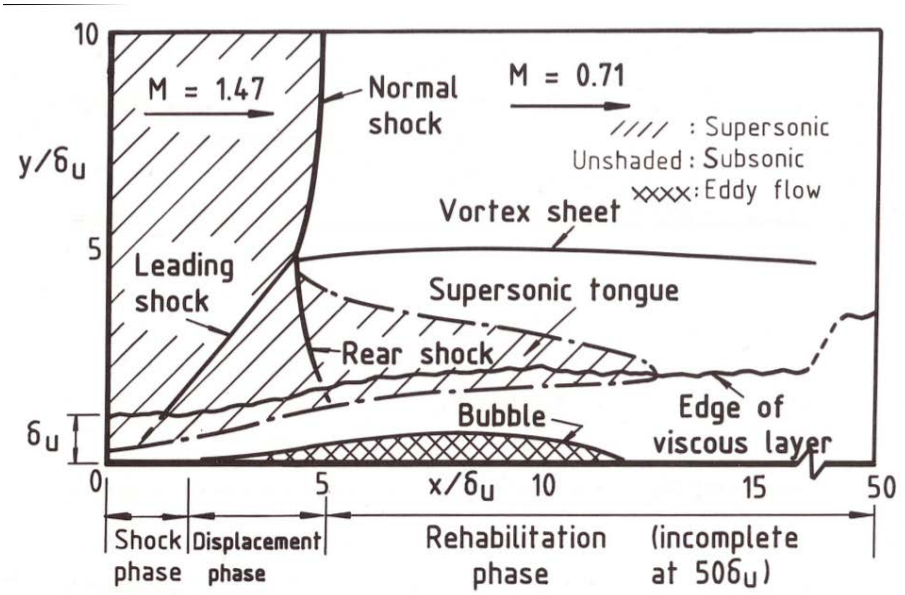

Figure A.1: Schéma descriptif de l'interaction entre une onde de choc normale et une couche limite turbulente avec décollement (tiré de Seddon and GoldSmith [156]).

L'objectif de cette thèse est de concevoir un contrôle fluidique de cette interaction forte avec décollement à l'aide d'optimisations s'appuyant sur des calculs numériques. Le but du contrôle fluidique est de diminuer la taille de la zone de recirculation, d'agir sur les écoulements de coin et ainsi d'homogénéiser l'écoulement en aval tout en réduisant les pertes liées au décollement.

1.b Contexte: le contrôle d'écoulement

Le Chapitre I présente un état de l'art des différentes méthodes de contrôle de l'interaction onde de choc / couche limite. La méthode qui apparait comme prometteuse est l'utilisation de micro-jets qui en interagissant avec l'écoulement principal vont former des tourbillons qui vont permettre de réinjecter de l'énergie cinétique dans la couche limite amont. La couche limite ainsi redynamisée supporte mieux l'onde de choc et l'interaction produit des décollements de plus petites tailles.

Le champ de vorticité produit par l'interaction entre un jet perpendiculaire et un écoulement transverse a été largement étudié dans la littérature. L'interaction produit principalement deux tourbillons longitudinaux contra-rotatifs qui sont visibles sur la Figure A.2.

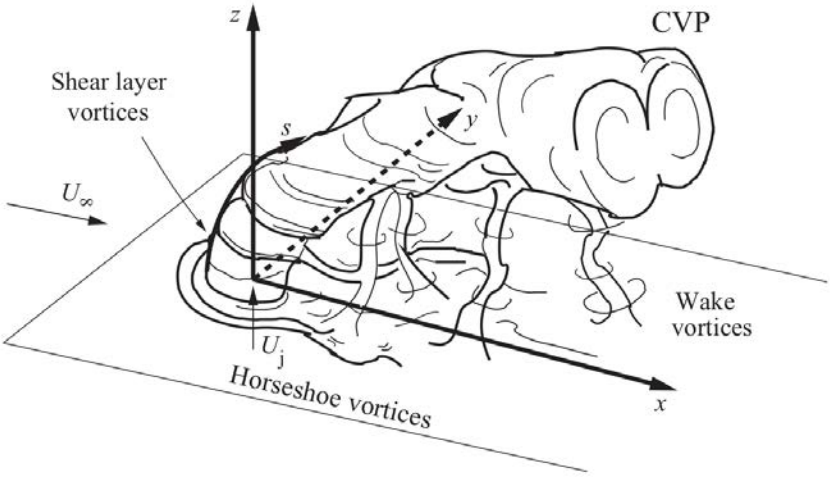

Figure A.2: Principales structures de vorticité produites par l'interaction entre un jet perpendiculaire et un écoulement transverse (tiré de Karagozian [100]).

Les structures développées par des jets inclinés en tangage et en lacet diffèrent de celles développées par des jets perpendiculaires. Un état de l'art des études(Compton and Johnston [34], Zhang [181], Bray and Garry [15], Han et al. [88], Khan and Johnston [102], Rixon and Johari [140] Godard and Stanislas [84], Shapiro et al. [157], Kostas et al. [105], Beresh et al. [13], Dai et al. [41]) sur les jets inclinés est résumé dans les tableaux I.2 et I.1 (en anglais). La complexité de l'interaction n'a pour l'instant pas permis de définir un modèle simple de la vorticité produite par un jet incliné.

Des jets ont déjà été utilisés dans des études précédentes pour contrôler l'interaction onde de choc / couche limite. Cependant, le grand nombre de paramètres à optimiser (nombre de jets, positions, orientations, pression et débit) en fait un moyen de contrôle moins étudié que les générateurs de tourbillons (VGs) mécaniques (Lin [116], Lu et al. [120], Panaras and Lu [132], Titchener and Babinsky [167], Bur et al. [20]) qui sont plus simples à mettre en œuvre. Un résumé des articles (Lin et al. [115], Hansen and Bons [89], Kumar and Alvi [108, 109], Garnier [75], Chabert [24], Rao [138], Pearcey et al. [135], Souverein and Debiève [159], Dandois et al. [44], Molton et al. [125]) traitant du contrôle fluidique est présenté dans les tableaux I.3 et I.4 (en anglais). L'état de l'art ne permet pas de définir une configuration optimale de contrôle même si plusieurs études considèrent que des configurations avec des angles de tangage de 30° et de lacet de 60° permettent dans certaines situations le meilleur contrôle par rapport aux autres moyens de contrôle testés.

i Décollement de coin

Dans le cas d'une interaction dans un canal rectangulaire, un décollement de coin se forme aussi le long des parois latérales de la veine. Ces décollements sont visibles sous la forme de foyers (« foci ») sur la Figure A.3. Ces décollements de coin ont été peu étudiés et il existe peu d'articles traitant de leur contrôle.

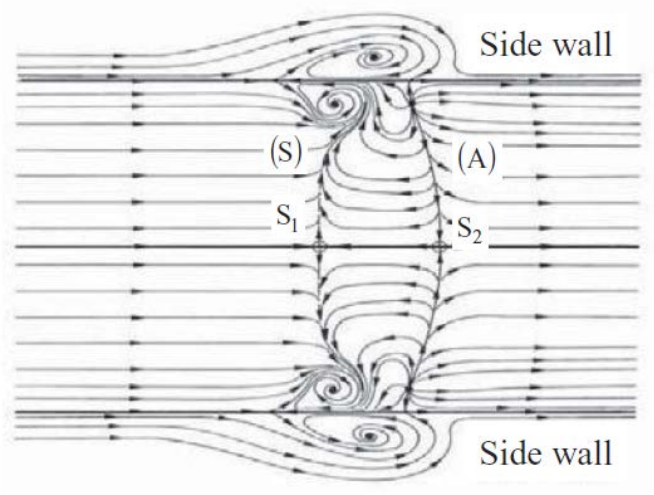

Figure A.3: Topologie 3D des lignes de frottements d'une interaction onde de choc / couche limite dans une veine rectangulaire, issu de Babinsky and Harvey [6].

1.c Outils pour l'étude

Le chapitre II présente les moyens expérimentaux et numériques mis en œuvre dans cette thèse.

i Soufflerie S8Ch et moyens de mesure

L'étude est réalisée dans la soufflerie transsonique S8Ch de l'ONERA Meudon et porte plus précisément sur la configuration de la bosse de Délery utilisée dans de précédentes études(Bur et al. [20], Galli et al. [71], Galli [70], Sartor et al. [152, 154], Merienne et al. [124]). La forme de la bosse a été dimensionnée de manière de générer des gradients de pression provoquant le décollement de la couche limite turbulente.

La soufflerie est présentée sur la Figure A.4 ainsi que le champ de nombre de Mach calculé qui permet de localiser l'interaction onde de choc / couche limite décollée dans la soufflerie. Cette soufflerie a été équipée en capteurs de pression stationnaires et instationnaires ainsi que d'un banc strioscopique. Un peigne de Pitot a été conçu et réalisé, afin de mesurer la pression d'arrêt sur un plan en aval de l'interaction. Sa position est visible sur la Figure A.4b.

ii PIV tomographique

Dans la section II.2 sont développés le principe et l'application de la Vélocimétrie par images de particules tomographique (PIV tomographique). Les principes fondamentaux de cette méthode sont la reconstruction de la position 3D de petites particules d'ensemencement placées dans l'écoulement à l'aide de plusieurs caméras, et la reconstruction d'un champ 3D de vitesse à l'aide de deux images prises à des instants très proches.

La reconstruction des positions des particules est effectuée à l'aide d'une initialisation MLOS (Lignes de vue multiplicatives), suivi de l'algorithme SMART (Technique de reconstruction simultanée par algèbre multiplicative), présentés en détail dans Atkinson and Soria [5].

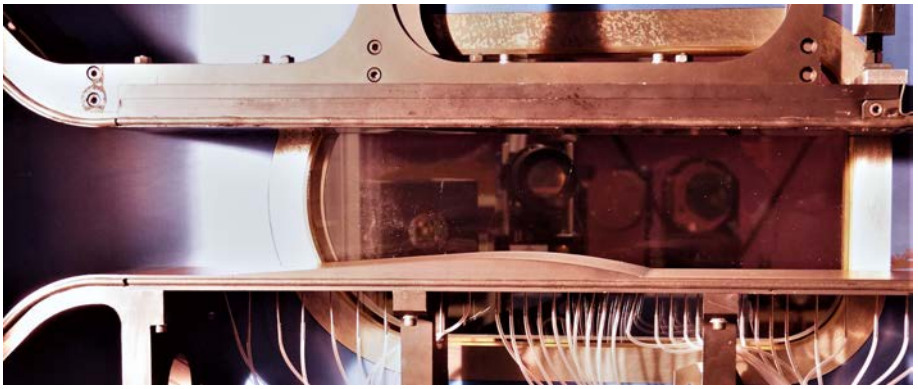

(a) Photographie

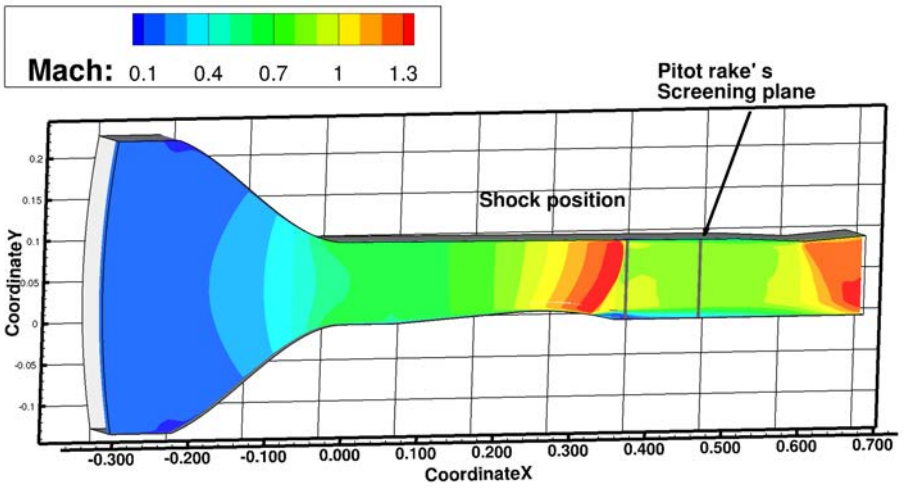

(b) Repère de référence.

Figure A.4: Présentation de la soufflerie S8Ch.

Le montage de PIV Tomographique est présenté sur la Figure A.5. On y voit les quatre caméras positionnées de part et d'autre de la veine ainsi que le laser qui est introduit verticalement dans la veine par le plafond. Ce montage permet de limiter les reflets sur les parois latérales de la veine. Cependant, la forte puissance du laser nécessaire à l'illumination d'un volume de $100 \times 100 \times 20$ mm, génère de forts reflets sur le plancher de la veine. Afin de pallier ce problème, de la rhodamine (une peinture fluorescente) a été appliquée sur le plancher de la veine et des filtres permettant d'observer uniquement le laser incident ont été apposés sur les objectifs des 4 caméras. Néanmoins, le reflet résiduel et la géométrie de la bosse empêchent de reconstituer un champ de vitesse à moins de 2 mm du plancher. Les reconstructions calculées à l'aide des deux caméras perpendiculaires à la veine permettant les meilleures résolutions proches parois, elles seront privilégiées par rapport aux reconstructions à 4 caméras dans la suite de l'étude.

iii Méthodes numériques

Dans la section II.3, les différentes simulations numériques utilisées dans cette étude sont présentées. Une simulation Reynolds Averaged Navier Stokes (RANS) fermée par le

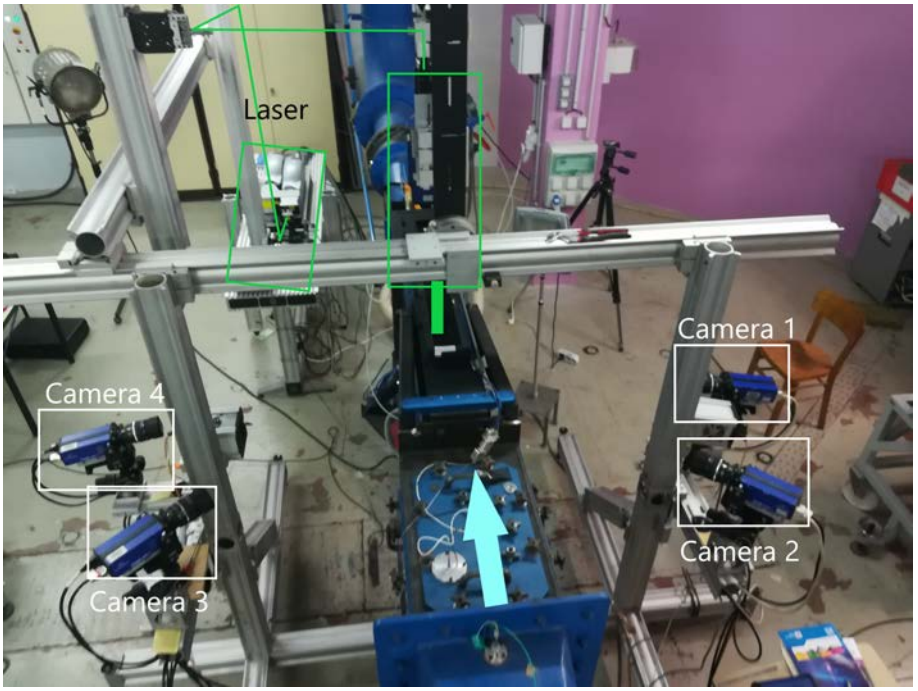

Figure A.5: Vue du dessus de l'installation de PIV tomographique.

modèle de turbulence de Spalart Allmaras (Spalart and Allmaras [160]) a été choisie pour l'optimisation du fait de son faible coût de calcul et de sa bonne précision. Une méthode de calcul instationnaire nommée Zonal Detached Eddy Simulation a été retenue pour l'écoulement du cas de référence. Cette approche, présentée dans Deck [46] et en français dans Laraufie [110], Renard [139], est une méthode hybride entre la modélisation RANS et la modélisation Large Eddy Simulation(LES) plus précise mais encore trop coûteuse en temps de calcul.

Les différents maillages et conditions limites utilisés sont présentés.

1.d Validation de la modélisation RANS en vue de l'optimisation

Le cas de référence, non contrôlé a été calculé à l'aide du modèle RANS. Cette simulation numérique a été confrontée à différents résultats de précédentes études expérimentales sur cette configuration : mesures pariétales et de champ de pressions stationnaire et instationnaire, lignes de frottement ainsi que des mesures de champ de vitesse effectuées à l'aide de PIV 2D. Le champ de vitesse longitudinale calculé dans le plan médian de la soufflerie est comparé à la mesure PIV 2D de Sartor et al. [152] sur la Figure A.6. L'accord satisfaisant avec l'expérience permet de valider l'utilisation de la modélisation RANS pour la suite de l'étude et notamment l'optimisation numérique du contrôle.

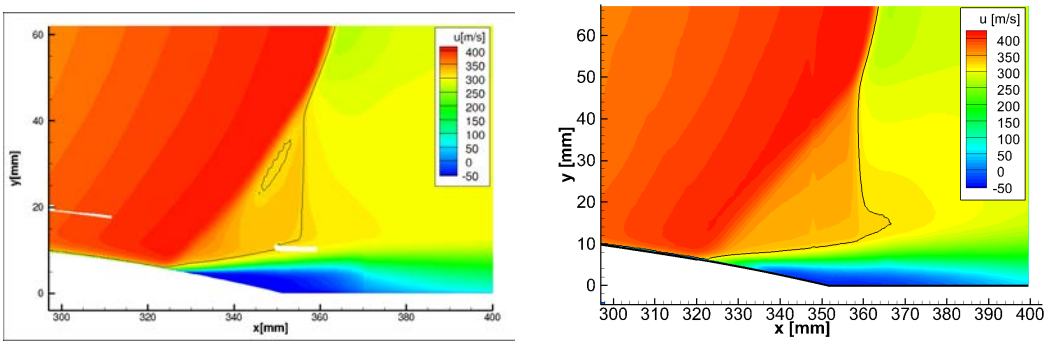

(a) Résultats RANS (b) Mesure PIV 2D de Sartor et al. [152].

Figure A.6: Champ de vitesse longitudinale sur le plan médian de la soufflerie.

1.e Optimisation du contrôle

Le chapitre IV présente la démarche d'optimisation appliquée au contrôle fluidique de l'interaction onde de choc / couche limite. Après une première section présentant les différentes méthodes d'optimisation par méta-modèles existantes, la section IV.1 détaille l'algorithme d'optimisation construit sur un modèle de régression nommé Krigeage avec erreur de mesure(Krige [107], Forrester et al. [66]), enrichi à l'aide de la fonction d'amélioration espérée (Expected Improvement).

i Paramètres

La difficulté de l'optimisation des jets fluidiques réside dans le grand nombre des paramètres à choisir (pression, nombre, positions, orientation). Afin de limiter les calculs numériques coûteux (un équivalent 3800h CPU) qui augmentent de façon exponentielle avec le nombre de paramètres, la présente étude considère uniquement les angles de tangage et de lacet des jets dans un premier temps. Dix jets de diamètre 1 mm sont positionnés par analogie avec les meilleurs résultats de l'étude de Bur et al. [20] utilisant des VGs mécaniques sur la même configuration (jets en position contra-rotative).

ii Objectif

L'objectif choisi pour cette étude est un objectif d'homogénéité de l'écoulement dans la veine. Un critère d'homogénéité nommé $DC50$ est défini à partir d'un autre critère utilisé par les motoristes sur des veines à section circulaire nommé $DC60$ Goldsmith and Seddon [86], Garnier [75]. Ce critère est calculé à partir de pressions d'arrêt mesurés en aval de l'interaction au niveau du peigne de Pitot, visible pour le cas de référence sur la Figure A.7. Les zones de pertes de pressions d'arrêt sont dues au décollement central et au décollement de coin visualisées par des surfaces blanches sur la demie-veine, voir la Figure A.7.

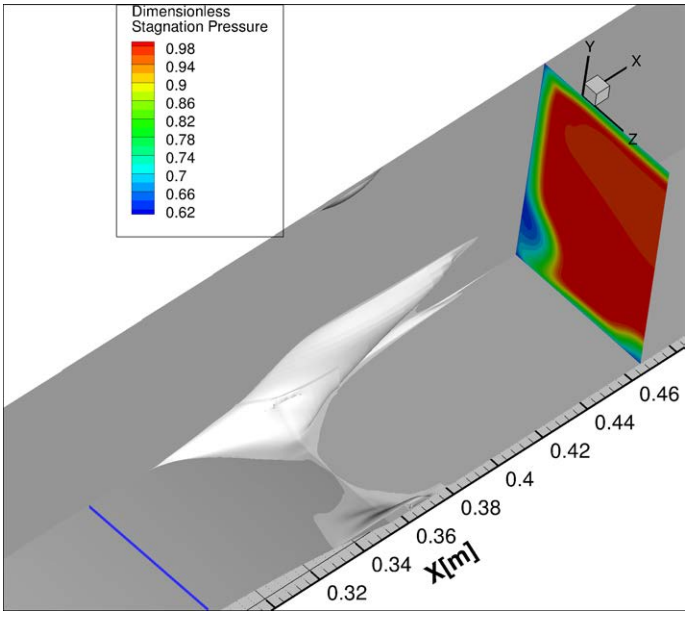

Figure A.7: Pression d'arrêt adimensionnée en aval de l'interaction et régions de décollement, délimitées par la surface blanche. La ligne bleue représente la position des VGs fluidiques.

iii Première optimisation

La première optimisation présentée dans la section IV.2, est considérée convergée lorsqu'au bout de 36 calculs numériques RANS, le méta-modèle de Krigeage cesse d'être modifié à chaque itération.

L'algorithme a permis d'explorer une grande variété de configurations présentant diverses formes de répartitions et d'intensité de vorticité. Les champs de vorticité engendrés sont présentés sur plusieurs images.

Le méta-modèle obtenu permet de distinguer deux zones particulièrement intéressantes dans lesquelles le critère d'optimisation est diminué de 11 et 22%. Ces deux zones correspondent à des cas pour lesquels les jets sont orientés légèrement à contre-courant. Le contrôle obtenu à l'aide de la configuration optimale de la première optimisation est présenté sur la Figure A.8. On observe une forte diminution du décollement central, et une modification du décollement de coin qui diminue son impact en aval de l'interaction.

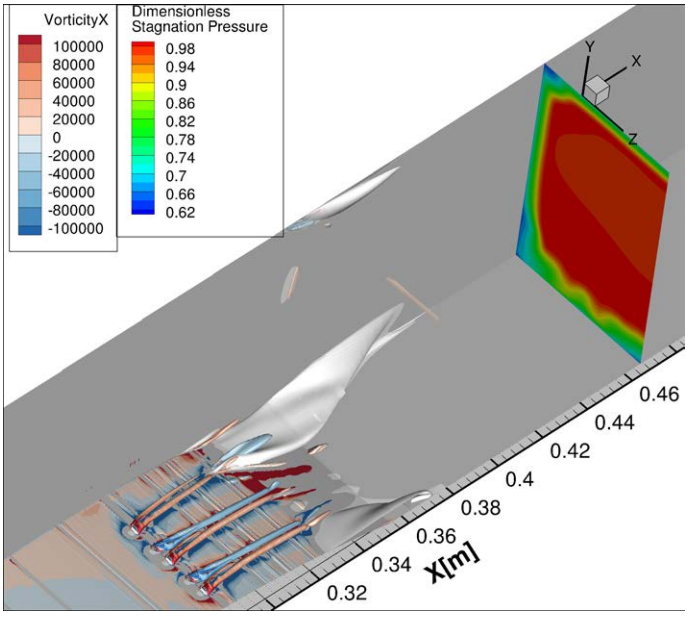

Figure A.8: Pression d'arrêt adimensionnée en aval de l'interaction, régions de décollement délimitées par la surface blanche et iso-surface de critère Q égal à $3 \cdot 10^8$, colorée par la vorticité longitudinale pour le cas optimal de la première optimisation.

iv Seconde optimisation

Afin d'améliorer le résultat de la première optimisation, une seconde optimisation est entreprise dans la section IV.3. Cette optimisation se concentre sur le contrôle du décollement de coin. Puisque ce type de contrôle est moins étudié dans la littérature, plus de paramètres ont été optimisés. Les quatre paramètres choisis sont les angles de tangage et de lacet ainsi que la position longitudinale et latérale. Cette optimisation est réalisée sur un jet ajouté proche de la paroi latérale et les 5 jets d'une demie- configuration de la précédente optimisation.

Malgré un méta-modèle globalement peu sensible aux variations des paramètres, l'algorithme a réussi à trouver une zone d'intérêt de faible envergure dans laquelle le critère $DC50$ est fortement diminué. Le cas optimal présenté sur la Figure A.9 permet de réduire significativement les pertes de pression d'arrêt dans la veine en aval de l'interaction et de diminuer le critère de $DC50$ de 61% par rapport au cas de référence. Dans la zone optimale, le jet de coin est légèrement orienté à contre-courant et placé très proche de la paroi latérale. Sa localisation vis-à-vis de la région d'interaction semble être un paramètre moins sensible de l'optimisation.

v Analyse des champs de vorticité

Une analyse plus approfondie des champs de vorticité est effectuée afin de comprendre plus précisément la raison de l'efficacité des jets orientés légèrement à contre-courant. Des modèles de Krigeage de différentes caractéristiques de la vorticité longitudinale produite par un jet sont construits en fonction des angles de tangage et de lacet. Ces modèles permettent d'affirmer que le supplément d'efficacité des jets à contre courants provient du fait que leur champ de vorticité génère une plus grande vitesse longitudinale que les jets

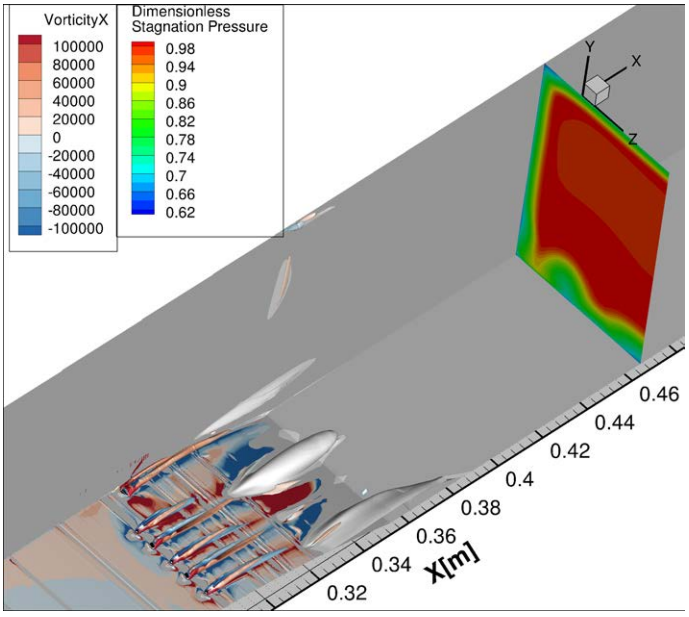

Figure A.9: Pression d'arrêt adimensionnée en aval de l'interaction, régions de décollement délimitées par la surface blanche et iso-surface de critère Q égal à $3 \cdot 10^8$, colorée par la vorticité longitudinale pour le cas optimal de la seconde optimisation

orientés selon l'écoulement.

1.f Conception des configurations de contrôle

Le chapitre V présente la démarche de conception du dispositif de contrôle fluidique implémenté dans la soufflerie. Il comprend des actionneurs qui ont été caractérisés à différentes fréquences ainsi qu'un système de barrettes permettant de changer de configuration de contrôle facilement. Le montage est présenté sur la Figure A.10.

Les deux configurations de contrôle retenues sont détaillées dans le Tableau A.1. Le cas de « Contrôle 1 » s'appuie sur le cas optimal de l'optimisation tandis que le cas de « Contrôle 2 » est plus proche du cas de contrôle « classique » trouvé dans la littérature, à savoir des jets orientés dans le sens de l'écoulement principal.

Table A.1: Caractéristiques des configurations de contrôle choisies pour les tests en soufflerie

Nom	Distribution	$\alpha_{centre}[^\circ]$	$\beta_{centre}[^\circ]$	$\alpha_{coin}[^\circ]$	$\beta_{coin}[^\circ]$	$DC50$
Contrôle 1	Optimisation	60	± 135	50	± 105	0.63
Contrôle 2	Corrigée	30	± 60	30	± 60	0.69

Les champs de pression d'arrêt prédits par les calculs numériques RANS, pour les trois configurations étudiées, sont présentés sur la Figure A.11. On peut voir sur la figure du cas de référence les zones de pertes de pression d'arrêt dues au décollement de coin (sur la gauche) et au décollement central (sur la droite). Dans les deux cas contrôlés, une diminution du décollement de coin se fait au prix d'un accroissement de la perte de pression d'arrêt due à la couche limite entre les deux décollements. La diminution du

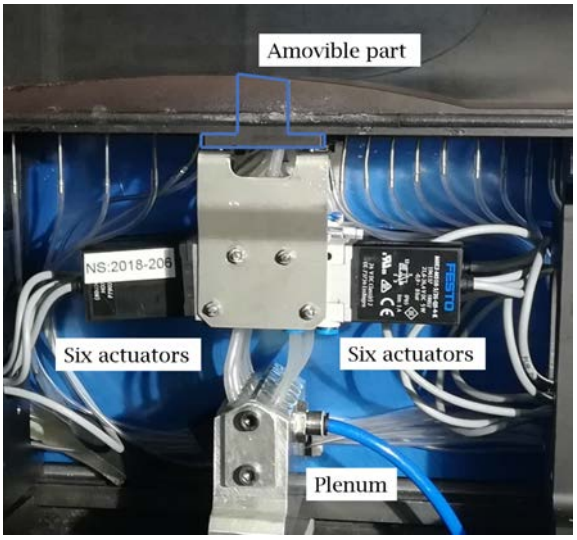

Figure A.10: Actionneurs fluidiques montés dans la soufflerie (sous la bosse, en amont de l'interaction).

décollement de coin est plus marquée dans le cas du Contrôle 1.

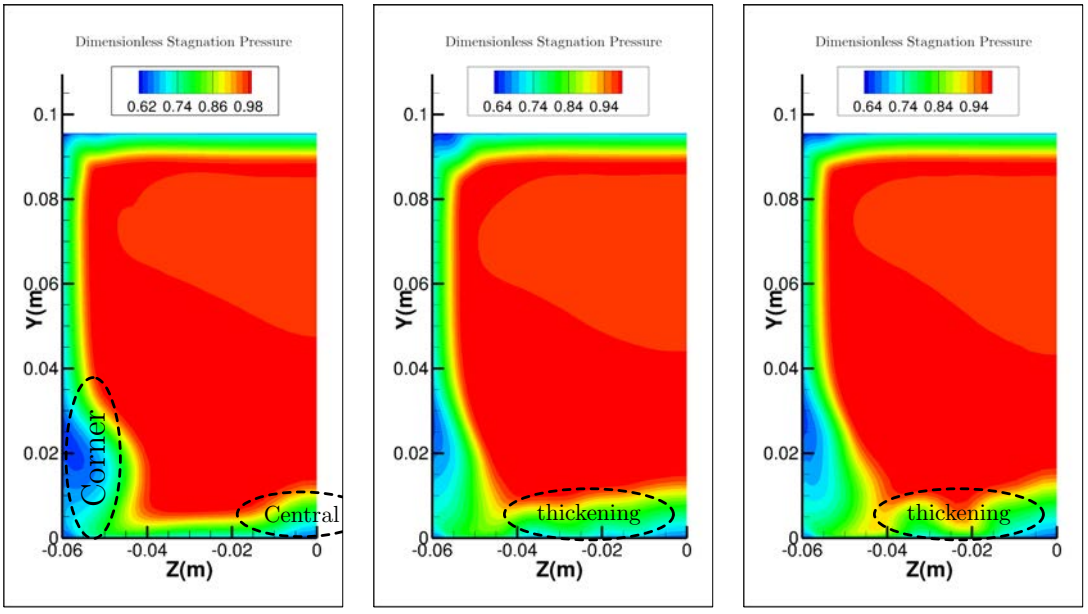

(a) Cas de référence (b) Contrôle 1 (c) Contrôle 2

Figure A.11: Pression d'arrêt adimensionnée en aval de l'interaction en $x = 468\,\text{mm}$, issue des calculs numériques RANS pour les trois cas testés expérimentalement.

1.g Caractérisation du cas de référence

Le chapitre VI présente la caractérisation expérimentale du cas de référence. Les résultats expérimentaux sont comparés aux calculs RANS et ZDES. Les comparaisons de résultats

sur la visualisation strioscopique, les mesures de pression stationnaires et les lignes de frottement pariétal permettent de considérer que le calcul RANS rend bien compte de la physique de l'interaction tandis que la ZDES présente un défaut non physique avec retard aux développements des fluctuations résolues au niveau du décollement. Ce défaut est sans doute lié à un maillage trop lâche au niveau de cette zone éloignée de la paroi.

Les mesures de pression d'arrêt par le peigne Pitot ont permis de confirmer l'impact du décollement de coin sur la pression d'arrêt en aval de l'interaction. Cependant, des difficultés d'ordre matériel ont empêché son utilisation dans les cas contrôlés.

i Validation de la PIV tomographique

Dans la sous-section 1.e, la PIV tomographique est tout d'abord comparée à des mesures de vélocimétrie laser à effet Doppler de Délery [49] et à des mesures de PIV 2D de Sartor et al. [152]. Ces comparaisons effectuées dans le plan médian de la soufflerie permettent de valider les mesures par PIV tomographique jusqu'à 2 cm de la paroi. A titre d'exemple, la comparaison de la vitesse longitudinale dans le plan médian est présentée sur la Figure A.12. La zone noire visible sur le champ de vitesse de la PIV tomographique est la zone dans laquelle la mesure est invalidée à cause des reflets sur le plancher de la veine.

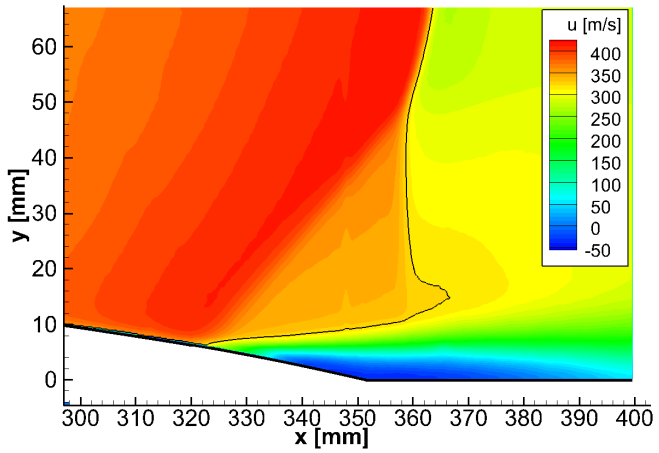

(a) PIV 2D issue de Sartor et al. [152].

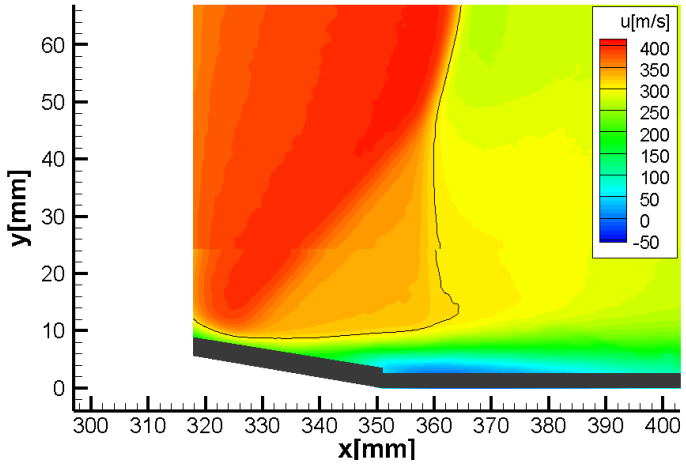

(b) PIV tomographique.

Figure A.12: Comparaison du champ de vitesse longitudinale sur dans le plan médian, $z = 0\,\text{mm}$, entre la PIV 2D de Sartor et al. [152] et la PIV tomographique.

L'utilisation de la PIV tomographique permet d'observer la topologie de l'onde de choc et de la zone de décollement selon l'envergure de la veine. Des iso-surfaces de vitesse présentées sur la Figure A.13 montrent un décollement qui diminue fortement lorsque l'on s'éloigne du centre de la veine. Cela confirme le fait que le phénomène ne peut être considéré bidimensionnel que sur une faible envergure de veine et est influencé par la présence du décollement de coin. Du fait de reflets sur la paroi latérale de la veine, les mesures de vitesse dans la zone située le long de la paroi n'ont pas pu être clairement reconstituées.

Les mesures de pressions instationnaires ont par ailleurs permis de retrouver les deux fréquences caractéristiques de l'interaction : celle liée au battement du choc à 300 Hz et celle liée à l'instabilité de Kelvin Helmholtz à 4 kHz. La ZDES, malgré son défaut physique, présente des fréquences énergétiques proches de celles mesurées expérimentalement ainsi que des modes de décomposition spectrale orthogonale (SPOD Taira et al. [164], Towne et al. [169]) proches des modes décrits par Sartor et al. [154].

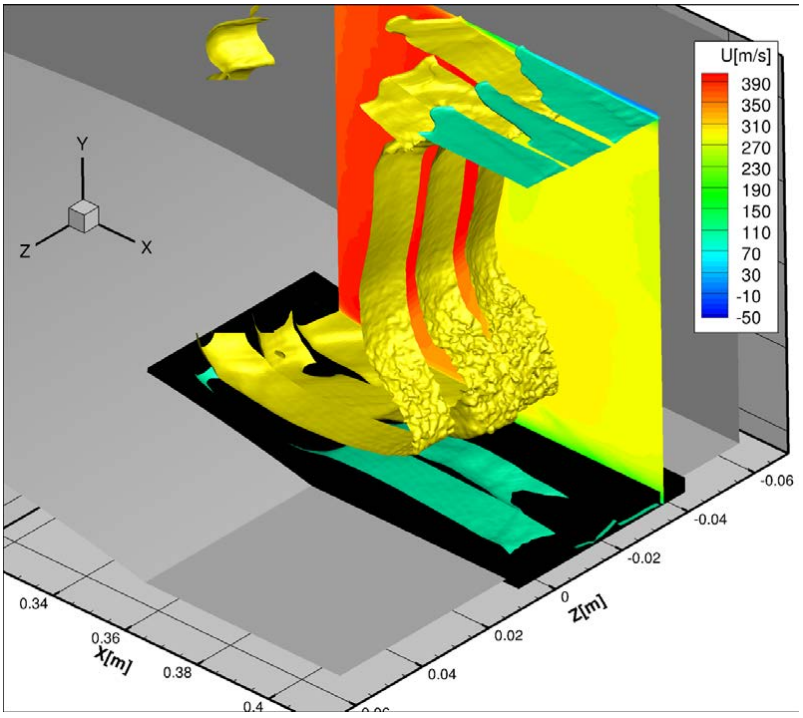

Figure A.13: Visualisation 3D de l'interaction pour le cas de référence, deux iso-surfaces à $u = 300\,\mathrm{m\,s^{-1}}$ (en jaune) et $u = 100\,\mathrm{m\,s^{-1}}$ (en vert). Le plan $z = -40\,\mathrm{mm}$ est représenté. La zone en noir représente la région dans laquelle la PIV tomographique est aveuglée par la réflexion du laser sur la paroi.

1.h Caractérisation des cas contrôlés

Le chapitre VII présente les résultats expérimentaux caractérisant les cas contrôlés par VGs fluidiques.

i Contrôle 1

La configuration de Contrôle 1 proche du cas optimal de l'optimisation numérique, génère une forte modification de l'interaction. Les lignes de frottement obtenues à l'aide de visualisations par enduit visqueux (bouillies colorées) pour le cas de référence et le cas de Contrôle 1 sont présentées sur la Figure A.14. On observe que l'interaction devient pleinement tridimensionnelle avec une division de la zone de décollement centrale en plusieurs petites zones, paires de foyers (foci, notés F). La zone de décollement et son impact sont réduits. On note aussi une modification de la structure du décollement de coin dont le volume est diminué. Ces structures sont globalement bien prédites par le calcul RANS.

La PIV tomographique présentée sur la Figure A.15 permet de confirmer une modification de la nature tridimensionnelle de l'onde de choc ainsi que du décollement central. Cependant, sa limitation au niveau de la paroi basse n'a pas permis de caractériser finement la modification des zones de décollement.

Différentes variantes du contrôle ont aussi été caractérisées à l'aide des mesures de pression. Les jets des actionneurs ont été activés à différentes fréquences entre 100 et 600Hz. La conclusion de cette étude est que l'efficacité du contrôle est liée au temps

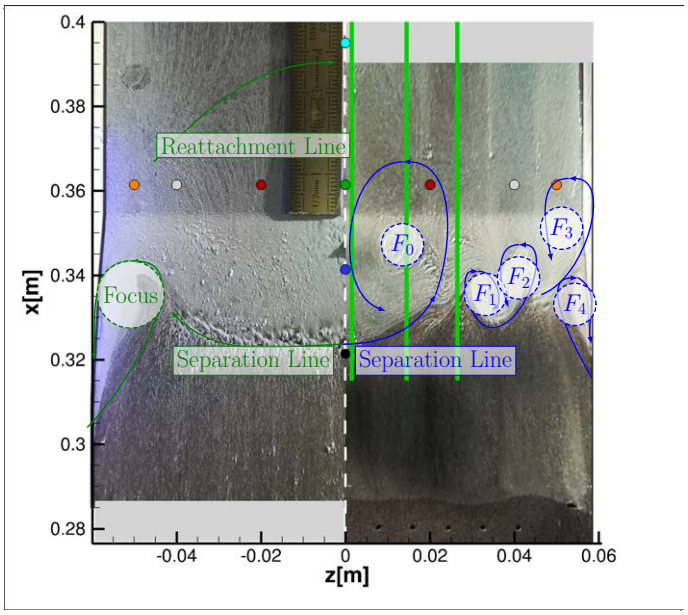

Figure A.14: Lignes de frottement sur le plancher de la soufflerie veine, comparaison entre le cas non contrôlé et le cas du Contrôle 1 respectivement gauche et droite. Les trois lignes vertes représentent les plans médians des trois volumes de PIV tomographique.

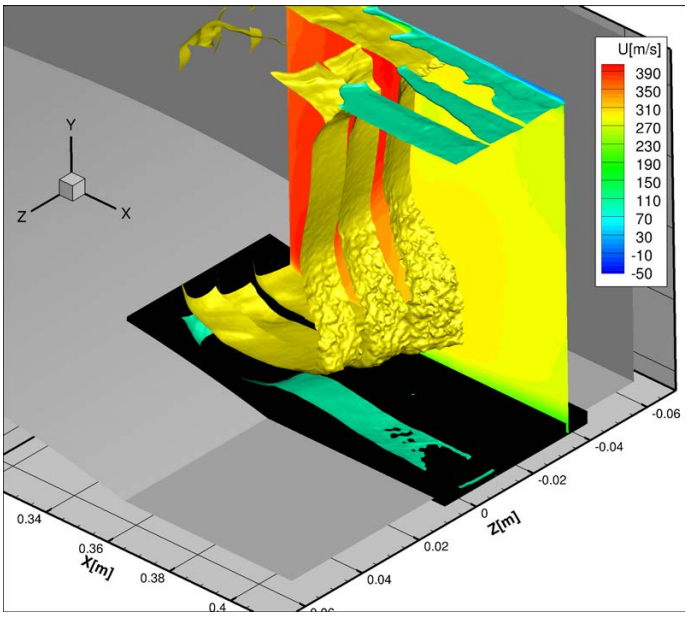

Figure A.15: Visualisation 3D de l'interaction pour le cas du Contrôle 1, deux iso-surfaces à $u = 300\,\mathrm{m\,s^{-1}}$ (en jaune) et $u = 100\,\mathrm{m\,s^{-1}}$ (en vert). Le plan $z = -40\,\mathrm{mm}$ est représenté. La zone en noir représente la région dans laquelle la PIV tomographique est aveuglée par la réflexion du laser sur la paroi

d'ouverture des jets sur un cycle plus qu'à la fréquence utilisée de l'actionneur.

Le contrôle a aussi été utilisé sans les jets de coin et les mesures de pression ont permis de valider que le contrôle du décollement de coin influence le décollement central.

ii Contrôle 2

La configuration de Contrôle 2 est caractérisée dans la section VII.2. Cette configuration, proche d'un cas classique de contrôle fluidique, génère elle aussi une structure tridimensionnelle de l'interaction, comme cela est visible sur la Figure A.16. La zone de décollement central est réduite, mais le décollement de coin est amplifié (et pas diminué) dans ce cas.

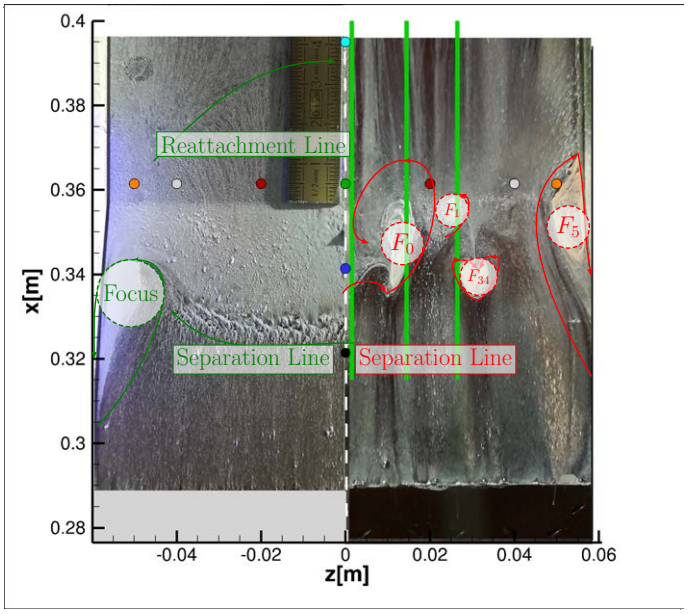

Figure A.16: Lignes de frottement sur le plancher de la veine, comparaison entre le cas non contrôlé et le cas du Contrôle 2 respectivement gauche et droite. Les trois lignes vertes représentent les plans médians des trois volumes de PIV tomographique.

Le calcul numérique diffère plus des résultats expérimentaux dans ce cas de contrôle que dans les cas précédents. Les zones de décollement sont moins bien prédites. Néanmoins, ces zones de faible extension spatiale (petites hauteurs et envergures) sont plus complexes à mesurer.

La mesure de PIV tomographique présentée sur la Figure A.17 confirme bien une forte diminution de la zone de décollement et une remontée du choc dans le canal, caractéristique des cas contrôlés. Ceci est lié au fait que la diminution du décollement implique d'avoir un choc quasi-normal de plus forte intensité.

De même que dans le cas de Contrôle 1, des variantes du Contrôle 2 ont été caractérisées à l'aide des mesures de pression. Elles confirment les conclusions de l'étude du cas de Contrôle 1, à savoir un impact du contrôle du décollement de coin sur le décollement central, quelle que soit la fréquence de fonctionnement de l'actionneur.

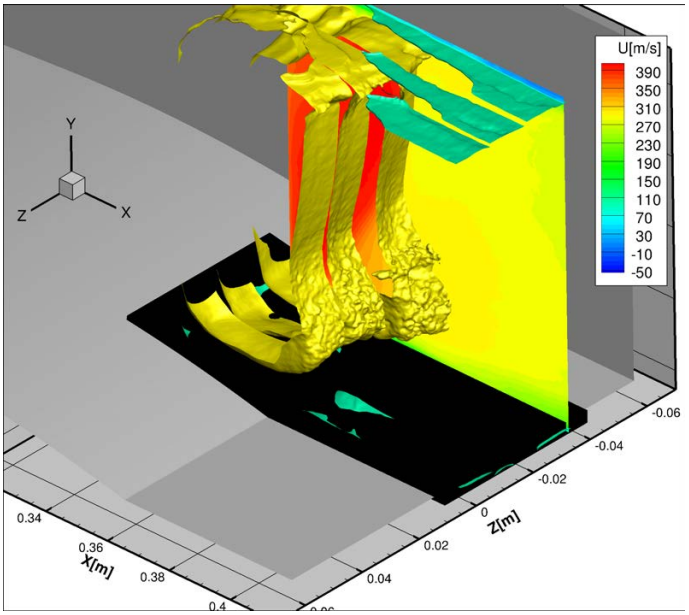

Figure A.17: Visualisation 3D de l'interaction pour le cas du Contrôle 2, deux iso-surfaces à $u = 300\,\mathrm{m\,s^{-1}}$ (en jaune) et $u = 100\,\mathrm{m\,s^{-1}}$ (en vert). Le plan $z = -40\,\mathrm{mm}$ est représenté. La zone en noir représente la région dans laquelle la PIV tomographique est aveuglée par la réflexion du laser sur la paroi

1.i Conclusions et perspectives

Cette étude a décrit l'ensemble du processus de conception, d'optimisation et de test expérimental d'un dispositif de contrôle fluidique d'une interaction onde de choc / couche limite avec décollement dans un écoulement de canal. Après une optimisation en deux étapes du contrôle fluidique, celui-ci a été adapté et testé en soufflerie. En outre, une configuration de contrôle dite classique (c'est-à-dire pour des jets orientés dans la direction principale de l'écoulement) a été ajoutée.

Cette étude a permis de comparer finement les résultats obtenus à la fois par des méthodes de calcul RANS à ceux de différents moyens de mesure sur une interaction transsonique tridimensionnelle. Elle montre que les calculs RANS sont d'un niveau de précision suffisant pour un usage dans le cadre d'une optimisation numérique.

Une modélisation ZDES mode 2 du cas de référence a été calculée. Cette modélisation souffre d'un défaut au niveau du développement de l'instabilité de Kelvin-Helmhotz vraisemblablement dû à un défaut de maillage. Cependant, cette modélisation permet de retrouver les niveaux de fréquences caractéristiques et des structures d'écoulement proches de celles mesurées en soufflerie.

Au cours de ces travaux, un montage de PIV tomographique a été conçu et utilisé. Il a permis d'effectuer des mesures volumiques des trois composantes du champ de vitesse pour chacune des configurations testées, malgré des limitations techniques inhérentes à cette méthode.

Les travaux expérimentaux ont confirmé la capacité des VGs fluidiques à contrôler l'interaction de manière aussi efficace que les VGs mécaniques. Ils ont par ailleurs mis en avant le fait que le contrôle du décollement de coin est primordial dans le cas d'une interaction dans un canal rectangulaire.

En perspectives de ces travaux, une nouvelle modélisation ZDES pourra être envisagée avec un maillage plus fin dans la couche de cisaillement de l'écoulement.

Pour ce qui est de la PIV tomographique, de nouvelles formes de fenêtres d'interrogations pourront améliorer grandement la résolution du champ de vitesse proche de la paroi.

A.2 DC50 model of the first optimization enriched with the vorticity patterns generated by the jets configurations.

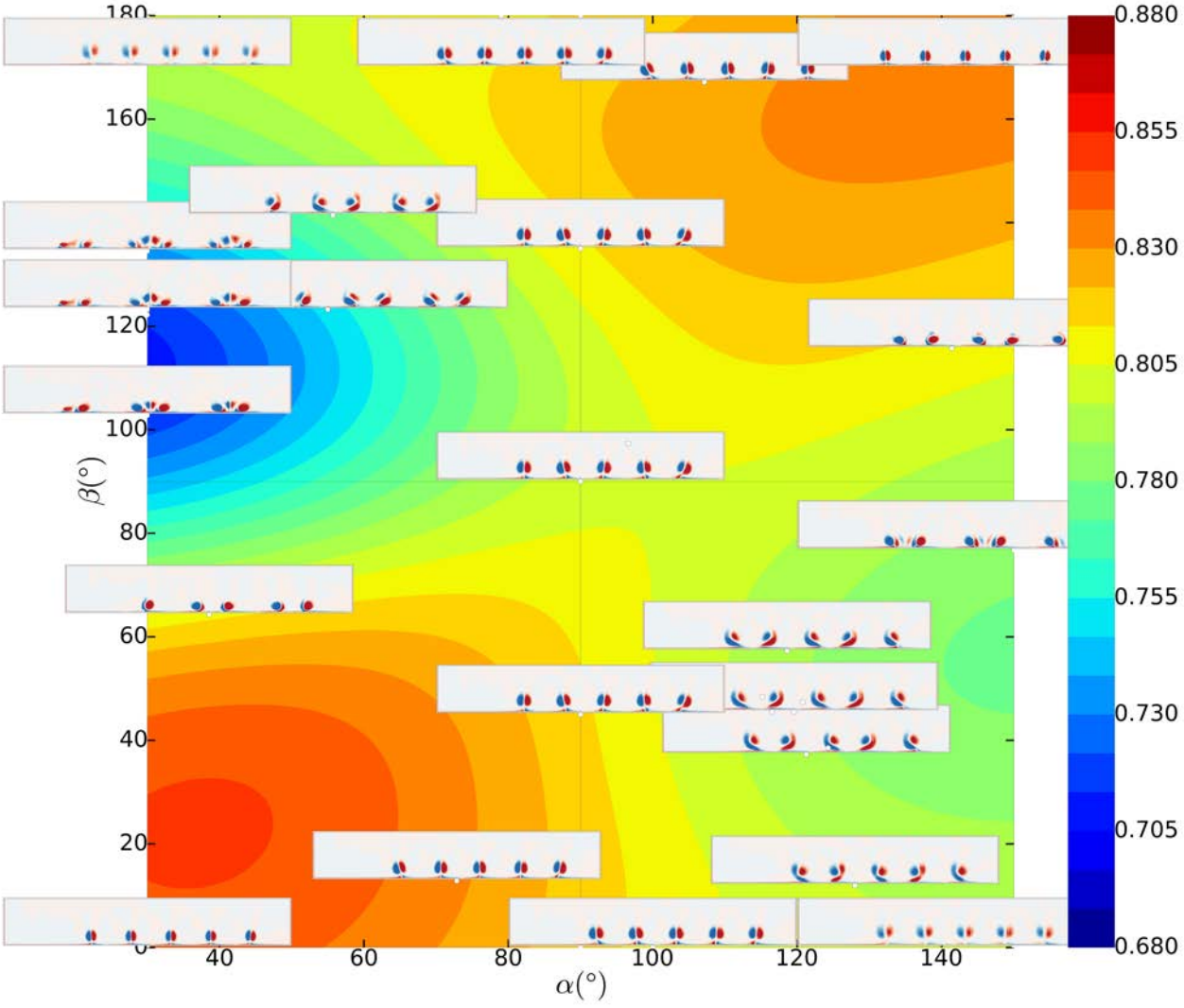

Figure A.18: DC50 model of the first optimization enriched with the vorticity patterns generated by the jets configurations.

A.3 DC50 model of the second optimization with respect to the pitch and skew angles, and to the longitudinal and lateral position for the jet controlling the corner separation.

The complete model obtained in the second step of optimization is presented on Fig. A.19, and a zoom on the most interesting zone is shown in Fig. A.20.

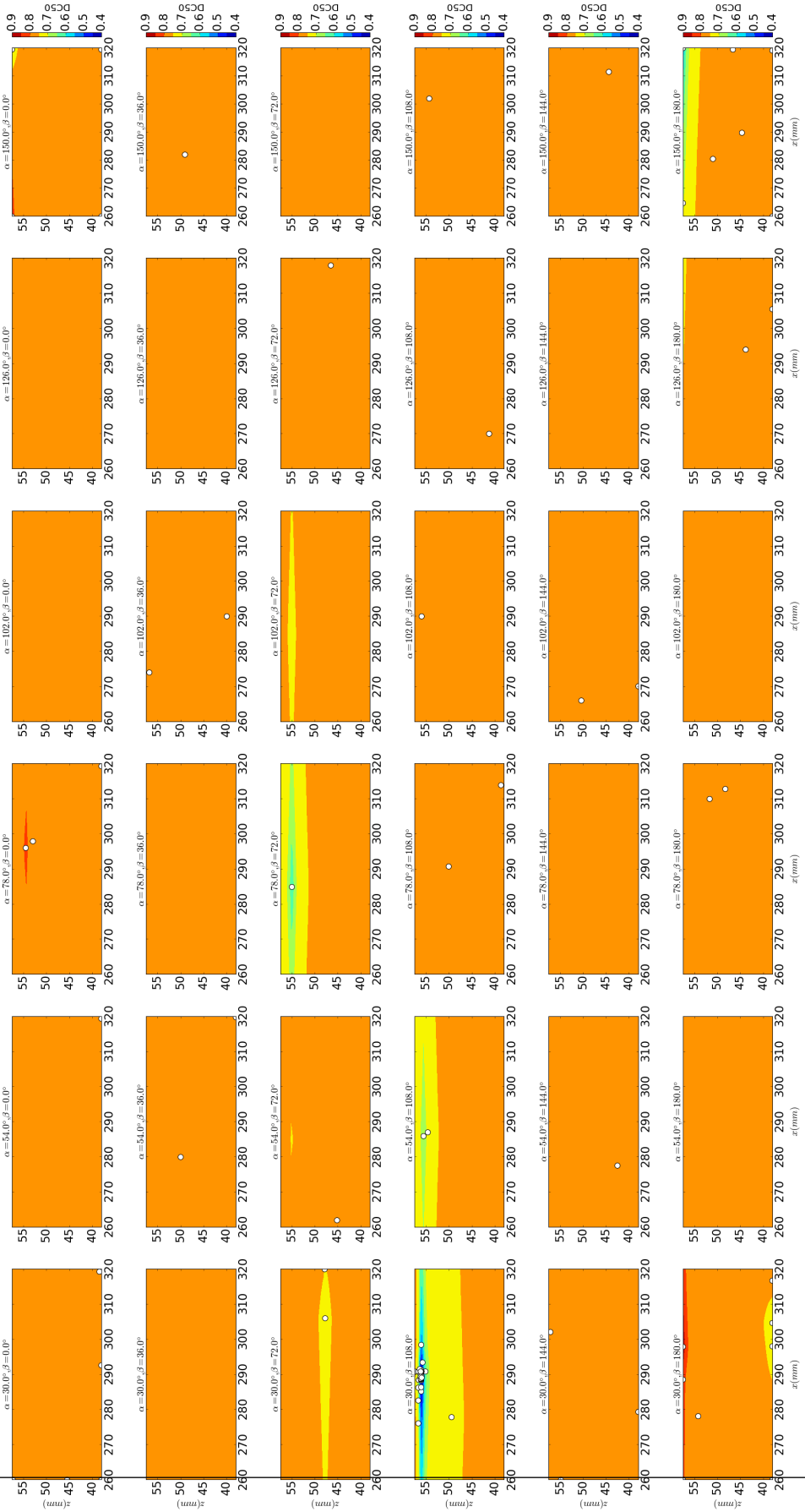

Figure A.19: Model of DC50 with respect to all pitch and skew angles, and to the longitudinal and lateral position for the jet controlling the corner separation.

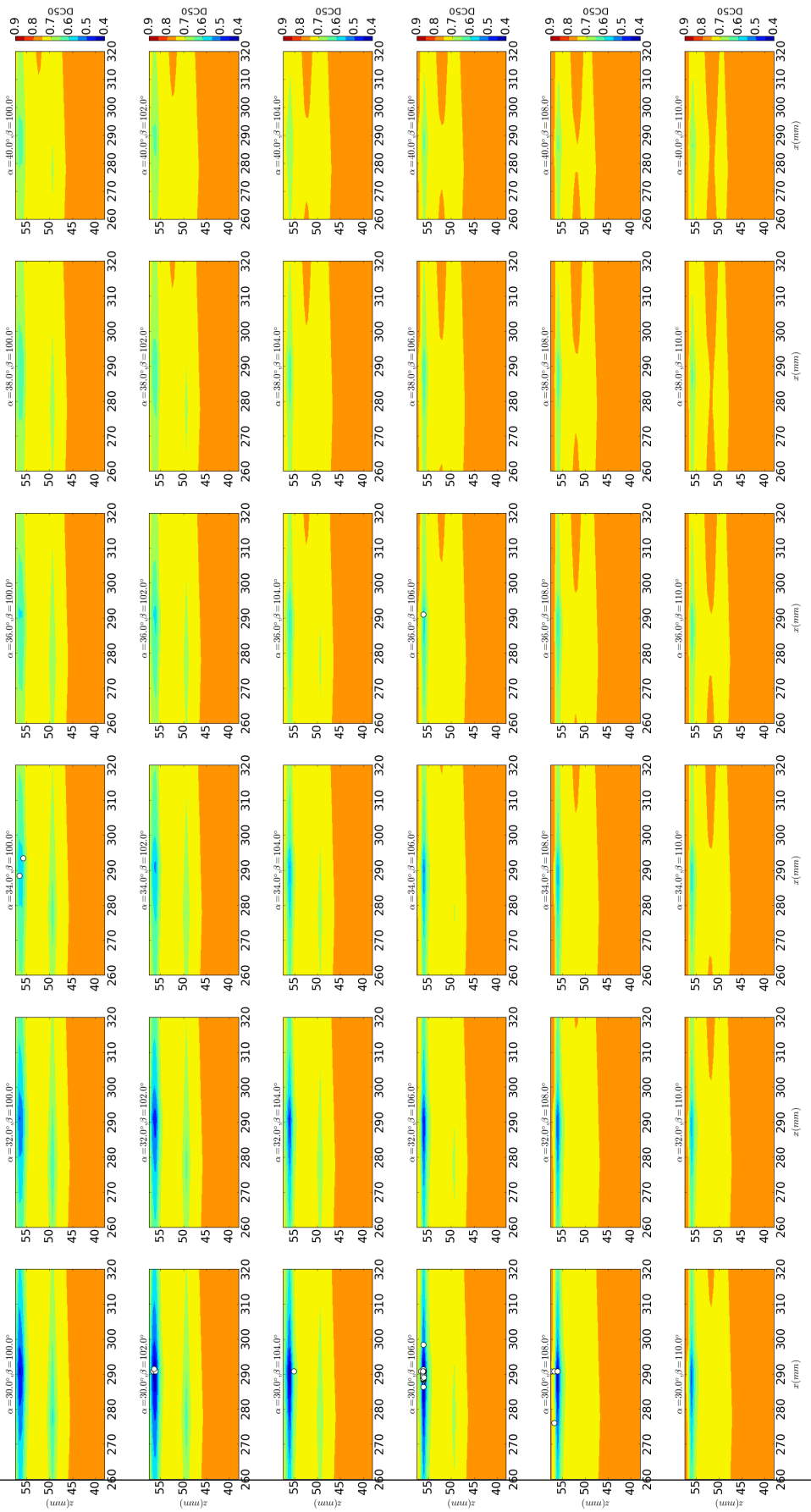

Figure A.20: Model of DC50 with respect to pitch and skew angles from $(\alpha, \beta) = (30°, 100°)$ to,$(\alpha, \beta) = (40°, 110°)$ and to the longitudinal and lateral position for the jet controlling the corner separation.

A.4 Control set-ups blueprint

Vue Implantation
Echelle 1:2

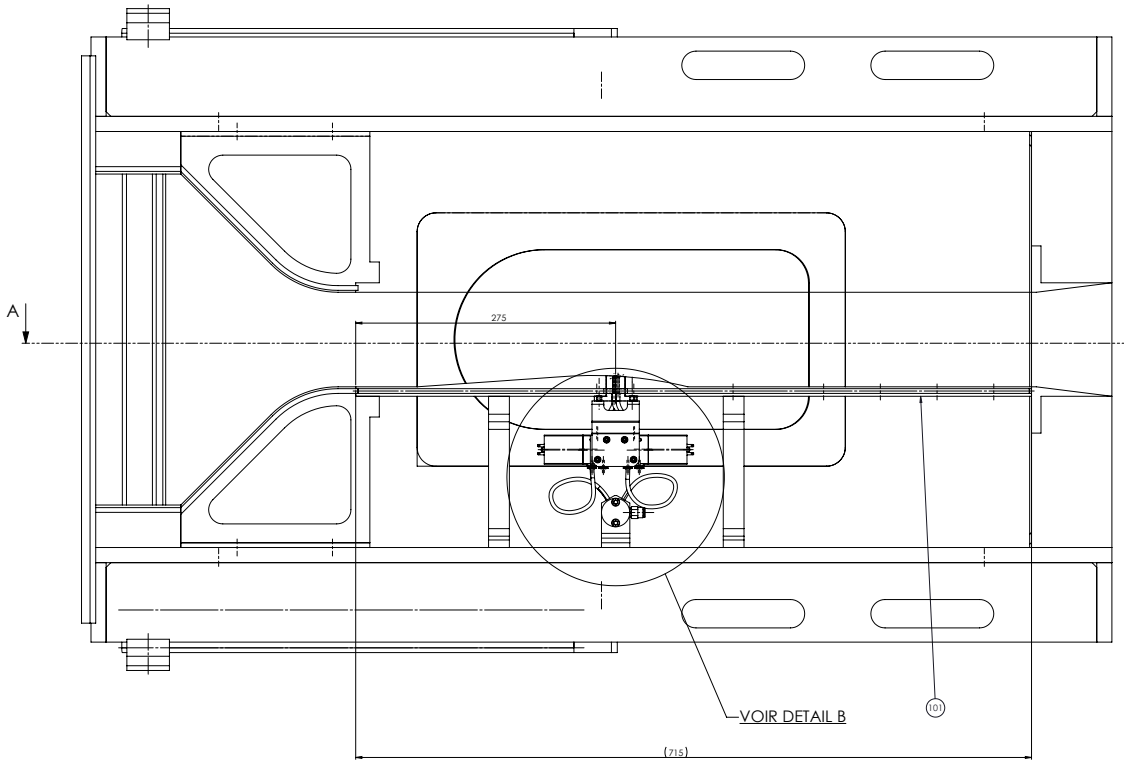

DETAIL D
ECHELLE 2 : 1

CONFIGURATION 1

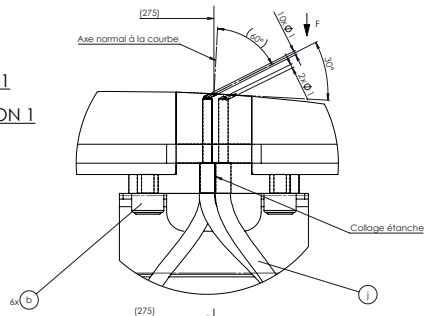

DETAIL D
ECHELLE 2 : 1

CONFIGURATION 2

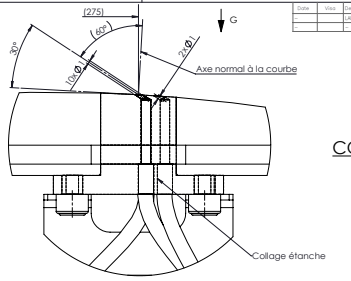

VUE F
ECHELLE 2 : 1

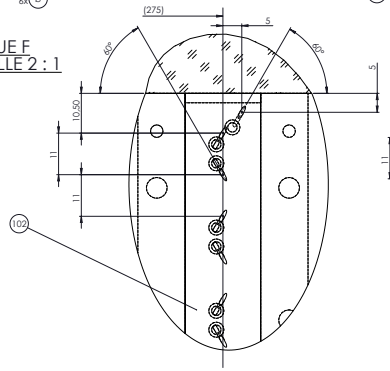

VUE G
ECHELLE 2 : 1

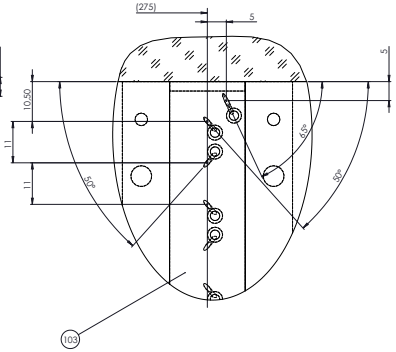

COUPE A-A
ECHELLE 1 : 2

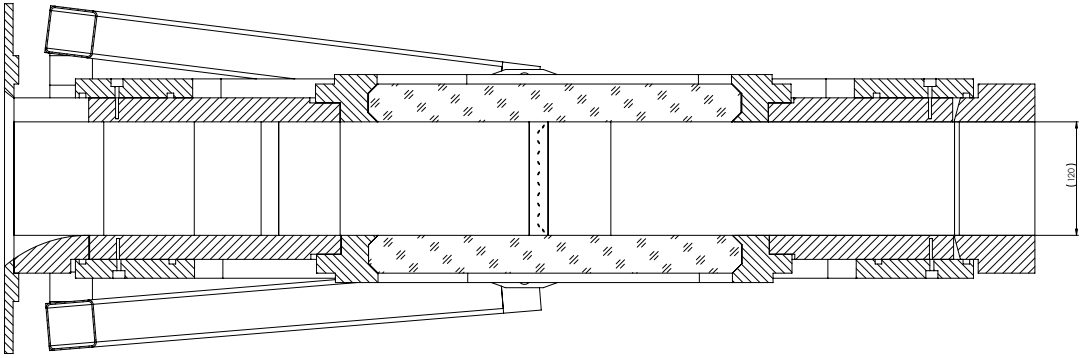

DETAIL B
ECHELLE 1 : 1

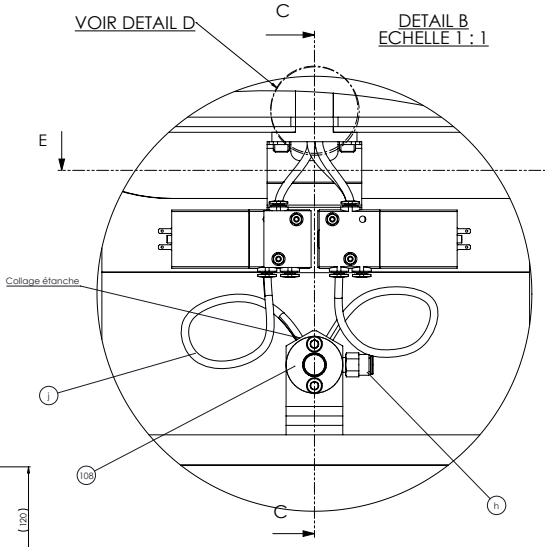

COUPE C-C

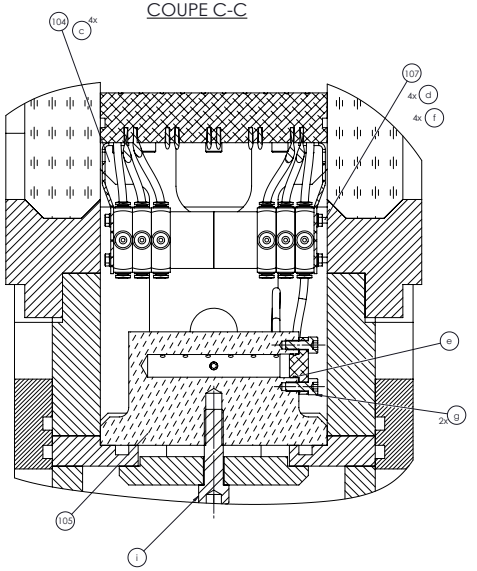

COUPE E-E

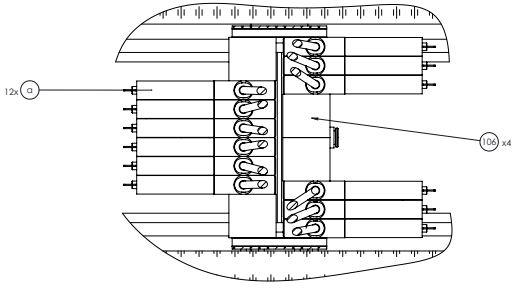

TOLERANCES GENERALES	ONERA MFE Office National d'études et de recherches Aérospatiales
LONGUEURS: JS11 - js11	Département d'Aérodynamique Fondamentale et Expérimentale
ALESAGES: H11	1660-PR-OPOSSUM-MEROVEE 3D
ARBRES: h11	ENSEMBLE TUYERE INJECTEUR SBB
CASSER LES ANGLES VIFS	
ETAT DE SURFACE Ra : 3,2	
Dessiné par: CONCEPT 21	Approuvé par: LAMBERT
Date: 04 / 06 / 18	ECHI: 1:1
	Planche: 1/1
	1660-100

N° –

Date	Visa	Demandeur	N° fiche A	Modifications	Indice
–		LAMBERT		Plan d'origine	A
–		–		–	–

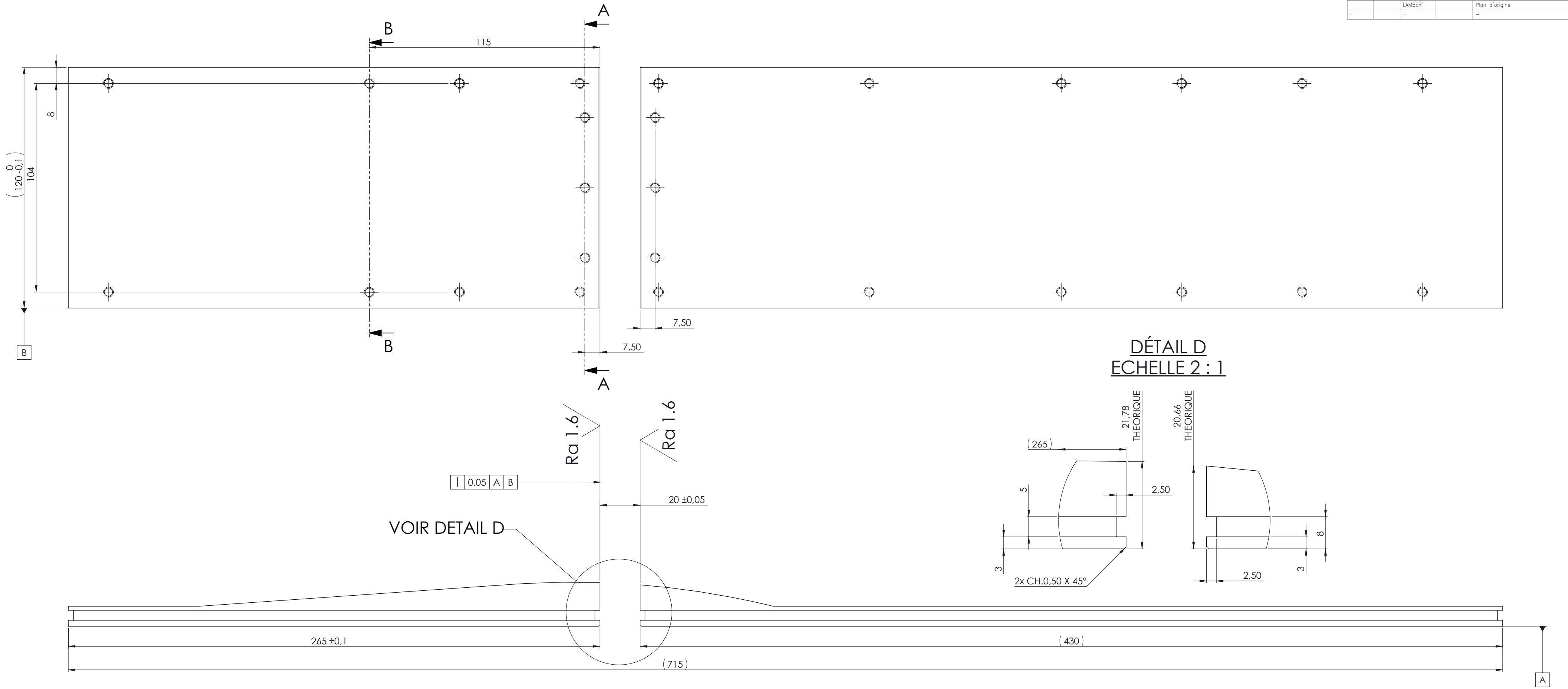

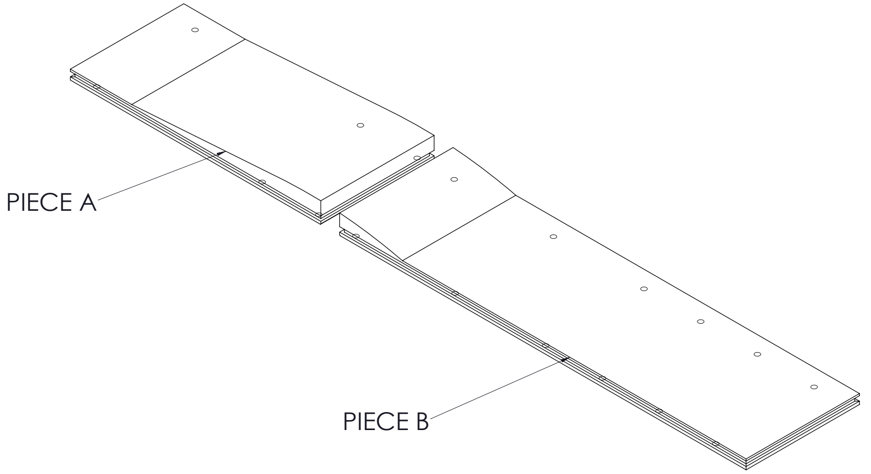

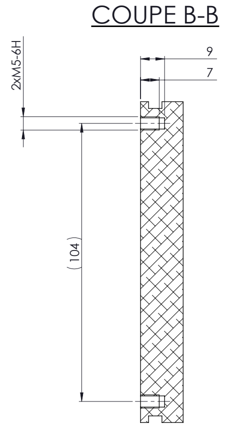

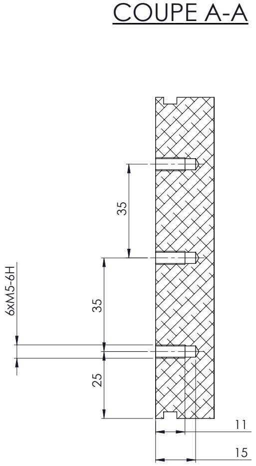

Note: Reprise paroi n°1 suivant plan n°1514.001C

1 – – – – –
AU2GN ANODISATION NOIR MAT

Format | No de plan ou repere | Ind. de mod. | G D Nombre | DESIGNATION | dimensions de l'element brut ou No du modele | Nature et etat de la matiere | Etat de surface ou protection ou observations | Calcule | pese | poids unitaire fini

Pour 1 ensemble No 1660–100 il faut 1 pieces No 1660–101 } Poids total 2.75 Kg –

Ce plan, propriete de l'ONERA, ne peut etre detenu, reproduit ou communique sans son autorisation

TOLERANCES GENERALES
LONGUEURS: JS11–js11
ALESAGES: H11
ARBRES: h11

CASSER LES ANGLES VIFS
ETAT DE SURFACE Ra : 3,2

ONERA
MFE
Office National d'etudes et de recherches Aerospatiales

Bureau d'études DAFE
Installations de Recherches
Département d'Aérodynamique
Fondamentale et Expérimentale

1660–60–PR–OPOSSUM–MEROVEE 3D
PLANCHER TUYERE (REPRISE)

	Dessine par			Approuve par		
Nom	Mr: Concept 21			LAMBERT		
Visa						
Date	20	03	18			

ECH: 1:1
Planche: 1/1

1660–101 –

N° –

Date	Visa	Demandeur	N° fiche A	Modifications	Indice
–		LAMBERT		Plan d'origine	A
–		–		–	–

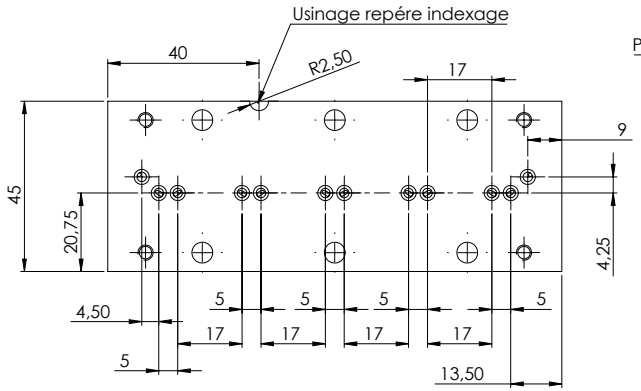

DETAIL B
ECHELLE 2 : 1

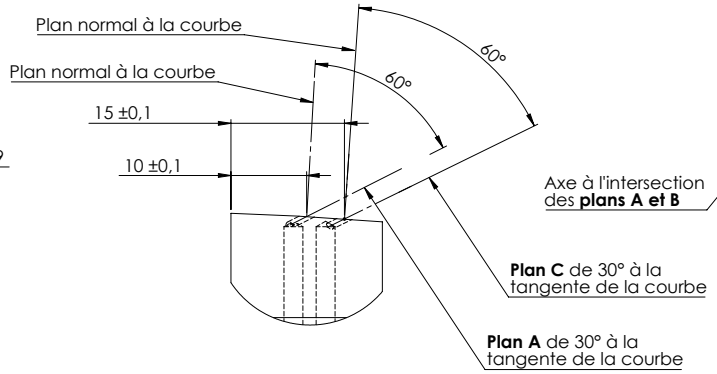

COUPE C-C
ECHELLE 2 : 1

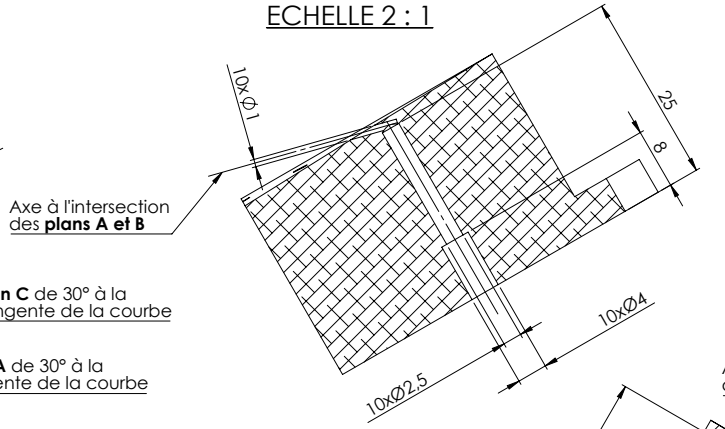

COUPE D-D
ECHELLE 2 : 1

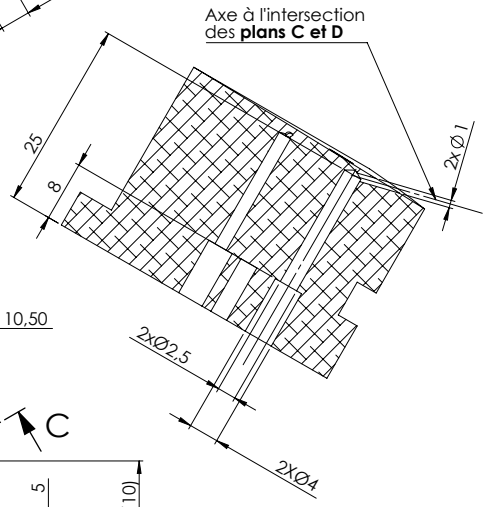

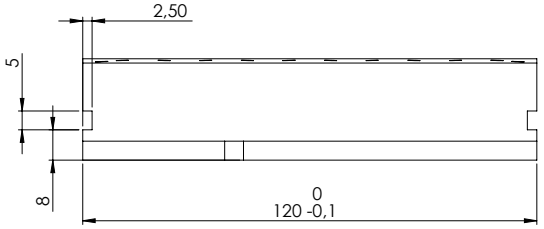

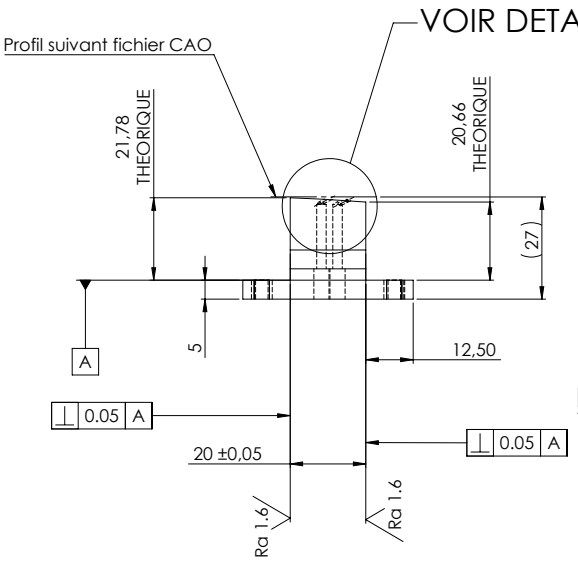

DETAIL A
ECHELLE 2 : 1

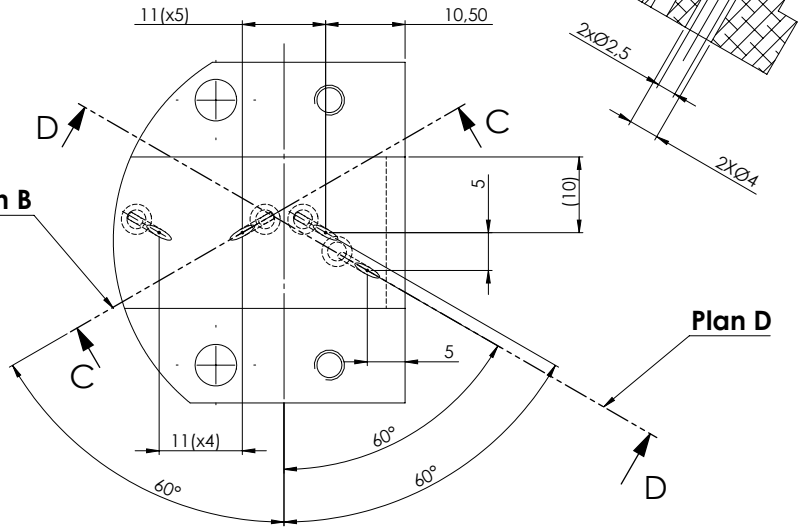

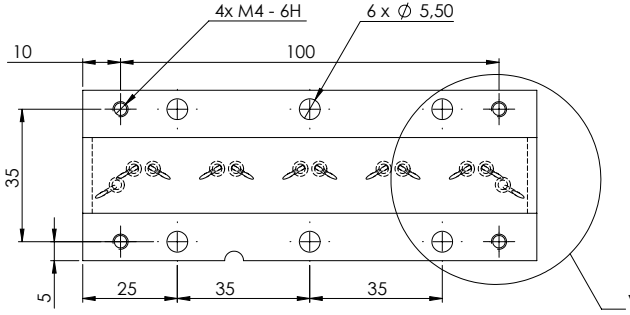

2	–							2017A ANODISATION NOIR MAT			
Item	No de plan ou repere Ind. de mod.		G	D Nombre	DESIGNATION	dimensions de l'element brut ou No du modele	Nature et etat de la matiere	Etat de surface ou protection ou observations	Calcule	pese poids unitaire fini	
Pour 1 ensemble No 1660–100 il faut 1 pieces No 1660–102									Poids total	0.2Kg	–

TOLERANCES GENERALES
LONGUEURS: JS11–js11
ALESAGES: H11
ARBRES: h11
CASSER LES ANGLES VIFS
ETAT DE SURFACE Ra : 3,2

ONERA
MFE
Office National d'etudes et de recherches Aerospatiales

Bureau d'études DAFE
Installations de Recherches
Département d'Aérodynamique Fondamentale et Expérimentale

1660–PR–OPOSSUM–MEROVEE 3D
CASSETTE CONFIGURATION 1

	Dessine par	Approuve par
Nom	Mr: CONCEPT 21	LAMBERT
Visa		
Date	04 04 18	

ECH: 1:1
Planche: 1/1

1660–102

A.5 Schlieren visualization of reference case

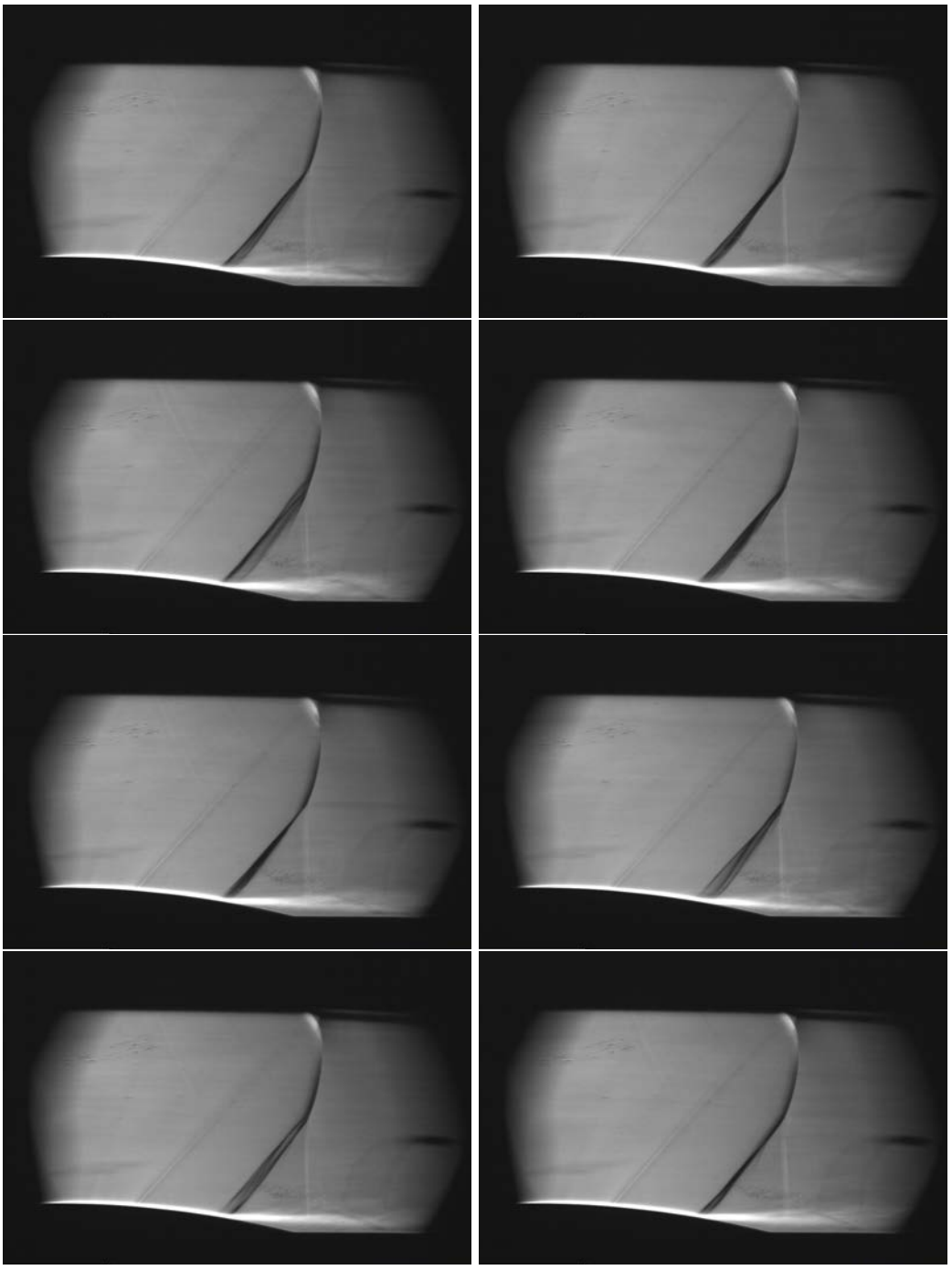

Figure A.21: Schlieren visualizations of the 3D variations of structure of the shock wave along time.

As it can be seen on Fig. A.21, due to unsteadiness, the position and shape of the shock wave pattern can vary along time with a change in position of the triple point. Also it is visible that the thickness of the shock wave (actually the thickness of the integral of

the density gradient along the span of the wind tunnel) changes. This indicates that the shock wave undergoes lateral variation. This phenomenon is not well understood, it may be linked to incoming turbulent structures in the boundary layer. These structures modify locally the shock wave position (see Humble et al. [92], Yang et al. [180]). Nevertheless, the boundary layer is thinner in the current topology compared to these studies. These variations may also be linked to the longitudinal variation along the mixing layer or the corner flow separations.

A.6 Study of the shock wave position

In order to emphasize the importance of the precise shock wave positioning in the unsteady pressure measurements, the longitudinal position of the shock wave have been varied for the uncontrolled case. The static pressure distribution of the three cases are presented on Fig. A.22 and the corresponding pre-multiplied spectra obtained by the Kulite sensors are exposed in Fig. A.23. It can be seen that the shock wave position influences the size of the separation zone, as it is visible on the static pressure distribution. However, the dynamic response of the sensors are not modify apart from the sensor positioned at the foot position of shock wave. The intensity seen by this sensor is strongly dependent of its distance with the shock wave. Nevertheless, the intensity distribution along the frequencies is kept unchanged with a peak close to 300Hz.

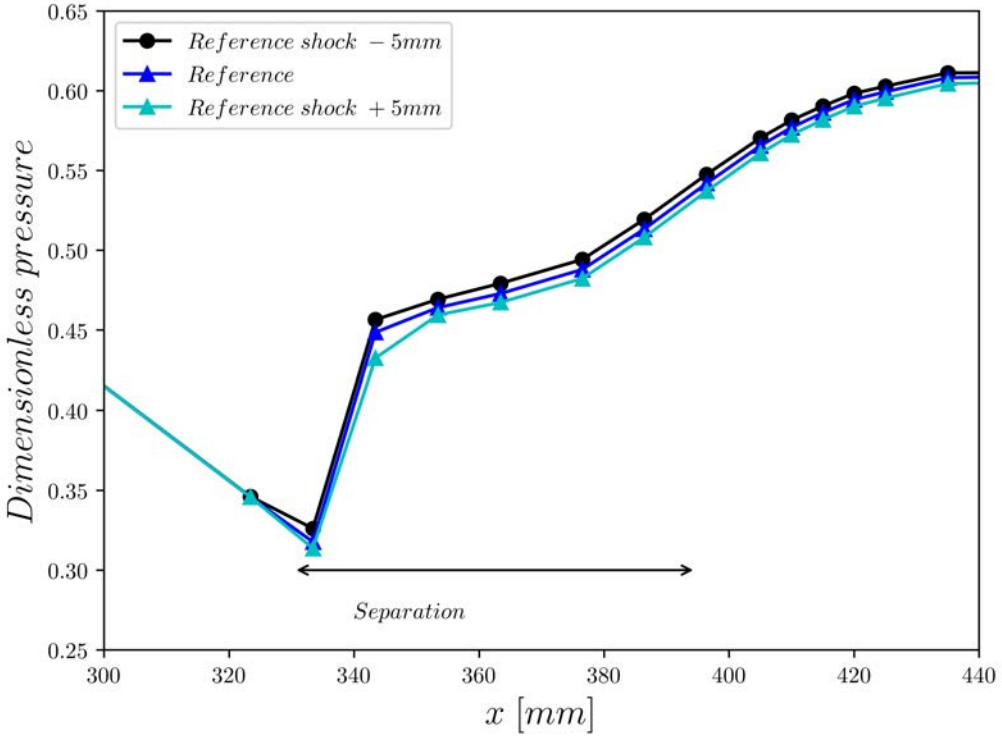

Figure A.22: Static pressure distribution in the median plane for the reference case with various position of the shock wave with respect to the one used in the thesis.

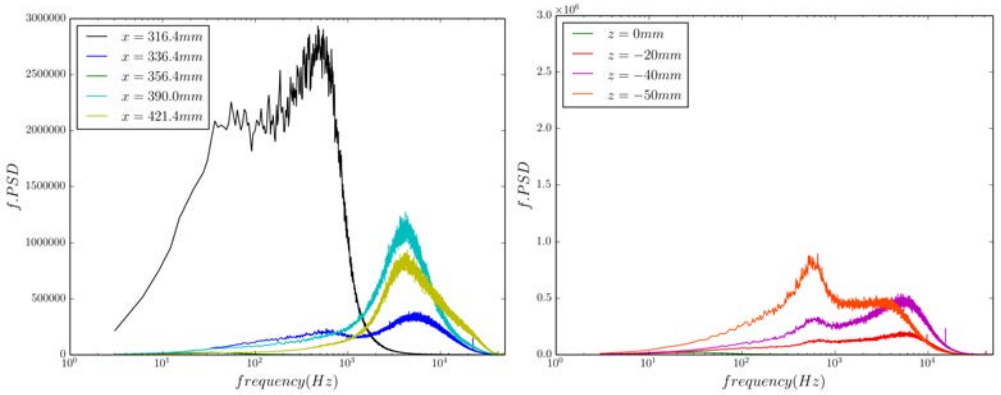

(a) Central sensors shock position -5mm

(b) Lateral sensors shock position -5mm

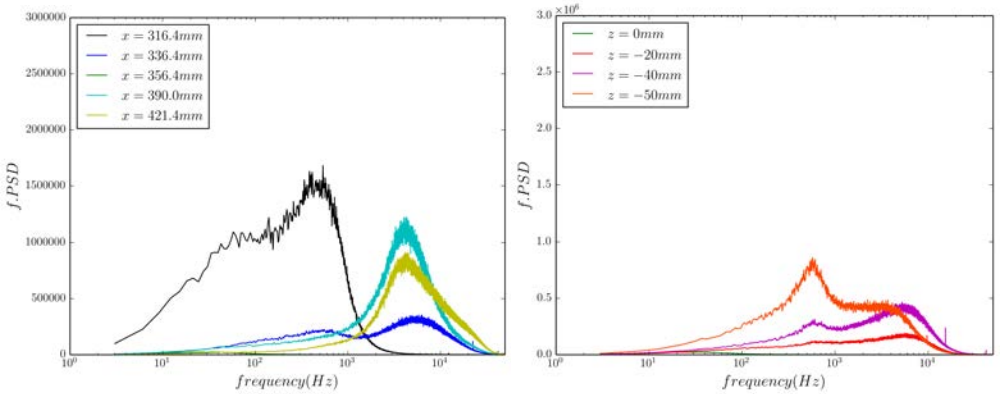

(c) Central sensors Control 1 Center only

(d) Lateral sensors Control 1 Center only

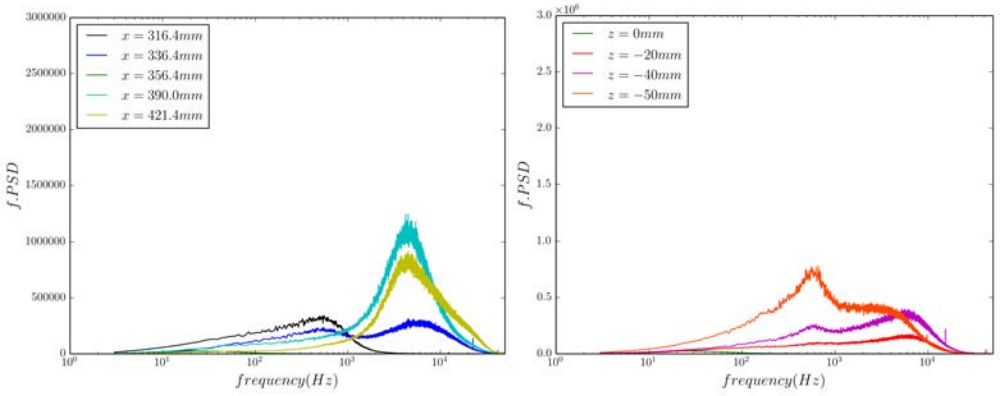

(e) Central sensors shock position +5mm

(f) Lateral sensors shock position +5mm

Figure A.23: Pre-multiplied spectra obtained by the Kulite sensors of variation of shock wave position in the reference case.

List of Figures

List of Tables

Bibliography

[1] L. Albugues. *Analyse expérimentale et numérique d'un jet débouchant dans un écoulement transverse*. PhD thesis, Ecole Nationale Supérieure de l'Aéronautique et de l'Espace, 2005.

[2] B. Anderson, H. Baust, and J. Agrell. Management of Total Pressure Recovery, Distortion and High Cycle Fatigue in Compact Air Vehicle Inlets. December 2002.

[3] B. Anderson, J. Tinapple, and L. Surber. Optimal control of shock wave turbulent boundary layer interactions using micro-array actuation. In *3rd AIAA Flow Control Conference*, 2006.

[4] P.R. Ashill, J.L. Fulker, and K.C. Hackett. A review of recent developments in flow control. *The Aeronautical Journal*, 109(1095):205–232, 2005.

[5] C. Atkinson and J. Soria. An efficient simultaneous reconstruction technique for tomographic particle image velocimetry. *Experiments in Fluids*, 47(4):553, Aug 2009.

[6] H. Babinsky and J.K. Harvey. *Shock Wave-Boundary-Layer Interactions*. Cambridge University Press, September 2011.

[7] H. Babinsky and H. Ogawa. Sbli control for wings and inlets. *Shock Waves*, 18(2): 89, Jun 2008.

[8] H. Babinsky, N. Makinson, and C. Morgan. Micro-Vortex Generator Flow Control for Supersonic Engine Inlets. In *45th AIAA Aerospace Sciences Meeting and Exhibit*. American Institute of Aeronautics and Astronautics, 2007.

[9] H. Babinsky, Y. Li, and C. Pitt Ford. Microramp control of supersonic oblique shock-wave/boundary-layer interactions. *AIAA journal*, 47(3):668–675, 2009.

[10] A. Bannier. *Contrôle de la traînée de frottement d'une couche limite turbulente au moyen de revêtements rainurés de type riblets*. PhD thesis, Université Pierre et Marie Curie - Paris VI, June 2016.

[11] E. Baydar, F.K. Lu, and J.W. Slater. Vortex generators in a two-dimensional external-compression supersonic inlet. *Journal of Propulsion and Power*, pages 1–18, 2018.

[12] C. Benoit, S. Péron, and S. Landier. Cassiopee: A CFD pre- and post-processing tool. *Aerospace Science and Technology*, 45:272–283, Sep 2015.

[13] S.J. Beresh, J.F. Henfling, R.J. Erven, and R.W. Spillers. Vortex structure produced by a laterally inclined supersonic jet in transonic crossflow. *Journal of propulsion and power*, 23(2):353–363, 2007.

[14] T.P. Bray. *A parametric study of vane and air-jet vortex generators.* PhD thesis, Cranfield University, 1998.

[15] T.P. Bray and K.P. Garry. Optimisation of air-jet vortex generators with respect to system design parameters. *The Aeronautical Journal (1968)*, 103(1028):475–480, 1999.

[16] P.J.K. Bruce, D.M.F. Burton, N.A. Titchener, and H. Babinsky. Corner effect and separation in transonic channel flows. *Journal of Fluid Mechanics*, 679:247–262, 2011.

[17] Vincent Brunet and Sébastien Deck. Zonal-detached eddy simulation of transonic buffet on a civil aircraft type configuration. pages 182–191, 2008.

[18] R. Bur, B. Corbel, J. Dé, and lery. Study of passive control in a transonic shock wave/boundary-layer interaction. *AIAA journal*, 36(3):394–400, 1998.

[19] R. Bur, R. Benay, A. Galli, and P. Berthouze. Experimental and numerical study of forced shock-wave oscillations in a transonic channel. *Aerospace science and technology*, 10(4):265–278, 2006.

[20] R. Bur, D. Coponet, and Y. Carpels. Separation control by vortex generator devices in a transonic channel flow. *Shock Waves*, 19(6):521–530, 2009.

[21] D.M.F. Burton and H. Babinsky. Corner separation effects for normal shock wave/turbulent boundary layer interactions in rectangular channels. *Journal of Fluid Mechanics*, 707:287–306, 2012.

[22] L. Cambier, S. Heib, and S. Plot. The Onera elsA CFD software: input from. *Mechanics & Industry*, 14(3):159–174, 2013.

[23] A. Cartieri, D. Hue, Q. Chanzy, and O. Atinault. Experimental investigations on common research model at onera-s1ma–drag prediction workshop numerical results. *Journal of Aircraft*, 55(4):1491–1508, 2017.

[24] T. Chabert. *Contrôle expérimental en boucle fermée du décollement sur un volet.* PhD thesis, Université Pierre et Marie Curie - Paris VI, January 2014.

[25] F. Champagnat, A. Plyer, G. Le Besnerais, B. Leclaire, S. Davoust, and Y. Le Sant. Fast and accurate piv computation using highly parallel iterative correlation maximization. *Experiments in fluids*, 50(4):1169, 2011.

[26] F. Champagnat, P. Cornic, A. Cheminet, B. Leclaire, G. Le Besnerais, and A. Plyer. Tomographic piv: particles versus blobs. *Measurement Science and Technology*, 25 (8):084002, 2014.

[27] Q. Chanzy and A.J. Keane. Analysis and experimental validation of morphing UAV wings. *The Aeronautical Journal*, 122(1249):390–408, March 2018.

[28] N. Chauvet, S. Deck, and L. Jacquin. Zonal detached eddy simulation of a controlled propulsive jet. *AIAA journal*, 45(10):2458–2473, 2007.

[29] A. Cheminet. *Development of tomographic PIV for the study of turbulent flows*. PhD thesis, Paris Saclay, 2016.

[30] A. Cheminet, B. Leclaire, F. Champagnat, A. Plyer, R. Yegavian, and G. Le Besnerais. Accuracy assessment of a lucas-kanade based correlation method for 3d piv. In *17th International Symposium on Applicationsof Laser Techniques to Fluid Mechanics*, 2014.

[31] R. Chriss, JR. T. Keith, W. Hingst, A. Strazisar, and A. Porro. An lda investigation of three-dimensional normal shock-boundary layer interactions in a corner. 1987.

[32] N.T. Clemens and V. Narayanaswamy. Low-frequency unsteadiness of shock wave/turbulent boundary layer interactions. *Annual Review of Fluid Mechanics*, 46(1):469–492, 2014.

[33] G.S. Cohen and F. Motallebi. Sub boundary-layer vortex generators for the control of shock induced separation. *The Aeronautical Journal (1968)*, 110(1106):215–226, 2006.

[34] D.A. Compton and J.P. Johnston. Streamwise vortex production by pitched and skewed jets in a turbulent boundary layer. *AIAA Journal*, May 1992.

[35] P. Cornic, C. Illoul, Y. Sant, A. Cheminet, G. Besnerais, and F. Champagnat. Calibration drift within a tomo-piv setup and self-calibration. In *11th international symposium on particle image velocimetry*, 2015.

[36] P. Cornic, C. Illoul, A. Cheminet, G. Le Besnerais, F. Champagnat, Y. Le Sant, and B. Leclaire. Another look at volume self-calibration: calibration and self-calibration within a pinhole model of scheimpflug cameras. *Measurement Science and Technology*, 27(9):094004, 2016.

[37] A. Coschignano and H. Babinsky. Influence of near-leading edge curvature on the performance of aero-engine intake lips at high-incidence. In *American Institute of Aeronautics and Astronautics*. American Institute of Aeronautics and Astronautics, June 2016.

[38] A. Coschignano and H. Babinsky. Onset of unsteadiness in aero-engine intakes at incidence. In *American Institute of Aeronautics and Astronautics*. American Institute of Aeronautics and Astronautics, January 2017.

[39] A. Coschignano, H. Babinsky, C. Sheaf, and G. Zamboni. Normal-shock/boundary-layer interactions in transonic intakes at high incidence. *AIAA Journal*, pages 1–14, 2019.

[40] W. Crowther, M. Jabbal, and S. Liddle. Flow control fallacies: a review of commonpitfalls in flow control research. *Proceedings of the Institution of Mechanical Engineers, Part G: Journal of Aerospace Engineering*, 225(1):1–11, 2011.

[41] C. Dai, L. Jia, J. Zhang, Z. Shu, and J. Mi. On the flow structure of an inclined jet in crossflow at low velocity ratios. *International Journal of Heat and Fluid Flow*, 58: 11–18, 2016.

[42] C.L. Dailey. Supersonic diffuser instability. *Journal of the Aeronautical Sciences*, 1955.

[43] J. Dandois. Improvement of Corner Flow Prediction Using the Quadratic Constitutive Relation. *AIAA Journal*, 52(12):2795–2806, Dec 2014.

[44] J. Dandois, V. Brunet, P. Molton, J.-C. Abart, and A. Lepage. Buffet control by means of mechanical and fluidic vortex generators. In *5th Flow Control Conference*, 2010.

[45] S. Deck. *Simulation numérique des charges latérales instationnaires sur des configurations de lanceur*. PhD thesis, Orléans, 2002.

[46] S. Deck. Recent improvements in the zonal detached eddy simulation (zdes) formulation. *Theoretical and Computational Fluid Dynamics*, 26(6):523–550, 2012.

[47] S. Deck, F. Gand, V. Brunet, and S. Ben Khelil. High-fidelity simulations of unsteady civil aircraft aerodynamics: stakes and perspectives. application of zonal detached eddy simulation. *Philosophical Transactions of the Royal Society A: Mathematical, Physical and Engineering Sciences*, 372(2022):20130325, 2014.

[48] J. Délery. Analysis of separation due to shock-turbulent boundary layer interaction in transonic flow. *La Recherche Aerospatiale*, pages 305–320, 1978.

[49] J. Délery. Experimental investigation of turbulence properties in transonic shock/boundary-layer interactions. *AIAA journal*, 21(2):180–185, 1983.

[50] J. Délery. Shock wave/turbulent boundary layer interaction and its control. *Progress in Aerospace Sciences*, 22(4):209–280, January 1985.

[51] J. Délery. Robert Legendre and Henri Werlé: toward the elucidation of three-dimensional separation. *Annual review of fluid mechanics*, 33(1):129–154, 2001.

[52] J. Délery and R. Bur. The physics of shock wave/boundary layer interaction control: last lessons learned. *Office National d'Etudes et de Recherches Aérospatiales ONERA-PUBLICATIONS-TP*, 181, 2000.

[53] J. Délery and Marvin. Shock wave boundary layer interactions. *AGARDograph*, 1986.

[54] J. Delva. Synthèse de la caractérisation d'une vanne Festo MHE2-MSH1-3/2G-QS-4-K. 2018.

[55] P. Doerffer, C. Hirsch, J.-P. Dussauge, H. Babinsky, and G.N. Barakos. *Unsteady Effects of Shock Wave Induced Separation*. Springer Science & Business Media, November 2010.

[56] D.S. Dolling. Fifty years of shock-wave/boundary-layer interaction research: what next? *AIAA journal*, 39(8):1517–1531, 2001.

[57] J. Dréo, A. Pétrowski, P. Siarry, and E. Taillard. *Metaheuristics for hard optimization: methods and case studies*. Springer Science & Business Media, 2006.

[58] P. Dupont, C. Haddad, J.P. Ardissone, and J.F. Debiève. Space and time organisation of a shock wave/turbulent boundary layer interaction. *Aerospace Science and Technology*, 9(7):561–572, October 2005.

[59] J.-P. Dussauge, P. Dupont, and J.-F. Debiève. Unsteadiness in shock wave boundary layer interactions with separation. *Aerospace Science and Technology*, 10(2):85 – 91, 2006.

[60] G. Elsinga. *Tomographic particle image velocimetry and its application to turbulent boundary layers*. PhD thesis, TU Delft, 2008.

[61] G. Elsinga, F. Scarano, B. Wieneke, and B. van Oudheusden. Tomographic particle image velocimetry. *Experiments in fluids*, 41(6):933–947, 2006.

[62] A.J. Evans, C.P. Caulfield, and A.W. Woods. Linear estimation of flux sensitivity to uncertainty in porous media. *Journal of Fluid Mechanics*, 768:600–622, Apr 2015.

[63] Y.-Y. Feng, Y.-P. Song, and R.E. Breidenthal. Model of the trajectory of an inclined jet in incompressible crossflow. *AIAA Journal*, pages 1–7, 2017.

[64] A. Ferri and L.M. Nucci. The origin of aerodynamic instability of supersonic inlets at subcritical conditions. 1951.

[65] P. Flaszynski and R. Szwaba. Optimization of streamwise vortex generator for subsonic flow. In *8th International Symposium on Experimental and Computational Aerothermodynamics of Internal Flows, Lyon, France*, 2007.

[66] A. Forrester, A. Sobester, and A. Keane. *Engineering design via surrogate modelling: a practical guide*. John Wiley & Sons, 2008.

[67] A.I. Forrester, A. Sóbester, and A.J. Keane. Multi-fidelity optimization via surrogate modelling. *Proceedings of the royal society a: mathematical, physical and engineering sciences*, 463(2088):3251–3269, 2007.

[68] A.I.J. Forrester and A.J. Keane. Recent advances in surrogate-based optimization. *Progress in Aerospace Sciences*, 45(1):50–79, 2009.

[69] D.V. Gaitonde. Progress in shock wave/boundary layer interactions. *Progress in Aerospace Sciences*, 72:80 – 99, 2015.

[70] A. Galli. *Contrôle de l'oscillation d'une onde de choc en écoulement transsonique de canal*. PhD thesis, Université de Provence Aix-Marseille, January 2005.

[71] A. Galli, B. Corbel, and R. Bur. Control of forced shock-wave oscillations and separated boundary layer interaction. *Aerospace Science and Technology*, 9(8):653–660, Nov 2005.

[72] F. Gand. *Dynamics of turbulent junction flows*. PhD thesis, Université Pierre et Marie Curie - Paris VI, September 2011.

[73] B. Gardarin, L. Jacquin, and P. Geffroy. Flow Separation Control With Vortex Generators. In *4th Flow Control Conference*. American Institute of Aeronautics and Astronautics, 2008.

[74] E. Garnier. Stimulated detached eddy simulation of three-dimensional shock/boundary layer interaction. *Shock Waves*, 19(6):479, 2009.

[75] E. Garnier. Flow Control by Pulsed Jet in a Curved S-Duct: A Spectral Analysis. *AIAA Journal*, 53(10):2813–2827, 2015.

[76] E. Garnier, P. Sagaut, and M. Deville. Large eddy simulation of shock/boundary-layer interaction. *AIAA journal*, 40(10):1935–1944, 2002.

[77] E. Garnier, N. Adams, and P. Sagaut. *Large eddy simulation for compressible flows*. Springer Science & Business Media, 2009.

[78] E. Garnier, M. Leplat, J.C. Monnier, and J. Delva. Flow control by pulsed jet in a highly bended s-duct. In *6th AIAA Flow Control Conference*, 2012.

[79] C.W. Gear. Algorithm 407: Difsub for solution of ordinary differential equations [d2]. *Communications of the ACM*, 14(3):185–190, 1971.

[80] W.K. George. Recent advancements toward the understanding of turbulent boundary layers. *AIAA journal*, 44(11):2435–2449, 2006.

[81] F.B. Gessner. The origin of secondary flow in turbulent flow along a corner. *Journal of Fluid Mechanics*, 58(1):1–25, 1973.

[82] R.H.M. Giepman, A. Srivastava, F.F.J. Schrijer, and B.W.v. Oudheusden. Mach and Reynolds Number Effects on the Wake Properties of Microramps. *AIAA Journal*, 54(11):3481–3494, 2016.

[83] G. Godard and M. Stanislas. Control of a decelerating boundary layer. Part 1: Optimization of passive vortex generators. *Aerospace Science and Technology*, 10 (3):181–191, April 2006.

[84] G. Godard and M. Stanislas. Control of a decelerating boundary layer. Part 3: Optimization of round jets vortex generators. *Aerospace Science and Technology*, 10 (6):455–464, September 2006.

[85] G. Godard, J.M. Foucaut, and M. Stanislas. Control of a decelerating boundary layer. Part 2: Optimization of slotted jets vortex generators. *Aerospace Science and Technology*, 10(5):394–400, July 2006.

[86] E.L. Goldsmith and J. Seddon. *Practical intake aerodynamic design*. Amer Inst of Aeronautics &, 1993.

[87] E. Goncalves and R. Houdeville. Turbulence model and numerical scheme assessment for buffet computations. *International Journal for Numerical Methods in Fluids*, 46 (11):1127–1152, 2004.

[88] D. Han, V. Orozco, and M.G. Mungal. Gross-entrainment behavior of turbulent jets injected obliquely into a uniform crossflow. *AIAA journal*, 38(9):1643–1649, 2000.

[89] L. Hansen and J. Bons. Flow measurements of vortex generator jets in separating boundary layer. *Journal of Propulsion and Power*, 22(3):558–566, 2006.

[90] J.H. Holland et al. *Adaptation in natural and artificial systems: an introductory analysis with applications to biology, control, and artificial intelligence*. MIT press, 1992.

[91] D. Hue, Q. Chanzy, and S. Landier. DPW-6: Drag Analyses and Increments Using Different Geometries of the Common Research Model Airliner. *Journal of Aircraft*, Jan 2017.

[92] R. Humble, G. Elsinga, F. Scarano, and B. Van Oudheusden. Three-dimensional instantaneous structure of a shock wave/turbulent boundary layer interaction. *Journal of Fluid Mechanics*, 622:33–62, 2009.

[93] G. Humrutha, M. Kaushik, and K.P. Sinhamahapatra. Shock-Boundary Layer Interaction Control using Innovative Micro-Vortex Generators in Supersonic Intake. In *47th AIAA Fluid Dynamics Conference*. American Institute of Aeronautics and Astronautics, June 2017.

[94] D.J. J. Toal, N.W. Bressloff, and A.J. Keane. Kriging hyperparameter tuning strategies. *AIAA journal*, 46(5):1240–1252, 2008.

[95] L. Jacquin. Phenomenological description and simplified modeling of the vortex wake issuing from a jet in a cross-flow. *RECHERCHE AEROSPATIALE*, (2):117–133, 1994.

[96] H. Johari. Scaling of fully pulsed jets in crossflow. *AIAA journal*, 44(11):2719–2725, 2006.

[97] D.R. Jones. A taxonomy of global optimization methods based on response surfaces. *Journal of global optimization*, 21(4):345–383, 2001.

[98] R. Joslin, R. Kunz, and D. Stinebring. Flow control technology readiness - Aerodynamic versus hydrodynamic. In *18th Applied Aerodynamics Conference*, 2000.

[99] A.R. Karagozian. Transverse jets and their control. *Progress in Energy and Combustion Science*, 36(5):531 – 553, 2010.

[100] A.R. Karagozian. The jet in crossflow. *Physics of Fluids*, 26(10):101303, 2014.

[101] J. Kennedy and R. Eberhart. Particle swarm optimization (PSO). In *Proc. IEEE International Conference on Neural Networks, Perth, Australia*, 1995.

[102] Z.U. Khan and J.P. Johnston. On vortex generating jets. *International Journal of Heat and Fluid Flow*, 21(5):506 – 511, 2000.

[103] S. Koike and H. Babinsky. Vortex generators for corner separation caused by shock-wave/boundary-layer interactions. *Journal of Aircraft*, 56(1):239–249, 2018.

[104] A.N. Kolmogorov. Local turbulence structure in incompressible fluids at very high reynolds numbers. In *Dokl. Akad. Nauk SSSR*, 1941.

[105] J. Kostas, J.M. Foucaut, and M. Stanislas. The Flow Structure Produced by Pulsed-jet Vortex Generators in a Turbulent Boundary Layer in an Adverse Pressure Gradient. *Flow, Turbulence and Combustion*, 78(3):331–363, Jun 2007.

[106] A. Kourta, G. Petit, J.C. Courty, and J.P. Rosenblum. Buffeting in transonic flow prediction using time-dependent turbulence model. *International Journal for Numerical Methods in Fluids*, 49(2):171–182, 2005.

[107] D.G. Krige. A statistical approach to some basic mine valuation problems on the witwatersrand. *Journal of the Southern African Institute of Mining and Metallurgy*, 52(6):119–139, 1951.

[108] V. Kumar and F.S. Alvi. Use of High-Speed Microjets for Active Separation Control in Diffusers. *AIAA Journal*, 44(2):273–281, 2006.

[109] V. Kumar and F.S. Alvi. Toward Understanding and Optimizing Separation Control Using Microjets. *AIAA Journal*, 47(11):2544–2557, 2009.

[110] R. Laraufie. *Simulations avancées de turbulence pariétale à haut nombre de Reynolds sur des géométries curvilignes par une approche hybride RANS/LES*. PhD thesis, Université Pierre et Marie Curie, Jan 2012.

[111] G. Laruelle. Air Intakes : Role, Constraints and Design. In *ICASS Congress*, Jan 2002.

[112] S. Lee, E. Loth, and H. Babinsky. Normal shock boundary layer control with various vortex generator geometries. *Computers & Fluids*, 49(1):233 – 246, 2011.

[113] T. Leweke, S. Le Dizès, and C.H. Williamson. Dynamics and instabilities of vortex pairs. *Annual Review of Fluid Mechanics*, 48(1):507–541, 2016.

[114] M.J. Lighthill. On boundary layers and upstream influence ii. supersonic flows without separation. *Proceedings of the Royal Society of London. Series A. Mathematical and Physical Sciences*, 217(1131):478–507, 1953.

[115] J. Lin, F. Howard, D. Bushnell, and G. Selby. Investigation of several passive and active methods for turbulent flow separation control. In *AIAA 21st Fluid Dynamics, Plasma Dynamics and Lasers Conference*, Jun 1990.

[116] J.C. Lin. Review of research on low-profile vortex generators to control boundary-layer separation. *Progress in Aerospace Sciences*, 38(4–5):389–420, May 2002.

[117] M.-S. Liou. A sequel to ausm: Ausm+. *Journal of computational Physics*, 129(2): 364–382, 1996.

[118] C. Lopez Hernandez. PRF MEROVEE 3D Rapport de synthèse. 2019.

[119] H. Loyau, P. Batten, and M.A. Leschziner. Modelling shock/boundary-layer interaction with nonlinear eddy-viscosity closures. *Flow, turbulence and combustion*, 60 (3):257–282, 1998.

[120] F.K. Lu, Q. Li, and C. Liu. Microvortex generators in high-speed flow. *Progress in Aerospace Sciences*, 53:30–45, 2012.

[121] R.J. Margason. Fifty years of jet in cross flow research. *AGARD, Computational and Experimental Assessment of Jets in Cross Flow 10 p(SEE N 94-28003 07-34)*, 1993.

[122] G. Matheron. Principles of geostatistics. *Economic geology*, 58(8):1246–1266, 1963.

[123] F.R. Menter. Two-equation eddy-viscosity turbulence models for engineering applications. *AIAA journal*, 32(8):1598–1605, 1994.

[124] M.-C. Merienne, P. Molton, R. Bur, and Y.L. Sant. Pressure-Sensitive Paint Application to an Oscillating Shock Wave in a Transonic Flow. *AIAA Journal*, 53(11): 3208–3220, 2015.

[125] P. Molton, J. Dandois, A. Lepage, V. Brunet, and R. Bur. Control of Buffet Phenomenon on a Transonic Swept Wing. *AIAA Journal*, 51(4):761–772, 2013.

[126] M.D. Morris and T.J. Mitchell. Exploratory designs for computational experiments. *Journal of statistical planning and inference*, 43(3):381–402, 1995.

[127] H. Ogawa, H. Babinsky, M. Patzold, and T. Lutz. Shock-wave/boundary-layer interaction control using three-dimensional bumps for transonic wings. *AIAA Journal*, 46(6):1442–1452, 2008.

[128] K. Oswatitsch. Pressure recovery for missiles with reaction propulsion at high supersonic speeds (the efficiency of shock diffusers). pages 290–323, 1944.

[129] R. Pain, P.-E. Weiss, and S. Deck. Zonal detached eddy simulation of the flow around a simplified launcher afterbody. *AIAA Journal*, 52(9):1967–1979, 2014.

[130] P.-Y. Pamart. *Contrôle des décollements en boucle fermée*. PhD thesis, Université Pierre et Marie Curie, 2011.

[131] M. Pamiès. *Contrôle d'une couche limite turbulente au moyen d'un micro-sytème distribué*. PhD thesis, Université de Lille, October 2008.

[132] A.G. Panaras and F.K. Lu. Micro-vortex generators for shock wave/boundary layer interactions. *Progress in Aerospace Sciences*, 74:16 – 47, 2015.

[133] C. Paulson. pyKriging Toolbox, 2017. URL https://zenodo.org/record/21389.

[134] H.H. Pearcey. *Shock induced separation and its prevention*. Pergamon, 1961.

[135] H.H. Pearcey, K. Rao, and D.M. Sykes. Inclined air-jets used as vortex generators to suppress shock-induced separation. *AGARD, Computational and Experimental Assessment of Jets in Cross Flow 10 p(SEE N 94-28003 07-34)*, 1993.

[136] S. Piponniau, J.P. Dussauge, J.F. Debiève, and P. Dupont. A simple model for low-frequency unsteadiness in shock-induced separation. *Journal of Fluid Mechanics*, 629:87–108, June 2009.

[137] P.K. Rabey, S.P. Jammy, P.J.K. Bruce, and N.D. Sandham. Two-dimensional unsteadiness map of oblique shock wave/boundary layer interaction with sidewalls. *Journal of Fluid Mechanics*, 871, July 2019.

[138] M.R. Rao. *An experimental investigation of the use of air jet vortex generators to control shock induced boundary layer separation.* PhD thesis, City University London, 1988.

[139] N. Renard. *Simulations numériques avancées et analyses physiques de couches limites turbulentes à grand nombre de Reynolds.* PhD thesis, Université Pierre et Marie Curie - Paris VI, January 2016.

[140] G.S. Rixon and H. Johari. Development of a steady vortex generator jet in a turbulent boundary layer. *Journal of fluids engineering*, 125(6):1006–1015, 2003.

[141] D.P. Rizzetta, O.R. Burggraf, and R. Jenson. Triple-deck solutions for viscous supersonic and hypersonic flow past corners. *Journal of Fluid Mechanics*, 89(3):535–552, 1978.

[142] J.C. Robinet and G. Casalis. Etude des instabilités globales dans des écoulements turbulents décollés en présence d'une onde de choc. 2014.

[143] J.-P. Rosenblum. An overview of flow control activities at Dassault Aviation over the last 25 years. *The Aeronautical Journal*, 120(1225):391–414, March 2016.

[144] C. Roussel. *Modelisation et simulation de l'interaction onde de choc/couche limite turbulente en écoulement interne avec effets de coins.* PhD thesis, 2016.

[145] M. Rybalko, H. Babinsky, and E. Loth. Vortex generators for a normal shock/boundary layer interaction with a downstream diffuser. *Journal of Propulsion and Power*, 28(1):71–82, 2012.

[146] K. Sabnis and H. Babinsky. Nozzle geometry effects on corner boundary layers in supersonic wind tunnels. *AIAA Journal*, 57(8):3620–3623, 2019.

[147] P. Sagaut. *Large eddy simulation for incompressible flows: an introduction.* Springer Science & Business Media, 2006.

[148] P. Sagaut and S. Deck. Large eddy simulation for aerodynamics: status and perspectives. *Philosophical Transactions of the Royal Society of London A: Mathematical, Physical and Engineering Sciences*, 367(1899):2849–2860, July 2009.

[149] P. Sagaut, S. Deck, and M. Terracol. *Multiscale and multiresolution approaches in turbulence: LES, DES and hybrid RANS/LES methods: applications and guidelines.* World Scientific, 2006.

[150] N.D. Sandham, Y.F. Yao, and A.A. Lawal. Large-eddy simulation of transonic turbulent flow over a bump. *International Journal of Heat and Fluid Flow*, 24(4): 584–595, 2003.

[151] F. Sartor. *Unsteadiness in transonic shock-wave/boundary-layer interactions: experimental investigation and global stability analysis.* PhD thesis, Aix-Marseille Université, March 2014.

[152] F. Sartor, G. Losfeld, and R. Bur. PIV study on a shock-induced separation in a transonic flow. *Experiments in fluids*, 53(3):815–827, 2012.

[153] F. Sartor, G. Losfeld, B. Leclaire, and R. Bur. Characterization by PIV of the effect of vortex generators in a transonic separated flow. In *PIV13; 10th International Symposium on Particle Image Velocimetry, Delft, The Netherlands, July 1-3, 2013*, 2013.

[154] F. Sartor, C. Mettot, R. Bur, and D. Sipp. Unsteadiness in transonic shock-wave/boundary-layer interactions: experimental investigation and global stability analysis. *Journal of Fluid Mechanics*, 781:550–577, 2015.

[155] F. Scarano. Tomographic piv: principles ans practice. *Measurement Science and Technology*, 24(012001), 2013.

[156] J. Seddon and E. GoldSmith. *Intake Aerodynamics*. Collins Professional and Technical Books, 1985.

[157] S.R. Shapiro, J. King, R.T. M'Closkey, and A.R. Karagozian. Optimization of controlled jets in crossflow. *AIAA journal*, 44(6):1292–1298, 2006.

[158] J. Smagorinsky. General circulation experiments with the primitive equations: I. the basic experiment. *Monthly weather review*, 91(3):99–164, 1963.

[159] L.J. Souverein and J.-F. Debiève. Effect of air jet vortex generators on a shock wave boundary layer interaction. *Experiments in Fluids*, 49(5):1053–1064, November 2010.

[160] P. Spalart and S. Allmaras. A one-equation turbulence model for aerodynamic flows. In *30th aerospace sciences meeting and exhibit*, 1992.

[161] P. Spalart, W. Jou, M. Strelets, and S. Allmaras. Comments on the feasibility of les for wings, and on a hybrid rans/les approach. In *Symp. Eng. Turb. Modelling and Measurements*, May 1998.

[162] P.R. Spalart, S. Deck, M.L. Shur, K.D. Squires, M.K. Strelets, and A. Travin. A new version of detached-eddy simulation, resistant to ambiguous grid densities. *Theoretical and computational fluid dynamics*, 20(3):181, 2006.

[163] L. Surber and J. Tinapple. Inlet Flow Control Technology: Learning from History, Reinventing the Future. In *American Institute of Aeronautics and Astronautics*. American Institute of Aeronautics and Astronautics, January 2012.

[164] K. Taira, S.L. Brunton, S.T. Dawson, C.W. Rowley, T. Colonius, B.J. McKeon, O.T. Schmidt, S. Gordeyev, V. Theofilis, and L.S. Ukeiley. Modal analysis of fluid flows: An overview. *Aiaa Journal*, pages 4013–4041, 2017.

[165] F. Ternoy, J. Dandois, F. David, and M. Pruvost. Overview of Onera Actuators for Active Flow Control. *HAL archives-ouvertes.fr*, pages 1–14, August 2015.

[166] N. Titchener and H. Babinsky. Shock Wave/Boundary-Layer Interaction Control Using a Combination of Vortex Generators and Bleed. *AIAA Journal*, 51(5):1221–1233, 2013.

[167] N. Titchener and H. Babinsky. A review of the use of vortex generators for mitigating shock-induced separation. *Shock Waves*, 25(5):473–494, 2015.

[168] E. Touber and N.D. Sandham. Large-eddy simulation of low-frequency unsteadiness in a turbulent shock-induced separation bubble. *Theoretical and Computational Fluid Dynamics*, 23(2):79–107, 2009.

[169] A. Towne, O.T. Schmidt, and T. Colonius. Spectral proper orthogonal decomposition and its relationship to dynamic mode decomposition and resolvent analysis. *Journal of Fluid Mechanics*, 847:821–867, 2018.

[170] S. Trapier, P. Duveau, and S. Deck. Experimental study of supersonic inlet buzz. *AIAA journal*, 44(10):2354–2365, 2006.

[171] S. Trapier, S. Deck, and P. Duveau. Delayed Detached-Eddy Simulation and Analysis of Supersonic Inlet Buzz. *AIAA Journal*, 46(1):118–131, 2008.

[172] S.B. Verma, C. Manisankar, and P. Akshara. Control of shock-wave boundary layer interaction using steady micro-jets. *Shock Waves*, 25(5):535–543, Sep 2015.

[173] A.W. Vreman. *Direct and large-eddy simulation of the compressible turbulent mixing layer*. PhD thesis, 1995.

[174] R. Wallis. The use of air jets for boundary layer control. 1952.

[175] B. Wang, N.D. Sandham, Z. Hu, and W. Liu. Numerical study of oblique shock-wave/boundary-layer interaction considering sidewall effects. *Journal of Fluid Mechanics*, 767:526–561, 2015.

[176] B. Wieneke. Volume self-calibration for 3D particle image velocimetry. *Experiments in fluids*, 45(4):549–556, 2008.

[177] X. Xiang. *Corner effects for oblique shock wave/turbulent boundary layer interactions in rectangular channels*. PhD thesis, University of Cambridge, 2018.

[178] X. Xiang and H. Babinsky. An experimental study of corner flow control applied to an oblique shock-wave/boundary-layer interaction. In *2018 AIAA Aerospace Sciences Meeting*, 2018.

[179] X. Xiang and H. Babinsky. Corner effects for oblique shock wave/turbulent boundary layer interactions in rectangular channels. *Journal of Fluid Mechanics*, 862:1060–1083, 2019.

[180] Y. Yang, J. Tang, and C. Liu. LES Analysis on Shock-Vortex Ring Interaction . In | *54th AIAA Aerospace Sciences Meeting*, Jun 2016.

[181] X. Zhang. Computational analysis of co-and contra-rotating streamwise vortices in a turbulent boundary layer. In *23rd Fluid Dynamics, Plasmadynamics, and Lasers Conference*, 1993.

Optimization of fluidic control of separation in a transonic channel flow

Flow control of transonic shock-wave / boundary-layer interactions is investigated in the context of transonic air inlets. A shock-wave / turbulent boundary-layer configuration with separation zone is considered in the transonic wind tunnel S8Ch. Simulations using Reynolds Averaged Navier-Stokes (RANS) and Zonal Detached Eddy Simulation (ZDES, an hybrid method between RANS and Large Eddy Simulation, LES) modeling are carried out to compute the mean flow and its fluctuations in the interaction region. The main separation occurring in the middle of the test section is controlled by fluidic Vortex Generators (VGs). Using RANS modeling, ten VGs are positioned along the span, upstream of the interaction. A first Kriging algorithm is then used to optimize the pitch and skew angles of the VGs. An optimal configuration found is thereafter defined and a second Kriging algorithm is used to enhance the efficiency of the control of the corner flow by two more VGs, which position and angles are varied. The goal of these optimizations is to minimize the total pressure losses downstream of the interaction. The optimal configuration leads to slightly reverse jets with respect to the main flow. A comparison of the vorticity patterns generated by aligned or reverse jets is therefore conducted.

This control set-up and a more standard fluidic control (with jets oriented downstream) are adapted to the transonic wind tunnel test section. These control set-ups, as well as the clean case, are described using notably static and unsteady pressure measurements and tomographic Particle Image Velocimetry (PIV). These measurements allow to precisely quantify the efficiency of the two different control set-ups and confirm the interest of slightly reverse jets in order to improve the efficiency of the control of corner flow separation.

Keywords :

TRANSONIC ; SHOCK-WAVE ; BOUNDARY LAYER ; SEPARATION ; CONTROL ; OPTIMIZATION

Optimisation du contrôle fluidique de décollement en écoulement transsonique de canal

La présente étude porte sur le contrôle de l'interaction onde de choc / couche limite dans le cadre des prises d'air d'avions transsoniques. On considère une configuration d'interaction onde de choc / couche limite turbulente avec décollement dans la soufflerie transsonique S8Ch. Des simulations Reynolds Averaged Navier-Stokes (RANS) et Zonal Detached Eddy Simulation (ZDES, méthode hybride entre la méthode RANS et la méthode Large Eddy Simulation, LES) sont entreprises afin de modéliser le champ moyen et les fluctuations de l'écoulement dans la région de l'interaction.

Le décollement principal en milieu de veine est contrôlé à l'aide de générateurs de tourbillons fluidiques (VGs). En utilisant la modélisation RANS, dix VGs sont positionnés selon l'envergure et en amont de l'interaction. Un premier algorithme de Krigeage est utilisé pour optimiser les angles d'incidence et de dérapage des VGs. Une configuration optimale est ainsi définie et un second algorithme de Krigeage est utilisé pour améliorer l'efficacité du contrôle du décollement de coin en ajoutant deux VGs, dont les positions et angles d'orientation sont variés. Le but de ces optimisations est de minimiser la perte de pression d'arrêt en aval de l'interaction. La configuration optimale conduit à des orientations de jets à contre-courant de l'écoulement principal. Ce dispositif de contrôle ainsi qu'un contrôle plus standard (avec des jets orientés vers l'aval) sont montés dans la veine d'essais de la soufflerie transsonique. Ces configurations contrôlées, ainsi que le cas non contrôlé, sont qualifiées notamment grâce à des mesures de pressions continues et instationnaires ainsi que de la Particle Image Velocimetry (PIV) tomographique. Ces mesures permettent de quantifier avec précision l'efficacité des deux dispositifs de contrôle et confirme l'intérêt des jets orientés légèrement à contre-courant pour augmenter l'efficacité du contrôle des décollements de coin.

Mots-clés :

TRANSSONIQUE ; ONDE DE CHOC ; COUCHE LIMITE ; DECOLLEMENT ; CONTROLE ; OPTIMISATION

ONERA
THE FRENCH AEROSPACE LAB

BP 80100 - Chemin de la Hunière FR-91123 PALAISEAU CEDEX - Tél. : +33 1 80 38 60 60 - Fax : +33 1 80 38 65 10

www.onera.fr